



Veröffentlichungen der DGK

Ausschuss Geodäsie der Bayerischen Akademie der Wissenschaften

Reihe C

Dissertationen

Heft Nr. 855

Nicolas Garcia Fernandez

**Simulation Framework for Collaborative Navigation:
Development - Analysis - Optimization**

München 2020

Verlag der Bayerischen Akademie der Wissenschaften

ISSN 0065-5325

ISBN 978-3-7696-5267-3

Diese Arbeit ist gleichzeitig veröffentlicht in:

Wissenschaftliche Arbeiten der Fachrichtung Geodäsie und Geoinformatik der Universität Hannover

ISSN 0174-1454, Nr. 363, Hannover 2020



Veröffentlichungen der DGK

Ausschuss Geodäsie der Bayerischen Akademie der Wissenschaften

Reihe C

Dissertationen

Heft Nr. 855

Simulation Framework For Collaborative Navigation: Development – Analysis – Optimization

Von der Fakultät für Bauingenieurwesen und Geodäsie
der Gottfried Wilhelm Leibniz Universität Hannover
zur Erlangung des Grades
Doktor-Ingenieur (Dr.-Ing.)
genehmigte Dissertation

Vorgelegt von

M. Sc. Nicolas Garcia Fernandez

Geboren am 12.06.1988 in Betanzos, Spain

München 2020

Verlag der Bayerischen Akademie der Wissenschaften

ISSN 0065-5325

ISBN 978-3-7696-5267-3

Diese Arbeit ist gleichzeitig veröffentlicht in:
Wissenschaftliche Arbeiten der Fachrichtung Geodäsie und Geoinformatik der Universität Hannover
ISSN 0174-1454, Nr. 363, Hannover 2020

Adresse der DGK:



Ausschuss Geodäsie der Bayerischen Akademie der Wissenschaften (DGK)

Alfons-Goppel-Straße 11 • D – 80 539 München
Telefon +49 – 331 – 288 1685 • Telefax +49 – 331 – 288 1759
E-Mail post@dgk.badw.de • <http://www.dgk.badw.de>

Prüfungskommission:

Vorsitzender: Prof. Dr.-Ing. habil. Monika Sester

Referent: Prof. Dr.-Ing. Steffen Schön

Korreferenten: Prof. Dr. Andreas Wieser (ETH Zürich)
Prof. Dr.-Ing. habil. Christian Heipke

Tag der mündlichen Prüfung: 08.06.2020

© 2020 Bayerische Akademie der Wissenschaften, München

Alle Rechte vorbehalten. Ohne Genehmigung der Herausgeber ist es auch nicht gestattet,
die Veröffentlichung oder Teile daraus auf photomechanischem Wege (Photokopie, Mikrokopie) zu vervielfältigen

Abstract

Applications such as Intelligent Transportation Systems (ITS) heavily rely on the continuous availability of Position, Navigation and Timing (PNT) information in order to guarantee the safety of the users. This goal depends largely on the availability of Global Navigation Satellite Systems (GNSS) signals. However, it is well known that although GNSS represents a fairly continuous and time stable source of information for the localization, its performance is degraded in urban areas. To overcome the weakness of the GNSS standalone solution, the GNSS measurements are fused with measurements carried out with additional sensors, that increase the awareness of the ego vehicle with respect to the elements of the environment. The development of Vehicle to Everything (V2X) communication protocols enable the expansion of the principle of multi-sensor estimation to multi-vehicle approaches, giving birth to Collaborative Positioning (CP). CP is a network-based navigation technique, that is potentially suitable to increase the performance of the navigation solution, and the robustness against outliers and sensor failures.

The concept of CP resembles a geodetic network in which the nodes (vehicles) are moving. Thus, as in the case of geodetic static networks, the purpose of this thesis is to aid the understanding of the dynamic network sensitivity with respect to changes in its geometry, changes in the motion of the objects, or changes in the observations. Later, the findings can be used in order to determine the steps to follow in order to achieve an optimum solution. For this purpose, a simulation framework is designed, suitable to cost-effectively reproduce a wide range of collaborative scenarios. In this simulation framework, the measurements carried out with sensors mounted in different vehicles are fused in a Collaborative Extended Kalman Filter (C-EKF) in which the state parameters of all vehicles are simultaneously estimated. Then, the performance of the C-EKF is evaluated in different simulated scenarios, designed in order to highlight the most representative features of the estimation. In particular, the performance of the filter is evaluated by means of Monte Carlo (MC) simulations with different execution strategies, namely localization, localization with landmark uncertainty and SLAM. Then, the response of the estimation to changes in the sensor architecture and sensor measurement quality (changing geometries and observations) is evaluated. Also, the challenges that arise from the changing vehicle dynamics in the estimation are assessed, identifying the most vulnerable situations given a certain selected filter configuration, and establishing strategies that enable the identification of the processing parameters that maximize the performance of the filter.

Finally, the benefits of CP with respect to single vehicle approaches are explored. The initial assumptions are validated in a ten-vehicle collaborative scenario, analyzing the results both, locally (individual nodes) and globally (the whole network). In the local evaluation, the significant advantages of C-EKF obtained in vehicles that are individually equipped with disadvantageous sensor architectures are obtained at the cost of the vehicles with supportive sensor architectures, particularly in dynamic networks involving low number of vehicles. Finally, the global test results illustrate the beneficial outcome of CP techniques with respect to single vehicle approaches.

Keywords: Collaborative Navigation, Dynamic Network Optimization, (Collaborative) Extended Kalman Filter, Simulation Framework, Monte Carlo Simulation, Localization, SLAM, Multi-Sensor Fusion.

Kurzfassung

Verkehrstelematik (engl. Intelligent Transportation Systems (ITS)) und ähnliche Anwendungen sind in hohem Maße auf die kontinuierliche Verfügbarkeit von Positions-, Navigations- und Zeitinformationen (PNT) angewiesen, um die Sicherheit der Benutzer zu gewährleisten. Dieses Ziel hängt entscheidend von der Verfügbarkeit von Signalen eines globalen Navigationssatellitensystem (GNSS) ab. Während GNSS im Allgemeinen eine vergleichungsweise kontinuierliche und zeitstabile Informationsquelle für die Lokalisierung darstellt, ist jedoch bekannt, dass die Verfügbarkeit in städtischen Gebieten beeinträchtigt ist. Um die Fehleranfälligkeit der alleinstehenden GNSS-Lösung zu minimieren, werden die GNSS-Informationen mit Messungen zusätzlicher Sensoren kombiniert, wodurch die Wahrnehmung der Umgebung des Fahrzeugs verbessert wird. Neuerdings ermöglicht die Entwicklung von Vehicle to Everything (V2X) Kommunikationsprotokollen die Ausweitung des Prinzips der Multisensorschätzung auf Ansätze für mehrere Fahrzeuge, wodurch der Forschungsbereich der kollaborativen Positionierung (CP) begründet ist. CP ist ein netzwerkbasierter Navigationsansatz, der möglicherweise geeignet ist, die Performanz der Navigationslösung und die Robustheit gegen Ausreißer oder Sensorausfälle zu steigern.

Das Konzept von Collaborative Positioning (CP) ähnelt einem geodätischen Netzwerk, in dem sich die Knoten (Fahrzeuge) bewegen. Ähnlich wie bei statischen geodätischen Netzwerken ist deshalb das Ziel dieser Arbeit die Reaktion des dynamischen Netzwerks auf Änderungen seiner Geometrie, der Bewegung der Objekte oder der Beobachtungen zu verstehen. Später können die Ergebnisse verwendet werden, um die Schritte zu bestimmen, die zu befolgen sind, um eine optimale Lösung zu erreichen. Zu diesem Zweck, wird ein eigenes Simulationsframework entwickelt. In diesem Framework werden die Sensormessungen verschiedener Fahrzeuge in einem kollaborativen erweiterten Kalman-Filter (C-EKF) zusammengeführt, der gleichzeitig die Zustandsparameter jedes Fahrzeugs schätzt. Anschließend wird die Leistung des C-EKF in verschiedenen simulierten Szenarien, untersucht die so erstellt wurden, dass die repräsentativsten Eigenschaften der Positionsschätzung hervorgehoben werden. Anschließend wird die Reaktion der berechneten Lösung auf Änderungen der Sensorarchitektur und der Sensormessqualität (Änderungen der Geometrien und der Beobachtungen) bewertet. Des Weiteren werden die Herausforderungen untersucht, die sich aus der sich ändernden Fahrzeugdynamik bei der Lösungsberechnung ergeben. Dabei werden bei einer festgelegten Filterkonfiguration die fehleranfälligsten Situationen ermittelt und Strategien ausgewählt, mit denen die Parameter identifiziert werden können, die die Performanz des Filters maximieren.

Schließlich werden die Vorteile von CP im Vergleich zu Ansätzen basierend auf einzelnen Fahrzeugen untersucht. Durch dieses Experiment werden die anfänglichen Annahmen validiert und die Ergebnisse sowohl lokal (einzelne Knoten) als auch global (das gesamte Netzwerk) analysiert. Bei der lokalen Evaluierung werden signifikante Vorteile des C-EKF in Fahrzeugen erzielt, die mit nachteiligen Sensorarchitekturen aufweisen. Dies geschieht jedoch zum Nachteil der Fahrzeuge, die vorteilhafte Sensorarchitekturen ausgestattet sind, und gilt insbesondere für dynamische Netzwerke mit einer geringen Anzahl an Fahrzeugen. Die globalen Evaluationsergebnisse hingegen veranschaulichen den Vorteil von CP-Techniken im Vergleich zu Einzelfahrzeugansätzen.

Keywords: Kollaborative Navigation, dynamische Netzwerkoptimierung, (kollaborativer) erweiterter Kalman-Filter, Monte-Carlo-Simulation, Lokalisierung, SLAM, Multisensor-Fusion.

Acronyms

ADAS	Advanced Driver Assistance Systems
AL	Alert Limit
AT	Along-Track
BLS	Batch Least-Squares
C-EKF	Collaborative-Extended Kalman Filter
CP	Collaborative Positioning
DTRCV	Decoupled Constant Turn Rate and Constant Velocity
DARE	Discrete Algebraic Riccati Equation
DCM	Direction Cosine transformation matrix
DGNSS	Differential GNSS
DOP	Dilution of Precision
DSRC	Direct Short Range Communication
DTM	Digital Terrain Model
EKF	Extended Kalman Filter
FOD	First Order Design
IKG	Institut für Kartographie und Geoinformatik
ITS	Intelligent Transportation Systems
GBAS	Ground Based Augmentation Systems
GDOP	Geometric Dilution of Precision
GHM	Gauß - Helmert Model
GIS	Geographic Information Systems
GLONASS	Globalnaja Nawigazionnaja Sputnikowaja Sistema

GMM	Gauß- Markov Model
GNSS	Global Navigation Satellite Systems
GPS	Global Positioning System
HDOP	Horizontal Dilution of Precision
IMU	Inertial Measurement Unit
INS	Inertial Navigation Systems
IT	Information Technology
KF	Kalman Filter
LBS	Location-Based Services
LiDAR	Light Detection and Ranging
LKF	Linearized Kalman Filter
LoD	Level of Detail
LOS	Line-of-Sight
LS	Least-Squares
MC	Monte Carlo
MDB	Minimal Detectable Biases
NLOS	non-Line-of-Sight
PDF	Probability Density Function
PDOP	Position Dilution of Precision
PE	Position Error
PL	Protection Level
PNT	Position, Navigation and Timing
PoC	Proof of Concept
PPP	Precise Point Positioning
PRC	Pseudorange Corrections
PSD	Power Spectral Density
RADAR	Radio Detection and Ranging

RMSE	Root Mean Square Error
RRC	Range Rate Corrections
RSS	Received Signal Strength
RTK	Real Time Kinematic
SBAS	Satellite Based Augmentation Systems
SD	Standard Deviation
SLAM	Simultaneous Location and Mapping
SOD	Second Order Design
TDOP	Time Dilution of Precision
THOD	Third Order Design
ToA	Time of Arrival
ToF	Time of Flight
UAVs	Unmanned aerial vehicles
UWB	Ultra-wide band
V2X	Vehicle to Everything
V2I	Vehicle to Infrastructure
V2P	Vehicle to Pedestrian
V2V	Vehicle to Vehicle
VANET	Vehicular Ad-Hoc Networks
VCM	Variance-Covariance Matrix
VDOP	Vertical Dilution of Precision
WLAN	Wireless Local Area Network
XT	Cross-Track
ZOD	Zero Order Design

Contents

1	Introduction	1
1.1	Motivation and Research Questions	1
1.2	Objective Definition and Contributions	4
1.3	Outline of the Thesis	5
2	Theory and Related Work in Geodetic Network Analysis	7
2.1	Parameter Estimation in a Gauß-Markov Model	7
2.2	Parameter Estimation in a Gauß-Helmert Model	8
2.3	Geodetic Network Optimization: Theoretical Background and Related Work	10
2.3.1	Network Quality Criteria	10
2.3.2	Objective Functions and Optimality Criteria	14
2.3.3	Types of Optimization Problems	17
2.4	Discussion	18
3	Theoretical Background in Positioning and Navigation	21
3.1	Global Navigation Satellite Systems	21
3.1.1	GNSS Observables	22
3.1.2	GNSS positioning techniques	23
3.2	Inertial Navigation Systems	24
3.2.1	Coordinate Frames	24
3.2.2	Mechanization in the Navigation Frame	26
3.2.3	INS/GNSS Integration	28
3.3	Filtering Techniques	29
3.3.1	Bayes Filter	29
3.3.2	Kalman Filter	30
3.3.3	Linearized Kalman Filter	31
3.3.4	Extended Kalman Filter	32
3.4	Multi-Sensor Fusion	33
3.4.1	Laser Scanner	33
3.4.2	Stereo Cameras	34
3.4.3	Localization Versus Simultaneous Location and Mapping	34
4	State of the art in Collaborative Positioning	37
4.1	Introduction	37
4.2	Communication Architectures	38

4.3	Collaborative Positioning	39
4.3.1	GNSS Collaborative Positioning Approaches	39
4.3.2	Inertial Measurement Collaborative Positioning	40
4.3.3	Collaborative Positioning with Laser Scanner	40
4.3.4	Collaborative Positioning with Vision-Based Sensors	41
4.3.5	Collaborative Positioning Using Other Sensors	42
4.4	Simulation Technologies	43
4.4.1	Simulation Environments: Overview	43
4.4.2	Monte Carlo Methods	45
4.5	Discussion	46
5	Simulation Framework for Collaborative Scenarios	49
5.1	Design and Implementation	49
5.1.1	Vehicle Trajectories Simulator	49
5.1.2	Environmental Model	52
5.1.3	Measurement Generation	55
5.1.4	Collaborative-Extended Kalman Filter	62
5.1.5	Collaborative SLAM	66
5.1.6	Localization with Landmark Uncertainty	68
5.2	Application Example	69
5.2.1	Scenario and Setup	69
5.2.2	Sample Run	74
5.3	Discussion	88
6	Sensitivity Analysis of Dynamic Sensor Networks	91
6.1	Geodetic Network Optimization Problems for Dynamic Networks	91
6.2	Best Sensor Combination	93
6.2.1	Scenario and Sensor Setup	94
6.2.2	Sensitivity Results	96
6.3	Vehicle Dynamics Evaluation	102
6.3.1	Simulation Scenario and Setup	103
6.3.2	Process Noise Assessment	104
6.3.3	Process Noise to Measurement Noise Selection	113
6.4	Summary and Conclusions	115
7	Collaboration Versus Single Vehicle Estimation	117
7.1	Collaborative Navigation: Concept	117
7.2	Experiment Scenario and Setup	119
7.3	Collaboration Results	121
7.3.1	Accuracy and Precision Analysis	121
7.3.2	Integrity Analysis	126
7.4	Summary and Discussion	128

8	Conclusions	131
8.1	Summary	131
8.2	Outlook	134
	Bibliography	136
	Acknowledgements	147
	Curriculum Vitae	149

1 Introduction

1.1 Motivation and Research Questions

In recent years, the importance and scope of continuous Position, Navigation and Timing (PNT) information has increased significantly. Applications such as Intelligent Transportation Systems (ITS), Advanced Driver Assistance Systems (ADAS), pedestrian/ground/maritime/aerial-based navigation or Location-Based Services (LBS) are some of the multiple examples that rely on the continuous PNT information to ensure the safety of the user. The scope of this thesis is focused in particular on land-based navigation. In this matter, GNSS -space-based PNT- is the primary source to obtain continuous position, velocity and timing solutions globally, and it can be strengthened by Ground and/or Space-Based Augmentation Systems (GBAS and SBAS). However, GNSS-only solutions are rather fragile and require an open-sky view to achieve the highest performance. Otherwise, the solution obtained is degraded or unavailable, especially in urban environments, tunnels, car parks, and in relevant indoor applications (e.g. teams of firefighters). Multi-GNSS, differential GNSS or Precise Point Positioning (PPP) method can be used to increase the performance, but the performance is yet vulnerable to diffraction, interference and/or multipath. For this reason, it is not sufficient to rely on GNSS-only method, particularly for real-time critical applications, such as ADAS.

In order to overcome these shortcomings, the GNSS measurements are coupled with additional proprioceptive sensors (able to measure the values internal to the system, such as Inertial Measurement Unit (IMU)) or exteroceptive sensors (acquire information from the environment, like e.g. laser scanner, odometer, monocular or stereo cameras, radar, etc.) using so-called multi-sensor fusion techniques. The multi-sensor combinations not only lead in general to an enhancement of the navigation solution, but they increase the capabilities of the system in the geospatial data acquisition as well.

Moreover, the global civilian necessities require a higher amount of transportation of personnel and goods every year, with consequences at personal (safety), economical and environmental (increasing CO₂ emissions) levels (PAPDIMITRATOS ET AL., 2009). In the year 2018, Germany registered an annual mileage of 735 billions of kilometers covered by road itineraries. From the total amount, approx. 85% are carried out with passenger cars (KRAFTFAHRT-BUNDESAMT, 2018), thus the expanding interest in the development of technologies that improve safety, efficiency (congestion level reduction) and mobility. In the scope of this paradigm, the term ITS was born, which comprises all the new technologies designed in order to aid and warn drivers about potentially hazardous events, and ultimately, turn them into mere task supervisors. It is here where the pre-

viously mentioned multi-sensor solutions are crucial factors to enlarge the awareness of the agents and favor the connectivity between them. Geo-spatial information (maps) is considered the main infrastructure of the modern Information Technology (IT) world and enables the global finding and locating of individuals or devices.

With the release of intelligent vehicles, the exchange of information between the agents in a navigation scenario becomes crucial. For example, two vehicles approaching an intersection can modify their behavior in order to adapt to each other's maneuver. If this idea is expanded to groups of vehicles, the optimization of the outcome would result not only in a much more efficient traffic flow, but also prevent possible collisions. In addition, the capacities of the aided vehicle can be enhanced by sharing information from an aiding vehicle in better geometrical or visibility conditions (BEREFELT ET AL., 2004; DE PONTE-MÜLLER ET AL., 2016). In this context, the coordination between agents is achieved by establishing a communication scheme with the different elements liable to interfere with the traffic by using the so-called Vehicle to Everything (V2X) communication architecture (5GAA, 2016). This definition incorporates other more specific types of communication. Vehicle to Infrastructure (V2I) transfers information between vehicles and elements of the environment. In the message, information about traffic rules (e.g. time to red light) can be shared in order to anticipate possible factors that alter the predicted trajectory of the vehicle. It is equally important to communicate with the other moving objects, such as vehicles (Vehicle to Vehicle (V2V)) or pedestrians (Vehicle to Pedestrian (V2P)). Altogether, the situation of awareness of the different agents improves significantly, and therefore the most challenging events can be anticipated in order to optimize the traffic flow and reduce the probability of accidents. The scheme in which several multi-sensor systems enhance the performance in the navigation solution by sharing information between each other or with the elements of the environment is known as Collaborative Positioning (CP). This scheme could be regarded as the natural upgrade of multi-sensory solutions (KEALY ET AL., 2015).

The concept of CP resembles the same principle used in traditional geodetic networks, where the inter-nodal measurements are carried out in order to enhance the network capabilities in terms of accuracy, precision, reliability and economy (GRAFAREND, 1974). The geometrical similarities between both dynamic and static networks allow to predict the advantages (e.g. an increase in the redundancy of the adjustment enhances the precision and reliability of the system) that can be obtained with a network-based methodology by analyzing the findings from the classical geodetic network adjustment, optimization and deformation, which were mainly studied in the 1980s and 1990s (SCHMITT, 1985a; GRAFAREND AND SANSÒ, 1985; KUANG, 1996). However, in collaborative scenarios (dynamic networks), a large number of challenges arise due to the motion of the nodes, that must be analyzed in order to determine the strengths and weaknesses of CP techniques with respect to single vehicle approaches. The establishment and verification of hypotheses within the dynamic network field is fundamental to settle the current status of the research, and also to define the ground rules to be followed in future investigations.

Given this background, this thesis analyzes the potential benefits of collaborative techniques, in which the navigation scenario is understood as a dynamic network where the nodes (vehicles or multi-sensor systems) are inter-connected with V2V measurements. Consequently, the first step

in the research must consider the design and implementation of an algorithm that enables the simultaneous estimation of diverse multi-sensor systems navigating in a common area. Later, the performance of the algorithm must be analyzed with regard to the target of the research (dynamic network analysis).

Regarding the collaborative methodology, the existing Extended Kalman Filter (EKF) procedures are adapted to the simultaneous estimation of state parameters from different vehicles. The algorithm considers the processing of observations carried out with the sensors available in the research training group *Integrity and Collaboration in Dynamic Sensor Networks* (i.c.sens) project (SCHÖN ET AL., 2018), as well as the necessary V2V measurements to characterize the dynamic network. As a consequence, it is not difficult to forecast some challenges that emanate from collaborative estimations. On the one hand, it is necessary to deal with the logistic issues derived from the consideration of large amounts of data. The processing of data collected with exteroceptive sensors is normally associated to the necessity of additional algorithms for feature identification and reconstruction, which given the highly dynamic character of the scenes to be processed, can be fairly troublesome. On the other hand, the consideration of different vehicles elevates the degree of heterogeneity of the network. In dynamic estimations, the symbiotic relation between the vehicle dynamics and sensor observations should not be neglected. Hence, the complexity of the estimation increases significantly by the fact that the dynamic characteristics defined by the vehicles are invariably changing. As a result, the inefficacy of fixed or unique processing strategies can be anticipated.

The spotlight is thus put on the following research questions:

- What is the overall performance of the collaborative Extended Kalman Filter in terms of the navigation performance metrics (e.g. accuracy, integrity, reliability)?
- In which situations is the algorithm particularly capable or vulnerable?

The posterior dynamic network analysis is built upon the designed algorithm. For this reason, the answer to the previous research questions is essential to establish the foundation for the rest of the analysis.

Multi-sensor estimations are based on the combination of sensor measurements of different characteristics in order to overcome the limitations of each individual sensor and enhance the robustness of the navigation solution. This statement might easily lead to the assumption that the more sensors are used, the better is the understanding about the environment and the robustness of the vehicle localization. The same conclusion can be drawn from the addition of inter-connected vehicles to the network of interest. However, the addition of assets (sensors or vehicles) to the estimation, increases the overall cost of the system. Ultimately, the excessive cost and complexity of the product can be a decisive reason to prevent its commercialization. At the same time, the expanding development of sensors with different cost and characteristics offers the users a great flexibility to select the most suitable sensor combination to fulfill the desired need. Thus, additional questions arise:

- Which are the most adequate processing parameters (e.g. process noise power spectral density) that maximize the performance of the algorithm?
- What is the impact of each of the available sensors on the filter?
- Which sensor combination would drive down the cost of the sensor suite while still obtaining an acceptable result?

Finally, collaboration is the central topic of this thesis. In collaborative approaches, the number of vehicles and the quality of the V2V observations are the most distinctive factors. Accordingly, one additional set of research questions arises from the utilization of the promoted techniques:

- What are the benefits of collaborative techniques in comparison with single vehicle methodologies?
- How does the number of vehicles involved in the navigation scenario affect the overall estimation?
- Does the quality of the V2V observations strengthen or diminish the improvement of the outcome?

The contributions of this thesis aim to provide an answer to all of these research questions, both in terms of theoretical methodologies and practical experiments.

1.2 Objective Definition and Contributions

The goal of this thesis is to provide an extensive analysis of the suitability of CP compared to single vehicle approaches. In order to achieve this goal, the following contributions are made:

- **Design and implementation of a simulation environment.** In order to evaluate the potential of CP, experiments with numerous vehicles must be carried out. However, these would not only imply an extraordinary large amount of resources, but their realization in meaningful areas could be potentially hazardous as well. As a result, it is deemed suitable to implement a simulation environment capable to cost-effectively and safely represent realistic collaboration scenarios. The tool must consider the possibility to simulate the dynamics of a group of vehicles, the environment where they navigate and the sensor observations from the available sensors.
- **Collaborative-Extended Kalman Filter (C-EKF).** The design and implementation of a sensor measurement fusion algorithm suitable for the simultaneous estimation of state parameters from a group of vehicles is a crucial step in this thesis. All the experiments used for the analysis and evaluation are built upon this algorithm. It must also be able to process observations carried out with proprio- and exteroceptive measurements, as well as the necessary V2V observations.

- **Extensive analysis.** All factors to take into account in dynamic sensor networks are evaluated by means of Monte Carlo (MC) simulation techniques.
 - **Best sensor configurations.** The impact of each individual sensor on the estimation is extensively analyzed in a localization approach. Subsequently, the impact of the observation quality on the state estimation is evaluated. Here, if the measurement quality is related to real sensor specifications and their cost, conclusions can be taken on the configurations that yield acceptable results while driving down the cost of the sensor suite.
 - **Processing parameter analysis.** The wide variety of vehicle maneuvers produces a high impact on the state estimation. Abrupt maneuvers are translated into inconsistencies between the motion model selected to describe the vehicle dynamics and the actual physical model described by the vehicles, which are compensated with the addition of process noise to the motion model. In this thesis, an experiment is designed to analyze in detail the effects caused by inadequate process noise or motion model selection.
 - **Impact of collaboration.** Finally, there is an assessment of the suitability of collaborative approaches with respect to single vehicle approaches, identifying its most important strengths and drawbacks.

Lastly, the experiments carried out in the scope of this thesis are built upon the developed sensor measurement algorithm and further general assumptions. Some of them, although fully theoretical, enable the enhancement of features that could emerge in real datasets, masked by other dominant effects. Therefore, the object of the study is highlighted to efficiently approach the analysis of the research questions.

1.3 Outline of the Thesis

Following this introductory chapter, the thesis can be divided into seven additional chapters.

Chapter 2 contains an introduction to the theory and related work in geodetic network analysis, where the available methodologies to optimize geodetic networks in terms of the navigation performance criteria are discussed.

Chapter 3 introduces the basic concepts of positioning and navigation techniques, as well as the basic measurement fusion techniques necessary to understand the methodologies presented in this thesis.

Chapter 4 surveys the available methodologies developed in collaborative positioning, classifying them by means of the sensors used for the realization of the V2V measurements.

Chapter 5 discusses the design and implementation of the simulation environment used to answer the established research questions, together with the details about the sensor measurement fusion algorithm developed.

Chapter 6 contains a detailed analysis on the sensitivity of the dynamic network to changes in the configuration.

Chapter 7 discusses extensively the potential benefits and suitability of collaborative techniques with respect to single vehicle estimations.

Finally, the thesis is concluded with clear answers to the underlying research questions and a summary of the contributions. Furthermore, several starting points for further research are given.

2 Theory and Related Work in Geodetic Network Analysis

The analysis presented in this thesis is built upon the idea that the snapshot at every epoch of a collaborative navigation scenario can be understood as a geodetic network. Accordingly, the background, concepts, quality criteria and related literature for geodetic network optimization are introduced in this chapter.

Nevertheless, the chapter starts with the introduction to two adjustment techniques that are essential to understand the methodologies proposed in this thesis. The discussion starts with an introduction of the Gauß-Markov Model (GMM), crucial for the understanding of the later introduced methodologies for geodetic network optimization. Subsequently, the Gauß-Helmert Model (GHM) estimation methodology which allows the establishment of constraints between parameters and observations is explained.

2.1 Parameter Estimation in a Gauß-Markov Model

It is well known that a linear equation system consisting of the same number of equations as unknowns can have a unique solution. However, in overdetermined systems (equation systems with more linearly independent equations than unknowns), an optimal solution can only be estimated based on additional criteria. Overdetermined systems are advantageous, since the increased redundancy enables the enhancement of the accuracy, the internal reliability of the system and facilitates the identification of outliers. In these cases, the solution can be computed by minimizing the sum of the squared observation residuals, with a so-called Least-Squares (LS) estimation.

The GMM (KOCH, 1988) is a linear mathematical model developed for explicit measurement equations. In this model, the non-linear dependencies between the observations and parameters are linearized through Taylor expansion at an initial value for each parameter \mathbf{x}_0 . The system can be described by Eq. (2.1) and (2.2), which represent the *functional* and *stochastic* models, respectively

$$E(\mathbf{l}) = \mathbf{f}(\mathbf{x}_0) + \left. \frac{\partial \mathbf{f}}{\partial \mathbf{x}} \right|_{\mathbf{x}=\mathbf{x}_0} (\mathbf{x} - \mathbf{x}_0) = \mathbf{a}_0 + \mathbf{A} \Delta \mathbf{x}, \quad (2.1)$$

$$D(\mathbf{l}) = \mathbf{C}_l = \sigma_0^2 \mathbf{Q}_l = \sigma_0^2 \mathbf{W}_l^{-1}, \quad (2.2)$$

where

$E(\cdot)$ and $D(\cdot) :=$	expectation and dispersion operator, respectively,
$\mathbf{l} :=$	$n \times 1$ observation vector,
$\mathbf{A} :=$	$n \times u$ Jacobian/design matrix,
$\mathbf{W}_l :=$	$n \times n$ weight matrix of the observations,
$\mathbf{a}_0 :=$	$u \times 1$ vector of order 0 used in the Taylor expansion,
$\mathbf{f} :=$	$n \times 1$ functional relation between observations and parameters,
$\Delta \mathbf{x} :=$	$u \times 1$ vector of parameter increments,
$\mathbf{x}_0 :=$	$u \times 1$ initial parameter values
$\sigma_0^2 :=$	a-priori variance factor,

n being the total number of measurements and u the number of unknowns.

Eq. (2.1) can be rewritten as:

$$\mathbf{v} = \mathbf{A} \Delta \hat{\mathbf{x}} - (\mathbf{l} - \mathbf{a}_0). \quad (2.3)$$

where \mathbf{v} is the $n \times 1$ vector of residuals and $\Delta \hat{\mathbf{x}} = \hat{\mathbf{x}} - \mathbf{x}_0$

Since $n > u$, the system is overdetermined, and an unique solution is obtained by applying the weighted sum of the squared residuals minimization condition

$$\Omega = \mathbf{v}^T \mathbf{W}_l \mathbf{v} \rightarrow \min \quad \Delta \hat{\mathbf{x}} = \operatorname{argmin}_x \Omega. \quad (2.4)$$

The vector of estimated deviations with respect to the a-priori values can be computed as:

$$\Delta \hat{\mathbf{x}} = (\mathbf{A}^T \mathbf{W}_l \mathbf{A})^{-1} \mathbf{A}^T \mathbf{W}_l (\mathbf{l} - \mathbf{a}_0). \quad (2.5)$$

The estimated parameters, observations and residuals, as well as cofactor matrices can be obtained as:

$$\hat{\mathbf{x}} = \mathbf{x}_0 + \Delta \hat{\mathbf{x}}, \quad \mathbf{Q}_{\hat{x}\hat{x}} = (\mathbf{A}^T \mathbf{W}_l \mathbf{A})^{-1}, \quad (2.6)$$

$$\hat{\mathbf{l}} = \mathbf{Q}_{\hat{l}\hat{l}} \mathbf{W}_l \mathbf{l} \quad \mathbf{Q}_{\hat{l}\hat{l}} = \mathbf{A} \mathbf{Q}_{\hat{x}\hat{x}} \mathbf{A}^T, \quad (2.7)$$

$$\hat{\mathbf{v}} = -\mathbf{Q}_{\hat{v}\hat{v}} \mathbf{W}_l (\mathbf{l} - \mathbf{a}_0), \quad \mathbf{Q}_{\hat{v}\hat{v}} = \mathbf{Q}_l - \mathbf{Q}_{\hat{l}\hat{l}}. \quad (2.8)$$

An unbiased estimate for the a-posteriori variance factor is obtained by applying

$$\hat{\sigma}_0^2 = \frac{\hat{\mathbf{v}}^T \mathbf{W}_l \hat{\mathbf{v}}}{n - u}. \quad (2.9)$$

2.2 Parameter Estimation in a Gauß-Helmert Model

It was explained in the previous section that the functional model expresses the observations as an explicit function of the unknown parameters. However, this statement is not valid in some relevant

cases. As an example, assume that the parameters of an unknown plane (defined by its normal vector $\mathbf{n} = [a \ b \ c]$ and its distance to the origin d) are to be estimated from a set of observed 3D points $\mathbf{p}_{3D,i} = [p_x \ p_y \ p_z]_i^T$ (for $i = 1 \dots N$) that belong to it, fulfilling the *Hesse normal form* (KOCH, 1988):

$$\mathbf{n} \cdot \mathbf{p}_{3D,i}^T - d = 0 \quad i = 1 \dots N \quad \text{with} \quad |\mathbf{n}| = 1. \quad (2.10)$$

In this example the target is to find the optimal estimation of $\hat{\mathbf{n}}$ and \hat{d} so that the fitted (observed) points $\mathbf{p}_{3D,i} + \hat{\mathbf{v}}$ together with the estimated parameters fulfill the minimization condition given in Eq. (2.4). This is achieved by defining the functional model as a function of the observations and unknown parameters, such as:

$$\mathbf{g}(\mathbf{l} + \mathbf{v}, \mathbf{x}_0 + \Delta \mathbf{x}) \stackrel{!}{=} \mathbf{0}, \quad (2.11)$$

$$D(\mathbf{l}) = \sigma_0^2 \cdot \mathbf{Q}_l. \quad (2.12)$$

On the one hand, the functional model in Eq. (2.11) can be linearized and rewritten as:

$$\begin{aligned} \mathbf{g}(\mathbf{l}, \mathbf{x}_0) + \frac{\partial \mathbf{g}}{\partial \mathbf{l}} \bigg|_{\mathbf{l}, \mathbf{x}_0} \mathbf{v} + \frac{\partial \mathbf{g}}{\partial \mathbf{x}} \bigg|_{\mathbf{l}, \mathbf{x}_0} \Delta \mathbf{x} + \dots &= \mathbf{0} \\ \mathbf{w} + \mathbf{B} \mathbf{v} + \mathbf{A} \Delta \mathbf{x} &= \mathbf{0}. \end{aligned} \quad (2.13)$$

where \mathbf{B} is the Jacobian matrix for the observations and \mathbf{g} is the function of constrained dependencies between observations and parameters.

Since residuals $\mathbf{v}_w = \mathbf{B} \cdot \mathbf{v}$, with $\mathbf{v}_w = -(\mathbf{A} \Delta \mathbf{x} + \mathbf{w})$, we arrive at the equivalence with the GMM in (cf. Eq. (2.3)), and the minimization condition expressed in Eq. (2.4) can be applied.

On the other hand, the stochastic model can be also rewritten after the linearization as:

$$\mathbf{Q}_{ww} = \mathbf{B} \mathbf{Q}_l \mathbf{B}^T \quad \text{and} \quad \mathbf{W}_{ww} = (\mathbf{B} \mathbf{Q}_l \mathbf{B}^T)^{-1}. \quad (2.14)$$

As in Section 2.1 the normal equation, correlation vector, as well as cofactor matrices can be computed as:

$$\Delta \hat{\mathbf{x}} = (\mathbf{A}^T \mathbf{W}_{ww} \mathbf{A})^{-1} \mathbf{A}^T \mathbf{W}_{ww} (-\mathbf{w}), \quad \mathbf{Q}_{\hat{x}\hat{x}} = (\mathbf{A}^T \mathbf{W}_{ww} \mathbf{A})^{-1}, \quad (2.15)$$

$$\mathbf{c}_w = \mathbf{W}_{ww} (\mathbf{I} - \mathbf{A} \mathbf{Q}_{\hat{x}\hat{x}}^{-1} \mathbf{A}^T \mathbf{W}_{ww}) (-\mathbf{w}), \quad \hat{\mathbf{v}} = \mathbf{Q}_l \mathbf{B} \mathbf{c}_w. \quad (2.16)$$

In an iterative approach, the a-posteriori residual can be added to the original observation in order to obtain the iterated observation

$$\check{\mathbf{l}} = \mathbf{l}_0 + \hat{\mathbf{v}}, \quad (2.17)$$

and then the process can be repeated in order to converge into the optimum solution given by the adjustment.

2.3 Geodetic Network Optimization: Theoretical Background and Related Work

Optimization can be defined as the process or methodology of making something as effective or functional as possible. For instance, the parameters that describe the precision and/or reliability of geodetic networks depend only on the initial coordinates, the selected observation weights and the observation plan but not on the actual values of the observations. Therefore, these parameters can be determined in advance. This aids in the design step and guides the decision about how the network should be created or which instruments must be selected to obtain an optimum solution. The optimality of a network can be defined in the shape of an objective function, that once minimized or maximized represents the criteria used to define the quality of the network. The main purpose of the optimization is to aid the understanding of the network response with respect to changes in its geometry, or the weight distribution of the observations. In addition, an already created network can be optimized with the methodologies presented, although only small improvements are admitted in these cases.

Networks can be optimized with respect to different quality criteria. The available literature for geodetic network optimization discusses only methodologies for network optimization with respect to *precision*, *reliability* and *economy* (GRAFAREND AND SANSÒ, 1985). However, the nowadays increasing availability of sensors and algorithms for collaborative positioning demands the investigation of additional metrics to describe in detail the performance of a navigation system and the dynamics of the network. As a result, this section starts with an overview of the modern quality criteria for the navigation/positioning solutions (cf. Section 2.3.1). Then, the geodetic network optimality criteria for classic geodetic network optimization (SCHMITT (1982), GRAFAREND AND SANSÒ (1985), JÄGER (1988) and (KUANG, 1996)) are introduced in section 2.3.2, followed by the accepted classification for geodetic optimization problems in section 2.3.3.

2.3.1 Network Quality Criteria

The performance of a navigation system is normally described in terms of accuracy, precision, reliability, integrity, continuity and availability (HOFMANN-WELLENHOF, 2008). These metrics have been investigated in order to establish homogeneous standards that describe the specific levels of performance necessary to ensure safety in many civilian applications (KEALY ET AL., 2015).

Accuracy is defined as the degree to which an estimation, measurement or specification agrees to the true or correct value. This can be quantified by the weighted distance between estimated and true value (measured not only in metric units). In the navigation field, the accuracy is normally quantified using the Root Mean Square Error (RMSE) (Eq. (2.18)) (MISRA AND ENGE, 2006).

$$\text{RMSE} = \sqrt{\frac{\sum_{k=1}^K (\hat{\mathbf{x}}_k - \mathbf{x}_k^0)^2}{K}} \quad (2.18)$$

where $\hat{\mathbf{x}}_k$ and \mathbf{x}_k^0 are the estimated and true states to be compared, respectively. k is the measurement index and K represents the total number of measurements used to compute the RMSE.

Precision can be defined as the degree of refinement with which an operation is performed or the degree of repeatability of consecutive measurements under the same conditions. The difference with respect to accuracy must be clarified, since a set of biased observations carried out with the same sensor can show high precision (small deviations with respect to the mean value), but not high accuracy if the mean value is far from the nominal value. The Variance-Covariance Matrix (VCM) of the estimated states contains the precision information.

In geodetic network applications, precision can refer either to *local* or *global* precision. The *local* precision evaluates the precision of a node, quantified normally using confidence ellipses. For a confidence level of $1 - \gamma$, the 2D (Eq. (2.19)) and 3D (Eq. (2.20)) confidence ellipses can be computed using the following quadratic equations:

$$P \left\{ (\hat{\mathbf{x}}_V - \mathbf{x}_V)^T \mathbf{C}_{\hat{x}\hat{x}V}^{-1} (\hat{\mathbf{x}}_V - \mathbf{x}_V) \leq \chi_{2,1-\gamma}^2 \right\} = 1 - \gamma, \quad (2.19)$$

$$P \left\{ (\hat{\mathbf{x}}_V - \mathbf{x}_V)^T \mathbf{C}_{\hat{x}\hat{x}V}^{-1} (\hat{\mathbf{x}}_V - \mathbf{x}_V) \leq \chi_{3,1-\gamma}^2 \right\} = 1 - \gamma, \quad (2.20)$$

where P refers to probability, $\hat{\mathbf{x}}_V$ and \mathbf{x}_V are the vector of estimated and true coordinates of the node V respectively, and $\mathbf{C}_{\hat{x}\hat{x}V}^{-1}$ is the VCM sub-matrix of the node V extracted from $\mathbf{C}_{\hat{x}\hat{x}}$. The eigenvectors $\boldsymbol{\nu}_i$ and eigenvalues λ_i of $\mathbf{C}_{\hat{x}\hat{x}V}$ yield the orientation and the semi-axis length of the confidence ellipse.

The *global* precision evaluates the overall precision of the network and the relation between points. This metric can be derived from the $\mathbf{C}_{\hat{x}\hat{x}}$ matrix, obtaining the so called Helmert form:

$$\sigma_H^2 = \frac{\text{tr}(\mathbf{C}_{\hat{x}\hat{x}})}{k} = \frac{1}{k} \sum_{i=1}^k \lambda_i, \quad (2.21)$$

where the operator tr represents the trace of the matrix and k refers to the epoch.

Reliability. The reliability of the estimated results plays a crucial role in the evaluation of the robustness. The indepotent matrix $\mathbf{C}_{\hat{v}\hat{v}} \mathbf{W}_{ll}$ contains the reliability information (Eq. (2.8)).

The goal of reliability analysis is to identify gross errors and the evaluation of the network deformations caused by non-detectable errors. In order to achieve this goal, the influence that each error has on the residual is measured by computing the redundancy numbers r_i :

$$r_i = (\mathbf{Q}_{\hat{v}\hat{v}} \mathbf{W}_{ll})_{i,i}. \quad (2.22)$$

In classical networks, the redundancy number of each observation gives information about its controllability, allowing to classify them into observations with high reliability (but maybe unnecessary, $r_i \geq 0.9$), good reliability ($0.3 \leq r_i < 0.9$), bad reliability ($r_i < 0.3$) and uncontrolled observations ($r_i = 0$), always assuming uncorrelated observations.

As in the case of precision, two different types of reliability can be evaluated: *internal* and *external* reliability. The *internal* reliability consists in evaluating how well the measurements agree geometrically with each other. Also, the limit over which a gross error can be detected (also known as Minimal Detectable Biases (MDB), $\nabla l_{0,i}$) can be computed with (BAARDA, 1968):

$$\nabla l_{0,i} = \delta_{0,i}(\gamma_0, \beta_0) \cdot \frac{\sigma_{l_i}}{\sqrt{r_i}}, \quad (2.23)$$

where β_0 is the significant level at the hypothesis test with detection power γ_0 , and $\delta_{0,i}$ is the non-centrality parameter of the distribution, here assuming a normal distribution and uncorrelated observations.

In the *external* reliability, the effect that an undetected outlier has on the overall adjustment is evaluated by computing (BAARDA, 1968)

$$\nabla \mathbf{x}_{0,i} = \frac{\delta_{0,i}}{\sqrt{r_i}} \cdot \mathbf{C}_{\hat{x}\hat{x}} \bar{\mathbf{a}}_i^T = \mathbf{Q}_{\hat{x}\hat{x}} p_i \bar{\mathbf{a}}_i^T \nabla l_{0,i}. \quad (2.24)$$

Also, the network deformation can be considered as a global measure for the *external* reliability and it can be computed as:

$$\|\nabla_{0,\hat{x}}\|_{\mathbf{C}_{\hat{x}\hat{x}}^{-1}} = \frac{\nabla_0 l_i}{\sigma_{l_i}} \cdot \sqrt{\bar{\mathbf{a}}_i^T \mathbf{Q}_{\hat{x}\hat{x}} \bar{\mathbf{a}}_i} p_i = \frac{\nabla_0 l_i}{\sigma_{l_i}} \sqrt{u_{x_i}} = \delta_{0,i} \cdot \sqrt{\frac{u_{x_i}}{r_i}}. \quad (2.25)$$

Integrity is the level of trust that can be placed in the solution provided by the system, and/or the capacity of the system to provide warnings when the system cannot perform the expected operation. The integrity is normally characterized by means of an *integrity risk*, that can be defined as the probability that an undetected gross error is processed by the system without issuing an alert. This probability of miss-detection shows a clear synergy with the external reliability. In contrast with the typical significance levels used for the evaluation of the accuracy (5% – 0.01%), the integrity risks are typically defined with much smaller values (10^{-7} – 10^{-9}) due to the higher safety requirements. The integrity is measured by means of the concepts *Alert Limit*, *Integrity Risk*, *Protection Level* and *Time to Alert* (ICAO, 2006).

- *Alert Limit* (AL) is the threshold of the positioning solution not to be exceeded without alerting the user. In autonomous navigation, one proposal it is to define the lateral and longitudinal AL as a function of the vehicle and road dimensions (REID ET AL., 2019):

$$\text{Lateral AL} = (w_r - w_v)/2, \quad (2.26)$$

$$\text{Longitudinal AL} = (l_r - l_v)/2, \quad (2.27)$$

where w_r and l_r are the dimensions (width and length) of the bounding box that would guarantee that the vehicle is contained in the road lane, and w_v and l_v are the vehicle dimensions.

- *Time to Alert* is the maximum allowed time for the system out of tolerance to display the alert.
- *Integrity Risk* is the probability that the position error exceeds the alert limit at any time.
- *Protection Level* (PL) is an statistical bound error that guarantees that the probability of the error is smaller than the integrity risk. Depending on the intended purpose, the PL can be computed following different methodologies. One way is defined by the International Civil

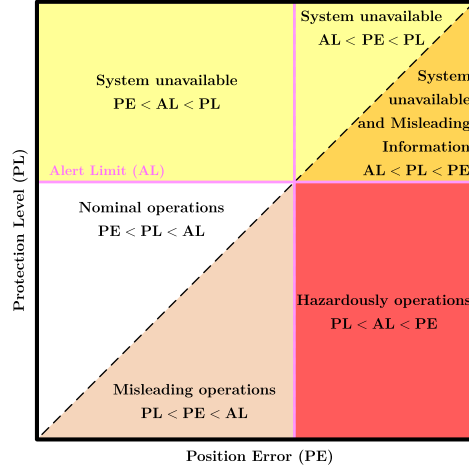


Figure 2.1: Integrity Stanford Diagram (NAVIPEDIA, 2014)

Aviation Organization (ICAO), based on the cofactor matrix $\mathbf{Q}_{\hat{x}\hat{x}}$ (transferred to the local topocentric frame):

$$\text{HPL} = \kappa_H \sigma_0 \sqrt{\frac{q_{nn} + q_{ee}}{2} + \sqrt{\left(\frac{q_{nn} - q_{ee}}{2}\right)^2 + q_{ne}^2}}, \quad (2.28)$$

$$\text{VPL} = \kappa_V \sigma_0 \sqrt{q_{uu}}, \quad (2.29)$$

where q_{nn} , q_{ee} , q_{uu} and q_{ne} correspond to the north, east and up variances, and covariance between north and east coordinate, respectively. σ_0 is the a-priori variance factor of the distribution, κ_H and κ_V are critical values derived from the Rayleigh distribution. ICAO (2006) defines $\kappa_H = 6.0$ and $\kappa_V = 5.33$ in precision approaches and approaches with vertical guidance.

According to REID ET AL. (2019), it is also possible to compute the lateral and longitudinal PL by means of the vehicle and road dimensions as:

$$\text{Lateral PL} = \delta_{lat} + (\delta_{lon} + l_v/2) \delta\psi + \delta_{vert} \delta\theta, \quad (2.30)$$

$$\text{Longitudinal PL} = \delta_{lon} + (\delta_{lat} + w_v/2) \delta\psi + \delta_{vert} \delta\phi, \quad (2.31)$$

$$\text{VPL} = \delta_{vert} + (\delta_{lat} + w_v/2) \delta\theta + (\delta_{lon} + l_v/2) \delta\phi, \quad (2.32)$$

where δ_{lat} , δ_{lon} and δ_{vert} are the lateral, longitudinal and vertical deviations relative to the nominal position; and $\delta\phi$, $\delta\theta$ and $\delta\psi$ are the errors in the orientation.

The integrity (and the previously described concepts) is normally evaluated using *Stanford diagrams* (NAVIPEDIA, 2014) (See Figure 2.1). This consists on a graphical representation of the integrity events that allows the distinction between *misleading information* (when the Position Error (PE) exceeds the PL but not the AL) and *hazardously misleading information* (when the position error exceeds the AL).

Continuity of the system is the capability to perform the intended task without non-scheduled interruptions. This metric is directly related to integrity and reliability, since in order to maintain

its performance continuously, a system must perfectly identify the outliers and hazardous events and give the user the chance to abort the operation.

Availability: a system is available when accuracy, precision, reliability, integrity and continuity criteria are fulfilled.

Moreover, DE PONTE-MÜLLER (2017a) introduces additional requirements for the performance evaluation of multi-sensor systems where ranging sensor measurements are considered (e.g. detecting range and/or field of view). Also, in collaborative scenarios, where safety related driver assistance applications are being under investigation, an accurate time synchronization between agents is required. Thus, the time delay between inter-nodal measurements is a fundamental requirement to ensure time synchronized solutions. In order to achieve this goal, it is also crucial that the sensors produce an output with a high rate. For more information about the output rates of the sensor measurements in driver assistance operations we refer the reader to WALLENTOWITZ AND REIF (2010).

2.3.2 Objective Functions and Optimality Criteria

In this section, the objective functions discussed in the available literature for classic network optimization with respect to precision, reliability and economy criteria are introduced.

Network Precision

The main indicator of the precision of an adjustment is the VCM of the estimated parameters. Both *local* and *global* objective functions can be derived from it. Since, the target of the study is to evaluate the overall precision of the network (*global precision*), and the *local* objective functions describe in detail only the precision of each individual point, only objective functions and optimality criteria for *global precision* analysis are discussed in this section.

The *global* objective functions can be represented with the eigenvalues λ_i of the cofactor matrix $\mathbf{Q}_{\hat{x}\hat{x}}$, given that they must remain invariant with regard to rotation and translation of the network (GRAFAREND, 1974). With the designations that GRAFAREND (1974) and GRAFAREND AND SANSÒ (1985) applied to geodetic networks it is possible to state that when the value of an objective function is minimal, the geodetic network meets the optimality requirement (JÄGER, 1988; SCHÖN, 2003).

A-optimal: When the average variance is a minimum:

$$Z_A = \sigma_0^2 \cdot \text{tr}(\mathbf{Q}_{\hat{x}\hat{x}}) = \sigma_0^2 \sum_{i=1}^n \lambda_i \quad (2.33)$$

D-optimal: When the generalized variance is a minimum:

$$Z_D = \sigma_0^2 \cdot \det(\mathbf{Q}_{\hat{x}\hat{x}}) = \sigma_0^2 \prod_{i=1}^n \lambda_i, \quad (2.34)$$

where the operator \det stands for the determinant of the matrix.

E-optimal: When the maximum eigenvalue of the VCM is a minimum:

$$Z_E = \sigma_0^2 \lambda_{max} \quad (2.35)$$

N-optimal: When the Frobenius-Norm of the VCM is a minimum:

$$Z_N = \|\mathbf{C}_{\hat{x}\hat{x}}\|_{\mathbf{F}} = \sigma_0^2 \sqrt{\sum_{i=1}^n \lambda_i^2} \quad (2.36)$$

S-optimal: When the spread of the spectrum of the VCM is a minimum:

$$Z_S = \sigma_0^2 (\lambda_{max} - \lambda_{min}). \quad (2.37)$$

Furthermore, *local* criteria are available that enable a detailed and individual analysis of the relative and absolute point error situation. They can be expressed in the form of semi-major and semi-minor axes of the error ellipses (see Eq. (2.19) and (2.20)) or by criterion matrices. The concept of the ideal VCM is that all ellipses have the same shape (*homogeneity*) and the semi-axis lengths are equal (*isotropy*) (GRAFAREND AND SANSÒ, 1985).

Several approaches to compute criterion matrices are shown in BILL (1985), including how to build diagonal criterion matrices (non-correlated parameters) or refined criterion matrices (correlated parameters). The behavior of the correlation functions depends on the *characteristic distance*.

Detailed explanation of the computation of criterion matrices can be found in GRAFAREND AND SANSÒ (1985), BILL (1985) and SCHÖN (2003).

Network Reliability

SCHMITT (1982) stated that the realization of an analytical formulation of reliability as a risk function is hardly achievable. Therefore, the amount of research targeting the geodetic network optimization with respect to reliability is significantly lower than with respect to precision. However, formulations for objective functions can be found in SCHAFFRIN (1985).

According to BAARDA (1968), the reliability is the ability of the network to resist gross errors in the observations. Therefore, one searches for high reliability of the network in the design step by minimizing the magnitude of the undetectable gross errors in observations (*internal reliability*) and minimizing the effects that the undetected gross errors produce in the estimated parameters (*external reliability*) (see Section 2.3.1). Also, BAARDA (1968) and KUANG (1991) show that both high external and internal reliability can be combined. Given that the larger the redundancy numbers (Eq. (2.22)), the lower is the minimum detected bias, and thus the better the controllability of the observation (assuming non-correlated measurements), the requirement to guarantee optimally reliable networks is to maximize the redundancy numbers (BAARDA, 1968).

$$\min(r_i, i = 1, \dots, n) = \text{maximum} \quad (2.38)$$

Then, the vector norms can be considered as simple objective functions (SCHÖN, 2003).

$$Z_{\mathbf{r},p} = \|(\mathbf{Q}_{\hat{v}\hat{v}} \mathbf{W}_l)_{ii}\|_p. \quad (2.39)$$

This implies that the ability of the network to detect gross errors should be the same in every part of the network. Thus, parts with larger undetectable gross errors show lower controllability, and should be improved locally (KUANG, 1991).

As was stated in Section 2.3.1, the limit for the minimum detectable gross error (Eq. (2.23)) is considered as a metric for the *internal reliability*. Therefore, to guarantee the *internal reliability* of a network, the non detectable gross errors $\nabla l_{0,i}$ must be minimized. Therefore, if

$$\nabla_0 \mathbf{l} = (\nabla l_{0,1}, \dots, \nabla l_{0,n}), \quad (2.40)$$

it is possible to build the objective function:

$$Z_{\nabla_0 \mathbf{l}} = \nabla_0 \mathbf{l}^T \mathbf{M}^T \mathbf{M} \nabla_0 \mathbf{l} \quad (2.41)$$

where \mathbf{M} is the matrix used for the unit unification.

Finally, the network deformation $\|\nabla_{0,\hat{\mathbf{x}}}\|_{\mathbf{C}_{\hat{\mathbf{x}}\hat{\mathbf{x}}}^{-1}}$ is the metric used to analyze the *external reliability* (see Eq. (2.25)). To guarantee the *external reliability* of a network, the gross errors must show as little effect on the estimated parameters as possible. Thus, with the vector that contains the distortions being

$$\boldsymbol{\delta}^2 = (\delta_{0,1}^2, \dots, \delta_{0,n}^2)^T, \quad (2.42)$$

the sum of the network distortions $\delta_{0,i}^2$ can be written as objective function as (KUANG, 1991):

$$Z_{\delta^2} = \sum_{i=1}^n (\mathbf{W}_l \bar{\mathbf{A}} \mathbf{Q}_{\hat{\mathbf{x}}\hat{\mathbf{x}}} \bar{\mathbf{A}}^T \mathbf{W}_l)_{ii} \nabla l_{0,i}. \quad (2.43)$$

where $\bar{\mathbf{A}}$ is the Jacobian sub-matrix that contains the coefficients to estimate the positioning components (without the consideration of additional network orientation or scale factor parameters).

Network Economy

A geodetic network design is considered to be optimum when it satisfies the user precision and reliability with the least cost (KUANG, 1991). SCHAFFRIN (1985) depicts these three metrics as a *magic triangle*, that illustrates the increase of the cost when high precision or reliability are required and vice versa. However, the precision and reliability are not completely independent, so a *multi-purpose optimization* is proposed.

$$\alpha_p \cdot (\text{precision}) + \alpha_r \cdot (\text{reliability}) + \alpha_c \cdot (\text{costs})^{-1} = \max. \quad (2.44)$$

By assuming that the smaller the weight of an observation, the less expensive it is to observe (SCHAFFRIN, 1985), the simplified cost criterion can be written as

$$\|\mathbf{W}_l\| = \text{minimum}. \quad (2.45)$$

More approaches to discuss the optimization of the economy of a network can be found in the collection GRAFAREND AND SANSÒ (1985).

Table 2.1: Geodetic Network Optimization Problems: Fixed and Free parameters

<i>Optimization Problem</i>	Fixed Param.	Free Param.
Zero Order Design	\mathbf{A}, \mathbf{W}_l	\mathbf{G}, \mathbf{t}
First Order Design	$\mathbf{W}_l, \mathbf{Q}_{\hat{x}\hat{x}}$	\mathbf{A}
Second Order Design	$\mathbf{A}, \mathbf{Q}_{\hat{x}\hat{x}}$	\mathbf{W}_l
Third Order Design	$\mathbf{Q}_{\hat{x}\hat{x}}$	\mathbf{A}, \mathbf{W}_l

2.3.3 Types of Optimization Problems

According to SCHMITT (1985a), several decisions are to be made in the design step of a geodetic network. On the one hand, it is necessary to decide on the location of the points and the types of observations to be used, and on the other hand, on the distribution of observational work according to the precision of the measurements. In the adjustment step, it is also necessary to decide on an optimum relative or absolute datum.

The optimization problems are usually classified into different orders depending on the fixed and free parameters of the optimization (summarized in Table 2.1). GRAFAREND (1974) classifies the network optimization problems in four groups: *Zero Order Design* (ZOD) problem, *First Order Design* (FOD) problem, the *Second Order Design* (SOD) problem (also called *weight problem*) and the *Third Order Design* (THOD).

The Zero Order Design (ZOD) problem (also known as *datum problem*) deals with the search of an optimum datum or coordinate system for the network that is normally described in terms of the nullspace to determine the datum (\mathbf{G}) and the datum parameters \mathbf{t} that comprise the correspondent translations, rotations and scale factors of the transformation. JÄGER (1988) proposes to solve the Zero Order Design (ZOD) problem using pseudo-inverse matrices. A complete description of these approaches, as well as the S-transformation, with which the VCM can be transformed to the desired datum, can be found in TEUNISSEN (1985).

The First Order Design (FOD) problem deals with the search for the optimum positions of the points and the observation plans. Here, the geometry and topology of the network change under a fixed selected datum. Criterion matrices suitable to find the solution of First Order Design (FOD) problem in free networks (networks where the datum must be chosen first) can be found in KOCH (1985). KUANG (1996) also show methodologies for the FOD optimization, where significantly improved objective functions can be achieved by shifting considerably some points of the network.

The Second Order Design (SOD) problem consists of finding precision measures for the geodetic and non-geodetic observations to be used as weights (\mathbf{W}_l) in an adjustment (given a fixed configuration), that lead to the fulfillment of any of the desired quality criteria (see Section 2.3.1). Many Second Order Design (SOD) solutions available in the literature are achieved by introducing all weights as parameters, obtaining small weight values. However, the small weight values cause for the observations to have almost no influence on the objective function, and therefore can be deleted from the observation plan, optimizing in this way the topology of the network.

SCHMITT (1985b) proposes three different SOD approaches: two that try to approximate the criterion matrix itself, and a third one where an inverse was approximated using a least-squares solution based on GMM, linear or non-linear programming. Finally, the weight results obtained from the used methodology should be used in order to select the instruments which specifications best fit the precision measures obtained.

The Third Order Design (THOD) problem is the task to improve, extend or densify an existing network in an optimal way by the addition of points or observations. This may refer to the optimal improvement of the network or the optimal design for the network densification (SCHMITT, 1985c). These problems can be solved with methodologies to randomly optimize procedures, and with criterion matrices for the points in the area of interest.

2.4 Discussion

In the classical geodetic network field, the main purpose of optimization is to aid the understanding of the network response with respect to changes in its geometry, weight distribution and/or observational work. However, the concept of network presented in this thesis differs significantly from the concepts described in the literature as surveyed in this chapter. In modern navigation terms, the traditional geodetic network methodologies would be defined as a *static, time-invariant* system. The term *static* refers to the static character of the nodes (fixed geometry), and *time-invariant* characterizes the fact that the observational work taken into account remains stable over time. It is essential to establish a clear differentiation between the two terms, since a stationary network might be affected by important changes in the observational work and vice versa (for example, in steady-state estimations SIMON (2006)). As opposed to this definition, the collaborative navigation network estimations are considered to be highly dynamic, and time-variant systems. This means that not only some of the nodes of the network are moving (varying geometry), but that the observational work changes as well. Consequently, it is necessary to take into account additional factors for the complete understanding of the dynamic network problem. Nevertheless, the overall analysis of the network can be carried out in terms of the same navigation performance and network analysis criteria, and the optimization problems can be associated within the previously introduced optimization problems (see Section 2.3.3).

Theoretical investigations to understand the network as a modern range-based cooperative positioning problem is presented in HENG AND GAO (2017). Here, the relationship between accuracy and connectivity is analyzed by means of a lower bound on the expectation of average geometric dilution of precision (LB-E-AGDOP). The evaluation is carried out over the best network geometries given a particular distribution of sensor nodes (unknown-location nodes) and anchors (known-location nodes). Although the usage of the LB-E-AGDOP proves to be useful in order to characterize the relation between accuracy and connectivity, the results are evaluated over static networks. WIN ET AL. (2018) takes the approach one step further, by including the IMU as intra-nodal measurements to anticipate the movement of the nodes, as well as inter-node range and angle measurements. In this theoretical exploration, the effects of spatio-temporal cooperation were char-

acterized with a promising outcome that increases drastically the localization performance, although solutions for information fusion for high-accuracy localization in GNSS-challenging environments remains an open question.

Finally, the research mentioned above (HENG AND GAO, 2017; WIN ET AL., 2018) was carried out with the same *didactic* purposes as the one developed in this thesis. Nevertheless, the investigation of the network response to changes in the parameters that actually describe the motion of the nodes (e.g. motion model selection, process noise, etc.), and to epoch-wise changes in its configuration, are hardly ever mentioned. This research space is filled in this thesis, with not only an evaluation of the effects, but with the proposition of hypotheses and alternatives that could mitigate the negative effects caused by suboptimal estimations. The investigations are assessed in dynamic networks (collaborative scenarios) with a higher degree of complexity regarding both, the motion of the nodes, and the observational work.

3 Theoretical Background in Positioning and Navigation

In this chapter, the theoretical notions necessary to understand the collaborative navigation techniques used in this thesis are introduced. First, GNSS and Inertial Navigation Systems (INS) are discussed, together with an overview on coordinate frames and transformations. In addition, the different ranging sensors available in the i.c.sens project (SCHÖN ET AL., 2018) (e.g. laser scanner, stereo cameras) normally used to increase the robustness of the available navigation algorithms are introduced, along with their strengths and weaknesses. Additional regularly used sensors like radar or odometer are unavailable in the project, and thus not introduced.

Another important aspect to discuss in order to introduce the complete background in collaborative positioning techniques is the used estimator. Here, the Bayesian estimator Kalman filter is introduced in both, its linear and non-linear form. The estimation can be executed using several approaches, depending if the vehicle is assumed to be placed at a unknown location in a known or unknown environment. If the environment information is assumed to be known a priori, the solution is obtained straight-forward solving the problem as a *localization problem*. However, the environment information is not always available, forcing the vehicle to perform the task to build a consistent map of its environment while simultaneously determining its location (Simultaneous Location and Mapping (SLAM) problem). The methodologies to solve both problems are recapitulated in this chapter.

3.1 Global Navigation Satellite Systems

The fundamental technique of GNSS is to locate a receiver by measuring the pseudoranges to a few simultaneously observed satellites (HOFMANN-WELLENHOF, 2008). Several organizations and countries have been developing their own GNSS, like e.g. the American Global Positioning System (GPS) (GPS-STANDARD, 2008), the Russian Globalnaja Nawigazionnaja Sputnikowaja Sistema (GLONASS) (GLONASS, 2016), the European Union Galileo (NURMI ET AL., 2015) and the Chinese Compass/Beidou-2 (BEIDOU, 2012).

The GNSS can be divided into three segments: space segment, control segment and user segment (HOFMANN-WELLENHOF, 2008). The space segment is formed by the satellites that orbit around the Earth at a height of approximately 20000 km. The control segment is organized in monitoring stations in charge of the maintenance of the system (e.g. satellite tracking for orbital and clock

parameters, ionosphere parameters, data encryption, etc.). The user segment is constituted by any device capable to receive GNSS signals.

3.1.1 GNSS Observables

The basic GNSS observables are code pseudo-ranges, carrier phases and Doppler measurements.

Code pseudoranges: the ranges are estimated by measuring the Time of Arrival (ToA) of the satellite signal (BORRE ET AL., 2007), which is emitted by the satellite at time t^j , propagates through the atmosphere at the speed of light c , and it is received at the antenna of the receiver at time t_i . However, in reality the heterogeneous characteristics of the transmitting medium lead to the fact that the measured path is bended and delayed. In addition, the signal is also affected by additional sources of error, such as Earth and loading tides, multipath and relativistic effects. Taking into account the geometric characteristics of the signal and the error sources that alter the path of the signal, the pseudorange model can be written as (XU, 2007):

$$\rho_i^j(t) = r_i^j(t_i, t^j) + c\delta t_i^j + \epsilon_\rho, \quad (3.1)$$

where $r_i^j(t_i, t^j) = \sqrt{(x^j - x_i)^2 + (y^j - y_i)^2 + (z^j - z_i)^2}$ is the range between the receiver i placed at position (x_i, y_i, z_i) and the satellite j at position (x^j, y^j, z^j) at time (t_i, t^j) , $c\delta t_i^j$ is the synchronization error between the satellite and the receiver clocks, ϵ contains the atmospheric and measurement errors that affect the geometric range measurement. Then, it is possible to see in Eq. (3.1) that the three-dimensional position of a receiver can be estimated by measuring the ranges to at least four satellites.

Carrier Phases are the difference between the phases of the receiver-generated carrier replica and the received carrier signal at t_i , measured in meters. Although the carrier phase can be measured with high precision, the initial integer number of cycles between satellite and receiver, also called *integer ambiguity* (N), is unknown. Considering the above-mentioned error sources that affect the GNSS signal, the carrier phase model can be written as:

$$\Phi_i^j = r_i^j(t_i, t^j) + c\delta t_i^j + \lambda N_i^j + \epsilon_\Phi, \quad (3.2)$$

where λ is the wavelength of the carrier on which the measurement is made. In this model, the corrections are significantly lower, and the ionospheric delay is of equal magnitude but opposite sign as compared to the pseudorange measurements.

Doppler measurement is the frequency shift of the electromagnetic signal caused by the relative motion of the satellite and the receiver, measured in meters per second. Taking into account the errors produced by drifts in the satellite and receiver clocks, and the additional atmosphere and measurement corrections, the Doppler model can be written as (WIESER, 2007):

$$\dot{\Phi}_i^j = \dot{r}_i^j(t_i, t^j) + c\dot{\delta t}_i^j + \epsilon_{\dot{\Phi}}, \quad (3.3)$$

where $\dot{r}_i^j(t_i, t^j)$ is the change in the geometric range due to the relative motion between satellite and receiver, $c\dot{\delta t}_i^j$ represent the satellite and receiver clock drifts, and $\epsilon_{\dot{\Phi}}$ are the atmospheric and measurement errors.

For detailed information about the error sources caused by physical influences on the GNSS signal and ambiguity resolution techniques, please refer to HOFMANN-WELLENHOF (2008).

3.1.2 GNSS positioning techniques

In the previous Section 3.1.1, the GNSS observables to determine the position of an individual GNSS receiver are introduced. In this section, GNSS techniques that focus on the error mitigation in order to improve the performance of GNSS positioning are discussed.

Differential GNSS (DGNSS) is a positioning technique that aims at the real-time determination of the coordinates of a roving receiver, that uses the Pseudorange Corrections (PRC) and Range Rate Corrections (RRC) calculated by a second receiver placed in a base station with known coordinates to improve its position (HOFMANN-WELLENHOF, 2008). With these corrections, the rover is able to reduce the atmospheric and other errors.

Since the satellites orbit high above the Earth, the propagation paths from the satellite to the receivers pass through similar atmospheric conditions, unless the base station and rover are far apart. For this reason, the amount of improvement is dependent on the distance between the rover and the base station receivers. Normally, the closer the base station, the more correlated the errors between the base station and rover are, and therefore the better the positioning.

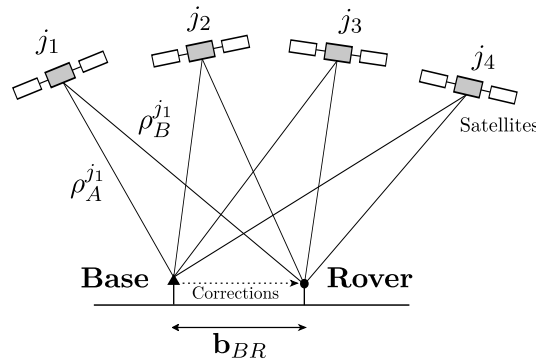


Figure 3.1: Concept Differential GNSS

Precise Point Positioning (PPP) is a technique that uses precise satellite clock and orbit corrections in order to mitigate the effect of the GNSS error sources in the positioning of a single receiver. This technique estimates the position, clock error, tropospheric delay and carrier-phase ambiguities with an estimation technique (like e.g. Extended Kalman Filter (EKF) or least-squares). PPP can be used in static or kinematic modes, and it yields highly accurate solutions at the centimeter and decimeter levels, respectively (TEUNISSEN AND KHODABANDEH, 2014).

Relative positioning is a technique where the coordinates of an unknown point are determined with respect to a known point. The goal is to estimate the vector \mathbf{b}_{BR} between the base station and the rover (cf. Figure 3.1), also called as *baseline* (HOFMANN-WELLENHOF, 2008)

$$\mathbf{x}_R = \mathbf{x}_B + \mathbf{b}_{BR} \quad \text{where} \quad \mathbf{b}_{BR} = \begin{bmatrix} x_R - x_B \\ y_R - y_B \\ z_R - z_B \end{bmatrix} = \begin{bmatrix} \Delta x_{BR} \\ \Delta y_{BR} \\ \Delta z_{BR} \end{bmatrix}. \quad (3.4)$$

Assuming simultaneous carrier phase observations from the base and the rover stations to at least two satellites at two different epochs, differences can be formed leading to single-differences, double-differences and triple-differences (HOFMANN-WELLENHOF, 2008).

Real Time Kinematic (RTK) is a technique that uses carrier-phase observables to compute a positioning solution that is two-three orders of magnitude more precise than the code pseudoranges. Like all carrier-phase based approaches, Real Time Kinematic (RTK) comprises the determination of the number of carrier cycles (N) between satellite and rover, using the so-called *ambiguity resolution*. Here, the atmospheric, clock drifts and ephemeris errors are compensated by transmitting measurements from the base station to the rover. With this methodology, centimeter accuracy can be achieved.

Finally, it is also worth mentioning that the DGNSS and relative positioning concepts can also be advanced from the base/rover situation to a two rover setup, usually known as moving baseline (DE PONTE-MÜLLER, 2017a). This concept enables the possibility to interlink receivers mounted in several vehicles, and therefore enables to treat the navigation situation as a dynamic network.

3.2 Inertial Navigation Systems

Inertial navigation deals with the problem of estimating the pose (position and orientation) and velocity of a moving object by performing measurements with inertial sensors such as accelerometers and gyroscopes. Orthogonally mounted gyroscopes to measure the angular rates, and accelerometers to measure the specific forces (accelerations), constitute the IMU. In the INS, the IMU measurements are combined with the mechanization equations (processor) (NOURELDIN ET AL., 2013).

In this section, the so called *strap-down* system is discussed. Positioning is the task to determine the coordinates of an object in a certain coordinate frame. Thus, an introduction to the concept of a coordinate frame is given prior to the discussion of the INS.

3.2.1 Coordinate Frames

To describe the position, orientation and motion of objects, coordinate frames formed by an origin and a set of three orthogonal non-coplanar axes are used (GROVES, 2013). General knowledge of the common coordinate frames used in navigation is fundamental for understanding the INS concepts described in the following sections.

Earth-Centered Inertial Frame, (*i-frame*). The term *inertial* is applied to any coordinate frame that is defined stationary in space, or moving with constant velocity. This frame is nominally centered at the Earth's center of mass, the z-axis points along the Earth's rotation axis. The y- and x-axis lie within the equatorial plane but do not rotate with the Earth. The y-axis points 90° ahead of the x-axis in the direction of rotation of the Earth and the x-axis is defined as the direction from the Earth to the vernal equinox (GROVES, 2013).

This frame is specially suitable to analyze the satellite motion, given that it is fixed to the stars. Finally, it is also worth mentioning that this frame experiences acceleration while orbiting around the sun, and its rotation axis moves. Hence it is not strictly an inertial frame. Nonetheless, the measurement noise yielded by the inertial sensors is much larger than this effects, so the i-frame is considered as a true inertial frame in the navigation community.

Earth-Centered Earth-Fixed Frame, (*e-frame*). In the e-frame all axes remain fixed with the Earth with its origin in the center of the reference ellipsoid, the z-axis being the rotation axis, and the x-axis pointing to the intersection between the equator and 0° Greenwich meridian. The remaining y-axis points to the intersection between the equator and the 90° meridian.

The e-frame is the frame typically used in satellite navigation techniques, since it provides the position of the user relative to the Earth.

Local Navigation frame, (*n-frame*). The origin of the n-frame is coincident with the origin of the object to be positioned. The axes are aligned with the topographic directions (North, East and vertical). The z-axis points downwards in the direction normal to the surface of reference. This direction differs slightly from the direction of the gravity vector. Then, the x- and y-axis follow the North and East directions, respectively. North, East and Down is the most common order (GROVES, 2013).

This frame is very important in vehicular navigation because it is used as reference to compute the orientation of the body (attitude). The attitude is defined as the rotation that has to be applied to an object in order to orient its axis parallel to the n-frame. The attitude is expressed by means of three rotations, one with respect to each axis. Here, the roll (ϕ), pitch (θ) and yaw (ψ) (also called *Euler angles*) are the rotations around the x-, y- and z-axis, respectively (cf. Figure 3.3)

Local Topocentric frame, (*t-frame*). The t-frame can be defined as a local navigation frame (n-frame) where the origin is fixed at a certain point on the Earth. In addition, the z-axis is normally pointing in the opposite direction to the center of mass of the Earth. The x- and y-axis are defined in the North and East directions from the predefined origin. This frame is very adequate for multi-body problems (such as collaborative positioning) where the agents are not really far from each other, so that the effect of the Earth curvature can be neglected.

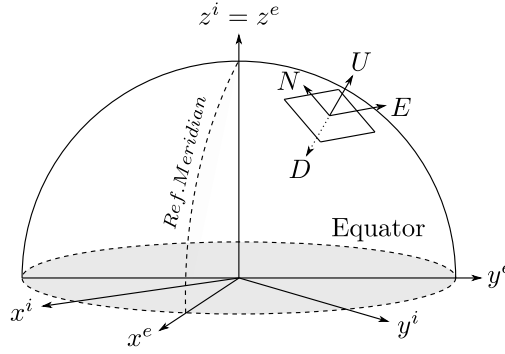


Figure 3.2: Important coordinate frames in inertial navigation systems. In the figure, the Earth-Center Inertial frame ($x^i y^i z^i$), Earth-Center Earth-Fixed frame ($x^e y^e z^e$), Local Topocentric frame ($N E U$) and Local Navigation frame ($N E D$) are represented.

Body frame, (*b-frame*). Also called vehicle frame in some literature, is the coordinate frame fixed to the object described by the navigation solution. The origin of the b-frame can be arbitrarily defined within the object, and it is used to define subsequently the origin of the n-frame. The most common axis convention is the one where the x-axis points forward, the z-axis points up and the y-axis completes the right handed orthogonal set pointing to the right (cf. Figure 3.3).

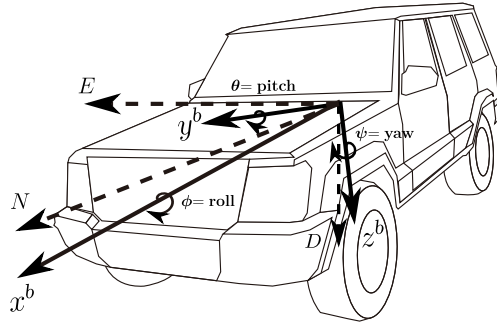


Figure 3.3: Body frame (b-frame) and attitude concept

3.2.2 Mechanization in the Navigation Frame

Mechanization can be defined as the recursive determination of the position, velocity and attitude using the output from Inertial Measurement Units (NOURELDIN ET AL., 2013). To fulfill this task, the *strap-down algorithm* is used. Here, the angular rates ω_{ib}^b are integrated in order to obtain the attitude ($\phi \ \theta \ \psi$). As can be seen in Fig. 3.3, the roll, pitch and yaw represent the rotations of the vehicle-frame axis with respect to the navigation frame in the x-, y-, and z-axis respectively. With this knowledge, the Earth gravitational force \mathbf{g}^n can be subtracted from the specific forces \mathbf{f}^b , considering its deviation with respect to the direction of the Down coordinate in the navigation frame. Finally, the result is integrated once to obtain the velocity, and the velocity is later integrated to obtain the position. The output parameters obtained with the strap-down algorithm are the position \mathbf{p}_{eb}^n of the vehicle in the n-frame, the velocity \mathbf{v}_{eb}^n and the attitude (ϕ, θ, ψ). The position

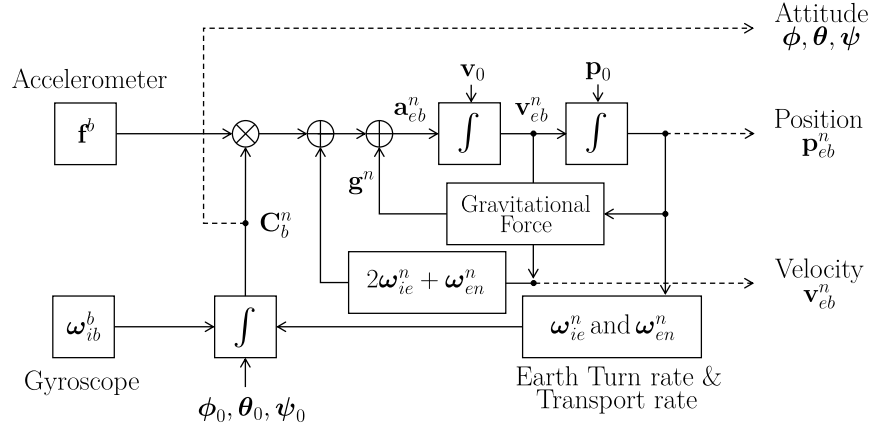


Figure 3.4: Strap-Down Navigation Algorithm diagram (GROVES, 2013)

results can be also expressed in other coordinate frames (GROVES, 2013; NOURELDIN ET AL., 2013). This is an explanation that can be completed with the complete strap-down navigation algorithm shown in Figure 3.4.

Equations of Motion

The mathematical equations that define the motion of an object are called equations of motion (PETOVELLO, 2003). Following the approach described in NOURELDIN ET AL. (2013), the mechanization equations in the n-frame can be written as:

$$\begin{bmatrix} \dot{\mathbf{p}}_{eb}^n \\ \dot{\mathbf{v}}_{eb}^n \\ \dot{\mathbf{C}}_b^n \end{bmatrix} = \begin{bmatrix} \mathbf{v}_{eb}^n \\ \mathbf{C}_b^n \mathbf{f}^b - (2\boldsymbol{\Omega}_{ie}^n + \boldsymbol{\Omega}_{en}^n) \mathbf{v}_{eb}^n + \mathbf{g}^n \\ \mathbf{C}_b^n (\boldsymbol{\Omega}_{ib}^b - \boldsymbol{\Omega}_{in}^b) \end{bmatrix}, \quad (3.5)$$

where

- $\boldsymbol{\Omega}_{bc}^a$ is the skew symmetric matrix of the rotation rate vector $\boldsymbol{\omega}_{bc}^a$.
- $\boldsymbol{\omega}_{bc}^a$ represents the rotation rate of the c -frame, relative to b -frame, expressed in the a -frame
- \mathbf{C}_b^n represents the Direction Cosine transformation matrix (DCM).
- $(2\boldsymbol{\Omega}_{ie}^n + \boldsymbol{\Omega}_{en}^n) \mathbf{v}_{eb}^n$ is the Coriolis compensation

The DCM matrix in Eq. (3.5) is used to rotate the coordinates from the b-frame to the n-frame, and can be constructed by means of the Euler angles GROVES (2013).

$$\mathbf{C}_b^n = \begin{bmatrix} \sin \theta \cos \psi & \sin \phi \sin \theta \cos \psi - \cos \phi \sin \psi & \cos \phi \sin \theta \cos \psi + \sin \phi \sin \psi \\ \cos \theta \sin \psi & \sin \phi \sin \theta \sin \psi + \cos \phi \cos \psi & \cos \phi \sin \theta \sin \psi - \sin \phi \cos \psi \\ -\sin \theta & \sin \phi \cos \theta & \cos \phi \cos \theta \end{bmatrix} \quad (3.6)$$

Moreover, an overview on further rotation matrices that allow the transformation between coordinate frames can be found in FARRELL (2006).

It can be seen in this section that the discussed mechanization equations do not provide any information about the errors of the system. In practice, Kalman Filter (KALMAN, 1960) algorithms are used to estimate the filter errors to improve the performance. The full derivation of this approach can be found in NOURELDIN ET AL. (2013) or JEKELI (2000).

Furthermore, it can be seen in Eq. (3.5) that the changes in the state are estimated. Thus, initialization requires the specification of the initial values for position, velocity and attitude. Self-alignment techniques use the inertial measurements together with knowledge about \mathbf{g}^n to align the body to the n-frame (the system is then assumed to be stationary at a known position). For a detailed overview on the self-alignment techniques, see FARRELL (2006).

3.2.3 INS/GNSS Integration

On the one hand, inertial navigation is a navigation technique that provides the user with a high-rate (above 100 Hz in most cases) continuous solution, invulnerable to jamming and interference. However, it needs initialization and the solution degrades with time (GROVES, 2013). On the other hand, the GNSS (standalone) provide a stable solution with respect to time, that degrades when the signal is affected by multipath, diffraction and obstruction. Therefore, the advantages and weaknesses of both sensors are complementary, hence the combination of both techniques to provide a high-rate, long-term accurate solution.

The architecture of the INS/GNSS integration methodology depends on how the corrections are applied, and how the GNSS user equipment is aided by the INS, and the integration algorithm. The most widely used architectures are as follows (GROVES, 2013):

- In the *loosely coupled* INS/GNSS integration, the GNSS position and velocity solutions are used as an input in the integration algorithm. In this technique, a non-linear Kalman filter can be used in order to estimate the errors instead of the solution.
- A *tightly coupled* integration uses the GNSS pseudoranges and Doppler measurements as inputs to the algorithm (also CP can be used). The advantage of this architecture with respect to the loosely coupled one is that no position or velocity solutions are required, so that it is possible to compute a solution with less than four satellites in view.
- In *deeply coupled* integration the GNSS and INS are no independent systems anymore, and the GNSS measurements are used to calibrate the INS and at the same time the INS is used to aid the GNSS receiver tracking loops during challenging conditions. The biggest advantage of this method is that tracking loops can be designed with a higher rate, producing smaller errors in the measurements.

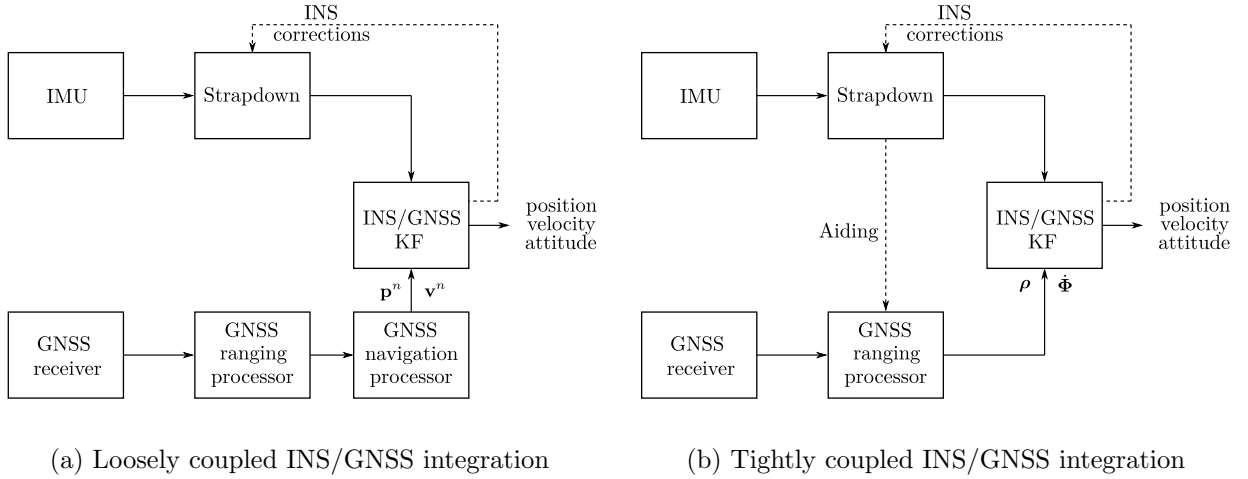


Figure 3.5: INS/GNSS integration architectures

3.3 Filtering Techniques

In this section, theoretical background is introduced in order to understand the filtering techniques used for the multi-sensor fusion algorithm proposed in this thesis.

3.3.1 Bayes Filter

The estimation methods described in Sections 2.1 and 2.2 are suitable for a static estimation of deterministic unknown parameters. However, some information and stochastic characteristics of the parameter to be estimated are known and should be considered in the estimation. For instance, the position and/or velocity of a dynamic object at a certain time k depend on its previous states ($\mathbf{x}_{0:k}$). Given the state vector \mathbf{x} this situation can be expressed mathematically as

$$p(\mathbf{x}_k | \mathbf{x}_{0:k}). \quad (3.7)$$

With the Bayesian rule, it is possible to compute the posterior probability distribution $p(\mathbf{x} | \mathbf{l})$ (probability of obtaining \mathbf{x} given a set of observations \mathbf{l}) out of the available prior probability distribution $p(\mathbf{x})$ and the measurement probability distribution $p(\mathbf{l} | \mathbf{x})$ (probability of obtaining \mathbf{l} given \mathbf{x}) as (THRUN ET AL., 2006):

$$p(\mathbf{x}_k | \mathbf{l}_k) = \frac{p(\mathbf{l}_k | \mathbf{x}_k) \cdot p(\mathbf{x}_k)}{p(\mathbf{l}_k)}, \quad (3.8)$$

where if \mathbf{x}_k is known, past and future data are assumed to be independent (*Markov Assumption* (THRUN ET AL., 2006)).

The Bayes filter is defined as a recursive estimation. To derive the recursive Bayesian filter, two assumptions are used: the states follow a first order Markov process, and the observations are

independent from the states. Assuming \mathbf{l}_k as a set of observations $\mathbf{l}_{0:k} = \{l_0, \dots, l_k\}$, Eq. (3.8) can be derived obtaining:

$$\begin{aligned}
 p(\mathbf{x}_k | \mathbf{l}_k) &= \frac{p(\mathbf{l}_k | \mathbf{x}_k) \cdot p(\mathbf{x}_k)}{p(\mathbf{l}_k)} \\
 &= \frac{p(l_k, \mathbf{l}_{k-1} | \mathbf{x}_k) \cdot p(\mathbf{x}_k)}{p(l_k, \mathbf{l}_{k-1})} \\
 &= \frac{p(l_k, \mathbf{l}_{k-1} | \mathbf{x}_k) \cdot p(\mathbf{l}_k | \mathbf{x}_k) \cdot p(\mathbf{x}_k)}{p(l_k, \mathbf{l}_{k-1}) \cdot p(\mathbf{l}_{k-1})} \\
 &= \frac{p(l_k, \mathbf{l}_{k-1} | \mathbf{x}_k) \cdot p(\mathbf{x}_k | \mathbf{l}_k) \cdot p(\mathbf{l}_{k-1}) \cdot p(\mathbf{x}_k)}{p(l_k, \mathbf{l}_{k-1}) \cdot p(\mathbf{l}_{k-1}) \cdot p(\mathbf{x}_k)} \\
 &= \frac{p(l_k | \mathbf{x}_k) \cdot p(\mathbf{x}_k | \mathbf{l}_{k-1})}{p(l_k | \mathbf{l}_{k-1})}.
 \end{aligned} \tag{3.9}$$

As can be seen in Eq. (3.9) the Bayes filter is divided into two steps: prediction and update. The *prediction* $p(\mathbf{x}_k | \mathbf{l}_{k-1})$ defines the knowledge of the model. The *state transition model* is used to propagate the state from \mathbf{x}_{k-1} to \mathbf{x}_k .

$$p(\mathbf{x}_k | \mathbf{l}_{k-1}) = \int p(\mathbf{x}_k | \mathbf{x}_{k-1}) \cdot p(\mathbf{x}_{k-1} | \mathbf{l}_{k-1}) d\mathbf{x}_{k-1} \tag{3.10}$$

The *update* step, modifies the prediction at the state \mathbf{x}_k with the set of observations.

$$p(\mathbf{x}_k | \mathbf{l}_k) = \int p(l_k | \mathbf{x}_k) \cdot p(\mathbf{x}_k | \mathbf{l}_{k-1}) d\mathbf{x}_k \tag{3.11}$$

3.3.2 Kalman Filter

The Kalman Filter (KF) (KALMAN, 1960) is a type of Bayesian filter where the prior and posterior probability functions are represented by multivariate Gaussian distributions such as:

$$N(\mathbf{x}; \mu, \sigma) = \frac{1}{\sqrt{2\pi\sigma}} \cdot e^{-\frac{1}{2} \cdot \left(\frac{\mathbf{x}-\mu}{\sigma}\right)^2}. \tag{3.12}$$

Let us assume the following linear discrete-time system

$$\mathbf{x}_k = \Phi_{k-1} \mathbf{x}_{k-1} + \Gamma_{k-1} \mathbf{u}_{k-1} + \mathbf{w}_{k-1} \quad \mathbf{w}_{k-1} \sim N(\mathbf{0}, \mathbf{Qd}_{k-1}) \tag{3.13}$$

$$\mathbf{l}_k = \mathbf{h}(\mathbf{x}_k) = \mathbf{H}_k \mathbf{x}_k + \mathbf{v}_k \quad \mathbf{v}_k \sim N(\mathbf{0}, \mathbf{R}_k) \tag{3.14}$$

where \mathbf{x}_k is the state vector, \mathbf{u}_{k-1} is the known control input vector, \mathbf{l}_k is the measurement vector, Φ_{k-1} is the state transition matrix, Γ_{k-1} is the input control matrix, \mathbf{H}_k is the measurement model that links the states to the measurements, \mathbf{Qd}_{k-1} is the process noise covariance matrix, \mathbf{w}_{k-1} and \mathbf{v}_k are the process and measurement noise vectors (FARRELL, 2006; SIMON, 2006).

Taking into account Eq. (3.13), the process noise can be defined as

$$\mathbf{w}_k = \int_{k-1}^k e^{\mathbf{F}(k-\lambda)} \cdot \mathbf{\Lambda}(\lambda) \mathbf{w}(\lambda) d\lambda, \tag{3.15}$$

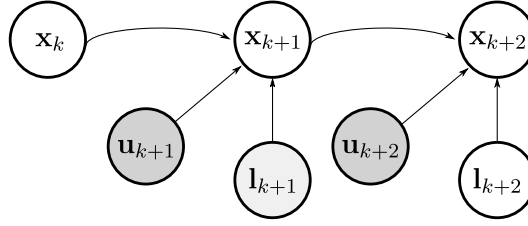


Figure 3.6: Graph of the KF state-space model

where $\Lambda(\lambda)$ is the stochastic input matrix, \mathbf{F} is the time continuous representation of the Φ matrix, \mathbf{Q} is the process noise matrix, and λ is an integration variable. Assuming that \mathbf{w} is a white noise process, the matrix $\mathbf{Qd}_k = \text{cov}(\mathbf{w}_k)$ can be computed as

$$\mathbf{Qd}_k = \int_{k-1}^k \Phi(k, s) \mathbf{L}(s) \mathbf{Q}(s) \mathbf{L}^T(s) \Phi^T(k, s) ds. \quad (3.16)$$

where \mathbf{L} is the continuous-time representation of Λ .

As in the case of the Bayes filter, the KF estimation is carried out in two steps, prediction (*a-priori* with the '-' superscript) $\hat{\mathbf{x}}_k^- = \mathbb{E}[\mathbf{x}_k | l_1, l_2, \dots, l_{k-1}]$ and update (*a-posteriori* with the '+' superscript) $\hat{\mathbf{x}}_k^+ = \mathbb{E}[\mathbf{x}_k | l_1, l_2, \dots, l_n]$ (cf. Figure 3.6).

Assuming that the initial state $\hat{\mathbf{x}}_0$ and the initial covariance \mathbf{P}_0^+ are known, the linear form of the prediction step can be written as:

$$\hat{\mathbf{x}}_k^- = \Phi_{k-1} \hat{\mathbf{x}}_{k-1}^+ + \Gamma_{k-1} \mathbf{u}_{k-1} \quad (3.17)$$

$$\mathbf{P}_k^- = \Phi_{k-1} \mathbf{P}_{k-1}^+ \Phi_{k-1}^T + \mathbf{Qd}_{k-1} \quad (3.18)$$

where \mathbf{Qd}_{k-1} is the process noise covariance matrix (FARRELL, 2006). Now the measurement update equations are derived by taking the \mathbf{l}_k measurements into account:

$$\mathbf{K}_k = \mathbf{P}_{k-1} \mathbf{H}_k^T (\mathbf{H}_k \mathbf{P}_{k-1} \mathbf{H}_k^T + \mathbf{R}_k)^{-1} \quad (3.19)$$

$$\hat{\mathbf{x}}_k^+ = \hat{\mathbf{x}}_k^- + \mathbf{K}_k (\mathbf{l}_k - \mathbf{H}_k \hat{\mathbf{x}}_k^-) \quad (3.20)$$

$$\mathbf{P}_k^+ = (\mathbf{I} - \mathbf{K}_k \mathbf{H}_k) \mathbf{P}_k^- (\mathbf{I} - \mathbf{K}_k \mathbf{H}_k)^T + \mathbf{K}_k \mathbf{R}_k \mathbf{K}_k^T \quad (3.21)$$

where \mathbf{I} is the identity matrix and \mathbf{R}_k is the covariance matrix of the measurements (equivalent to the matrix \mathbf{W}_{ll}^{-1} in GMM Eq. (2.2)). \mathbf{K}_k is the Kalman gain matrix, which shows the influence of each measurement on the estimation of each state. \mathbf{K}_k contains values between 0 and 1, the values closer to 0 related with measurements having little effect on the state estimation, and values closer to 1 related to measurements having strong influence on the state estimation (THRUN ET AL., 2006).

3.3.3 Linearized Kalman Filter

SIMON (2006) points out that all problems are ultimately non-linear. As a result, non-linear estimators must be explored. In this section, the process to linearize a non-linear system is introduced,

and then, the Kalman filter equations are used to estimate the deviations of a state with respect to a nominal value.

First, the following non-linear system is considered (SIMON, 2006):

$$\dot{\mathbf{x}} = \mathbf{f}(\mathbf{x}, \mathbf{u}, \mathbf{w}, k) \quad \mathbf{w} \sim N(\mathbf{0}, \mathbf{Q}) \quad (3.22)$$

$$\mathbf{l} = \mathbf{h}(\mathbf{x}, \mathbf{v}, k) \quad \mathbf{v} \sim N(\mathbf{0}, \mathbf{R}_k) \quad (3.23)$$

where the system $f(\cdot)$ and measurement $h(\cdot)$ models are non-linear functions.

These functions are expanded around the nominal values for the state (\mathbf{x}_0), control (\mathbf{u}_0), measurement (\mathbf{l}_0) and noise values (\mathbf{w}_0 and \mathbf{v}_0) by using Taylor series. The results obtained differ from the nominal values due to mismodeling, disturbances or additional unexpected effects. After the linearization with Taylor series Eq. (3.22) can be written as:

$$\dot{\mathbf{x}} \approx \mathbf{f}(\mathbf{x}_0, \mathbf{u}_0, \mathbf{w}_0, k) + \left. \frac{\partial \mathbf{f}}{\partial \mathbf{x}} \right|_0 \cdot (\mathbf{x} - \mathbf{x}_0) + \left. \frac{\partial \mathbf{f}}{\partial \mathbf{u}} \right|_0 \cdot (\mathbf{u} - \mathbf{u}_0) + \left. \frac{\partial \mathbf{f}}{\partial \mathbf{w}} \right|_0 \cdot (\mathbf{w} - \mathbf{w}_0) \quad (3.24)$$

$$\approx \mathbf{f}(\mathbf{x}_0, \mathbf{u}_0, \mathbf{w}_0, k) + \mathbf{F} \cdot \Delta \mathbf{x} + \mathbf{G} \cdot \Delta \mathbf{u} + \mathbf{L} \cdot \Delta \mathbf{w}$$

$$\mathbf{l} \approx \mathbf{h}(\mathbf{x}_0, \mathbf{v}_0, k) + \left. \frac{\partial \mathbf{h}}{\partial \mathbf{x}} \right|_0 \cdot (\mathbf{x} - \mathbf{x}_0) + \left. \frac{\partial \mathbf{h}}{\partial \mathbf{v}} \right|_0 \cdot (\mathbf{v} - \mathbf{v}_0) \quad (3.25)$$

$$\approx h(\mathbf{x}_0, \mathbf{v}_0, k) + \mathbf{H} \cdot \Delta \mathbf{x} + \mathbf{M} \cdot \Delta \mathbf{v}$$

where the 0 subscript of the derivatives means that the derivation is carried out with respect to the nominal value. This is crucial in order to differentiate it from the EKF for non-linear functions.

Given the model in Eq. (3.24), the prediction and update Eq. (3.17)-(3.21) of the KF for linear problems can be rewritten as:

$$\Delta \hat{\mathbf{x}}_k^- = \Phi_{k-1} \Delta \hat{\mathbf{x}}_{k-1}^+ + \Gamma_{k-1} \Delta \mathbf{u}_{k-1} \quad (3.26)$$

$$\mathbf{K}_k = \mathbf{P}_{k-1} \mathbf{H}_k^T (\mathbf{H}_k \mathbf{P}_{k-1} \mathbf{H}_k^T + \mathbf{R}_k)^{-1} \quad (3.27)$$

$$\Delta \hat{\mathbf{x}}_k^+ = \Delta \hat{\mathbf{x}}_k^- + \mathbf{K}_k (\Delta \mathbf{l} - \mathbf{H}_k \Delta \hat{\mathbf{x}}_k^-) \quad (3.28)$$

where $\Delta \hat{\mathbf{x}}_k^+$ is the deviation of the estimated state vector with respect to the true state vector and $\Delta \mathbf{l}$ is the difference between the actual measurement and the nominal measurement. The final state can be computed by applying (SIMON, 2006):

$$\hat{\mathbf{x}} = \mathbf{x}_0 + \Delta \hat{\mathbf{x}} \quad (3.29)$$

Finally, the covariance prediction and update equations are dependent only on the measurements and therefore can be computed with Eq. (3.18) and (3.21).

3.3.4 Extended Kalman Filter

The Linearized Kalman Filter (LKF) algorithm is based on the linearization of the non-linear system around the nominal/a-priori state. For practical applications, the true state computation

is a challenging task, and in any case the computation is never perfect. In the EKF, this problem is tackled by performing the linearization around the filter estimate $\hat{\mathbf{x}}$.

Hence, the system model can be written as in Eq. (3.22), and the prediction step as in Eq. (3.17) and (3.18). The update step in the estimation with an EKF can be achieved by executing the following filter equations:

$$\hat{\mathbf{x}}_k^+ = \hat{\mathbf{x}}_k^- + \mathbf{K}_k (\mathbf{l}_k - \mathbf{h}(\hat{\mathbf{x}}_k^-, \mathbf{l}_k)) \quad (3.30)$$

In the EKF, Φ_{k-1} , Γ_{k-1} and \mathbf{H}_k are not achieved as in Eq. (3.24) since the Taylor series are expanded around the estimate $\hat{\mathbf{x}}$. Thus, these matrices can be computed as:

$$\Phi = \left. \frac{\partial \mathbf{f}}{\partial \mathbf{x}} \right|_{\hat{\mathbf{x}}_k^+} \quad \Gamma = \left. \frac{\partial \mathbf{f}}{\partial \mathbf{u}} \right|_{\hat{\mathbf{x}}_k^+} \quad \mathbf{H} = \left. \frac{\partial \mathbf{h}}{\partial \mathbf{x}} \right|_{\hat{\mathbf{x}}_k^-}. \quad (3.31)$$

In the EKF, the prediction state $\hat{\mathbf{x}}_k^-$ is considered the best estimate based on the measurement and system model information gathered up till epoch k . If the magnitude of the deviations between the estimated and nominal states at some point is too large, the obtained values for \mathbf{K}_k and \mathbf{P}_k^+ are close to 0. Taking into account the definition of \mathbf{K}_k in Eq. (3.19), this situation means that the observations used in the update step are ignored, and hence, the filter solution diverges.

3.4 Multi-Sensor Fusion

The automotive industry has developed and commercialized a wide spectrum of on-board sensors, such as radar, laser scanner or stereo cameras, that enable identifying and reconstructing the elements of the environment. The knowledge about the position of these sensors relative to the surrounding elements of the environment can be fused with the previously described sensor measurements for absolute positioning in order to increase the robustness of the solution. In this thesis, measurements carried out with laser scanners and stereo cameras are considered. Hence, the performance of these sensor measurements and the error sources that affect them are introduced and discussed in this section. Finally, details about the two main algorithms available to perform the sensor fusion are introduced.

3.4.1 Laser Scanner

Light Detection and Ranging (LiDAR) is a laser-based ranging system that measures the distance to a target by analyzing the Time of Flight (ToF) of the reflected laser beams (VOSSELMAN AND MAAS, 2010). A laser scanner combines the emission of the laser beams with a controlled rotation, capturing the distance to the elements of the surroundings. The devices that distribute the beams in a single plane are 2D (or line) laser scanners, whereas the ones that consider an additional perpendicular aperture angle are 3D laser scanners.

An overview of the precision of different 2D and 3D laser scanners can be found in DE PONTE-MÜLLER (2017b). The laser scanner operates with an precision between some centimeters up to

approximately 0.5 m in the range measurements. However, the environment characteristics and weather conditions can degrade this performance. The angular precision varies depending on the angular resolution, which is normally below 0.1° (DE PONTE-MÜLLER, 2017b).

Moreover, the performance evaluation of the ranging sensors is commonly associated to perception capabilities as perception range, field of view or obstructions, which depend as well on the laser scanner selected for the survey and the meteorological conditions.

3.4.2 Stereo Cameras

Camera-based solutions are crucial in order to collect complete and reliable information of the environment (FÖRSTNER AND WROBEL, 2016), that can be used to perform object detection, and collision avoidance tasks in an autonomously driven vehicle. Using a pair of cameras, the 3D reconstruction of a dynamic/static scene can be achieved. Although most of the techniques for image positioning are computationally expensive, some algorithms for the 3D reconstruction of a scene, or the 3D coordinates of an object run in real-time (GEIGER ET AL., 2011).

While the ranging measurements carried out with the laser scanner show rather linear errors over the distance, the precision of the 3D coordinates estimated with the cameras decreases quadratically with distance, and they therefore increase from a few centimeters to several meters if the detected object is far from the vehicle. These values also depend on the inner characteristics of the used cameras, such as focal length (that constrains the horizontal and vertical aperture of the image conic bundle) and the image resolution (pixel size). Setting aside the geometrical characteristics of the measurements, the laser scanner is generally more suitable to determine the distance to the elements of the environment, whereas the cameras provide additional qualitative information that allows to (re-)identify objects. The cameras allow to determine the distance to the surrounding elements too, but it is much more exposed to errors than laser scanners (due to the calibration, dense matching, base length, distance to objects, etc.). Finally, the performance of both sensors can be affected by the light and weather conditions, restricting its usage specially under fog and/or precipitations (rain or snow).

3.4.3 Localization Versus Simultaneous Location and Mapping

The multi-sensor fusion concept is based on the combination of different sensor measurements in order to overcome the flaws of each individual sensor. A common approach is to use ranging sensors to map the environment and measure the relative position of the vehicle with respect to the elements of the environment in order to increase the robustness of the INS/GNSS integrated solution. The inclusion of a map as prior knowledge allows the estimation of the complete pose of the vehicle by matching the map features with the detected ones in what is called *localization problem*. If no prior knowledge about the environment is included, the vehicle must be able to build the map of its environment while simultaneously localizing itself, in what is called Simultaneous Location and Mapping (SLAM) approach.

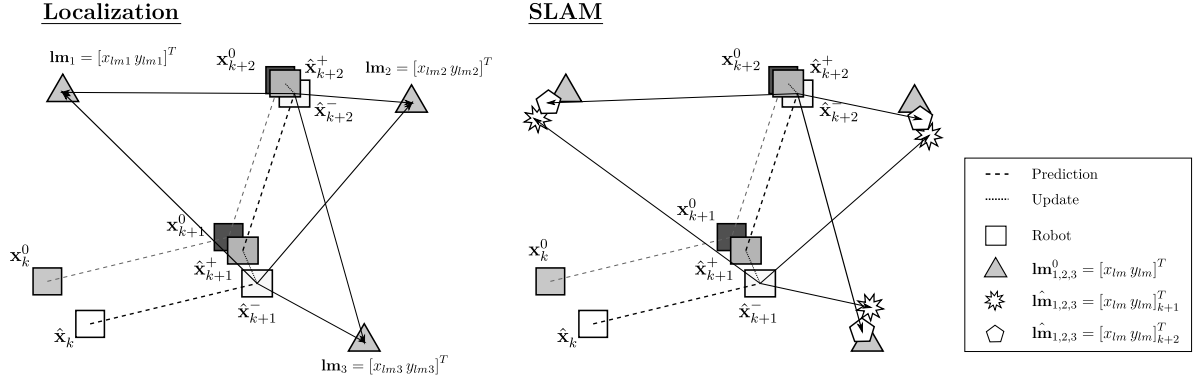


Figure 3.7: Localization and SLAM concepts using an EKF approach. The position of the robot is color-coded by the epoch in order to improve the readability. In both graphs, the superindex 0 indicates the nominal position of either the robot or the landmarks.

Let us assume that the 2D pose ($\mathbf{x}_k = [x_v \ y_v \ \psi]^T$) of a robot is to be estimated in an environment with three landmarks using an EKF algorithm as the one presented in Section 3.3.4. In the *localization approach*, the landmark coordinates $\mathbf{lm}_i = [x_{lm} \ y_{lm}]_i^T$ are assumed to be known. Thus, the predicted state solution $\hat{\mathbf{x}}_k^-$ can be corrected by measuring the relative position of the robot with respect to these landmarks, obtaining a more accurate and precise solution $\hat{\mathbf{x}}_k^+$.

In the SLAM approach, the landmark coordinates are assumed to be unknown. Hence, the ranging sensor measurements are used to determine their relative position with respect to the vehicle. Here, it is worth mentioning that the ranging measurements yield the relative position of the landmark with respect to the sensor in its own sensor frame. These coordinates must be transformed to the global frame selected for the absolute position and orientation of the vehicle in order to carry out the correction. Then, the relative positioning nature of the ranging sensors causes the uncertainty in the predicted position of the vehicle to be transferred to the position estimation of the landmarks. Hence, as opposed to the localization problem, the landmark position is estimated in the update step of the EKF, and their uncertain positions are simultaneously used to correct the predicted state (cf. Figure 3.7). Given the simultaneous 2D estimation of vehicle and landmark positions, the state vector can be written as:

$$\mathbf{x}_k = [x_v \ y_v \ \psi \mid x_{lm1} \ y_{lm1} \ x_{lm2} \ y_{lm2} \ x_{lm3} \ y_{lm3}]^T \quad (3.32)$$

where the suffix v refers to vehicle and the suffix (lm) refers to the landmarks. The recursive simultaneous estimation in consecutive epochs produces a decrease on the uncertainty of both landmark and vehicle positions, if the measurements are accurate enough to prevent the estimated trajectory from diverging from the nominal trajectory (the updated position of the robot is always closer to the nominal position in Figure 3.32). In 3D cases, the state vector must be obviously adapted to the consideration of z_v and z_{lm_n} components, as well as the remaining attitude parameters (i.e. ϕ and θ).

Finally, full mathematical examples of single-robot localization and SLAM problems can be found in THRUN ET AL. (2006).

4 State of the art in Collaborative Positioning

4.1 Introduction

Collaborative positioning is a technique in which the quality of the Position, Navigation and Timing (PNT) solution of a group of vehicles is enhanced by performing relative measurements between each other or to the elements of the environment (MURRAY, 2007). The relative localization between agents in a navigation scenario is a crucial piece of information in order to improve the performance of ADAS, that are designed in order to increase the safety and efficiency of driving, and rely on three pillars: perception, processing and actuation (DE PONTE-MÜLLER ET AL., 2016).

In order to improve the perception of the system, exteroceptive sensors are normally mounted on the vehicles (e.g. laser scanner or vision-based sensors). These sensors enable the detection and tracking of the elements of the surroundings. However, they show significant weaknesses. For instance, the ranging sensors have a limited perception range, and the measurements are easily obstructed. In order to overcome these limitations, collaborative techniques can be used.

As stated in the introduction of this document, the navigation situation where a group of vehicles navigate in a certain area, and where information about the relative pose between vehicles can be computed, is understood as a network. Within this networked navigation techniques, DE PONTE-MÜLLER (2017b) makes a distinction between cooperative and non-cooperative techniques. In this work, the author considers an algorithm to be collaborative/cooperative if the vehicles involved are taking part actively in the creation of a link measurement or a communication scheme between each other. For instance, the situation in which a vehicle serves as a reflecting surface for the ranging measurements taken from another vehicle is considered to be a non-collaborative passive technique, because the data must be segmented and clustered into objects that can later be used as landmarks in order to aid the positioning of the vehicle. In collaborative approaches based on V2V communication, the position information is directly computed at each vehicle, so the task to detect and identify other vehicles disappears. Hence, the laser scanner or stereo camera are by themselves non-collaborative sensors, according to this classification.

In this section, we start with an overview of the different available communication architectures, where we introduce some modern techniques for feature extraction using the available sensors in the i.c.sens project (SCHÖN ET AL., 2018), and that can be used to achieve collaborative positioning with these ranging sensors. Then, modern state-of-the-art solutions for collaborative navigation scenarios are introduced and discussed in detail, classifying them depending on the main sensor used in the algorithm. Lastly, the available simulation technologies are introduced, crucial for the research carried out within the scope of this thesis.

4.2 Communication Architectures

In order to implement collaborative positioning approaches, an efficient communication architecture has to be defined. KOKUTI ET AL. (2017) reviewed the field enumerating three bidirectional *Vehicle to everything (V2X)* architectures: Vehicle to Vehicle (V2V), bidirectional V2P, and V2I.

Vehicle to Vehicle (V2V): The V2V communication is established in order to share information between the road vehicles in a certain area. HARDING ET AL. (2014) contain the basic safety information that vehicles should share in order to facilitate warnings to the drivers concerning impending crashes. The European standard for V2V communications is the ITS-G5 (INTELLIGENT TRANSPORT SYSTEMS, ITS), developed from the American IEEE 802.11., and contains position, velocity and heading information in the message. This architecture is typically used in the so-called Vehicular Ad-Hoc Networks (VANET) (HARTENSTEIN AND LABERTEAUX, 2010), where the vehicles transmit data between each other, providing useful information in order to improve the performance of the navigation algorithm and to overcome the exteroceptive sensor limitations. Moreover, available feature extraction and urban scenario modeling algorithms allow to compute the V2V relative positioning between the detected and the ego vehicles using laser scanner (FAYAD AND CHERFAOUI, 2007; LINDNER AND WANIELIK, 2009) or vision-based approaches (COENEN AND ROTTENSTEINER, 2019; LI ET AL., 2018). The knowledge achieved with these methodologies allows the simultaneous estimation of the pose of vehicles.

Vehicle to Pedestrian (V2P) and Pedestrian to Vehicle (P2V): The link between the vehicles and the pedestrians is crucial in order to increase the safety of the pedestrians. Pedestrian safety solutions can be sensor based (NGUYEN ET AL., 2019; GAMDHI AND TRIVEDI, 2007) or communication based (BAGHERI ET AL., 2014). Given the vulnerability of the ranging sensors (e.g. limited line of sight), more research and interest is being directed towards the investigation of V2P solutions based on wireless communication (i.e. LTE or 5G), although the communication latency increases, affecting the accuracy and precision of the results.

Vehicle to Infrastructure (V2I) and Infrastructure to Vehicle (I2V): The aim of the V2I communications is to establish a connection between the fixed elements of the environment and the vehicles. As a result, the information of the urban furniture designed in order to regulate traffic can be shared in advance with the vehicles so that they can react to the events, maximizing the efficiency of the traffic flow and ensuring a safe reaction to hazardous episodes (5GAA, 2016). An example of WLAN-based positioning fused with GNSS measurements can be found in SCHLINGELHOF ET AL. (2008).

In addition, multi-sensor systems are able to capture and classify the information of the environment. This information is usually associated with map information known a-priori in order to improve the available algorithms for autonomous navigation, specially in urban areas.

4.3 Collaborative Positioning

Collaborative positioning relies on the availability of the architectures introduced in Section 4.2 for the vehicle communication within a VANET in order to overcome the limitations of multi-sensor solutions. The interest in the collaborative techniques has grown considerably in recent years, being considered in the navigation and robotics fields as a powerful approach to increase the robustness in the positioning solution specially in harsh or GNSS-denied environments (e.g. urban canyons, tunnels, highly covered vegetation areas, indoor, etc.). This motivated the development of many algorithms where the information from different sensors is fused and/or shared.

4.3.1 GNSS Collaborative Positioning Approaches

Numerous methodologies focus on the improvement of GNSS standalone solutions by sharing information between receivers.

First, it is worth mentioning that the Differential GNSS techniques explained in section 3.1.1 could be considered a real-time collaborative positioning technique, since a base station sends the corrections to be applied at the rover in order to mitigate the effect of the error sources that affect the signal propagation. Although expecting a weaker solution due to the changing position of the master, this technique can be adapted to a setup with at least two rovers (moving baseline). Understanding the vehicles equipped with GNSS receivers in a collaborative scenario as rovers, one vehicle with specially bad satellite visibility or in severe multipath conditions (target vehicle) can benefit from other vehicles of the surroundings that find themselves in more favorable signal reception conditions (aiding vehicle) by receiving shared pseudorange measurements from them (DE PONTE-MÜLLER ET AL., 2014; TAHIR ET AL., 2019). Additional collaborative approaches for the derivation of absolute positions are presented in BEREFEIT ET AL. (2004) and ROTH ET AL. (2012).

Also, some algorithms discuss the fusion of GNSS measurements with laser scanner (SOLOVIEV, 2008) and vision-based sensor measurements (LANEURIT AND BLANC, 2003). However, the usage of ranging or visual-based solutions requires that the vehicles find each other in Line-of-Sight (LOS). In collaboration, both ALAM ET AL. (2011) and MINETTO ET AL. (2019) discuss the usage of Direct Short Range Communication (DSRC) in order to achieve real-time communication between agents. Although this methodology has a contained time delay as an advantage, it also requires that the vehicles are in LOS. This problem is tackled in MINETTO ET AL. (2019) by developing a cooperative approach that relies on the GNSS observations and network connectivity in order to extract inter-vehicular distances even in the non-Line-of-Sight (NLOS) situations.

Furthermore, the fact that collaborative approaches are specially powerful in urban areas lead towards the consideration of maps or digital terrain/elevation models in order to aid the computations and improve the positioning (STRANDJORD AND AXELRAD, 2018; CHOE ET AL., 2018; TOLEDO-MOREO ET AL., 2009).

Last but not least, a collaborative approach used in order to improve the ambiguity resolution in RTK approaches (see section 3.1.1) using V2V DSRC communications is presented in ANSARI ET AL. (2013).

4.3.2 Inertial Measurement Collaborative Positioning

In many navigation problems, the inertial measurements are used simply as part of the INS/GNSS integration (see Section 3.2.2). At the same time, the obtained solution is used as an intermediate step in order to assign global coordinates to other relative positioning sensor measurements (laser scanner, radar, etc.). Also, specially the angular rate measurements describe the relative movement of the body with respect to the selected global frame. This means that part of the solution is only suitable for the computation of the ego/target vehicle solution. As a result, the interest towards investigations where inertial measurements are shared in a collaborative approach is almost non-existent.

However, it is worth mentioning the research carried out by CUCCI AND SKALLOUD (2019) where the understanding of networked navigation has a different interpretation than in the previously summarized literature, or this document. In this research, the dynamic network is defined by the interpretation of the discrete poses of a device (UAVs in this case), and/or the GNSS measurements used to prevent the solution from drifting. Then, the links are defined by the dependencies between nodes (poses or measurements), establishing in this way a graph where the relation between poses of consecutive epochs are defined by the inertial measurements. These dynamic networks are studied also in COLOMINA AND BLÁZQUEZ (2004), and the approach is known as pose-graph optimization in the robotics field (INDELMAN ET AL., 2013).

The major advantage of this methodology is that the adjustment is carried out in a single least-squares step (non-recursive), and hence all the methodologies described in section 2.3 could be applied to optimize the dynamic network. Nevertheless, the estimation of all inertial sensor observations (normally high-rate sensors easily have over 100 Hz) in a Batch Least-Squares (BLS) algorithm, leads to the consideration of a large number of unknowns, and hence to a computationally expensive task that constrains its usage in real time.

4.3.3 Collaborative Positioning with Laser Scanner

As stated before, the majority of navigation solutions combine the GNSS/INS integrated solution with additional sensors that provide rich information about their environment. The laser scanner (see Section 3.4.1) gives information about the relative positioning of the vehicle with respect of the fixed and dynamic surrounding elements. Then, complex point cloud segmentation algorithms are used in order to extract semantic information from the point cloud. This task consists of assigning a certain class to subsets of points so that objects can be identified. Taking this into account, it is possible to use the laser scanner to compute the relative positioning to other vehicles, pedestrians and/or to the different fixed elements of the environment, depicting a dynamic network situation.

HOWARD ET AL. (2002) describes a collaborative algorithm applying a maximum likelihood estimation using only the robots themselves as landmarks. This theoretical implementation is validated with an experiment where a laser scanner is used to compute the V2V measurements and establish the dynamic network. The maximum likelihood estimation algorithm is also used in THRUN ET AL. (2000) where 2D laser scanners are used in order to build large maps by fusing information collected with multiple hierarchically classified robots. In this approach, a robot uses its laser scanner measurements to localize itself in the map of the leader. THRUN (2001) also discusses the fusion of maps obtained from laser scanners placed in different robots using a maximum likelihood estimation. In addition, MARTINELLI ET AL. (2005) describes an approach to solve the simultaneous localization of a group of robots by using relative measurements. Although not specifying the type in the paper, the algorithm can be applied using laser scanner measurements.

As an alternative to the localization approaches, collaborative SLAM methodologies using laser scanners are also studied in KOCH ET AL. (2016), MOURIKIS AND ROUMELIOTIS (2006) and ZHOU AND ROUMELIOTIS (2006).

4.3.4 Collaborative Positioning with Vision-Based Sensors

Similar to laser scanners, vision-based sensors allow to obtain a 3D point cloud as a result of the reconstruction from a pair of stereo images or from a set of consecutive images (*bundle adjustment*). Thus, if inter-vehicle communication schemes are available, collaborative approaches can be applied in order to aid both the localization of the vehicle and the mapping of the environment.

PIASCO ET AL. (2016) discuss a collaborative methodology where stereo vision is used for the localization of a fleet of micro-air vehicles equipped with monocular cameras. Then, a formation scheme is proposed in order to maximize the necessary overlapping areas to guarantee stereo vision. A similar approach is proposed in ACHELNIK ET AL. (2011) where the relative pose of two robots is retrieved in real-time combining the advantages of both stereo and monocular vision to obtain a stereo rig. In addition, OLEYNIKOVA ET AL. (2015) propose a localization approach where an aerial robot and a ground robot locate themselves within a previously built map. A similar decentralized approach is presented in ZOU AND TAN (2013) where a collaborative SLAM is tested for collaborative mapping of both dynamic and static environments.

A disadvantage of the previously introduced approaches is that the robots do not share the self-collected data with each other, restricting the efficiency of the 3D reconstruction. This problem is tackled in the approaches by VIDAL-CALLEJA ET AL. (2011) or GUO ET AL. (2018), where the area is collaboratively mapped using robots and UAVs. These methodologies are based on the individual acquisition of submaps by each robot, and the posterior fusion in a common map using co-observations or additional measurements (e.g. GNSS measurements). This results in an increase in accuracy and precision of the generated map that at the same time increases the precision and accuracy of the robot team localization.

Large amounts of research are being carried out using SLAM techniques, since the environment recognition, used in order to aid the ego motion and vehicle localization is key to enable autonomous

navigation. Here, SCHMUCK AND CHLI (2018) introduce a centralized algorithm where a team of robots is equipped with monocular cameras, a processing board and a communication unit. The centralized architecture allows the estimation of the potentially large amount of information collected by the robots in a server with bigger computational capabilities. Additional literature that provides information about vision-based centralized SLAM can be found in RIAZUELO ET AL. (2014), MORRISON ET AL. (2016) and KARRER ET AL. (2018).

Although the centralized algorithms are suitable in order to assure data consistency, decentralized approaches are needed in a lot of tasks, since the large amounts of data collected do not have to pass through a central server. In this way, only the most critical data are sent to the central server. Decentralized algorithms with vision-based SLAM methodologies are discussed in CUNNINGHAM ET AL. (2013), where each robot performs a full SLAM or in DONG ET AL. (2015) and SOLÀ ET AL. (2008) where Unmanned aerial vehicles (UAVs) are considered.

Lastly, BRYSON AND SUKKARIEH (2009) discuss the implementation of an inertial SLAM algorithm for multi-vehicle UAVs approaches, in both centralized or decentralized approaches. The results are introduced by means of simulation experiments.

4.3.5 Collaborative Positioning Using Other Sensors

The previous sections contain a literature review on state-of-the-art collaborative approaches where the sensors considered in the approach presented in this thesis are discussed. However, a large number of collaborative approaches that build upon the usage of a sensor or communication scheme are not described. Given the extended use of Radio Detection and Ranging (RADAR) and Ultra-wide band (UWB) ranging measurements in CP, some relevant literature is briefly compiled in this section.

RADAR techniques allow to estimate the V2V links by measuring the Received Signal Strength (RSS) of a signal transmitted from another vehicle. PARKER AND VALAEE (2007) discuss a cooperative approach where RSS and velocity measurements are combined. In addition, DE PONTE-MÜLLER ET AL. (2016) propose a decentralized fusion framework in which cooperative positioning information is fused with on-board RADAR measurements, showing very good accuracy in vehicle-to-vehicle line-of-sight situations.

Ranging using UWB signals offers an alternative to GNSS in local positioning, specially in GNSS-compromised or GNSS-denied environments (WYMEERSCH ET AL., 2009; PETOVELLO ET AL., 2012). UWB measurements allow to measure the relative position between nodes with a short-time window of deployment, which makes it suitable for the definition of an *ad-hoc* network (KOPPANYI ET AL., 2018). Also, UWB technology offers highly accurate timing properties and the signal can travel through walls and other objects, so that it serves as the perfect complement to GNSS positioning. In WANG ET AL. (2016), a tightly-coupled GPS/UWB/INS cooperative positioning scheme based on KF estimation supported by V2I communication is presented.

4.4 Simulation Technologies

In the course of this thesis, the performance of the designed filter is tested. In multi-sensor systems, it is interesting to not only evaluate the performance of the filter in terms of the statistics introduced in Section 2.3.1 (e.g. accuracy, precision or integrity), but also in terms of processing capabilities as well. In general, the evaluation of the latter is done relative to the sensor combination selected. However, the wide variety of available sensors necessitate to select the optimum processing parameters that maximize the process efficiency.

Obviously, the evaluation of different sensor combinations in field testing would be expensive, and potentially unsafe, not only for the staff involved in the experiments, but also in terms of data collection and storage. To overcome these difficulties, an evaluation is carried out using a simulation environment.

Yet, simulations that contain statistical methods normally rely on random samples, sometimes following a particular distribution (GENTLE, 2003). In this thesis, a random number generation that generates samples fulfilling a uniform or normal distribution is used to generate the measurement errors, amongst other simulation variables (see Chapter 6). Thus, in order to mitigate the effect that a particular random distribution might have on the estimation, Monte Carlo simulation techniques are applied.

4.4.1 Simulation Environments: Overview

Nowadays, the collaborative navigation field is being explored in detail, conducting research in different directions (e.g. traffic flow analysis, efficiency and reliability of ADAS, and/or ego-vehicle perception and navigation solution) aiming to improve the performance of the existing methodologies for autonomous driving. Nevertheless, regardless of the research target, the realization of experiments in the design process of collaborative navigation components or algorithms is in general costly and hazardous in specific situations. Moreover, navigation algorithms normally contain factors with a random character that are vulnerable to the explicit characteristics of the experiment. Hence, a simulation environment that helps to cost-effectively and safely reproduce a wide spectrum of realistic schemes in order to evaluate the performance of different sensor setups and configurations under different environmental situations is developed.

The design of a collaborative navigation simulation tool is a complex task that must consider the generation of vehicle dynamics, and measurements performed with the sensors described in chapter 3 (GNSS, IMU, laser scanner and stereo cameras). Also, environmental models are studied in order to supply the necessary realism to the GNSS and relative positioning measurements. Furthermore, the inter-vehicle V2V measurements simulation is an imperative task in order to analyze various CP scenarios.

With this preconditions in mind, it is very challenging to find a suitable available simulation environment to fulfill the ultimate target of this thesis, without a significantly large amount of effort in its complete adaptation to our problem. However, simulation environments for the indi-

vidual components are discussed in numerous research articles, and also proposed as commercial products. First, simulation methodologies are frequently used in order to analyze the behavior of GNSS in a wide range of situations. For example, LEE ET AL. (2008) show a multi-GNSS simulation system developed to mitigate multi-path and improve the accuracy of the GNSS solutions. In addition, HEWITSON AND WANG (2006) propose the usage of GNSS simulators to analyze the integrity performance of multi-constellation GNSS. Moreover, commercial packages such as Spirent GNSS Simulator¹ or Bernese GNSS Software² which contains an option to simulate GNSS measurements and clock corrections, are convenient to perform a PPP estimation. Second, simulation and post-processing approaches for positioning using inertial measurements are presented on JWO ET AL. (2014), GÖRCKE ET AL. (2013), GIROUX ET AL. (2003), and GADE (2005). These approaches solve the IMU navigation equations (Eq. 3.5) by first generating a set of values for the specific forces (output from the accelerometers) and angular rates (output from the gyroscopes) using the methodology presented in Section 3.2. Also, PARÉS ET AL. (2015) discusses the inertial measurement generation from a set of waypoints. Although these works represent valid simulation methodologies, they only consider the processing of a single sensor measurement type (only GNSS or only IMU), and neither the environment, nor inter-vehicle measurements are contemplated. ZHANG ET AL. (2018) uses 3D city models in order to overcome the GNSS limitations in urban canyons using a collaborative approach, although no further sensor measurements are contained in the simulation.

Regarding collaborative simulation tools which contain all of the previously mentioned simulation components, TIDEMAN AND VAN NOORT (2013) introduce PreScan³ and ITS Modeller as commercial simulation tools for connected vehicle systems. PreScan allows the user to model the vehicle dynamics, sensor measurements, V2X communications (KOKUTI ET AL., 2017), environment characteristics and weather conditions to evaluate the connected vehicle systems. Additional projects as PreDrive C2X⁴, Drive C2X⁵, SAFESPOT⁶ and CVIS⁷ are also involved in the model built up and evaluation of collaborative systems.

In the simulation methodology developed and presented in this thesis, the following contributions are made. First, it offers four different approaches for the simulation of trajectories. These are built upon existing work such as GIROUX ET AL. (2003) or PARÉS ET AL. (2015), but additional features are used to provide a realistic representation of the vehicle paths. In this direction, the availability of open source GIS external software, Digital Terrain Model (DTM) and maps enable georeferencing designed trajectories, and hence, achieving a realistic maneuver distribution and an authentic geometric relation between the vehicle and the elements of the environment. Second, the approach contains three possibilities to model the environment: (i) by digitizing it using an external software (as with the trajectories); (ii) by using a 3D City Model with Level of Detail-2⁸;

¹Spirent GNSS Simulator: <https://www.spirent.com/>

²Bernese GNSS Software: <http://www.bernese.unibe.ch/docs/D0CU52.pdf>

³PreScan: Simulation of ADAS and active safety. <https://tass.plm.automation.siemens.com/prescan>

⁴PreDrive C2x: <https://www.fokus.fraunhofer.de/9f9e1f7a72e07755>

⁵Drive C2X: <https://connectedautomateddriving.eu/project/drive-c2x/>

⁶SAFESPOT: <http://www.safespot-eu.org/>

⁷CVIS: <http://inv.ccinshae.gob.mx/>

⁸3D City Model 2017. https://opengeodata.hannover-stadt.de/Stadtmodell_Hannover_CityGML_LoD2.zip

(iii) by using a pre-aligned terrestrial laser scanner point cloud. The usage of aerial based LiDAR point clouds is restricted to low flying heights, where most of the building facades are recorded. The missing lower parts of the buildings would limit its applicability in simulations for ground-driven vehicles. Third, the GNSS, IMU, laser scanner, and stereo camera measurements are simulated. Additional sensors (e.g. odometer, radar, etc.) regularly used in multi-sensor fusion are omitted in this thesis due to their unavailability within the i.c.sens project. Furthermore, the inter-vehicle V2V measurements are included in the system, exemplarily by computing GNSS baselines (see Eq. 3.4), given that the vehicles are assumed to be equipped with GNSS receivers. Finally, the generated measurements are fused in the proposed Collaborative-Extended Kalman Filter (C-EKF), which operates as a common EKF where the state parameters from a group of vehicles are simultaneously estimated.

The general description of the simulation framework defined in the previous paragraph entails an improvement with respect to collaborative simulation engines (such as PreScan) for the purpose of this thesis. PreScan offers the possibility for the user to recreate an environment by selecting elements of the urban furniture and buildings from libraries. Although the library contains a wide spectrum of elements, they must be individually selected to build up the scenario. This methodology is suitable if the simulation intends the evaluation to take place in a narrow area (e.g. for the evaluation ADAS in urban intersections), but becomes arduous for large-scale urban areas. In the simulation approach presented in this document, the environment can be modeled in three different ways depending on the target of the study (see Section 5.1.2). Also, PreScan enables the measurement generation using libraries that contain certainly a wider range of real commercial sensor geometries. However, in this thesis, the measurement geometry is often designed for a specific target, mitigating the importance of a larger availability.

In the present case, the situation described by the vehicles, landmarks and measurement distribution depicts a dynamic network. The versatility and potential of the tool is assessed by using it in a wide variety of scenarios with the challenge to evaluate the behavior of the dynamic networks regarding the navigation performance metrics described in Section 2.3.1.

4.4.2 Monte Carlo Methods

In any adjustment, the uncertainty of the estimated parameters is influenced by the uncertainty of the variable inputs through the functional model (e.g. Eq. (2.1) or (3.23)). In dynamic systems and KF estimations, an additional source of uncertainty on the motion model must be considered for the state estimation (e.g. Eq. (3.22)). Given that all these variable inputs cannot be completely described in a deterministic way, a stochastic model must be defined. Here, the uncertainty on the measurements is quantified using VCM and standard deviations.

The distribution of the uncertainty can be assumed to be known (probabilistic approaches) or unknown (interval mathematics). In either case, the simulation of an error contains always a part of randomness that produces effects which might affect the interpretation of the results.

This problem can be tackled by using Monte Carlo (MC) simulation (GENTLE, 2003). These methodologies rely on the generation of artificial sets of samples within a defined domain and under an assumed distribution, spacing the samples throughout the complete range of possible situations in which a real case scenario might fall into. With this in mind, MC techniques are applied in this thesis mainly in two different ways.

1. The measurement error is generated randomly with the selected standard deviation. Thus, the filter is repeated a number of times so that the epoch-wise span of error magnitudes is covered.
2. The standard deviation values selected for the process and measurement noise generation define the uncertainty on the estimated parameters. These parameters are selected in accordance with real sensor characteristics. Nevertheless, the wide availability of sensors and both its geometrical and physical characteristics, make the task to relate the sensors performance to a certain precision difficult. Thus, the interval between a theoretical high-end and a low-cost sensors can be characterized, in this way establishing the limits of the multi-dimensional space defined by the precision range of each sensor considered. Subsequently, samples are generated within the defined parameter space, obtaining numerical results (*scores*) that help to identify the regions of the parameter space that produce optimum results.

The number of samples varies depending on the type of simulation, and it might be heavily constrained by the computational efficiency of the adjustment. In multi-variate simulations, the number of runs can be quite large, and together with the fact that the process might be already computationally expensive, might lead to unachievable simulation times. In this cases, MC sampling can be used in order to generate the samples in a supervised way, using pattern recognition within the set of scores obtained with previous samples or basing the sample generation by means of the obtained Probability Density Function (PDF) with the scores. However, these techniques always lead to situations of parameter space under-sampling, which under the assumption of unknown error distribution might be insufficient for the adequate posterior accuracy assessment. For example, integrity risk analysis that focuses on events with low probabilities would need a complete parameter space sampling in order to guarantee justifiable conclusions.

4.5 Discussion

In this chapter, the state-of-the-art methodologies in collaborative navigation approaches were surveyed, classified in terms of their main sensor used for the collaboration. In the scope of this thesis, collaborative navigation is achieved by interconnecting the vehicles with GNSS baselines (moving baselines). This methodology differs slightly from the ones discussed in BEREFELT ET AL. (2004) and MINETTO ET AL. (2019). Both publications contain methodologies where the pseudo-ranges are shared in order to achieve a higher satellite visibility and more accurate corrections. Nevertheless, in the estimation proposed in this thesis, the GNSS observations are not introduced by means of the well-known GNSS observables discussed in Section 3.1.1, but as directly obtained positioning solution in the target reference frame. Here, satellite geometry information can be

introduced as prior-knowledge in order to generate a GNSS measurement noise model taking into account the satellite geometry (with periods of signal outage as well). In absence of this information, the GNSS observations are generated under the assumption that there are always more than four satellites in Line-of-Sight (LOS). Subsequently, since the V2V measurements are generated as a function of the GNSS positioning (see Eq. (3.4)) the errors in both measurement types are proportional.

Moreover, the reviewed literature can be classified using additional criteria. Regardless of the sensor architecture used, the presented approaches can be also classified in terms of the estimator type and the implementation strategy. These additional classification strategies add a diverse point of view, that is useful in order to justify the strategy pursued in this thesis. Most of the approaches that apply exteroceptive sensors use a Bayesian inference-based estimator. On the one hand, most of the SLAM algorithms where information collected from several vehicles (robots or UAVs) is used in order to improve the mapping and localization task are KF-based (PIASCO ET AL., 2016; ACHTELIK ET AL., 2011; VIDAL-CALLEJA ET AL., 2011). On the other hand, maximum likelihood estimation is used, although more often in localization approaches like HOWARD ET AL. (2002) and THRUN (2001). Less frequent is the application of BLS in collaborative approaches (GUO ET AL., 2018; GARCIA-FERNANDEZ AND SCHÖN, 2017), given its limited applicability in time-variant, dynamic operations. Alternatively, the discussion regarding the implementation strategy divides the issues between centralized and decentralized methodologies. The principal advantage of centralized algorithms is that it facilitates ensuring data consistency. However, this means that the data collected with several vehicles (generally, large amounts of data) must be processed within a central server, limiting its application in estimations with numerous vehicles.

Given this background, the algorithm developed in this thesis for the study of dynamic networks is implemented as a centralized C-EKF since the KF-based estimation enables the modeling of the vehicle dynamics (normally described by continuous differential equations) in the prediction step, and the discrete time measurement equations in the update step. Then, the network is characterized considering elements of the environment geo-location as known (localization) and unknown (SLAM) in order to evaluate the differences between both methodologies. Also, in the above mentioned literature, the laser scanner and stereo/monocular camera observations are rarely combined due to the difficulties that arise from the combination of large amounts of data. This problem could be tackled by the implementation of a decentralized approach (CUNNINGHAM ET AL., 2013; DONG ET AL., 2015). Nevertheless, a decentralized algorithm would split the task to estimate the pose of each node in separated estimators, complicating the assessment of the data consistency. As a consequence, the decentralized algorithm is considered to be more suitable for a local analysis (e.g. the benefits that a group of aiding vehicles infer on the ego vehicle) than for a global evaluation of the dynamic network performance (overall network analysis). Therefore, the centralized approach is the selected strategy. Subsequently, the problems that emanate from the high amount of data are handled in the simulation by reducing the number of observations with respect to real cases. In this way, a more moderate computation is achieved, together with a generally less overoptimistic set of observations obtained from the usage of a too generalized model of the environment (outliers, reflections and occlusions are not considered, see Section 5.1.2).

Finally, it is worth to remember that the selected estimator is designed and implemented in order to aid the understanding of the dynamic network response with respect to changes in its geometrical and observational characteristics. Hence, the research idea differs slightly from the typical design of engineering components, where additional factors of the algorithm performance must be discussed, and compared with the current state-of-the-art methodologies. For this reason, only the qualitative synergies with the methodologies of this section were discussed.

5 Simulation Framework for Collaborative Scenarios

In this thesis, the response of dynamic networks with respect to changes in its configuration and the impact of CP with respect to single-vehicle positioning is evaluated. Also, methodologies to determine the optimum sensor configuration and processing parameters are developed based on Monte Carlo techniques. To achieve this goal, a simulation tool for collaborative scenarios is designed and implemented using MATLAB (2019) software.

In this chapter, the main components of the simulation framework are discussed in Section 5.1. Subsequently, a sample run of a novel collaborative navigation scenario is designed in order to show the versatility of the developed simulation framework by comparing the results obtained using localization and SLAM approaches (cf. Section 5.2). In the evaluation, the strengths and weaknesses of the estimation are also assessed in order to point out the most important details to be evaluated more specifically in the following chapters.

5.1 Design and Implementation

In this section, different factors and steps needed to implement a simulation tool for collaborative navigation are discussed. The structure of the simulation tool is divided into four steps (see Figure 5.1): generation of trajectories, environmental model selection, generation of measurements and sensor measurement fusion algorithm.

5.1.1 Vehicle Trajectories Simulator

In this approach, trajectories consisting of attitude, position, velocity, angular rates and acceleration can be generated using different approaches.

Velocity and Attitude Time Series

GIROUX ET AL. (2003) propose the generation of a trajectory starting from a set of data points that represent a flight profile. These data points contain information about the airspeed (velocity), attitude (Euler angles), angle of attack and angle of side-slip of the aircraft at different times. This situation is transferred to land-based vehicles.

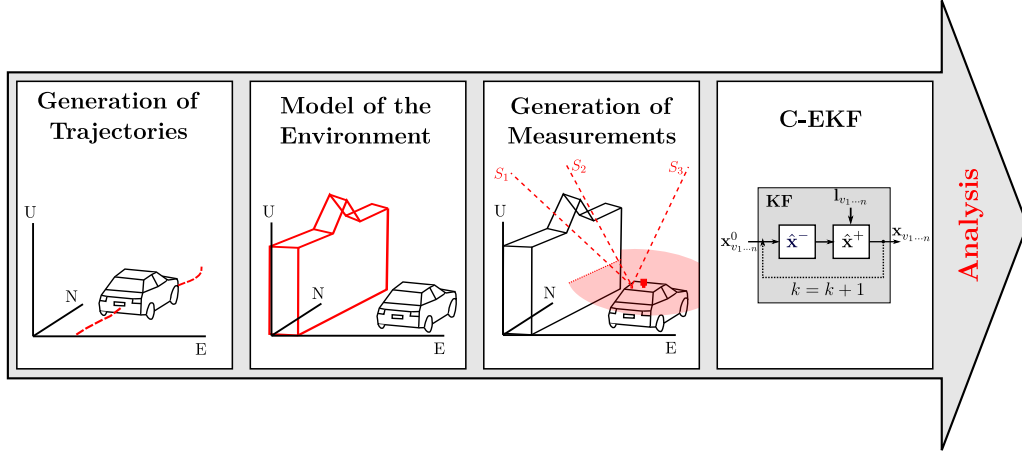


Figure 5.1: Overview of the developed simulation framework. The diagrams only show one vehicle for simplicity although n sets of measurements and trajectories can be simulated.

$$\mathbf{v}_k^b = [v_x \ 0 \ 0]^T, \quad \Psi_{bn_k}^n = [\phi \ \theta \ \psi]. \quad (5.1)$$

Assuming that the speed vector is parallel to the longitudinal axis of the vehicle (x-axis in the b-frame), the angle of attack and angle of side-slips can be neglected. This is the case of ground driven vehicles in most of the navigation situations (except when the vehicle is drifting or sliding). Then, cubic splines are used to interpolate the attitude values, and subsequently compute the rate of change of those variables:

$$\Psi_{bn_k}^n = \text{spline}(\Psi_{bn_k}^n), \quad \omega_{bn_k}^b = \frac{\partial \Psi_{bn_k}^n}{\partial k}. \quad (5.2)$$

Then, the attitude is used to compute the DCM (Eq. (3.6)) that allows the rotation of the velocity vector from the body to the navigation frame. Subsequently, the accelerations are directly derived from the velocity in the navigation frame (\mathbf{v}^n)

$$\mathbf{v}^n = \mathbf{C}_b^n \mathbf{v}^b, \quad \mathbf{a}_{eb_k}^n = \frac{\partial \mathbf{v}^n}{\partial k}. \quad (5.3)$$

Finally, the complete set of angular rates and accelerations can be used as input in the strap-down navigation algorithm, that yields the pose (position and attitude) of the vehicle at the desired rate.

This methodology is especially useful when the specific forces and the angular rates should be obtained in a consistent way. However, the input parameter selection of the desired trajectory is far from being intuitive and the positions are only available after integration.

Digitized Waypoints

This methodology consists of the digitization of a set of waypoints (coordinates) over a map. Then, the set of coordinates is referenced to a time scale, and subsequently interpolated using cubic polynomial in order to obtain a smooth trajectory

$$\mathbf{T}_k(\mathbf{s}_k) = a_k + b_k(\mathbf{s}_i - \mathbf{s}_k) + c_k(\mathbf{s}_i - \mathbf{s}_k)^2 + d_k(\mathbf{s}_i - \mathbf{s}_k)^3, \quad (5.4)$$

where \mathbf{s}_k is the vector of data points $\mathbf{S} = \{\mathbf{s}_1, \mathbf{s}_2, \dots, \mathbf{s}_n\}$ (with $\mathbf{s}_k \in \mathbb{R}$), \mathbf{s}_i is the vector of interpolation points (sampling rate), a_k, b_k, c_k and d_k are the coefficients of the interpolation and $\mathbf{T}_k(\mathbf{s}_k)$ is the vector/matrix of functional values to be interpolated. Later, the velocity and acceleration are directly obtained by computing the first and second derivatives of the position with respect to k , which are implicitly given by the spline interpolation algorithm.

Once the velocity is computed, the attitude (Euler angles) are obtained applying the non-holonomic

$$\psi = \arctan\left(\frac{v_E}{v_N}\right), \quad \theta = \arctan\left(\frac{v_D}{\sqrt{v_N^2 + v_E^2}}\right), \quad \phi \stackrel{!}{=} 0, \quad (5.5)$$

where ϕ , θ and ψ are the roll, pitch and yaw/heading angles respectively, and v_N , v_E and v_U are the North, East and Up components of the velocity vector in the local topocentric frame. Again, the angular rates are obtained by computing the first derivative of the attitude time series function.

A crucial step in the trajectory generation is referencing the trajectories to a known global frame so that the posterior computation of observational work with respect to the elements of the environment is realistic. Should the simulation scenario consider both absolute and relative measurements, it is possible to georeference the trajectory using external Geographic Information Systems (GIS) software packages.

Waypoints Obtained from Real Data

The execution of a measurement campaign within the scope of the i.c.sens project enables the computation of a set of coordinates (waypoints) applying existing positioning algorithms to the raw data collected. In this way, the obtained trajectory contains the same geometric characteristics as the one taken by a real vehicle. Finally, the obtained georeferenced waypoints are treated using the previously described methodology, so that all necessary parameters (position, velocity and attitude) are computed. A similar approach is used in BOFFI (2018), where the discrete points of an exemplary trajectory are replaced by cubic splines to obtain a smooth reference trajectory.

This methodology shows one explicit limitation. When the vehicle stops, the noisy waypoints lead to unrealistic direction changes within the velocity measurement simulation, and subsequently, unstable heading simulation. Hence, special attention needs to be put on this matter, in order to avoid unrealistic vehicle dynamics that might produce a negative effect on the overall estimation performance.

Further approaches such as *Frenet triad* (characterized by a power series expansion) (AVANZINI AND DE MATTEIS, 2001), or *differential geometry* (HAJIEGHRARY ET AL., 2018) can also be applied in path planning and collaborative investigations.

5.1.2 Environmental Model

The simulation of the scenario includes the selection of an environmental model. The geometrical representation of the environmental model affects the measurement generation step, since its features serve as a target for the laser scanner rays, GNSS LOS and stereo camera measurements (see Section 5.1.3). Subsequently, the measurements are included in the measurement fusion algorithm. This underlines the importance of the selection of an environmental model in accordance with the target to be achieved in the simulation. In this section, the different approaches to model the environment are introduced.

2D Digitized Map

Nowadays, online open-source data suppliers (e.g. OpenStreetMap geodata (OPENSTREETMAP CONTRIBUTORS, 2017)) provide users with virtually endless amounts of geographic information in shapefile format from the whole world. Their servers contain georeferenced information of roads, buildings, railway tracks, etc., suitable to be included in the simulation. With this in mind, a model of the environment is derived either by extracting geographic information from open-source platforms, or obtained by digitization using the geographic information as a reference.

To achieve this goal, external GIS software packages such as ARCMAP (2010) or QGIS (2019) can be used to determine the 2D shape of the static elements of the environment (e.g. buildings, poles, etc.). Then, the identified features are used as a target for the ray intersection (see Section 5.1.3) in the measurement generation step. In general, the typically used elements of the environment are items that are represented on a map as symbols (result from generalization), given their geometric distinction and long-term stability (SPANGENBERG ET AL., 2016). However, the identification of these features, and the posterior association to map elements are complex tasks to realize in real case scenarios. On the one hand, the objects might not be visible due to the intrinsic characteristics of the sensor used, or the velocity of the vehicle in kinematic scenarios. On the other hand, even if a certain object is reachable by the sensor, it is difficult to define a time-stable feature and its fixed position with an acceptable accuracy. As a result, other elements of the environment that are usually represented as plane features in maps (e.g. walls or facades) can be used as landmarks.

Also, the increasing necessity of digital cartographic information to support geographic information lead to the development of algorithms for automation of processes that guarantee the efficient digitization of large areas. However, the methodologies designed in order to extract features from the raw data (e.g. LiDAR point clouds, satellite/aerial/land-based images, etc.) result in generalization features derived from the scale of the input used, and also in additional errors in the geolocation of the features derived from the input resolution and/or the methodology deficiencies. As a result, the error in the determination of the map elements geo-location must be considered within the estimation as an additional source of uncertainty.

Consequently, this technique appraised to be suitable for simplified scenarios, in which errors caused by generalized shapes (with respect to the real features) or the digitization process are not

important. However, it provides a valid, easy and fast option for the analysis of small (low-scale) areas, and specific problems (e.g. a basic urban intersection).

3D City Model with Level of Detail-2

3D city model maps the urban districts of many cities in the world digitally and in three dimensions. In Hannover, it is offered in two Levels of Detail (LoD), and is based on a laser scanning survey of the year 2010. In total, approximately 131.000 buildings have been created in an automated process per LoD stage. The Level of Detail (LoD)-1 model is a *block model* in which the building heights are calculated from the average heights of eaves and ridge heights derived from the LoD-2 model. The height accuracy is about ± 5 m. In the LoD-2 model, standardized roof shapes are assigned to the buildings, which are aligned according to the actual ridge course. The height accuracy is approx. ± 1 m¹. The building shapes are created from cadastre map digitization (mostly from 1:1000 old paper maps) with an accuracy approximately at the decimeter level.

In this thesis, the 3D city model with LoD-2 is used, since it provides a realistic and accurate recreation of the urban area of Hannover. Still, it is computed as a generalization from a laser scanner point cloud, causing the omission of buildings with a small floor area (smaller than 15m), and areas in allotments. Also, complex shapes on building facades might be oversimplified. This is a crucial issue to be taken into account, particularly if the model is used to aid the positioning algorithms (i.e. ZHANG ET AL. (2018)). It is specially in this kind of analysis where the city model with LoD-2 represents a substantial improvement with respect to the LoD-1, since the building rooftop geometry is an essential piece of information for multipath analysis and correction (LE MARCHAND ET AL., 2009; BÉTAILLE ET AL., 2013; HSU ET AL., 2016).

Pre-aligned Laser Scanner Point Cloud

The measurement campaign carried out within the scope of the i.c.sens project (SCHÖN ET AL., 2018) allows also the consideration of a laser scanner point cloud as environmental model for the simulation tool.

In this experiment, three cars spent about 90 minutes actively recording data in the context of four different scenarios. During this time, two of these cars together recorded 4.3 billion and 1.8 billion points using a Velodyne and RIEGL VMX-250 Mobile Mapping System², respectively. Then, a high-accuracy version of the point cloud was computed by performing the geometrical adjustment introduced in BRENNER (2016). This paper shows that the presented approach can be mapped to a key/value MapReduce implementation, where every node operates independently on small chunks of data. This results in a map where the points have a precision of a few millimeters and where the RIEGL system solution is corrected from drift errors in its GNSS/IMU internal

¹3D City Model Product information: https://www.hannover.de/content/download/641518/15209724/file/Produktblatt_3DStadtmodell.pdf

²RIEGL VMX-250: http://www.riegl.com/uploads/tx_pxpriegldownloads/10_DataSheet_VMX-250_20-09-2012.pdf

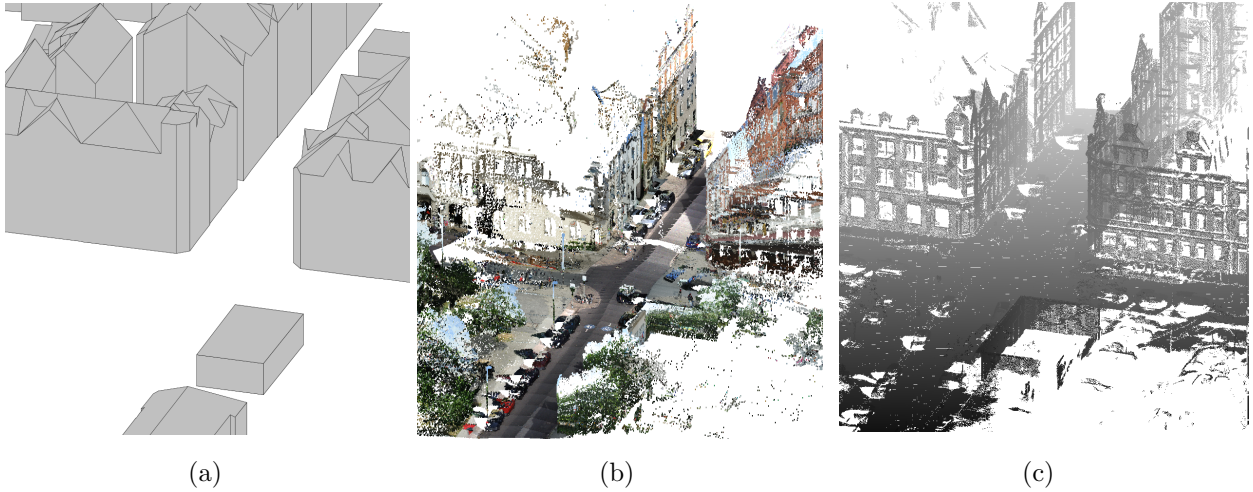


Figure 5.2: Comparison of models of the environment in an urban area (in Hannover). Figure 5.2a shows a screenshot of the 3D city model with LoD-2. Figure 5.2b shows the output from the RIEGL mobile mapping system operated at the IKG, where each point is back-projected to the images in order to obtain the RGB value for the point color (not used as model of the environment). Figure 5.2c shows the so-called *latent map* or aligned point cloud used as model of the environment.

solution. Simultaneously, the neighborhood relation between points on the small portions of data enables the possibility to identify surfaces. Hence, a normal vector is associated to each point, obtaining the continuous representation of a sparse data set.

This environmental model consists of an upgrade with respect to the previously introduced ones in terms of realism. In comparison with the digitized map methodology, the data obtained with the RIEGL system is able to capture a more detailed environment in 3D, in contrast to the 2D generalized information gathered by digitization.

In comparison with the 3D city model, the usage of pre-aligned laser scanner point cloud entails a series of strengths, but also a few weaknesses. The strengths of using a pre-aligned laser scanner point cloud with respect to the 3D city model are the following:

- It contains additional dynamic and fixed elements of the scene (e.g. cars, trees, traffic signs, etc.). Although they might add complexity to the identification of fixed elements, it brings the simulated environment one step closer to the representation of a real scene.
- It contains the result of measurement artifacts such as reflections or occlusions, in contrast to the 3D city model with LoD-2, where the building facades are continuous and free from interruptions caused by windows or urban furniture.
- It contains information about the urban vegetation, which is convenient to extend the analysis of the GNSS signal.
- It contains information on the ground plane. This is a relevant piece of information in order to aid the vehicle position in the up coordinate.

Even though the pre-aligned laser scanner point cloud is the most realistic model, its usage infers some inconveniences:

- The building rooftops are not represented in the model due to the constrained field of view of the laser scanner. This is an inconvenience especially if the aim of the study is to analyze the GNSS signal loss (or multipath), or if UAVs trajectories (instead of ground-driven vehicle trajectories) are simulated.
- The environmental model contains a huge amount of points, that increases both the complexity and run-time of the measurement generation and measurement fusion algorithms.

In summary, the selection of a model of the environment depends on the target of the study. In general, the employment of a pre-aligned point cloud leads to an increase in the amount of information used and subsequently, an increase in computation time. This makes it suitable in order to perform highly detailed but rather small simulations (e.g. urban intersections or narrow urban canyons). In this way, although an intersection would have a high level of detail, the simulation would still run in an acceptable amount of time. On the contrary, in collaborative simulations with numerous vehicles navigating in a large area, the computation with the generalized 3D city model might be the most efficient option. If it is required, outliers and occlusions can be artificially created during the measurement generation step (see Section 5.1.3).

5.1.3 Measurement Generation

In the discussed simulation framework, position and velocity measurements (assumed to be derived from GNSS observations), IMU specific forces and angular rates, laser scanner, stereo camera, and V2V measurements are generated. The GNSS and IMU measurements are used to determine the vehicle dynamics at every epoch k , whereas the laser scanner and stereo camera measurements represent the V2I measurements of the network. In Figure 5.3, two simulation examples with different sensor architectures and geometries are shown. Here, a vehicle is assumed to be navigating in an urban area (in Hannover) with four GPS satellites in LOS and one GPS satellite in NLOS situation (S-4). Also, the vehicle orientation is represented by the axis triad used to define the body frame (x- y- and z-axis represented in red, green and blue, respectively). The laser scanner measurement simulation is depicted using two different architectures. In architecture 1, only one profile laser scanner (2D) is considered, whereas in architecture 2, two tilted laser scanners are simulated imitating the RIEGL laser scanner ray bundles. Finally, the conic projections used to describe the geometry of the camera ray bundles and subsequently compute the stereo camera measurements are shown with the red (left camera) and green (right camera) triangles. Please note in Fig. 5.3 that the blue circles that describe the laser scanner measurements, as well as the red and green triangles that describe the camera measurements, depict only the geometrical characteristics of the sensor activity. The actual measurements (represented as magenta 'x' symbols) are computed subsequently from the intersection of the described rays with the building facades. In this section, the details of the sensor measurement simulations are introduced and discussed.

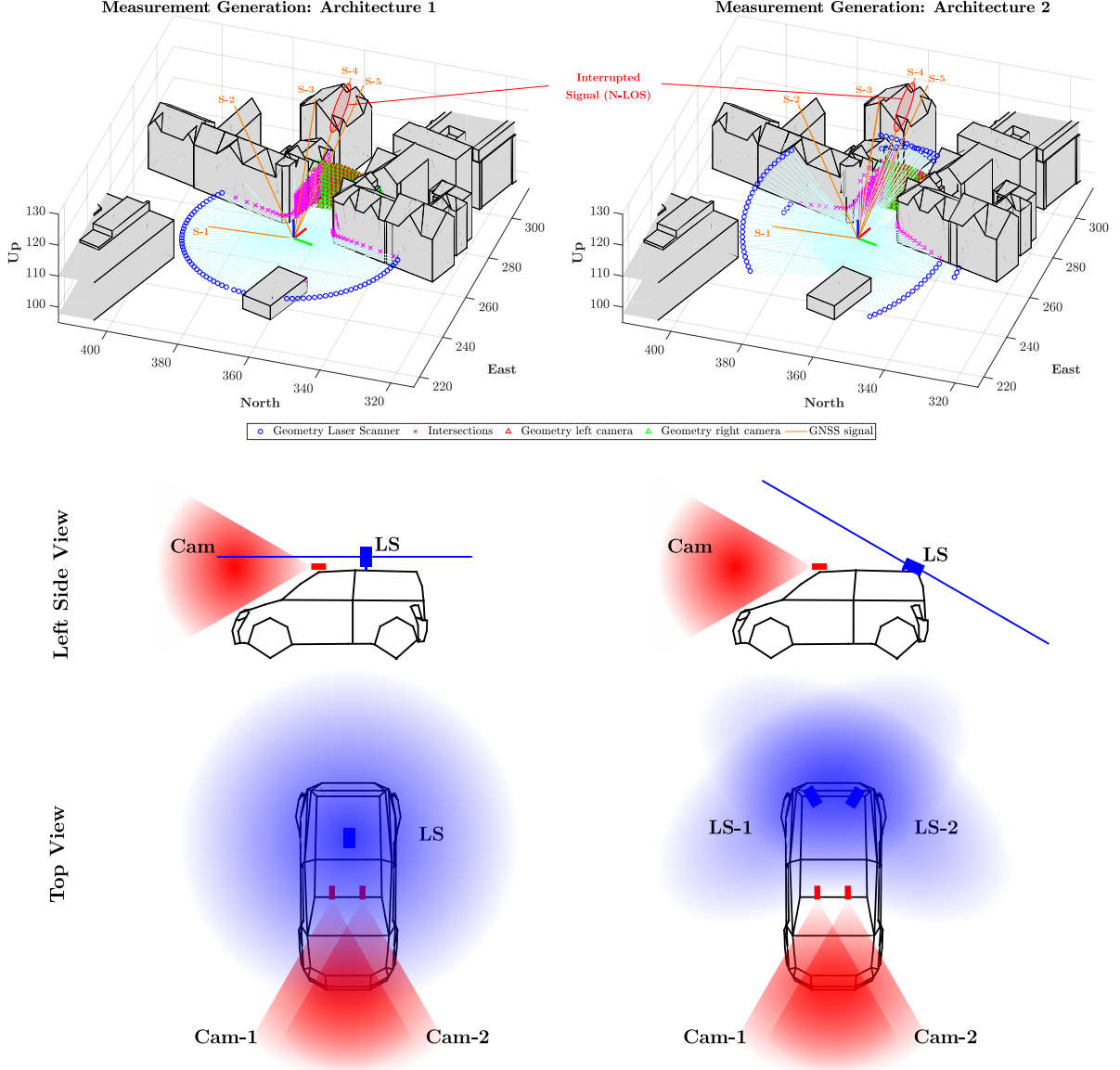


Figure 5.3: Measurement generation examples with two different sensor architectures, where the 3D city model with LoD-2 is the selected model of the environment. *Architecture-1* (left column) contains a GNSS receiver and an IMU placed in the origin of the body frame (not displayed in the diagrams to facilitate the view). A profile laser scanner (LS) and a pair of stereo cameras are mounted on the vehicle to complete the sensor architecture (the top and left side view diagrams do not keep proportions of the used leverarms). In *Architecture-2*, the same sensors as in *Architecture-1* are considered, although here, two laser scanner sensors are mounted in an inclined way, imitating the RIEGL laser scanner ray bundles assembly.

GNSS

Any vehicle equipped with at least one GNSS receiver can determine its position and velocity within the Earth Centered Earth Fixed frame by measuring the pseudo-range (see Eq. (3.1)) and the instant Doppler shift (Eq. (3.3)) at any epoch k . If more than two antennas are used, the obtained carrier phase measurements and a highly optimized ambiguity resolution method enable

the computation of attitude information (PARK AND TEUNISSEN, 2003). In the simulation tool, it is also possible to use the sets of coordinates obtained with the selected methodology for trajectory generation described in section 5.1.1, as position and velocity solutions.

In order to achieve collaborative positioning, measurements that link the different vehicles are considered. In this thesis, the assumption that GNSS receivers are mounted in each vehicle enables the possibility to compute the GNSS baseline (cf. Eq. (3.4)) between the ego and the aiding vehicles. These observations are considered in our centralized algorithm as the V2V observations.

Moreover, GNSS measurements are generally affected by different sources of error. Hence, it is essential to apply a convenient error model in order to approximate the measurement simulation to realistic situations.

The most elementary error model applicable to the mentioned GNSS pseudoranges and instance Doppler shift it is to apply Gaussian random noise (*white* noise) with a standard deviation selected in accordance to the precision of the positioning technique to be used (Section 3.1.2). However, the consideration of Gaussian noise yields an equivalent amount of error, regardless of the area where the receiver is located.

This is not the most realistic option, since it is well known that the GNSS positioning solution is constrained by the signal propagation conditions, affected by multipath, diffraction and obstructions (caused by the elements of the environment and/or due to the heterogeneous conditions of the media where the signal travels) (WIESER, 2007). Obstructions not only induce a signal deviation and a delay from the theoretical path but also decrease the amount of satellites in a LOS situation. Few satellites in LOS lead to a position estimation with low redundancy diminishing the chances to detect outliers or preventing it altogether. Hence, given that the accuracy, precision and reliability of the GNSS solution decrease in challenging areas, a suitable error model based on the satellite geometry is employed.

Taking advantage of the available environmental models, it is possible to check if the LOS from the simulated vehicle to each satellite is interrupted by any element of the environmental model (see the NLOS S-4 in Figure 5.3). Later, the quality of the satellite geometry is evaluated by computing the Dilution of Precision (DOP) factors. The DOP values are obtained from the cofactor matrix of the estimated parameters $\mathbf{Q}_{\hat{x}\hat{x}}$ shown in equation (2.15), where the weight matrix \mathbf{W}_l is replaced by the identity matrix (\mathbf{I}). Denoting the elements of the $\mathbf{Q}_{\hat{x}\hat{x}}$ matrix, obtained as a result of estimating the 3D position and synchronization error between the satellite and the receiver clocks $c\delta t_i^j$ as in Eq. (5.6)

$$\mathbf{Q}_{\hat{x}\hat{x}} = \begin{bmatrix} q_{xx} & q_{xy} & q_{xz} & q_{xt} \\ q_{xy} & q_{yy} & q_{yz} & q_{yt} \\ q_{xz} & q_{yz} & q_{zz} & q_{zt} \\ q_{xt} & q_{yt} & q_{zt} & q_{tt} \end{bmatrix}, \quad (5.6)$$

the different DOP values are computed as:

$$\text{Geometric DOP (GDOP)} = \sqrt{q_{xx} + q_{yy} + q_{zz} + q_{tt}} \quad (5.7)$$

$$\text{Position DOP (PDOP)} = \sqrt{q_{xx} + q_{yy} + q_{zz}} \quad (5.8)$$

$$\text{Horizontal DOP (HDOP)} = \sqrt{q_{xx} + q_{yy}} \quad (5.9)$$

$$\text{Vertical DOP (VDOP)} = \sqrt{q_{zz}} \quad (5.10)$$

$$\text{Time DOP (TDOP)} = \sqrt{q_{tt}}. \quad (5.11)$$

Hence, the quality of the GNSS positioning is considered in Eq. (5.12) by computing the amount of error as a function of the horizontal (for North- and East-coordinates) and vertical (for the up-coordinate) epoch-wise DOP values,

$$\hat{\mathbf{x}}^t = \mathbf{x}_0^t + \Delta \mathbf{x}^t \quad \Delta \mathbf{x}^t \sim \mathcal{N}(\mathbf{0}, sc \cdot (\mathbf{I}_{3 \times 3} \otimes \boldsymbol{\sigma}_{\text{DOP}})) \quad (5.12)$$

where $\hat{\mathbf{x}}^t = [\Delta N \ \Delta E \ \Delta U]$ is the estimated positioning vector that contains the difference of coordinates of the corresponding vehicle in the local topocentric frame, \mathbf{x}_0^t is the nominal positioning vector in the local topocentric frame, $\Delta \mathbf{x}^t$ is the amount of error applied to the measurement, sc is the scale factor applied to the DOP value vector to generate the positioning error, and $\boldsymbol{\sigma}_{\text{DOP}} = [\text{HDOP}^2 \ \text{HDOP}^2 \ \text{VDOP}^2]^T$ is the column vector that contains the epoch-wise DOP values. In this way, an error model, where the distributed errors are larger in GNSS challenging areas, is achieved and areas with fewer than four LOS satellites represent GNSS denied areas, with complete loss of GPS signal.

The computation of the DOP values in multi-GNSS requires to take into account the different coordinate and time systems used in each system. The differences between the International Terrestrial Reference Framework (ITRF) and the WGS-84 (used in GPS), CTRF (Galileo) and CGCS 2000 (BeiDou) are only a few centimeters, and therefore are neglected for navigation purposes. However, the individual clock error δk (unknown) must be considered for each constellation (TENG AND WANG, 2017), thus increasing the size of the matrix displayed as an example in Eq. (5.6).

IMU

The IMU measurements are considered in two different ways:

1. The attitude (computed from Eq. (5.5)) and acceleration values are introduced in the filter as measurements, following a *loosely coupled* approach, where the strap-down navigation algorithm (described in Section 3.2.2) is not considered.
2. The strap-down navigation algorithm is used to correct the specific forces \mathbf{f}_{ib}^b and the angular rates $\boldsymbol{\omega}_{ib}^b$. Later, the corrected accelerations \mathbf{a}_{eb}^n and angular rates $\boldsymbol{\omega}_{nb}^b$ are used as input control in the prediction step of the C-EKF.

In contrast to the GNSS-based solution, the accuracy of the IMU standalone solutions decrease with time due to drifts caused by sensor biases. Moreover, the IMU measurements are also affected

by sensor errors, such as random noise or misalignments (only in the case of gyroscopes). Thus, random walk ($\Delta \mathbf{l}_{\text{IMU}}$), scale factor (sf) and biases (b) are added to the \mathbf{f}_{ib}^b and $\boldsymbol{\omega}_{ib}^b$ observations (Eq. 5.13 - 5.14).

$$\hat{\boldsymbol{\omega}}_{ib}^b = sf \cdot \left(\boldsymbol{\omega}_{ib,0}^b \right) + b + \Delta \boldsymbol{\omega}_{ib}^b \quad \Delta \boldsymbol{\omega}_{ib}^b \sim \mathcal{N} \left(\mathbf{0}, \boldsymbol{\sigma}_{\omega}^2 \cdot \mathbf{I}_{3 \times 3} \right) \quad (5.13)$$

$$\hat{\mathbf{f}}_{ib}^b = sf \cdot \left(\mathbf{f}_{ib,0}^b \right) + b + \Delta \mathbf{f}_{ib}^b \quad \Delta \mathbf{f}_{ib}^b \sim \mathcal{N} \left(\mathbf{0}, \boldsymbol{\sigma}_{\mathbf{f}}^2 \cdot \mathbf{I}_{3 \times 3} \right) \quad (5.14)$$

The most realistic option is to use the strap-down navigation algorithm (option 2) where all the error sources are considered, and the corresponding values are selected according to some existing IMU specifications. However, the amount of information used in the estimation increases significantly with respect to option 1, causing also an increase in computation times and more complex evaluation of results. Accordingly, option 1 is still convenient for scenarios where the impact of the IMU measurements needs to be mitigated/neglected, in order to emphasize the behavior of other system components.

It is also worth mentioning that the position of the device with respect to the turning point of the vehicle has a strong influence on the IMU measurements. However, a vehicle model is not yet considered in the simulation, leading to the assumption that the device is mounted directly above the turning point. As a result, the effects caused by these displacements are neglected.

Laser Scanner

The computed nominal pose of every vehicle is used to implement the origin of the laser scanner measurements, using the selected environmental model as a target for the generated laser scanner rays (e.g. the cyan rays in Figure 5.3). Also, a certain threshold (normally 40 m) is used in order to eliminate measurements that exceed a distance that could be considered as impossible to achieve with a real laser scanner pulse. In this way, unrealistic measurements are avoided within the estimation. Then, the simulated rays are intersected with the planes that form the 3D city model or the 3D point cloud to obtain the error-free laser scanner observations.

Given the previously described geometry, the laser scanner observation in the sensor frame is divided into three components: horizontal angle (ρ), vertical angle (ϵ) and Euclidean distance (r) between the intersected point and the laser scanner position. With this in mind, a bundle of rays is generated imitating any desired commercial device (two examples are shown in Figure 5.3). In architecture 1, a horizontally mounted line laser scanner is used while in architecture 2 two tilted laser scanner devices are mounted, pointing to the ground plane. However, in the experiments carried out within the scope of this thesis, a 3D laser scanner is used, with a vertical aperture of 8° in each direction (up and down). Here, each degree contains one horizontal bundle of rays, describing a laser scanner with a total of 16 lines. Also, all the experiments are executed under the assumption that the laser scanner ray directions are perfectly calibrated. In other words, the values of the horizontal and vertical angles are unaffected by errors. As a result, the Euclidean distance (range measurement) is the only component that is introduced in the filter as laser scanner observation.

Two error models are defined to generate range measurement errors: (i) white noise, and/or (ii) as a function of the distance between intersected point and origin of the sensor frame. If the observations are assumed to be affected by random Gaussian noise, inliers are generated with the desired standard deviation. However, laser scanner measurement errors are normally associated to the distance from the sensor to the surface where the pulse is reflected. Therefore, the error model dependent on the range measurement can also be considered as a more realistic option:

$$\hat{\mathbf{r}} = \mathbf{r}_0 + \Delta\mathbf{r} \quad \text{i) } \Delta\mathbf{r} \sim \mathcal{N}(\mathbf{0}, \sigma_r^2) \quad \text{ii) } \Delta\mathbf{r} = f(\mathbf{r}, \sigma_r^2). \quad (5.15)$$

Stereo Cameras

In photogrammetry, camera measurements (images) are used to capture and/or learn information about the environment. Given the complexity of the available state-of-the-art algorithms developed for the simulation of images (DUDA ET AL., 2013; ZHU ET AL., 2019), this task is ignored in this thesis. However, *stereoscopy* enables the creation of the illusion of 3D depth from given 2D images. Thus, it is possible to reconstruct 3D elements of a certain scene by capturing them simultaneously with two different cameras (stereo pair) or by capturing them at different epochs using the same camera (*bundle adjustment*).

In order to simulate the camera measurements, two bundles of rays are simulated imitating the geometry of a pair of stereo cameras, following the approach explained in the laser scanner section (cf. 5.3). The dimensions of the bundles are implemented as a function of the distance between the cameras (b_c), focal length (f), and horizontal and vertical aperture angles. A numerical example is shown in Figure 5.4. Then, the generated rays are intersected with the selected environmental model (magenta points in Figure 5.3) to obtain the desired '3D reconstructed' environment. In the filter, the camera measurements are assumed to be the intersected point coordinates in the camera frame.

For this sensor, the error models implemented are the same as in the case of the laser scanner explained in the previous section. As a first option, *white noise* can be applied to the observations. However, in real cases, the amount of error depends on the distance from the camera to the captured object (or the *disparity value* d_j in case of stereo cameras), the cameras focal length and the distance between the cameras. For this reason, an error model based on the distance of the object point to the cameras projection center is implemented. The challenge here relies on the computation of image coordinates necessary to evaluate the errors. In the z_j^{cam} formula of the equation system (5.16), the focal length f , the (distance) baseline between cameras b_c , and the object coordinates in the sensor frame ($\mathbf{p}_{\text{cam},j} = [x_j^{\text{cam}} \ y_j^{\text{cam}} \ z_j^{\text{cam}}]$) obtained from the j^{th} ray to plane intersection are known. This way, the disparity d_j is computed. Subsequently, the image coordinates (x'_j, y'_j, x''_j, y''_j) of the point can be computed as (FÖRSTNER AND WROBEL, 2016):

$$x_j^{\text{cam}} = \frac{x'_j}{f} \cdot z_j^{\text{cam}} \quad y_j^{\text{cam}} = \frac{y'_j + y''_j}{2} \cdot \frac{z_j^{\text{cam}}}{f} \quad z_j^{\text{cam}} = -\frac{f}{d_j} \cdot b_c. \quad (5.16)$$

Subsequently, the standard deviation of the error in each direction can be computed applying:

$$\sigma_x = \frac{1}{\sqrt{2}} \frac{z_j^{\text{cam}}}{f} \cdot \sigma_{x'_j} \quad \sigma_y = \frac{1}{\sqrt{2}} \frac{z_j^{\text{cam}}}{f} \cdot \sigma_{x'_j} \quad \sigma_z = \frac{f \cdot b_c}{d_j^2} \cdot \sigma_{d_j}, \quad (5.17)$$

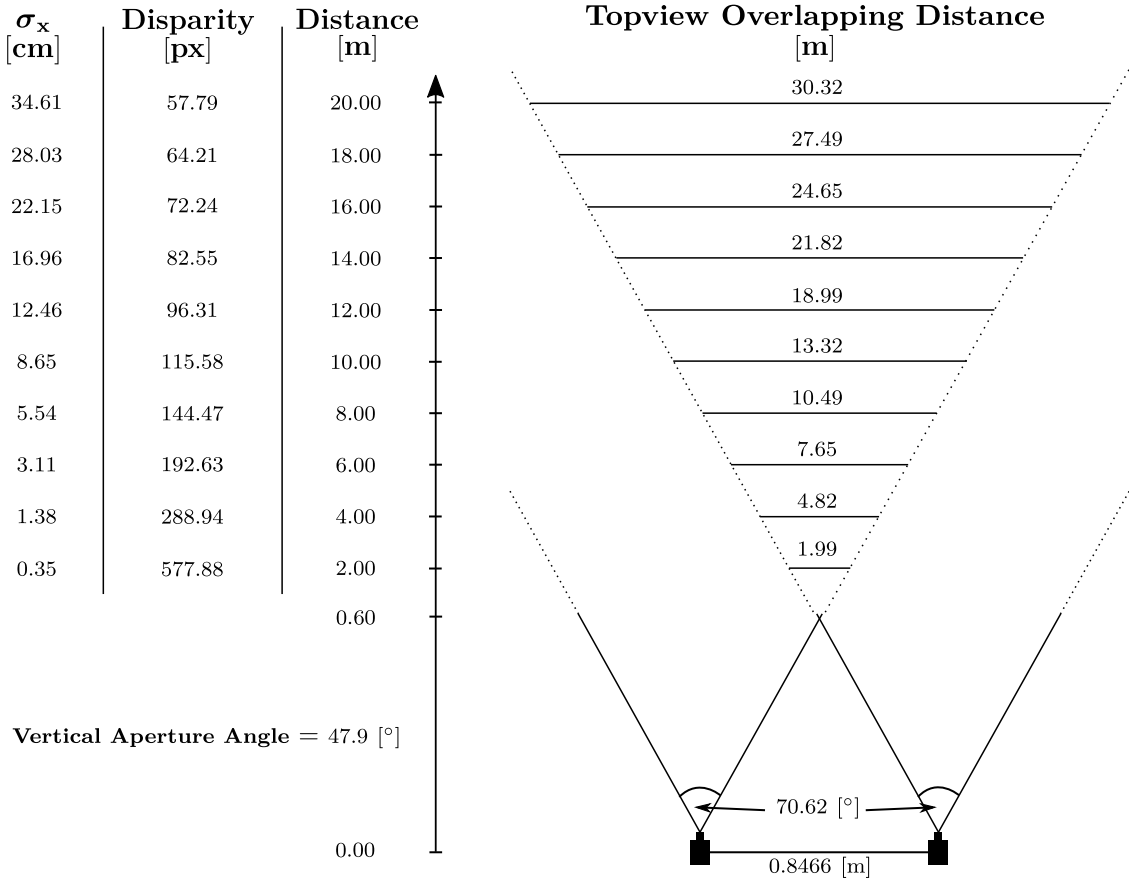


Figure 5.4: Numerical example of a stereo rig computation. It also contains the computation of d_j and the standard deviation in the forward direction of the camera frame. Please note that this figure is a sketchy representation of a stereo camera rig, that should help the visual interpretation of the numerical example computed. As a result, the represented angles and distances do match the given values.

where $\sigma_{x'_j}$ is the standard deviation assumed for the determination of the x component of the image point of interest, and σ_{d_j} is the standard deviation of the disparity. In our experiments, the value selected for the latter is $\sigma_{d_j} = 1$ pixel. In real cases, an additional error source coming from the estimation of b_c should be considered, since it leads to scaling errors in the 3D reconstruction. However, b_c is assumed to be perfectly obtained from calibration in the simulation, and hence neglected. Although the definition of the camera frame in the photogrammetry field considers the z -axis pointing forward, y -axis pointing upward, and the x -axis completes the definition, in the matter at hand, it is defined as a left-handed frame with the x -axis pointing forward (as in the case of the laser scanner).

Finally, it is worth saying that laser scanner and the cameras usually show outliers caused by reflections or occlusions. Using the 3D city model, the question of a specific outlier distribution is difficult to answer, so in the current implementation no outliers are considered. In order to diminish the overoptimistic effects caused by this assumption, the number of intersections considered for the

state estimation is significantly lower as in a real data point cloud (fewer than 1000 points per epoch in our approach against way more than 100,000 points per epoch in a real point cloud).

5.1.4 Collaborative-Extended Kalman Filter

The algorithm used to fuse the measurements described in the previous sections is the Collaborative-Extended Kalman Filter (C-EKF), where state parameters from different vehicles are simultaneously estimated. The filter operates as a common EKF, in which the dynamic system equations that describe the state mean and covariance propagation of the states are implemented in the *prediction step*. After the measurements are received, both the state mean and covariance are updated in the *update/correction step*. In this section, the filter components are introduced and discussed in detail.

C-EKF Overview

In this section, the overall assumptions and considerations taken into account in the filter design and implementation steps are outlined. On the one hand, the C-EKF operates as a regular EKF (cf. Section 3.3.4), in which state parameters from all the considered vehicles are estimated simultaneously in a centralized algorithm. So the following non-linear system is assumed:

$$\dot{\mathbf{x}} = \mathbf{f}(\mathbf{x}_{\mathbf{c}}, \mathbf{u}_{\mathbf{c}}, \mathbf{w}_{\mathbf{c}}, k) \quad \mathbf{w} \sim N(\mathbf{0}, \mathbf{Qd}_{\mathbf{c}}) \quad (5.18)$$

$$\mathbf{l} = \mathbf{h}(\mathbf{x}_{\mathbf{c}}, \mathbf{v}_{\mathbf{c}}, k) \quad \mathbf{v} \sim N(\mathbf{0}, \mathbf{R}_{\mathbf{c}}), \quad (5.19)$$

where the system $\mathbf{f}(\cdot)$ and measurement $\mathbf{h}(\cdot)$ models are non-linear functions, $\mathbf{x}_{\mathbf{c}}$ and $\mathbf{u}_{\mathbf{c}}$ are the state and input vectors for the collaborative approaches, and \mathbf{w} and \mathbf{v} are the process and measurement noise, respectively (same as shown in Eq. (3.22) and (5.19)).

In most of the experiments shown in this document, the C-EKF algorithm is executed in order to estimate the 3D pose (position and orientation) and 3D velocity of all vehicles contained in the scenario. Thus, in an estimation with n vehicles, the state vector of the estimation is written as:

$$\mathbf{x}_{\mathbf{c}} = \begin{bmatrix} \Delta N_1 \Delta E_1 \Delta U_1 \mid v_{N_1} v_{E_1} v_{U_1} \mid \phi_1 \theta_1 \psi_1 \parallel \Delta N_2 \Delta E_2 \Delta U_2 \mid v_{N_2} v_{E_2} v_{U_2} \mid \phi_2 \theta_2 \psi_2 \parallel \cdots \\ \cdots \parallel \Delta N_n \Delta E_n \Delta U_n \mid v_{N_n} v_{E_n} v_{U_n} \mid \phi_n \theta_n \psi_n \end{bmatrix}^T. \quad (5.20)$$

where $[\Delta N_i \Delta E_i \Delta U_i]$ is the vector that contains the difference of coordinates between the i^{th} vehicle position and the origin of the local topocentric frame (North, East and Up coordinates), $[v_{N_i} v_{E_i} v_{U_i}]$ are the North, East and Up components of the velocity in the local topocentric frame, and $[\phi_i \theta_i \psi_i]$ are the roll, pitch and yaw (Euler) angles that describe the orientation of the vehicle.

With this approach, information about the inter-vehicle parameter correlations and dependencies caused by the networked measurements can be directly obtained by analyzing the filter statistics. However, estimations with a large number of vehicles results in complex computations and long execution times. This flaw can be solved by using cascaded KF implementations, although versatility in the result evaluation would be lost. Thus, a tradeoff between the application of a computationally efficient and an analysis-oriented filter must be found. In other words, the implemented

filter must fulfill the ultimate analytical purpose of the research, being as fast as possible. In this project, special priority is given to the suitability for analysis in detriment of the computational efficiency, given the availability of computer clusters (both in the Leibniz Universität and in the i.c.sens project) that mitigate the disadvantages caused by heavy estimations.

On the other hand, both the 3D city model with LoD-2 and the continuous representation of the pre-aligned laser scanner point cloud model are built up using planes. This leads to the assumption that our exteroceptive sensors would be able to detect and reconstruct the elements of the environment which can be represented as planar elements, to be used as landmarks. Therefore, the filter is implemented as a plane-based algorithm. In the following sections, the details about the prediction and correction steps, as well as the observation vector used for the plane-based C-EKF are discussed.

Prediction Step

In the prediction step, the estimated mean and covariance are propagated through time applying:

$$\hat{\mathbf{x}}_{\mathbf{c},k}^- = \Phi_{\mathbf{c},k-1} \hat{\mathbf{x}}_{\mathbf{c},k-1}^+ + \Gamma_{\mathbf{c},k-1} \mathbf{u}_{\mathbf{c},k-1}, \quad (5.21)$$

$$\mathbf{P}_{\mathbf{c},k}^- = \Phi_{\mathbf{c},k-1} \mathbf{P}_{\mathbf{c},k-1}^+ \Phi_{\mathbf{c},k-1}^T + \mathbf{Q} \mathbf{d}_{\mathbf{c},k}. \quad (5.22)$$

Here, the notation used is the same as in Eq. (3.17) and (3.18), though the suffix \mathbf{c} is added to indicate that the variables are adapted to the collaborative approach.

First, the *prediction step* defines the knowledge of the vehicle dynamics. SCHUBERT ET AL. (2008) survey numerous motion models and compare their performance. In our experiments, we consider for simplicity a linear 3D version of the Decoupled Constant Turn Rate and Constant Velocity (DTRCV) as the motion model of the vehicles. Hence, the state transition matrix for a single vehicle Φ_{k-1} model can be written as

$$\Phi_{k-1} = \begin{bmatrix} \mathbf{I}_{3 \times 3} & \mathbf{I}_{3 \times 3} \Delta t & \mathbf{0}_{3 \times 3} \\ \mathbf{0}_{3 \times 3} & \mathbf{I}_{3 \times 3} & \mathbf{0}_{3 \times 3} \\ \mathbf{0}_{3 \times 3} & \mathbf{0}_{3 \times 3} & \mathbf{I}_{3 \times 3} \end{bmatrix} \quad (5.23)$$

where $\mathbf{I}_{3 \times 3}$ is the 3×3 identity matrix in 3D estimations, and Δt is the time difference between two consecutive EKF estimations, the state transition matrix for the collaborative approach ($\Phi_{\mathbf{c},k-1}$) is computed by

$$\Phi_{\mathbf{c},k-1} = \mathbf{I}_n \otimes \Phi_{k-1}, \quad (5.24)$$

assuming identical number of state parameters per vehicle.

Second, if the strap-down navigation algorithm described in Figure 3.4 is considered, the corrected specific forces \mathbf{a}_{eb}^n and angular rates $\boldsymbol{\omega}_{nb}^b$ are introduced as control input $\mathbf{u}_{\mathbf{c},k-1} = [\mathbf{a}_{eb}^n \ \boldsymbol{\omega}_{nb}^b]^T$. Again, if the input control matrix for one single vehicle Γ_{k-1} is written as

$$\Gamma_{k-1} = \begin{bmatrix} \frac{1}{2} \mathbf{I}_{3 \times 3} \Delta t^2 & \mathbf{0}_{3 \times 3} \\ \mathbf{I}_{3 \times 3} \Delta t & \mathbf{0}_{3 \times 3} \\ \mathbf{0}_{3 \times 3} & \mathbf{I}_{3 \times 3} \Delta t \end{bmatrix} \quad (5.25)$$

the input matrix for the C-EKF is obtained by applying

$$\mathbf{\Gamma}_{\mathbf{c},k-1} = \mathbf{I}_n \otimes \mathbf{\Gamma}_{k-1}. \quad (5.26)$$

Third and last, it is crucial to define the process noise, that represents the implicit noise of the motion model. The ratio between the process noise and measurement noise reveals whether the system is dominated by the motion model or by the measurements.

As an example, in a single vehicle approach in which the velocity and the attitude are considered random walk variables, the computation of \mathbf{Qd}_k with Eq. (3.15) for position, velocity and attitude results in

$$\mathbf{Qd}_k = \begin{bmatrix} \frac{\Delta t^3}{3} \mathbf{q}_{\text{vel } 3 \times 3} & \frac{\Delta t^2}{2} \mathbf{q}_{\text{vel } 3 \times 3} & \mathbf{0}_{3 \times 3} \\ \frac{\Delta t^2}{2} \mathbf{q}_{\text{vel } 3 \times 3} & \Delta t \mathbf{q}_{\text{vel } 3 \times 3} & \mathbf{0}_{3 \times 3} \\ \mathbf{0}_{3 \times 3} & \mathbf{0}_{3 \times 3} & \Delta t \mathbf{q}_{\text{att } 3 \times 3} \end{bmatrix}. \quad (5.27)$$

Finally, the $\mathbf{Qd}_{\mathbf{c},k}$ for the collaborative approach can be obtained by applying the same approach as with the state transition and input matrices described in Eq. (5.24) and (5.26).

Observation Vector

The observations generated within the simulation framework are introduced in Section 5.1.3, together with their respective error models. There, four different sensor measurements (GNSS, IMU, laser scanner and camera) are generated. Therefore, the observation vector for one single vehicle can be written as

$$\mathbf{l}_k = [\mathbf{l}_k^{\text{GNSS}} \ \mathbf{l}_k^{\text{IMU}} \ \mathbf{l}_k^{\text{LS}} \ \mathbf{l}_k^{\text{CAM}}]^T. \quad (5.28)$$

Later, the observation vector for a computation that involves n vehicles can be obtained by vertically concatenating the observation vectors for each vehicle with the V2V observations, as in the following equation:

$$\mathbf{l}_{\mathbf{c},k} = \begin{bmatrix} \mathbf{l}_{1_k} \\ \mathbf{l}_{2_k} \\ \vdots \\ \mathbf{l}_{n_k} \\ \dots \\ \mathbf{l}_{\text{V2V},k} \end{bmatrix}. \quad (5.29)$$

It is mentioned in the algorithm overview that the filter is implemented as a plane-based approach. This means that the planar elements of the environment (walls, facades, etc.) are the elements used as landmarks in the described C-EKF. Subsequently, the plane equations obtained from the geometrical elements used to build the model of the environment are introduced as prior knowledge in order to take complex object recognition in the building facades into account. Then, this information is used to identify which rays intersect with which plane (association). The correct ray to plane association, together with the fact that the model of the environment is built with planar elements, enables to state that no matter the amount of error that affects the observation,

the m intersection points must be contained in its respective associated plane. Hence, they fulfill the condition equality (5.30) for laser scanner, and (5.31) for camera observations.

$$\mathbf{n} \cdot \left[\mathbf{p}_{veh}^t + \mathbf{C}_b^t \cdot \left(\underbrace{\mathbf{C}_{LS}^b}_{\text{calibration}} \cdot \underbrace{\mathbf{r}}_{\text{observation}} \cdot \underbrace{\mathbf{C}(\rho, \epsilon) + \mathbf{t}_{LS}^b}_{\text{calibration}} \right) \right] + d \stackrel{!}{=} 0 \quad (5.30)$$

$$\mathbf{n} \cdot \left[\mathbf{p}_{veh}^t + \mathbf{C}_b^t \cdot \left(\underbrace{\mathbf{C}_{cam}^b}_{\text{calibration}} \cdot \underbrace{\mathbf{p}_{cam}}_{\text{observation}} + \underbrace{\mathbf{t}_{cam}^b}_{\text{calibration}} \right) \right] + d \stackrel{!}{=} 0 \quad (5.31)$$

where \mathbf{n} is the plane normal vector ($\mathbf{n} = [a \ b \ c]$), \mathbf{p}_{veh}^t is the vehicle position in the t-frame, \mathbf{C}_b^t is the rotation matrix from the b-frame to the t-frame, \mathbf{C}_{LS}^b and \mathbf{C}_{cam}^b are the rotation matrix from the laser scanner and camera frames to the b-frame, \mathbf{t}_{LS}^b and \mathbf{t}_{cam}^b are the leverarm (s-frame to b-frame) translations obtained from the platform calibration, r is the Euclidean distance between the intersected point and the laser scanner in the s-frame, $\mathbf{C}(\rho, \epsilon)$ is the ray direction vector which contains the known horizontal and vertical angles (ρ and ϵ , respectively), \mathbf{p}_{cam} are the 3D coordinates of the camera observations in the camera frame, and d completes the set of coefficients for the Hesse normal form.

In the EKF update step, the measurement model corresponds to the typical state estimation in the GMM (cf. Eq. (5.19)). However, it is visible that Eq. (5.30) and (5.31) are hard constrained implicit measurements that fulfill the functional model described by Eq. (2.11) (GHM). Therefore, the common EKF update step formulation has to be adapted to the consideration of observations that satisfy a non linear implicit constraint.

Correction Step

In the C-EKF correction step, observations of type GMM and GHM must be considered. PETERSEN AND KOCH (2010) show a proof of the equivalence between the KF correction step and a GHM. Also, DANG ET AL. (2009) propose to solve the problem at hand with a robust iterated EKF. In this document, the approach proposed by DANG ET AL. (2009) is upgraded to the consideration of a group of vehicles, and the iteration is neglected in order to leave the measurement impact unaltered and reduce the computation time. As a result, the system model introduced in Eq. (5.18) and (5.19) is completed with the implicit equations of type

$$\mathbf{g}(\mathbf{x}, \mathbf{l}) \stackrel{!}{=} 0. \quad (5.32)$$

In order to perform the C-EKF update, three different Jacobian matrices are computed:

$$\mathbf{H}_{ci,k} = \left. \frac{\partial \mathbf{h}}{\partial \mathbf{x}} \right|_{\hat{\mathbf{x}}_k^-}, \quad \mathbf{A}_k = \left. \frac{\partial \mathbf{g}}{\partial \mathbf{x}} \right|_{\hat{\mathbf{x}}_k^-}, \quad \mathbf{B}_k = \left. \frac{\partial \mathbf{g}}{\partial \mathbf{l}} \right|_{\mathbf{l}_k, \hat{\mathbf{x}}_k^-}. \quad (5.33)$$

As an example, the internal structure of the $\mathbf{H}_{\text{ci},k}$ matrix, in an theoretical 3D estimation (using the state vector in Eq. (5.20)) where direct ($l = x$) GNSS position and velocity, attitude, and V2V GNSS baseline measurements are carried out with sensors mounted on three vehicles would look as

$$\mathbf{H}_{\text{ci},k} = \left[\begin{array}{ccc|ccc|ccc} \mathbf{I}_p & \mathbf{0} & \mathbf{0} & & & & & & \\ \mathbf{0} & \mathbf{I}_v & \mathbf{0} & & \mathbf{0}_{9 \times 9} & & & \mathbf{0}_{9 \times 9} & \\ \mathbf{0} & \mathbf{0} & \mathbf{I}_{\text{att}} & & & & & & \\ \hline & & & \mathbf{I}_p & \mathbf{0} & \mathbf{0} & & & \\ & & & \mathbf{0} & \mathbf{I}_v & \mathbf{0} & & \mathbf{0}_{9 \times 9} & \\ & & & \mathbf{0} & \mathbf{0} & \mathbf{I}_{\text{att}} & & & \\ \hline & & & & & & \mathbf{I}_p & \mathbf{0} & \mathbf{0} \\ & & & & & & \mathbf{0} & \mathbf{I}_v & \mathbf{0} \\ & & & & & & \mathbf{0} & \mathbf{0} & \mathbf{I}_{\text{att}} \\ \hline -\mathbf{I}_{\text{Bas}} & \mathbf{0} & \mathbf{0} & \mathbf{I}_{\text{Bas}} & \mathbf{0} & \mathbf{0} & \mathbf{0} & \mathbf{0} & \mathbf{0} \\ -\mathbf{I}_{\text{Bas}} & \mathbf{0} & \mathbf{0} & \mathbf{0} & \mathbf{0} & \mathbf{0} & \mathbf{I}_{\text{Bas}} & \mathbf{0} & \mathbf{0} \\ \mathbf{0} & \mathbf{0} & \mathbf{0} & -\mathbf{I}_{\text{Bas}} & \mathbf{0} & \mathbf{0} & \mathbf{I}_{\text{Bas}} & \mathbf{0} & \mathbf{0} \end{array} \right] \begin{array}{l} \left. \begin{array}{c} \\ \\ \end{array} \right\} l_{V1} \\ \left. \begin{array}{c} \\ \\ \end{array} \right\} l_{V2} \\ \left. \begin{array}{c} \\ \\ \end{array} \right\} l_{V3} \\ \left. \begin{array}{c} \\ \\ \end{array} \right\} l_{V2V} \end{array}, \quad (5.34)$$

where \mathbf{I} is the 3×3 identity matrix, and the $\mathbf{0}$ matrices where the size is not specified are assumed also to have the same size as \mathbf{I} . Matrices \mathbf{A}_k and \mathbf{B}_k have a block diagonal internal structure, similar to $\Phi_{\text{c},k-1}$ and $\mathbf{G}_{\text{c},k-1}$.

Afterward, the matrices have to be concatenated in order to be able to perform the update for all measurement types in only one step.

$$\mathbf{O}_k = \begin{bmatrix} \mathbf{H}_{\text{ci},k} \\ \mathbf{A}_k \end{bmatrix} \cdot \mathbf{P}_k^- \cdot \begin{bmatrix} \mathbf{H}_{\text{ci},k}^T & \mathbf{A}_k^T \end{bmatrix} \quad \mathbf{S}_k = \begin{bmatrix} \mathbf{R}_k & \mathbf{0} \\ \mathbf{0} & \mathbf{B}_k \cdot \mathbf{R}_{\text{EC},k} \cdot \mathbf{B}_k^T \end{bmatrix} \quad (5.35)$$

where $\mathbf{R}_k = \text{diag}(\sigma_{l_i}^2)$ for the GNSS and IMU measurements, and $\mathbf{R}_{\text{EC},k}$ is equivalent to \mathbf{R}_k but for the exteroceptive sensors. Subsequently, the \mathbf{K}_k matrix and the vector of updated states $\hat{\mathbf{x}}_{\text{c},k}^-$ are computed by applying:

$$\mathbf{K}_k = \mathbf{P}^- \cdot \begin{bmatrix} \mathbf{H}_{\text{ci},k}^T & \mathbf{A}_k^T \end{bmatrix} \cdot (\mathbf{O}_k + \mathbf{S}_k)^{-1} \quad (5.36)$$

$$\mathbf{D}_k = \left(\begin{bmatrix} \mathbf{l}_k \\ \mathbf{0} \end{bmatrix} - \begin{bmatrix} \mathbf{h}(\mathbf{x}_k^-) \\ \mathbf{g}(\mathbf{x}_k^-, \mathbf{l}_k) \end{bmatrix} \right), \quad (5.37)$$

$$\hat{\mathbf{x}}_{\text{c},k}^+ = \hat{\mathbf{x}}_{\text{c},k}^- + \mathbf{K}_k \cdot \mathbf{D}_k. \quad (5.38)$$

It is interesting to see in the so-called *innovation vector* introduced in Eq. (5.37), that the exteroceptive sensor measurement observations are equal to 0, given that those measurements are hard constrained. Finally, the covariance can be propagated by applying:

$$\mathbf{P}^+ = (\mathbf{I} - \mathbf{K}_k \cdot \mathbf{A}_k) \cdot \mathbf{P}_k^- \cdot (\mathbf{I} - \mathbf{K}_k \cdot \mathbf{A}_k)^T + \mathbf{K}_k \cdot \mathbf{S}_k \cdot \mathbf{K}_k^T. \quad (5.39)$$

5.1.5 Collaborative SLAM

In the previous section, the C-EKF is implemented introducing the plane equations that define the objects of the environmental model as prior knowledge. This means that the state estimation is

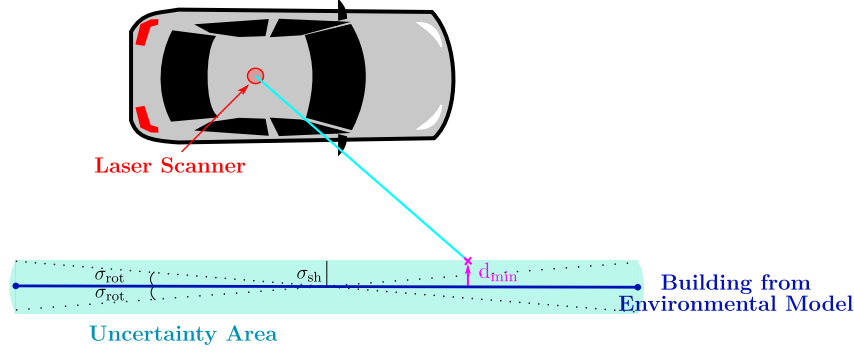


Figure 5.5: Measurement and environmental uncertainty.

carried out as a *localization problem*. However, the localization approach assumes the landmarks as perfectly georeferenced elements. Normally, the available open source maps, such as the 3D city model described in this section, are computed from large amounts of surveyed data. This results not only in the generalization of the mapped elements geometry, but also in the introduction of errors by the mapping techniques used. The assumption of landmarks affected by uncertainty leads to inconsistencies when they are combined with absolute measurements in a localization approach. This problem is tackled by taking into account the uncertainty of the landmarks, and considering it in the algorithm. As a result, the algorithm is capable to map the environment (correct the uncertainty on the landmark georeferencing) and use the newly estimated landmarks to simultaneously locate itself on the map, describing a full SLAM approach.

In the 3D city model used in this document, the specifications state that the vertices used to determine the faces of the buildings have an horizontal uncertainty at the decimeter level. The vertical uncertainty depends on the level of detail of the selected model. The relative positioning situation is depicted in Figure 5.5. There, it is possible to see that given the sensor performance, the intersected point (magenta cross) never lies in the plane. In the localization approach, the minimum distance from the intersected point to the plane must be equal to 0. However, the errors on the vertex lead to plane uncertainties that could be represented in the shape of rotations (σ_{rot}), shifts (σ_{sh}) or both simultaneously (light blue *uncertainty area* in Figure 5.5). For simplicity, the facade planes are always considered to be perfectly vertical. Thus, an additional source of error coming from the environment is considered on the system, transforming the laser scanner and stereo camera hard constrained measurements, described in Eq. (5.30) and (5.31), into the soft constrained equations described in (5.40) and (5.41).

$$\mathbf{n}(\alpha, \beta) \cdot \left[\mathbf{p}_{veh}^t + \mathbf{C}_b^t \cdot \left(\underbrace{\mathbf{C}_{LS}^b}_{\text{calibration}} \cdot \underbrace{r}_{\text{observation}} \cdot \underbrace{\mathbf{C}(\rho, \epsilon) + \mathbf{t}_{LS}^b}_{\text{calibration}} \right) \right] + d = 0 + v_{env} \quad (5.40)$$

$$\mathbf{n}(\alpha, \beta) \cdot \left[\mathbf{p}_{veh}^t + \mathbf{C}_b^t \cdot \left(\underbrace{\mathbf{C}_{cam}^b}_{\text{calibration}} \cdot \underbrace{\mathbf{p}_{cam}}_{\text{observation}} + \underbrace{\mathbf{t}_{cam}^b}_{\text{calibration}} \right) \right] + d = 0 + v_{env} \quad (5.41)$$

where $\mathbf{n}(\alpha, \beta) = \begin{bmatrix} \sin \alpha & \cos \beta \\ \cos \alpha & \cos \beta \\ \sin \beta \end{bmatrix}$ is the normal vector of the plane and v_{env} is the residual that represents the error caused by the landmark uncertainty.

Moreover, since the landmarks are affected by uncertainty, the parameters that define the plane equation must be also contained in the state vector to be estimated. Hence, the C-SLAM state vector results from aggregating the landmark parameters to the localization state vector $\mathbf{x}_{\mathbf{c}}$ represented in Eq. (5.20). In a case with n detected landmarks, the C-SLAM can be written as:

$$\mathbf{x}_{\text{SLAM}} = [\mathbf{x}_{\mathbf{c}} \parallel \alpha_1 \beta_1 d_1 \parallel \alpha_2 \beta_2 d_2 \parallel \cdots \parallel \alpha_n \beta_n d_n]^T, \quad (5.42)$$

leading to the following \mathbf{H}_{SLAM}

$$\mathbf{H}_{\text{SLAM}} = [\mathbf{H}_{\mathbf{c}} \parallel \mathbf{H}_{\pi}], \quad (5.43)$$

where

$$\mathbf{H}_{\mathbf{c}} = \begin{bmatrix} \mathbf{H}_{\mathbf{ci},k} \\ \mathbf{A}_k \end{bmatrix}. \quad (5.44)$$

Nevertheless, the large amount of planes available in the 3D city model leads to an increase of the computation time of the filter. Considering a typical scenario of three vehicles that navigate in an area with approximately 500 planes, the computation with the SLAM is approx. 30% slower than the localization. To mitigate this inconvenience, the detected planes are estimated at every individual epoch, which means that the size of the state vector varies with time. The estimated parameters from the planes that are lost from one epoch to another are stored in a data base together with their respective variances and covariances, so should they be needed again, they are not treated as a new detection, and the estimation of its parameters can continue with the newly received observations.

Finally, the correction step can be computed as

$$\hat{\mathbf{x}}_k^+ = \hat{\mathbf{x}}_k^- + \mathbf{K}_k \cdot \left(\begin{bmatrix} \mathbf{l}_k \\ \mathbf{v}_{\text{env}} \end{bmatrix} - \begin{bmatrix} \mathbf{h}(\mathbf{x}_k^-) \\ \mathbf{g}(\mathbf{x}_k^-, \mathbf{l}_k) \end{bmatrix} \right). \quad (5.45)$$

It is possible to see in Eq. (5.40) and (5.41) that the plane equations are not parametrized as in the Hesse's normal form, but with two rotations (an azimuth α and a vertical rotation β) and a distance to the origin d . This is because the normality constraint of the Hesse normal form introduced in Eq. (2.10) might be violated after the update step, producing an inconsistency on the filter estimation. With the parametrization introduced in Eq. (5.40) and (5.41), this problem is avoided, guaranteeing that $|\mathbf{n}| \stackrel{!}{=} 1$.

5.1.6 Localization with Landmark Uncertainty

In the last two sections, two different approaches to estimate the states of a group of vehicles that navigate in a completely known (localization) or unknown area (SLAM) were presented. However, the consideration of uncertainty in the landmarks enables one variation of the estimation methodology.

In the SLAM approach, the landmark parameters are updated using relative measurements, which means that their correction is carried out with respect to the estimated position of the vehicle where the sensor is mounted. This usually leads to a situation where the accuracy of the estimation depends mainly on the initial position and orientation of the vehicle, and on the measurements that are able to anchor the estimation to the selected global frame (e.g. GNSS position measurements). However, a map is available in the matter at hand. Hence, it is possible to carry out the estimation under the assumption that, although affected by uncertainty, the nominal number of landmarks and their distribution within the global frame is given by the map. In this way, it is possible to understand the given position and orientation of the landmark as the most probable position, and then solve the problem as a localization approach.

From the point of view of the estimation, the C-EKF solution is computed following the methodology described in Section 5.1.4, although considering the measurement equations for the exteroceptive sensors introduced in Section 5.1.5 (Eq. (5.40) and (5.41)). Thus, the uncertainty in the landmarks is considered in the estimation without the plane parameter estimation, leading to two fundamental advantages with respect to the SLAM approach:

1. The planes are anchored to the global frame, providing a more accurate solution than the SLAM.
2. The state vector contains the same number of parameters to estimate as the localization approach, leading to similar computation times.

5.2 Application Example

The versatility of the simulation framework is tested by analyzing and comparing the results obtained running the C-EKF as a localization approach (with and without uncertainty in the landmarks) and as a C-SLAM. Moreover, the performance of the filter components is evaluated. Therefore, the characteristic behaviors shown by the different filter implementation methodologies are identified and evaluated. In this way, a foundation for the overall filter performance is built, before approaching a more exhaustive research in the following chapters. At first, the characteristics of the scenario and simulation set up are introduced. Then, the results obtained by running the filter as localization (with and without landmark uncertainty) and C-SLAM approaches are compared.

5.2.1 Scenario and Setup

The analysis and evaluation of the filter behavior require the design and implementation of a suitable simulation scenario. This scenario must fulfill the necessary geometrical, topological and stochastic conditions that approximate the simulation to the maximum degree of realism possible, in order to extrapolate the obtained conclusions to real cases. In this section, the considerations taken into account to achieve the materialization of such an scenario are described, following the order described in Section 5.1 (cf. Figure 5.1).

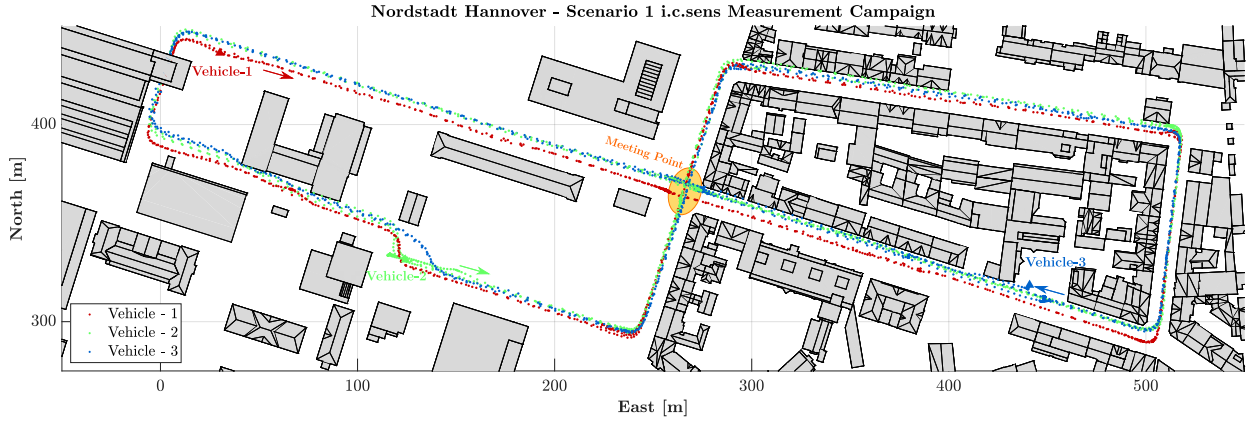


Figure 5.6: Top view of the selected scenario. The red, green and blue sequences of points mark the reference trajectories of the three vehicles, that circulate in an urban area in the Nordstadt, Hannover. The red, green and blue triangles and arrows mark the initial location of each vehicle and the direction of driving respectively. The meeting point of the three vehicles is marked in orange. The 3D city model of the environment with LoD-2 is depicted with gray polygons.

Table 5.1: Origin of the Local Topocentric Frame in the ECEF frame

X ECEF	Y ECEF	Z ECEF
3845236.996 [m]	658139.720 [m]	5029177.438 [m]

In this scenario, three trajectories of approximately 20 minutes are generated, where the vehicles navigate describing a *meet and greet* scenario (the vehicles meet each other at the same time in the intersection highlighted in orange) in an urban area of Hannover, Germany (cf. Figure 5.6). The selected methodology is the *Waypoints Obtained from Real Data* described in Section 5.1.1. Here, the data collected from the i.c.sens measurement campaign (SCHÖN ET AL., 2018) is used to compute the GNSS + IMU (Novatel SPAN-SE³ GNSS receiver and iMAR iIMU-FSAS⁴) tightly-coupled solution in the case of the first vehicle, and the loosely-coupled solution for the additional two vehicles (computed internally from the LORD MicroStrain GNSS/aided Inertial Navigation System GNSS/IMU⁵). The results obtained consist of a set of waypoints (WGS84 ECEF coordinates), that are subsequently transformed to the local topocentric frame. In order to perform the transformation, it is necessary to establish the coordinates of the local topocentric frame origin. The origin of the local topocentric frame is selected to be coincident with the local reference station installed at the Institut für Erdmessung, Leibniz Universität Hannover, whose coordinates are shown in Table 5.1. Later, the local topocentric frame coordinates are interpolated to 100 Hz using cubic splines as described in the *Digitalized Waypoints* methodology presented in Section 5.1.1.

The outcome obtained with this methodology guarantees the correct georeferencing of the trajectories and a realistic relative localization with respect to the fixed elements of the environment.

³Novatel SPAN-SE guide: <https://www.novatel.com/assets/Documents/Manuals/om-20000124.pdf>

⁴iMAR iIMU-FSAS: http://imar.de/downloads/IMU_FSAS.pdf

⁵LORD MicroStrain 3DM-GQ4-45: <https://www.microstrain.com/Inertial/3dm-gq4-45>

The latter constrains the correct geometry and topology of the exteroceptive sensor measurements, which is crucial in order to achieve valid conclusions.

The next step is to select the model of the environment. Here, a suitable option for the comparison between the 3D results obtained running the problem as a localization approach with the results obtained with the SLAM approach must be selected. Section 5.1.2 introduces the 3D City Model with LoD-2 and a pre-aligned laser scanner point cloud as possible models of the environment in 3D cases. Also, it is stated that the pre-align point cloud model consists of a more realistic model of the environment than the 3D City model with LoD-2 since it enables the consideration of measurement artifacts (e.g. reflections or occlusions), urban furniture, and a more realistic representation of the building facades (i.e. more complex shapes and windows are contained). Hence, the option that yields the most realistic results in a localization approach is the pre-aligned point cloud. However, the pre-aligned point cloud is a discrete representation of the environment, that must be transformed into a continuous representation prior to the simulation of the exteroceptive sensor measurements. This is achieved by the assignment of a normal vector to each point of the cloud using the algorithm discussed in BRENNER (2016). In the SLAM approach presented in this thesis, the plane parameters are simultaneously estimated together with the vehicle state parameters. Given that each simulated ray intersects with a different plane (the plane associated to the closest point), the execution of the SLAM approach requires a vector that includes one set of plane parameters (3 parameters) for each ray, leading to the following inconveniences:

- (i) Larger state vectors occur in larger estimations. The computation time and reserved memory requirements increase exponentially with the number of vehicles considered.
- (ii) Observability issues. At least three points are necessary to estimate the plane parameters, and each measurement causes the estimation of three plane parameters ($r = (n - u) < 0$).

Given that these issues prohibit the possibility to select the pre-aligned point cloud for SLAM problems, the 3D City model with LoD-2 is selected. With this model of the environment these issues are bypassed since always at least four rays intersect with the same plane, avoiding in this way negative redundancies and executing the adjustment in a computationally efficient way. Finally, the inconvenience of this selection is that the environmental model selected is much more generalized with respect to reality, leading to overoptimistic geometric results.

Subsequently, the availability of the vehicle dynamics and the representation of the environment enable the generation of measurements. In this scenario, GNSS position and velocity, IMU specific forces and angular rates, laser scanner, camera measurements and V2V measurements are considered.

First, the GNSS position and velocity measurements are generated (1 Hz, single antenna) by applying noise to the positions obtained in the trajectory generation step. In order to take into account the environment information, the amount of noise is applied as a function of the DOP values obtained in the measurement campaign. In Figure 5.7, the generated GNSS and IMU measurements are shown. In the top panel, it is possible to see the result from applying an amount of noise proportional to the HDOP (middle-left panel) to the horizontal coordinates. Although

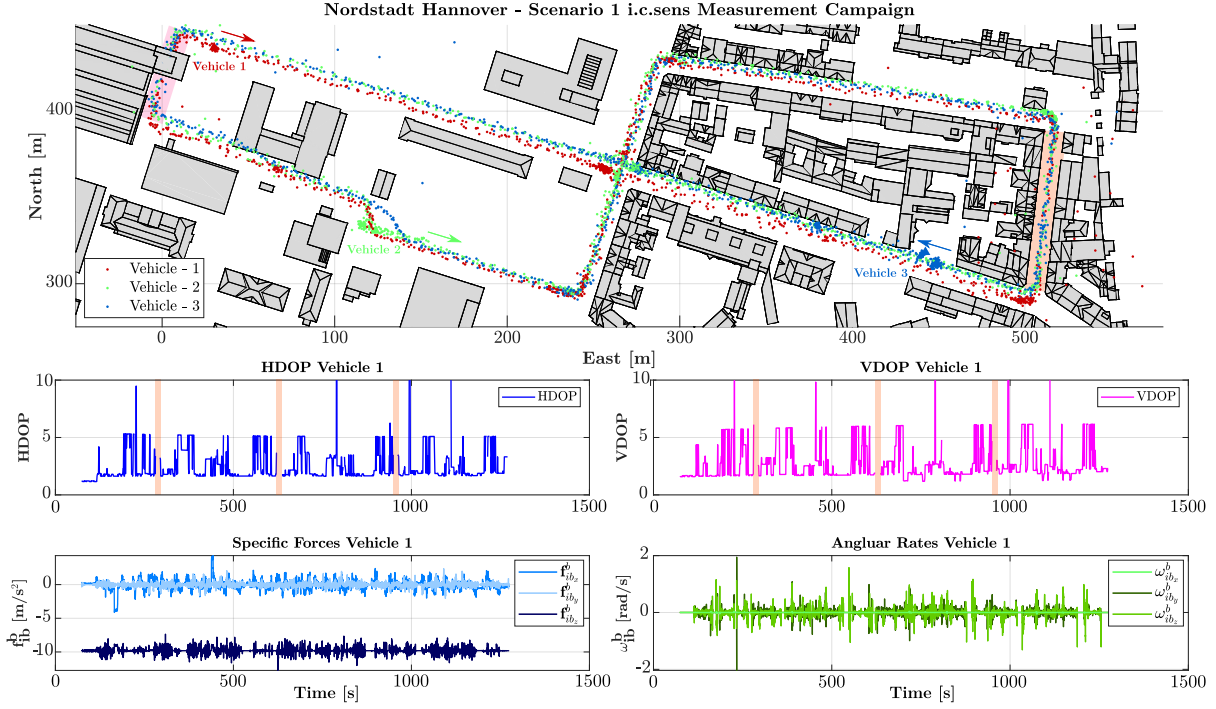


Figure 5.7: This figure shows the simulated GNSS and IMU measurements for vehicle 1 (red trajectory). The top panel shows the GNSS position measurements, where an error function of the HDOP (middle-left panel) obtained from the computation is applied as explained in Eq. (5.12). In addition, an error function of the VDOP (middle right panel) is applied to the vertical coordinate. The bottom-left and bottom-right panels show the error-free simulated specific forces (\mathbf{f}_{ib}^b) and angular rates ($\boldsymbol{\omega}_{ib}^b$), respectively. The vertical lines indicate the period of the trajectory in which vehicle 1 navigates in *Kniestrasse* (GNSS challenging area highlighted in orange), revealing that the vehicles revisit four times the same area.

it is not visible in the figure, the amount of error applied to the vertical coordinate is generated proportional to the VDOP (middle-right panel) values. The scene displays two areas where the GNSS positioning is specially challenging. The first one is in the area shadowed in orange (at the East side of the selected area) both at the scenario top view plot with the GNSS measurements and at the DOP plots. Here, the tight urban canyon causes the few visible satellites to be almost aligned. This situation yields a high DOP value and sometimes even the complete loss of signal. As a result, the noisy generated coordinates, that will be used as GNSS measurements in the filter (red, green and blue dots), are scattered all over the area, some of them showing errors above 30 m. The second GNSS area is shadowed in pink, where the vehicles navigate under a house passage. This of course produces a complete signal loss during a short interval of four or five seconds, and a poor positioning solution at the epochs directly before entering and exiting the tunnel. This situation affects also the V2V measurements, which depend on the satellite geometry.

Second, the IMU measurements are directly obtained from the trajectory generation step with 100 Hz data rate (cf. Figure 5.7 bottom-right and bottom-left panels). Then, random noise is added to both observations with a selected standard deviation (σ_ω for the angular rates and σ_f for the specific forces). If the error is applied to the measurements epoch-wise, it is accumulated

Table 5.2: Leverarm parameters of the exteroceptive sensors

	Leverarm Translations			Leverarm Rotations		
	X [cm]	Y [cm]	Z [cm]	r_x [°]	r_y [°]	r_z [°]
Laser S.	50	50	50	0	0	5
Camera 1	100	-42	50	0	0	0
Camera 2	100	42	50	0	0	0

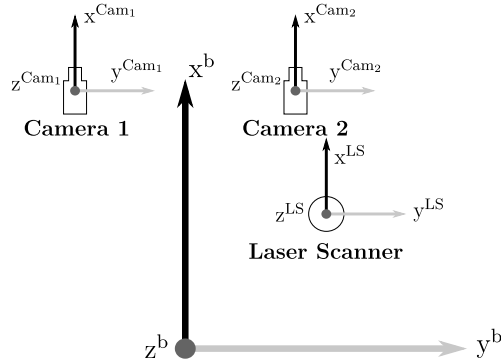


Figure 5.8: Diagram of the distribution of the exteroceptive sensors in the body frame. This sensor distribution is considered for the three vehicles of the simulation.

during the strapdown navigation algorithm, meaning that the solution drifts with respect to the true solution in a period of time dependent on the selected values for σ_ω and σ_f .

Third, laser scanner bundles are simulated with 1 Hz as described in Section 5.1.3. A vertical aperture angle is applied to the measurements, that contains a total of 16 rays. This is done in order to avoid the ill-posed estimations within the SLAM approach (a plane estimation from a line scanner has more than one solution). Moreover, the stereo camera measurements are generated with 1 Hz as described in Section 5.1.3 (cf. Figure 5.3). Given the high complexity of the vehicle dynamics and the selected environmental model, zero mean white noise is applied to the measurements in order to simplify the effects produced by these measurements and facilitate the posterior analysis.

In this experiment, the GNSS and IMU measurements are generated under the assumption that both devices are placed at the same position within the vehicle. However, this is not the case for the laser scanner and the pair of stereo cameras, which are assigned to a specific position within the body frame. The overall positions and orientations (leverarm parameters) of each sensor with in the body frame are summarized in Table 5.2 and Figure 5.7.

In Figure 5.8, the Z-axis of each considered frame is pointing upward. The dimensions and the slight misalignment of the laser scanner orientation with respect to the body frame are selected imitating the architecture considered in the measurement campaign.

Furthermore, the standard deviations applied to generate the measurement noise of all sensors are shown in Table 5.3. The last two parameters from this table are only considered in the SLAM and localization with landmark uncertainty (see Sections 5.1.5 and 5.1.6) approaches. They refer

Table 5.3: Sensor measurement standard deviation and update rate: sample run

<i>Sensor</i>	<i>Measurement</i>	σ	<i>Update Rate</i>
GNSS	$\mathbf{p}_{\text{GNSS}}^t$	$0.5 \text{ [m]} \cdot \delta_{\text{DOP}}$	1 Hz
	$\mathbf{v}_{\text{GNSS}}^t$	$0.1 \text{ [m/s]} \cdot \delta_{\text{DOP}}$	1 Hz
	V2V	$0.5 \text{ [m]} \cdot \delta_{\text{DOP}}$	1 Hz
IMU	\mathbf{f}^b	$0.002 \text{ [m/s}^2\text{]}$	100 Hz
	ω_{ib}^b	0.001 [rad/s]	100 Hz
Laser S.	r	0.1 [m]	1 Hz
Cameras	\mathbf{p}_{cam}	0.1 [m]	1 Hz
Env. Model	α	$3 [^\circ]$	1 Hz
	Shift	0.1 [m]	1 Hz

Table 5.4: Random walk process noise spectral density: sample run

<i>Parameter</i>	PSD
Velocity (\mathbf{q}_{vel})	$0.35 \text{ [m}^2\text{/s}^3\text{]}$
Attitude (\mathbf{q}_{att})	$0.1 \text{ [rad}^2\text{/s]}$

to the uncertainty applied to the planes in the model of the environment, respectively, in the shape of rotation and shift uncertainties. In this experiment, the planes from the 3D city model are considered to be perfectly vertical. Therefore, the uncertainty is only applied to the azimuth rotation, denoted as α in Eq. 5.42.

Finally, the filter processing parameters, divided in Power Spectral Density (PSD) and initial covariance of the state parameters, taken into account in the computation of Eq. 5.27 are shown in Tables 5.4 and 5.5, respectively. The PSD is implemented as a random walk, and anticipates the noise caused by the motion model selected on the prediction step.

Table 5.5: Initial covariance of the state parameters: sample run

<i>Parameter</i>	\mathbf{P}_0
Position	$0.90 \text{ [m}^2\text{]}$
Velocity	$0.20 \text{ [m}^2\text{/s]}$
Attitude	$0.005 \text{ [rad}^2\text{]}$

5.2.2 Sample Run

In this section, the qualitative and quantitative results obtained from a sample run in the above mentioned simulation scenario are presented and discussed. The high complexity of both the environment and the vehicle dynamics lead to a difficult identification and visualization of representative epoch-wise events of the plane-based estimation. Nevertheless, such a large and heterogeneous environment is suitable to identify the general patterns, that allow the evaluation of the overall filter

performance reached with each of the different execution techniques (localization and C-SLAM approaches). Subsequently, the analysis of the general filter specifics enable the establishment of a foundation, essential for the understanding of the additional experiments designed to support the statements formulated within the chapter at hand. The analysis is carried out in terms of accuracy (assessing the RMSE results), precision (assessing the standard deviation results) and integrity (evaluating the relation between PE, PL and AL).

Accuracy

In Table 5.6, the overall RMSE results obtained by running the C-EKF algorithm as localization (**L**) and C-SLAM (**C-S**) are displayed, adopting the GNSS + IMU loosely coupled solution (**G+I**) as a reference. Although the state vector estimates the three components of position in the local topocentric frame ($\mathbf{p}^t = [\Delta N \ \Delta E \ \Delta U]$), the **positioning results** are shown in Cross-Track (XT) and Along-Track (AT) directions. This is done as a consequence of the characteristic behavior shown in the plane-based localization estimation at hand. In urban areas, the prevailing landmark geometry is illustrated with planes oriented (almost) parallel to the direction of driving. This, together with the application of an error model to the exteroceptive sensor measurements that is not based on the distance to the intersected point (see Table 5.3), depicts a scene in which the mentioned observational work produces a higher impact on the y-axis of the vehicle frame direction (XT) than in the x-axis (AT).

To further investigate this finding, an elementary Monte Carlo (MC) simulation that enables the comparison of the outcomes obtained in two characteristic environmental situations (urban canyon and urban intersection) is carried out (cf. Figure 5.9). In this simulation the vehicle is equipped with a horizontally installed laser scanner (360° field of view and 16 lines of vertical aperture) and a GNSS receiver that enables to perform the geo-location task. The errors in the GNSS and ranging measurements are assumed to be Gaussian white noise ($\sigma_{\text{GNSS}} = 1 \text{ m}$ and $\sigma_{\text{LS}} = 0.01 \text{ m}$). Then, 200 runs are performed, obtaining the positioning results displayed in the graphs depicted in the mid-panels, and the histograms illustrated in the right panels. The outcome from the mentioned simulation shows that urban geometries with planar elements oriented parallel to the direction of driving have little (or no) effect on the AT estimation, displaying the solutions in the urban canyon much more extensively expanded over the East axis (driving direction) than over the North axis (XT). In this situation, the planes describe a situation of axial symmetry, causing the same exteroceptive sensor measurement distribution to be achieved, regardless of the position of the vehicle within the East axis. However, in the urban intersection, the environment depicts a situation of central symmetry, that can be understood as two overlapping urban canyons, acting as a cage that encloses the vehicle. Therefore, the favorable environmental geometry is extended to the AT direction and the solution is upgraded to sub-millimeter level. Of course, such an accuracy is only obtained due to the oversimplifications considered in the simulation, like e.g. absence of occlusions/outliers, assumption of a perfectly flat surface of the facades (no texture) and overoptimistic measurement noise selected in order to highlight the effects of the environmental geometry. In the estimation of the heading (ψ), the urban canyon situation is sufficient for its state update, since changes in the orientation vary the axial symmetry relation between the

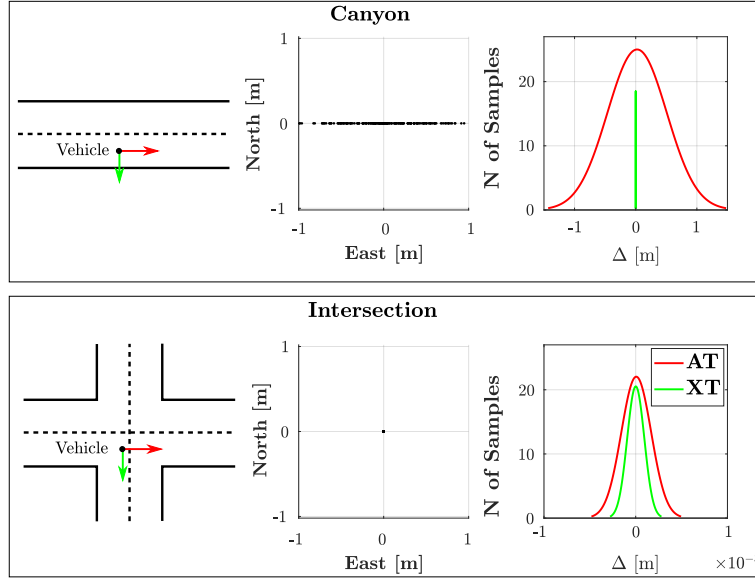


Figure 5.9: MC simulation that shows the influence of the environment on the state estimation with laser scanner (200 runs). Please note the different scales in the x-axis of the histogram plots.

x-axis of the body frame and the planar elements. Consequently, it can be stated that the detection of planes on both sides of the vehicle is satisfactory for the estimation of ψ but not for the complete 2D positioning, and planes oriented perpendicular to the direction of driving must be detected.

Despite displaying the results obtained using a much more complex scenario, the above mentioned event is easily identified in Table 5.6 by comparing the RMSE displayed in the two first columns of the **L** approach. With the configuration shown in Tables 5.3 to 5.5, the localization approach yields results below 4 cm in the XT direction, which means an improvement of approx. 60% with respect to the AT solutions, regardless of the vehicle. The obtained results could be anticipated given the value selected for the laser scanner and stereo camera measurement noise standard deviation of 0.1 m, thus highlighting a strong influence of the exteroceptive sensor measurements in this adjustment. The results shown in Table 5.6 contrast with the ones shown in Fig. 5.9, due to the higher error noise considered for the exteroceptive sensor measurements (e.g. $\sigma_{\text{ext}} = 1\text{cm} \rightarrow \sigma_{\text{ext}} = 10\text{cm}$) and the much higher complexity of both vehicle trajectories and environment. Furthermore, the overall 2D RMSE obtained are at the decimeter level, whereas the 3D results show a significant decrease in the accuracy, showing values in the range of the 0.4 m. This decrease is another consequence of the plane layout. As in the case of the AT estimation in urban canyons (cf. Figure 5.9), the assumption that the facades are always perfectly vertical, together with the absence of ground plane, reveal a permanent insufficient geometry for the estimation of the up-coordinate in ground-driven vehicles. Nevertheless, this situation does not represent a serious inconvenience, since the position of the vehicles is always constrained by the surface they stand on, and the up-component of the position is updated with both the GNSS position and velocity measurements. In UAVs navigation, the exteroceptive sensors are able to identify pieces of rooftops formed by oblique planes, which complement the missing piece of information, and enable the Up state update with the exteroceptive sensor measurements. By extension, the roll and pitch attitude components are also affected by these circumstances. As a result, since the estimation of the up-component, roll

Table 5.6: C-EKF RMSE results. The results obtained with the localization approach (**L**) are compared with the C-SLAM (**C-S**), and the solution that does not consider exteroceptive sensors (**G+I**, GNSS and IMU loosely coupled solution).

		RMSE							
		Position [m]				Velocity [m/s]			Attitude [°]
		XT	AT	2D	3D	v_N	v_E	v_U	ψ
L	V-1	0.030	0.074	0.088	0.332	0.182	0.157	0.182	0.052
	V-2	0.034	0.085	0.107	0.365	0.193	0.234	0.212	0.098
	V-3	0.039	0.093	0.119	0.368	0.194	0.172	0.180	0.111
C-S	V-1	0.311	0.307	0.463	0.566	0.181	0.187	0.183	1.266
	V-2	0.298	0.333	0.484	0.598	0.232	0.258	0.212	1.346
	V-3	0.263	0.301	0.424	0.546	0.202	0.181	0.180	1.283
G+I	V-1	0.314	0.302	0.466	0.568	0.181	0.187	0.183	1.301
	V-2	0.299	0.327	0.478	0.593	0.233	0.258	0.212	1.375
	V-3	0.268	0.300	0.428	0.549	0.202	0.182	0.180	1.138

and pitch remain unaffected by the laser scanner and stereo camera measurements, they are not displayed.

Although the overall results displayed in Table 5.6 help to analyze the global behavior of the filter, it is necessary to evaluate the **epoch-wise behavior** that the processing parameters show throughout the complete trajectory. To obtain answers in this direction, the time series of XT, AT and heading state parameters are shown in Figure 5.10 for each vehicle. The precision of the estimation is displayed by including in the three-sigma curves. In this figure, the highly dynamic character of the estimation is visible, as the accuracy and precision of the estimation improve or become worse epoch-by-epoch, showing a fairly low degree of repeatability in epoch-wise estimations. Naturally, the straightforward results obtained in the simulation shown in Figure 5.9 are not anymore achievable in this time-variant experiment, mainly due to the following factors:

1. In the 3D city model, the elementary situations described in Figure 5.9 are combined, resulting in complex environmental geometries (as in Figure 5.7)
2. The motion of the vehicles changes constantly.
3. The GNSS errors are generated as a function of the DOP values.

As a result, the repeated four tours carried out by the three vehicles in the proposed scenario are not anymore clearly discernible in the time series, unlike in the DOP measurement graphs shown in Figure 5.7. Also, these results support again the RMSE analysis from Table 5.6, as the estimation is more accurate in the XT direction (blue lines) than in the AT (magenta lines).

The time-series results in Figure 5.10 reveal also the effects caused in the estimation by trajectory mismodelling problems (orange dashed boxes). In these regions, the filter yields a fairly unstable solution, both in the 2D position and heading state parameter estimations. Taking a look at

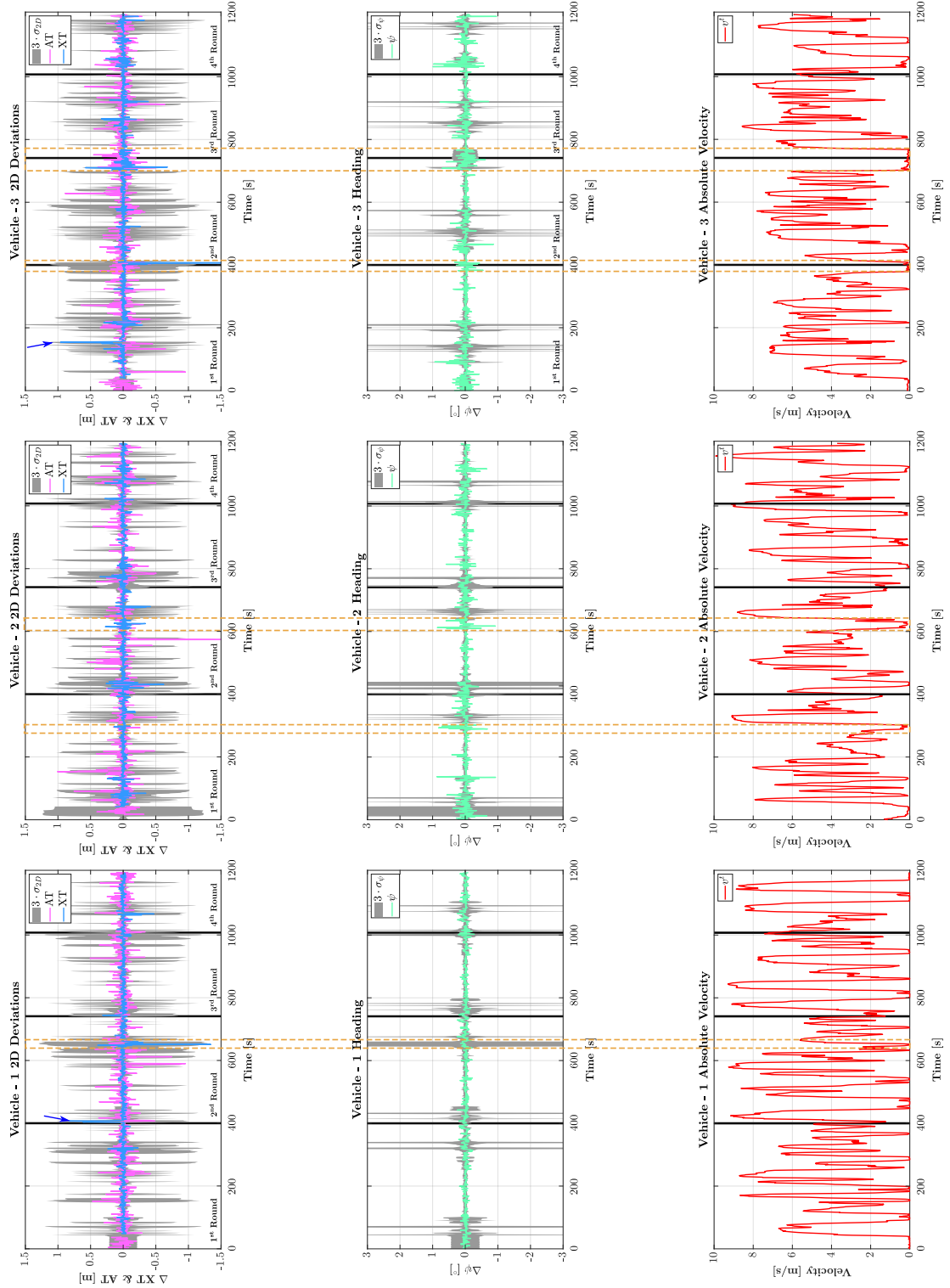


Figure 5.10: Time series of the results displayed in the localization solution of Table 5.6. The deviations relative to the reference solution of the three vehicles are displayed in the XT, AT (top row) and heading (middle row). In addition, the absolute velocity of the vehicle in the local topocentric frame is displayed (bottom row), so that the effects of attitude mismodelling have in the state estimation can be identified. The black vertical lines are used to mark the point where the vehicle starts a new round, facilitating the assessment of the solution repeatability.

the absolute velocity of the vehicle (bottom row) at those moments in time, it is possible to see that it always takes place where the vehicle is stopped. When the vehicle is stopped, the imperfect algorithm used in order to generate the waypoints produces epoch-wise solutions that differ marginally from each other, which should not be the case given that the vehicle is not moving. Subsequently, this situation is translated into the generation of non-existing and abrupt turning maneuvers that result in the disruption of the motion model at those epochs. Later, the C-EKF update step is performed with utterly unrealistic predicted measurements in $\mathbf{g}(\mathbf{x}_k^-, \mathbf{l}_k)$, yielding the mentioned output. This situation highlights the importance of efficient trajectory generation algorithms and multi-modal implementations, in which the filter is able to identify the most suitable model for the current physical situation of the vehicle. Given that the results are not representative for the estimation in these areas, these epochs are neglected from the overall RMSE computations within the analysis.

Regarding the **velocity**, the state parameters are estimated in the prediction step with the IMU specific forces, and updated with the GNSS velocity measurements. Here, the ratio between the noise considered in the IMU accelerations and the GNSS velocity measurements might lead to divergence problems, should the GNSS measurements not be precise enough to correct the estimation received from the prediction state. However, it is possible to see in Table 5.6, that under the selected configuration (cf. Tables 5.3 - 5.5) this is not the case, and the results obtained are on average, in the range of the 0.2 m/s. Furthermore, the velocity state parameters remain unaffected by the exteroceptive sensor measurements, and thus, they are displayed in the North (\mathbf{v}_N), East (\mathbf{v}_E) and Up (\mathbf{v}_U) components, and they yield a similar RMSE in the three components. Nevertheless, the velocity states are coupled with the positioning states in the motion model (Eq. (5.23)), leading to a marginal improvement (approx. 10%) of the localization (\mathbf{L}) results with respect to the ones yielded by the C-SLAM ($\mathbf{C-S}$) and ($\mathbf{G+I}$) approaches.

Moreover, the **heading** is the only attitude state parameter affected by the update with the exteroceptive measurements. It can be seen in Table 5.6 that its estimation achieves an accuracy below 0.2° for every vehicle (cf. last column in the localization results of Table 5.6). It was stated before that the estimation of the roll and pitch components of the attitude is not affected by the laser scanner and stereo camera measurements. If these parameters are not corrected, they would drift with respect to the nominal solution due to the errors applied to the gyro measurements. As the errors in the prediction are transferred to the innovation vector via the predicted measurements, and since the attitude and positioning are tightly coupled by Eq. (5.30) and (5.31) through the \mathbf{C}_b^t (cosine) matrix (Eq. 3.6), not only the estimation of the attitude parameters is affected by them, but the positioning parameters as well. Hence, the biases for roll and pitch are compensated in the prediction step in order to keep the errors in these parameters in the interval of $\pm 2^\circ$. The reason why this inconvenience is bypassed and not directly neglected by restricting the processing of the measurement equations is because if the pre-aligned point cloud model of the environment is selected, intersections with the ground plane would be obtained, providing the missing piece of geometrical information to estimate the roll, pitch and Up state parameters without further considerations.

As a result, the importance of an accurate pose estimation is underlined. In order to achieve the maximum performance of the plane-based C-EKF, the exteroceptive sensors must operate based on an accurate pose estimation.

If the filter is run as a C-SLAM approach (**C-S**), the first visible outcome is an overall decrease in the accuracy with respect to the localization (**L**) approaches in the positioning and heading estimations (cf. Table 5.6). This is expected, since SLAM approaches operate under the assumption of an unknown geo-location of the multi-sensor system. Here, the filter estimates the position and orientation of the planes with respect to the estimated position and orientation of the vehicles (relative positioning). As a result, the landmarks do not act as an anchor to the global frame, leaving the weight to georeference the dynamic network entirely to the GNSS measurements. Given this situation, two outcomes are possible:

- (i) In urban areas with GNSS signal outage (or degraded solution), the network is not anchored to the global frame as in the localization approach. In these conditions, an accurate overall solution can only be obtained if the initial position and orientation of the vehicles are accurately and precisely known, no matter the amount and the precision of exteroceptive sensors measurements considered. Even if a perfect initial estimation is achieved, the biased IMU measurements cause the positioning solution to drift away from the nominal solution. This uncertainty is mapped to the plane parameter state update, which motivates further decreases in accuracy, regardless of the exteroceptive sensor measurement precision. This situation, together with the prevailing areas with planes parallel to the direction of driving, lead to the immediate divergence of the solution. Hence, it is possible to state that under this configuration, the absence of GNSS measurements always results in immediate filter divergence, unless the plane layout is constantly perfect, and the initial position and orientation of the vehicles are perfectly known.
- (ii) Under adequate GNSS signal reception conditions, the uncertainty applied to the landmarks and the exteroceptive sensor measurement precision constrain the plane equation estimation, and therefore, the amount of improvement on the state estimation. In this situation, the GNSS measurements anchor the complete network, mitigating negative effects caused by outliers in the laser scanner and stereo camera measurements. The outcome in this situation is robust in terms of accuracy, and it yields a solution similar to the one obtained if no exteroceptive sensors are considered (compare **C-S** and **G+I** solutions in Table 5.6).

In this experiment, both these situations are found. The C-SLAM results displayed in Table 5.6 show a 2D RMSE of approx. 45 cm, where the IMU measurements mitigate the effect caused by the faulty GNSS solution. Comparing these results with the **G+I** ones, obtained considering only GNSS measurements in the update step, no significant differences are identified. This happens due to the situation previously described in point (ii) above, where the GNSS measurements are the only anchors of the network to the local topocentric frame. For this reason, also the characteristic accuracy improvement in revisiting areas is vague. In the filter, the measurements carried out with exteroceptive measurements are mainly used to estimate the plane related parameters, and have almost no impact on the positioning parameters.

Table 5.7: C-EKF RMSE results obtained from running the filter with uncertain map elements. The results from running the filter with a $\sigma_{rot} = 1^\circ$ and $\sigma_{sh} = 0.1$ m (reference solution **RS**) are used as reference. The filter is executed with the same parameters but varying the $\sigma_{rot} = 0.1^\circ$ in the **LR** (*low rotation uncertainty*) results, and varying the $\sigma_{sh} = 0.05$ m in the **LS** (*low shift uncertainty*) results. In this way, the impact that the different types of noise have on the filter estimation can be compared. The innovation (**I.**) of the overall results is analyzed by displaying the percentage of improvement in the XT, AT directions and in the ψ w.r.t the **RS** solution.

		RMSE							
		Position [m]				I. Pos. [%]		Att. [°]	I. Att. [%]
		XT	AT	2D	3D	XT	AT	ψ	ψ
RS	V-1	0.092	0.171	0.238	0.401	+0.00	+0.00	0.112	+0.00
	V-2	0.147	0.329	0.370	0.501	+0.00	+0.00	0.176	+0.00
	V-3	0.130	0.220	0.255	0.428	+0.00	+0.00	0.191	+0.00
LR	V-1	0.063	0.108	0.144	0.355	-31.5	-36.7	0.061	-45.2
	V-2	0.061	0.182	0.196	0.403	-58.6	-44.4	0.106	-40.0
	V-3	0.093	0.156	0.192	0.393	-28.2	-29.0	0.124	-35.3
LS	V-1	0.058	0.150	0.172	0.365	-37.2	-12.4	0.193	-11.9
	V-2	0.165	0.312	0.360	0.500	+12.3	-5.1	0.192	+9.1
	V-3	0.111	0.222	0.273	0.442	-14.8	-0.8	0.180	-5.6

Subsequently, the filter is executed as a localization approach with the consideration of uncertainty in the map elements (computation details explained in Section 5.1.6), obtaining the overall results shown in Table 5.7. Here, the results from running the filter with three different levels of environmental uncertainty are displayed. In the reference configuration (**RS**), the parameter estimation is carried out considering an uncertainty in the planes of $\sigma_{rot} = 1^\circ$ and $\sigma_{sh} = 0.1$ m. Then, the filter is run two additional times. A first one lowering the noise in the rotation (**LR**) to $\sigma_{rot} = 0.1^\circ$, keeping the σ_{sh} unaltered, and a second one lowering the noise in the shift (**LS**) to $\sigma_{sh} = 0.05$ m, keeping the value of σ_{rot} in the **RS** unaltered. In this way, the effect that each type of uncertainty applied to the planes can be evaluated. As it was explained before, the relative layout of the planes with respect to the trajectory of the vehicle leads to the fact that only the ΔN , ΔE and ψ parameters are affected by the update with the exteroceptive sensor measurements. Given that the rest of the parameters considered in the state vector are decoupled from these measurements, they are not shown in Table 5.7.

If the **RS** results from Table 5.7 are compared with the **L** results from Table 5.6, the first visible property is an expected global decrease in accuracy. However, the magnitudes are still at the decimeter level for the positioning results, and below 0.2° for the heading, revealing an acceptable solution for autonomous navigation. Moreover, the addition of uncertainty does not affect the characteristic event of plane based estimations, with more accurate estimation in the XT than in the AT direction. Then, if the uncertainty in the rotation is reduced, the accuracy increases significantly (approximately 30% in the case of positioning, and 40% in the heading). The fact that the innovations vary from one vehicle to another reveals the fact that the task to define adequate combinations of processing parameters in dynamic networks is a challenging exercise to accomplish.

The wide variety of plane layouts and vehicle maneuvers leads to strong variations on the filter mean and covariance propagation (see Figure 5.10). Consequently, parameters such as PSD or random process selected to model the vehicle dynamics, are only suitable for particular situations. Two visible examples are highlighted with blue arrows in Figure 5.10, where the position and heading accuracy of the solutions decreases abruptly, in situations where the vehicle undergoes significant dynamic changes (sequential breaking and accelerating maneuvers). As a result, it is possible to learn from Table 5.7 that the configuration is more convenient for vehicles 1 and 3 rather than for vehicle 2, showing more accurate overall results. In fact, the results obtained by considering a lower amount of uncertainty of the shift (**LS**) returns values slightly less accurate than the configuration used as a reference in vehicle 2, provided that the vehicle at hand navigates longer time in areas where the PSD is suboptimal, or in areas with weak geometry for the update.

In this thesis, the epochs with suboptimal estimations (e.g. unsuitable process noise to measurement noise ratio, amongst others) are identified and discussed, so that favorable situations are strengthened, and the negative effects of adverse estimations are mitigated. However, the highly dynamic and heterogeneous scenario used in this section is inconvenient for this task. Thus, suitable scenarios are designed and described in the following Chapter 6, in which the details about the dynamic network optimization are discussed.

Finally, if the results displayed in Table 5.6 are compared with Table 5.7, it is possible to see that even considering that the landmarks are affected with uncertainty, the results are more accurate than the results obtained in the C-SLAM (**C-S**) and the results obtained without the exteroceptive measurements (**G+I**). This highlights the fact that the usage of laser scanner and the cameras in localization approaches, leads to an overall increase in the accuracy, and that prior knowledge on the navigation area (map) boosts the overall accuracy of the solution.

Precision

The overall standard deviations show a similar behavior as the accuracy results (see Table 5.8). The C-EKF yields horizontal localization (**L**) results at the centimeter level whereas the C-SLAM (**C-S**) 2D results are at the decimeter level. The high precision of the heading solution in the localization approach is demonstrated since the values are in the range of a few hundreds of a degree. As in the case of accuracy, the solution of the C-SLAM does not present any significant difference to the solution where no exteroceptive sensor measurements are considered. Taking the localization results as reference, the quality of the geometry in C-SLAM approaches decreases, provided that the landmarks do not act anymore as anchors for the network. With this in mind, the achievement of similar outcomes in the latter two configurations is coherent.

If the localization results shown in Table 5.8 are compared with the results from the accuracy 5.6, it is possible to see that the standard deviations obtained are significantly lower than the magnitudes of the accuracy results. In plane-based algorithms, and specially in the EKF algorithms, the definition of the measurement noise as white noise with a selected standard deviation is not representative of the innovations generated in Eq. (5.37). Taking into account hard constrained equations (see Eq. (5.30) and (5.31)), the minimum distance of the intersected point to the plane

Table 5.8: C-EKF SD results. The results obtained with the localization approach (**L**) are compared with the C-SLAM (**C-S**), and the solution that does not consider exteroceptive sensors (**G+I**, GNSS and IMU loosely coupled solution).

		STANDARD DEVIATION							
		Position [m]				Velocity [m/s]			Attitude [°]
		ΔN	ΔE	2D	3D	v_N	v_E	v_U	ψ
L	V-1	0.021	0.028	0.040	0.423	0.168	0.169	0.182	0.015
	V-2	0.024	0.032	0.045	0.419	0.169	0.170	0.187	0.040
	V-3	0.019	0.033	0.042	0.417	0.168	0.172	0.187	0.018
C-S	V-1	0.389	0.373	0.613	0.765	0.187	0.187	0.187	1.685
	V-2	0.381	0.386	0.601	0.752	0.187	0.187	0.187	1.689
	V-3	0.381	0.386	0.601	0.751	0.187	0.187	0.187	1.693
G+I	V-1	0.397	0.397	0.621	0.773	0.187	0.187	0.187	1.711
	V-2	0.391	0.390	0.610	0.760	0.187	0.187	0.187	1.711
	V-3	0.390	0.390	0.609	0.759	0.187	0.187	0.187	1.711

must be equal to zero and the predicted measurements are not only computed as a function of the noisy range \mathbf{r}_k and camera \mathbf{p}^{cam} measurements, but also as a function of the previously estimated pose of the vehicle. Although the measurement uncertainty is considered by the \mathbf{R}_k matrix and the uncertainty in the estimation is considered in the predicted covariance matrix \mathbf{P}_k^- , improper PSD values in the process noise \mathbf{Qd}_k matrix and the effect of the data rate for the update lead to the fact that the values yielded within the covariance matrix are difficult to match by the updated states.

Table 5.8 highlights also the decoupled condition of the velocity states in the update estimation, showing the same overall values in the **C-S** and **G+I**. This is expected since in this approach, the noise is applied to the velocity measurements as a function of the Position Dilution of Precision (PDOP) value, and the effect of the exteroceptive sensor measurements in the position is not enough to cause an effect on the velocity estimation through the prediction step.

In the experiment discussed in this section, accuracy jumps caused by non-consistent Kalman gain (\mathbf{K}_k) are present in the 2D position and heading parameter. In multi-sensor estimations, the wide variety of sensor measurements lead to poorly conditioned Jacobian matrices (\mathbf{Hc}) that affect the accuracy of the solution through the computation of \mathbf{K}_k . In the available literature, ÅKESSON ET AL. (2007) propose to tackle this problem by using regularization terms. Following this approach, ZHANG AND OLIVER (2011) compare the results obtained by applying regularization either to the Kalman gain or to the covariance matrices for non-linear problems. The performance of the methodologies developed are based on the improvement in the Kalman gain estimates, quality of data prediction and the estimates of model variables. However, the application of regularization parameters is not a suitable solution in our case, since it would be necessary that the optimum value is selected for each case (epoch-wise optimization). Additional solutions like the ones proposed in SØRENSEN AND MADSEN (2004), such as Kalman gain smoothing or steady-state computations, are unfortunately not entirely suitable for our case either. First, the Kalman gain smoothing would not

solve the problem if the predicted covariance to measurement noise ratio is still not convenient for the estimation at that epoch, and second, the steady-state computation is a suboptimal estimator in time-variant systems (cf. Figure 5.10).

As a result, a methodology to find the optimum PSD values for the consistent computation of \mathbf{Qd}_k , \mathbf{R}_k and \mathbf{P}_k matrices is presented on Chapter 6. In this way, although not completely neglected, these negative effects can be mitigated.

Regarding the velocity parameter estimation, consistent results are obtained with the different configurations, given that they are not affected by the exteroceptive sensor measurements.

Filter Observability

The observability of the filter can be defined as the suitability of the estimation to produce an output $\hat{\mathbf{x}}_{\mathbf{c},k}^+$, given the set of available measurements \mathbf{l}_k . In linear cases, the measurement model is defined as in Eq. (3.14). Hence, the updated state vector can only be computed if the matrix \mathbf{Hc} has full column rank (FARRELL, 2006).

One might think that given the amount and variety of sensor observations, the full column rank of \mathbf{Hc} condition is always guaranteed. For instance, in a C-EKF estimation with three vehicles, the state vector would contain 27 state parameters, so at least 27 linearly independent measurements are needed to obtain a solution. This number seems fairly feasible, provided that sensor fusion algorithms are able to combine thousands of measurements in a single estimation. However, plane-based estimations lead to exemplary circumstances that can potentially lead to badly conditioned, or even to rank deficient Jacobian matrices.

In the experiment described in this section, the identification of vertical planes leads to the fact that the c parameter of the plane equation (cf. Eq. (5.30) and (5.31)) is always (almost) 0. This affects the computation of the \mathbf{Hc} coefficients, since

$$\frac{\partial g}{\partial \Delta U} = c. \quad (5.46)$$

As a result, the coefficients that belong to the up-component columns of sub-matrix $\bar{\mathbf{A}}$, are also close to 0 (given rounding errors), leading to bad conditioning (or even full deficiency if forced to be exactly 0). Thus, if only exteroceptive sensor measurements are considered, a parameter reduction must be applied to the state-vector in order to prevent a rank deficiency in \mathbf{Hc} .

The analysis of the filter observability reaches a special significance in SLAM approaches, provided that not only the vehicle parameters but also the plane parameters are being estimated. Besides the above mentioned general event, additional features must be discussed in terms of observability for the plane parameter estimations. Some of them are derived from the fact that the number of generated laser scanner and camera measurements is significantly lower than in real cases (see Section 5.1.3). Then, the intersection with the planar elements might cause their distribution to be highly inconvenient although the number of points is sufficient for the estimation of the plane parameters. One example is given if only a vertical or horizontal bundle of rays intersects with one

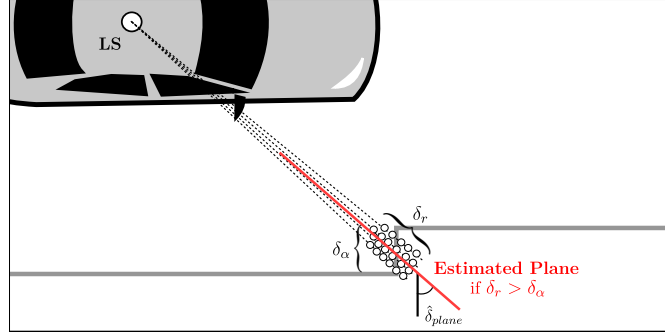


Figure 5.11: Observability problem diagram, where the error in the ranging measurements (δ_r) is higher than the horizontal distribution of ray bundles (δ_α), producing a biased estimation ($\hat{\delta}_{plane}$) of the plane (red) relative to the true orientation given by the 3D city model (gray).

plane. In this case, the sub-matrix from \mathbf{H}_π (cf. Eq. (5.44)) that contains the coefficients of the respective measurements is rank-deficient, since the problem of estimating a plane that contains n points linearly distributed has infinite solutions. Another example comes by the fact that the laser scanner measurement error is applied only to the range measurements (assuming perfectly calibrated horizontal and vertical angles). This results in a situation (depicted in Figure 5.11) in which the deviations caused by the error applied to the range measurements have a higher magnitude than the horizontal/vertical distribution of ray bundles, leading to the computation of the plane equation in the ray direction, and subsequently, introducing serious biases in the estimation.

In order to guarantee the filter observability throughout the complete trajectories, planes are not estimated if their \mathbf{H}_π is rank-deficient, and if they are to be estimated with less than 36 points (at least three LS columns, guaranteeing that $\delta_r < \delta_\alpha$).

Integrity Analysis

For a first overall approximation to the analysis of the system's integrity, the results obtained from running the filter as a localization approach (**L**), C-SLAM (**C-S**) and localization approach with landmarks uncertainty ($\sigma_{rot} = 1^\circ$, $\sigma_{sh} = 0.1$ m, **RS** results in Table 5.7) are depicted in Figure 5.12 expressed in terms of the Stanford diagram (cf. Figure 2.1) (TOSSAINT ET AL., 2006). To illustrate the integrity diagrams, the AL and PL are computed following the methodology described by REID ET AL. (2019) (see Section 2.3.1). To enhance the readability, both these statistics are computed under the assumption that a vehicle with width $w_v = 2.5$ m and length $l_v = 5.5$ m navigates in a bounding box of $w_r = 6$ m and $l_r = 9$ m, what leaves an alert limit AL of 1.75 m. Although these are in general fairly unrealistic values, it benefits the identification of general patterns that subsequently enable the comparison of the results with the above-mentioned filtering strategies. Later, although Table 5.7 shows variations in the RMSE of each vehicle, these differences are in general at the millimeter or centimeter level. Since these differences are in general several orders of magnitude lower than the fixed AL, only the results obtained with vehicle 1 are displayed as representative results for the complete set of vehicles.

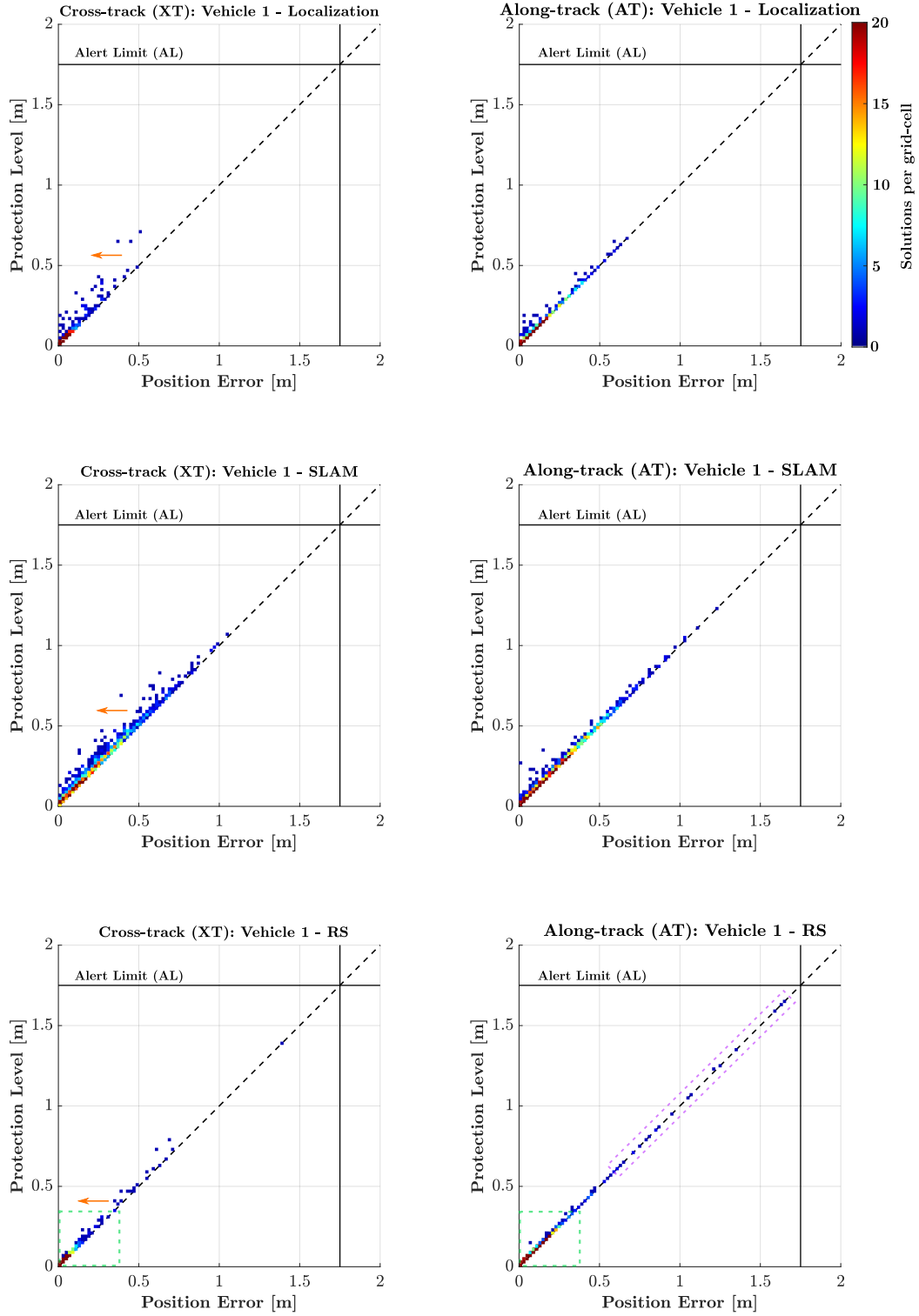


Figure 5.12: Integrity Results. The filter is run as a localization approach (top row, in accordance with **L** results in Table 5.6), C-SLAM (middle row, in accordance with the **C-S** results in Table 5.6), and as a localization approach considering uncertainty on the landmarks (bottom row, in accordance with **RS** configuration in Table 5.7). Again, the results are expressed by means of XT (left column) and AT (right column) deviations relative to the true solution.

In Figure 5.12, particular circumstances can be identified, regardless of the selected configuration. First, the computation of the PL using the deviations of the state parameters relative to the reference, leads to the fact that the magnitude of the PL is in most cases similar to the magnitudes of the deviations themselves, but always reflecting results in the *nominal operations* region (cf. Figure 2.1). That is the reason why mostly all graphs contain the solutions close to the dashed line that bisects the area under the AL in two different sections.

Second, the solutions are displayed in a grid with cells of 1 cm^2 , and color-coded by the number of solutions within the grid cell. This reveals the zones of the grid with a larger concentration of solutions, which lead to the perceptions of the most probable solutions for each configuration and each parameter. The localization approach (first row) shows most of the dark red tones in the lower part of the *nominal operations* triangle, showing both low PE and PL. The fact that the overall accuracy in the XT is higher than in the AT direction can be immediately seen by the fact that in the AT diagram (top right), the dark red pixels reach further into the higher PE direction than the XT diagram (top left). This event is easily identified also for the **C-S** and the **RS** results. Also, it is reflected on the fact that the colored points are more scattered in the direction of the orange arrows (lower PE).

Furthermore, comparing the results from the top and middle rows, it is possible to evaluate the effect that the consideration of unknown landmarks has on the state estimation. The results from the SLAM approach show the grid cells that contain the higher number of solutions (expressed in red tones) are grid cells with PE and PL in most cases lower than 0.4 m. However, the less accurate solution w.r.t. the solution obtained from the localization approach is reflected in the shape of a higher number of solutions in the interval between 0.5 m and 1 m (almost empty for the localization approach).

The localization solution with uncertainty on the planes (bottom row) shows a similar behavior to the full localization approach (top row). Although the higher amount of solutions are in the decimeter level, both for PE and PL. Here, a general loss of accuracy is shown within the dashed green rectangles, and PE solutions are closer to the PL and the solutions are in the limit to the *misleading information* area. More important in this discussion is the detection of epochs with a high amount of error (pink dashed rectangle in the bottom right diagram). These grid cells are colored in dark-blue tones, showing a low frequency of appearance (less than five solutions in every pixel). This demonstrates that the consideration of uncertainty enhances the effects derived from inadequate fixed processing parameters in dynamic time-invariant estimations. Nevertheless, all these solutions are contained in the *nominal operations area*, guaranteeing that the solution is always contained on the interval defined by the AL.

Lastly, the previous discussion can be referred to real integrity standards in order to obtain a representative idea about the degree of conformity of the described simulation (with the current configuration) with the real requirements. To achieve this task, REID ET AL. (2019) establish a classification of AL based on different vehicle and road sizes. In this way, the alarm would indicate that the vehicle has exceeded the road limits, thus a potentially hazardous estimation has been identified. Here, the AL are defined for an integrity risk of 10^{-8} (99.99999999%, or approx. 5.73σ),

assuming that the PE is Gaussian-distributed (not always the case). With these requirements, the AL defined are in the range of 0.4m. Taking into account this definition, it is possible to see that both results obtained with the localization approach fulfill this requirement, where 95% of the results are bounded in the interval of ± 0.15 m (confidence interval). Only around 0.5% of the observations would exceed the AL, and those are caused by the observability and stability problems characteristic in time-variant KF estimations (described in the *Precision* and *Observability* sections of this chapter). However, this is not the case for the SLAM results, since the PE is mainly dominated by the GNSS measurements, and they contain sometimes really large errors. Thus, the importance of the introduction of geo-located map information as prior knowledge is again underlined. Also, in absence of map information, the GNSS + IMU solution must be very efficient in order to fulfill the integrity requirements defined in REID ET AL. (2019).

5.3 Discussion

In this chapter, the different components of the developed simulation framework were discussed in detail. Lastly, a sample run in a complex scenario was executed in order to identify the specifics of dynamic network estimation.

On the one hand, the simulation framework contains different methodologies to model the vehicle dynamics, the environment, and sensor observations. Given the numerous methodologies available to model each simulation framework unit, their strengths and limitations were listed in each of its dedicated sections. Subsequently, the sensor observations were fused in a Collaborative-Extended Kalman Filter (C-EKF). The collaborative navigation methodology is implemented as a plane-based centralized approach, where the measurements carried out by different sensors, mounted in different vehicles, are fused in the one algorithm estimating the states from the complete set of vehicles simultaneously. Also, the C-EKF can be run following different strategies, depending on the degree of geolocation knowledge assigned to the detected elements of the environment. If the detected elements of the environment are related to (assumed to be) perfectly geolocated map elements, the filter is run as a localization approach (Section 5.1.4). However, the knowledge about the environment is not always available, forcing the vehicles to perform the task of mapping the environment while simultaneously locating themselves in it in a C-SLAM approach (Section 5.1.5). Finally, the map elements are normally associated to uncertainties. When combined with absolute measurements (e.g. GNSS measurements) this uncertainty must be considered. As a result, the presence of the landmark is guaranteed by the map, although with an appropriate uncertainty, leading to the execution of the filter as a localization approach with landmark uncertainty (Section 5.1.6).

On the other hand, the simulation framework and the designed algorithm were tested in a refined sample scenario, with three vehicles navigating in an urban area defined by the 3D city model. This model of the environment is essentially built up with planes, hence its suitability for the evaluation of the plane-based estimation. However, the absence of a ground plane reveals a permanent insufficient geometry for the estimation of the up-component of the position and the roll and pitch components

of the attitude. With this in mind, the results obtained with the three different strategies were compared, focusing mainly on the analysis of the 2D positioning and heading parameters. Here, it is possible to see that the most accurate and precise results are obtained by the localization approaches regardless of the landmark uncertainty, thus underlining the importance of the introduction of highly accurate map elements in the estimation to obtain a robust solution. In SLAM, the accuracy of the system is dominated by the GNSS measurements, provided that they are the only anchor to the global frame. With this strategy, the overall accuracy and precision of the estimations depend on the accuracy and precision of the initial pose of the vehicle.

In the epoch-wise analysis of the results, the dynamic character of the scenario is reflected in the time series of the estimated parameters. It can be seen in Figure 5.10 that the accuracy and precision of the estimated parameters vary from epoch to epoch, depending on the geometry of the detected landmarks, and on the vehicle dynamics. Both factors can be directly related to the system stability. Here, it was observed that in such a dynamic scene, the C-EKF solution rapidly becomes unstable. This arises due to different factors:

- The utilization of a linear constant velocity and constant turn rate is heavily disrupted in turning and accelerating/breaking maneuvers.
- Bad observability conditions of the estimation in some epochs are enhanced by the choice of unsuitable process noise.

The high complexity of the scenario in terms of vehicle dynamics and environmental model characteristics makes it difficult to visualize and quantify the epoch-wise effects caused by these issues. As a result, individual scenarios are designed to enhance the effects of different estimation matters, so that their effects can be evaluated and quantified.

6 Sensitivity Analysis of Dynamic Sensor Networks

In Chapter 5, the filter that constructs the foundation for the study of dynamic networks is introduced. Obviously, in the transition from geodetic to dynamic networks, the biggest challenge arises from the necessity to understand the effects caused by the motion of the nodes within the available adjustment techniques. However, the physical movement of the nodes is not the only factor in this matter, but the appropriateness of and the dependency between processing parameters must as well be considered as a crucial requirement. One example was already diagnosed in Section 5.2.2, where the utilization of fixed processing parameters in a time-variant scenario exposes suboptimal estimations. In this chapter, the analysis of the dynamic network problem is extended by assessing the sensitivity of the adjustment to the different configurations. To achieve this goal, Section 6.1 offers an overview on the geodetic network optimization groundwork, continuing the discussion about the issues that would emanate if these techniques were applied. Then, MC based experiments are presented in order to evaluate the performance of the different sensor combinations (Section 6.2) and the filter sensitivity to processing parameters (Section 6.3). The findings in this matter lead to the identification of the actions that maximize the adjustment performance in terms of the criteria defined in Section 2.3.1, and at the same time, reduce the effects caused by suboptimal epoch-wise estimations.

6.1 Geodetic Network Optimization Problems for Dynamic Networks

GRAFAREND (1974) classifies the network optimization in four design problems, depending on the fixed and free parameters of the optimization (see Section 2.3.3). Taking into account these definitions, a link between the ZOD and FOD and some events discussed in Chapter 5 can be easily defined.

First, the ZOD problem (also known as *datum problem*) is defined as the problem to geo-reference the network in a specific reference frame. Given the analysis carried out in Section 5.2.2, the evaluation of our collaborative scenario in terms of accuracy deals with the analysis of the network nodes' deviations relative to the reference trajectory computed in the local topocentric frame. The degree of conformity (level of accuracy) obtained depends on the amount of prior information introduced in the filter in terms of absolute coordinates, thus illustrating the connection to the filter observability (see Section 5.2.2). From this set of results two conclusions can be drawn:

1. The localization approach (even under the consideration of landmark uncertainty, like e.g. shown by Table 5.7) yields the most accurate results, revealing the map as a fundamental piece of information to anchor the network to the local topocentric frame. This statement is supported by the SLAM results, in which the presence of exteroceptive sensors does not induce a significant increase of accuracy with respect to the GNSS+IMU loosely coupled solution.
2. If the map is not introduced as prior knowledge in the estimation, the absolute GNSS position and velocity measurements are the main anchor measurements that provide the network with the necessary information for its location in the desired reference frame. In a SLAM approach, where no GNSS measurements are considered, the filter would yield a solution that depends entirely on the accuracy of the first position and orientation of the vehicles, provided that the solution is primarily computed with exteroceptive sensor measurements (relative positioning).

Second, the FOD problem can be defined in geodetic network optimization as the task to find out the optimum position of the nodes given a fixed configuration. This task does not necessarily have to be related with the ZOD in dynamic networks, since relative inter-nodal measurements used for the definition of the network (to other vehicles or elements of the environment) can be expressed in the ego-vehicle frame itself, as it is done in most of the decentralized collaborative approaches. Then, the network could be considered an (almost) rigid body with a particular position in a well known geodetic frame. Translating the parameters shown in Table 2.1 from the GMM notation to the C-EKF notation shown in this thesis, the FOD is carried out by considering \mathbf{R}_k and \mathbf{P}_k as fixed matrices, whereas the \mathbf{Hc} matrix is free. This, together with the configuration displayed by Tables 5.3 and 5.5 allows to understand the C-EKF filter as a FOD problem. In Table 5.3, the fixed standard deviation values used as weights in \mathbf{R}_k are displayed. The characterization of $\mathbf{Q}_{\hat{x}\hat{x}}$ in geodetic networks (Table 2.1) as a fixed parameter implies that the target of the optimization problem is formulated in its elements or as a function of $\mathbf{Q}_{\hat{x}\hat{x}}$. However, \mathbf{P}_k in dynamic networks (and more specifically in time-variant systems) is always computed as a function of the predefined measurements, detected landmarks and their noise (\mathbf{R}_k). This situation leads to a change in the characterization of \mathbf{P}_k , from a fixed parameter in the definition of GRAFAREND (1974) to a free parameter in dynamic networks. In steady-state KF filter estimations (SIMON, 2006), the system is time-invariant, and hence \mathbf{P}_∞ and \mathbf{K}_∞ can be considered to be partially fixed, since they are kept constant throughout the complete estimation time but they must be computed with the Discrete Algebraic Riccati Equation (DARE), which is a function of \mathbf{H}_k and \mathbf{R}_k . Finally, \mathbf{Hc}_k is computed as a function of $\hat{\mathbf{x}}_k^-$, being free regardless of the computation methodology.

The SOD problem (also known as *weight problem*) consists of the computation of the optimum weights for the estimation. However, the approaches described in the discussed literature are based in the definition of criterion matrices in GMM estimations. In this thesis, a KF-based methodology is used instead of a GMM. As a consequence, the solution using criterion matrices would force the introduction of iterative methodologies to compute \mathbf{P}_k^+ and \mathbf{K}_k , increasing the computational time, and affecting the effect that other parameters (e.g. \mathbf{Qd}) have on the estimation. The application of criterion matrices is smoother in steady-state estimations, given that the computation of \mathbf{P}_∞ and \mathbf{K}_∞ can be done in advance, and subsequently, they both remain unaltered epoch-

wisely. Nevertheless, these techniques are in general bypassed in this thesis, given that the steady-state estimation itself consists of a suboptimal estimation technique (SIMON, 2006). Moreover, given that the weights are also used to define the quality of the sensor measurements, a MC-based methodology is presented in Section 6.2 targeting the evaluation of the impact that the different sensors (with different measurement quality) have on the state estimation. Also, the sensor measurement precision can be introduced according to real sensor specifications, establishing in this way a relation to their cost (low-cost \rightarrow high-end), and expressing the results obtained in terms of cost efficiency relation of each sensor combination.

Furthermore, it is certainly possible to associate the Third Order Design (THOD) problem with the SOD as it is being understood in this thesis. Obviously, the precision of the used sensors produces an impact on the state estimation, but also does the variation in the number of measurements considered, as well as their geometric characteristics. Thus, the evaluation of the best sensor combinations would never be complete without the detailed analysis of the impact each sensor has on the state estimation.

Finally, in addition to the four geodetic network optimization problems, a special issue related with the node dynamics should be considered in dynamic networks. In dynamic systems, the movement of the object is defined by a motion model, and its discrepancies with the real physical model described by the object are compensated within the system by the process noise. The amount of fluctuation expected between the motion model and the real trajectory is defined by the PSD, and can be selected depending on the target of the estimation. Here, the negative effects of suboptimal process noise PSD have been already diagnosed in Section 5.2.2. Hence, a simulation scenario is presented in Section 6.3, where the sensitivity of the estimation to suboptimal PSD values is evaluated by means of Monte Carlo methodologies.

6.2 Best Sensor Combination

In the advent of autonomous navigation, a wide spectrum of sensors is developed and commercialized under numerous specifications and prices. This situation offers the users a great flexibility to select the most suitable sensor combination to fulfill the desired target. The principle of multi-sensor fusion is based on the association of different sensor measurements with different characteristics within the same algorithm in order to overcome the weaknesses of each individual sensor. This statement might easily lead to the assumption that if a large amount of sensors is used, the understanding of the environment and the overall robustness of the vehicle localization improves, rather than if only a few sensors are used. However, this rather sensible assumption (*more information in \rightarrow better result out*) is not always fulfilled. In general cases, the utilization of a larger amount of sensors is accompanied by an increase in the overall cost and complexity of the multi-sensor system, which grows significantly in collaborative scenarios. As a result, a good evaluation of each sensor's strengths and limitations can help to optimize the overall cost (both in the computational and economic sense) of the system, while still achieving the desired performance. An adequate

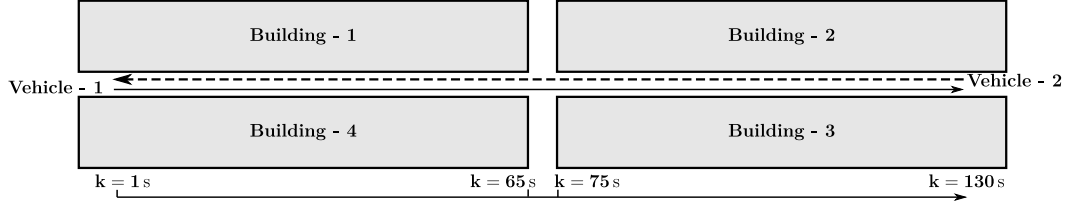


Figure 6.1: Scenario used for the identification of the best sensor combinations.

sensor combination would not only help to facilitate the commercialization, but also to increase the number of suitable applications of the final product.

In multi-sensor fusion methodologies, the intrinsic geometric and physical characteristics of every sensor govern the role that each particular sensor plays in the estimation. One example can be obtained in the analysis of the sample scenario in Section 5.2.2 (Table 5.6), where the overall results from running the filter as a localization and as a SLAM approach are compared. In spite of using the same sensor architecture, significantly different results are obtained depending on the level of prior knowledge from the environment introduced on the adjustment. In that case, the proprioceptive sensors feed the system with the necessary information to anchor the dynamic network to a well-known geodetic frame (in other words, provide information for the ZOD *datum* problem), and the exteroceptive sensors collect the additional information about the environment. However, the relative measurements carried out with the exteroceptive sensors are not sufficient to geolocate the vehicle in the absence of proprioceptive sensors. If the geolocation of the detected landmarks is known (localization), the exteroceptive sensor measurements are able to use this knowledge to correct the position of the object in which they are mounted, an amount proportional to the appropriateness of the landmark layout. On the contrary, the SLAM algorithm relies entirely on the proprioceptive sensors for adequate georeferencing of the objects involved in the navigation scenario (both fixed and dynamic).

With this in mind, the study on the impact induced on the state estimation by each individual sensor is carried out. Here, the analysis is divided into two different directions. On the one hand, it is crucial to obtain information about the outcome from running the filter with different sensor architectures. On the other hand, in addition to the sensor architectures (and their role within the estimation), the actual market provides a vast range of sensors with different qualities. Therefore, the sensitivity of the estimation to the different sensor combinations would never be complete without the consideration of the sensor measurement quality in terms of precision.

Hence, an MC-based experiment is designed in order to evaluate the sensitivity of the estimation in terms of the two previously discussed features.

6.2.1 Scenario and Sensor Setup

First, the focus is drawn to the design and implementation of an scenario that enhances the effects caused by the sensor measurements, and mitigates the inconsistencies caused by the other features of the filter (e.g. vehicle dynamics or motion model). This is achieved by the simulation of two

Table 6.1: Sensor measurement standard deviation and update rate: best sensor configuration experiment.

<i>Sensor</i>	<i>Measurement</i>	σ	<i>Update Rate</i>
GNSS	$\mathbf{p}_{\text{GNSS}}^t$	2 [m]	1 Hz
	$\mathbf{v}_{\text{GNSS}}^t$	0.2 [m/s]	1 Hz
	V2V	2 [m]	1 Hz
IMU	$\phi \ \theta \ \psi$	0.0001 [rad]	1 Hz
Laser S.	r	0.01 [m]	1 Hz
Cameras	\mathbf{p}_{cam}	0.01 [m]	1 Hz

trajectories of approx. two minutes each (130s), where the vehicles are assumed to navigate in an urban area describing two perfectly straight trajectories at a constant velocity, in opposite directions. Also, a rather elementary model of the environment is introduced, with four perfectly rectangular blocks of buildings (cf. Figure 6.1). The advantages provided by the simulation in this scenario are twofold:

- The constant velocity and constant turn rate described by the trajectory neglect the inconsistencies between the decoupled linear motion model selected and the actual motion of the vehicles, mitigating the importance of the process noise.
- The simplicity of the motion model outlines two predominant environmental geometries (i.e. urban canyon and intersection), facilitating the identification of the events caused by the geometric characteristics of the laser scanner and stereo cameras individually.

As a result, the isolation of the effects caused by the measurements themselves is guaranteed, being able to interpret the results disregarding the possibility that some of the features that are the object of the study are covered by the effect of other filter components.

Second, the error model established in the update is simplified significantly from the configuration shown in Section 5.2.1, aiming to facilitate the analysis. Initially, the GNSS measurement noise (both for positioning, velocity and V2V) is not computed as a function of the satellite geometry, and it is substituted by random Gaussian noise with the standard deviations shown in Table 6.1. In addition, the uncertainty of the environmental model elements is eliminated and the strap-down navigation tool is neglected, assuming the attitude measurements also to be only affected by random noise. Finally, in order to highlight their performance in urban areas, the quality of the laser scanners and stereo cameras is increased to the centimeter level.

The importance in the selection of suitable process noise values for the velocity and attitude decreases given the stationary characteristics of the vehicle dynamics, making the decoupled linear model shown in Eq. (5.23) perfectly suitable for the estimation. The values chosen are displayed in Table 6.2. Furthermore, the initial uncertainties of the estimation are adapted to the actual measurement noise model (see Table 6.3).

Finally, it is essential to define a suitable simulation strategy for the evaluation. In this first experiment, the filter is run 200 times as a localization approach with each of the sensor setups

Table 6.2: Random walk process noise spectral density: best sensor configuration experiment.

<i>Parameter</i>	PSD
Velocity (\mathbf{q}_{vel})	0.01 [m ² /s ³]
Attitude (\mathbf{q}_{att})	0.01 [rad ² /s]

Table 6.3: Initial variance of the state parameters: best sensor configuration experiment.

<i>Parameter</i>	P₀
Position	2 [m ²]
Velocity	0.50 [m ² /s]
Attitude	0.1 [rad ²]

Table 6.4: Sensor configurations

S	GNSS	IMU	Laser S.	S. Cameras	V2V
1	✓	✓	✓	✓	✓
2	✓	✓	✓	✗	✓
3	✓	✓	✗	✓	✓
4	✓	✓	✗	✗	✓

shown in Table 6.4. In each run, the measurement noise standard deviations are fixed, but the shared magnitudes are varied so that the effects that an individual error applied to an individual measurement has on the state estimation are generalized. As it can be seen from Table 6.4, the GNSS receiver and the IMU are always used, keeping it as the core sensors that collect the basic information to anchor the network (V2V measurements also maintained in all sensor setup) to the local topocentric frame. Then, **S-1** (sensor setup 1) assumes two vehicles fully equipped and is used as a reference solution, provided that it is expected to be the best solution in terms of both accuracy and precision. Subsequently, setups **S-2**, **S-3** and **S-4** neglect the stereo cameras, laser scanner and both exteroceptive sensors, respectively. In this way, the individual impact of each sensor measurement on the estimation is isolated, and interpretation of the results is made easier.

6.2.2 Sensitivity Results

Figure 6.2 illustrates the results obtained from the previously described MC simulation (Vehicle-1). The parameters selected for the analysis are the 2D (top row) and Along-Track (AT) (bottom row) position deviations of the estimated parameters relative to the true parameters. Then, the epoch-wise mean deviations (left column) and standard deviations (right column) of the 200 runs are displayed in solid red, dashed green, solid blue and solid black for each configuration, respectively. Looking into any of the four graphs displayed, the influence of the landmark layout can be easily identified. At the beginning, the filter takes approximately 20s to converge into a rather stable solution. Afterwards, the accuracy of the solution stays slightly below 0.5m in both AT and 2D estimations until 55s after the start. In this time interval, both vehicles navigate in an urban canyon

with two planes lying perfectly parallel to the direction of driving, producing an outcome in the XT direction at the sub-millimeter level in terms of accuracy and precision for any of the solutions computed with at least one exteroceptive sensor, thus it is not shown. Given that the estimation is dominated by the exteroceptive sensors and no additional source of uncertainty (texture of the facades, outliers or oclusions) are considered, the results obtained can be easily assessed. In the urban canyon situation, approx. 2600 exteroceptive sensor measurements (n) are processed, each of them with $\sigma = 0.01$. Thus, given that

$$\epsilon = \frac{\sigma}{\sqrt{n}} = \frac{0.01}{\sqrt{2600}} = 1.96 \cdot 10^{-4}[\text{m}], \quad (6.1)$$

the influence of the laser scanner and stereo camera measurements is demonstrated. Immediately afterward, the exteroceptive sensors are able to identify two additional planes that lie perfectly perpendicular to the direction of driving (urban intersection, characterized with a gray background), leading to a sudden increase in both accuracy and precision of the results. It is precisely under this geometric conditions where the influence of each individual sensor is evident. The first event that captures the attention is the fact that the **S-1** (solid red) and **S-2** (dashed green) solutions are almost equivalent (cf. Table 6.2). This event reveals the dominance of the laser scanner measurements with respect to the other sensors, since the addition of the stereo cameras to the laser scanner solution only represents a marginal improvement to the overall solution (sub-millimeter level differences). This statement is also confirmed by the fact that the area of sudden improvement illustrated by the **S-3** (without laser scanner, solid blue line) solution is significantly shorter (approx. 17 s) than the other solutions (approx. 30 s). In this time intervals, the 360° field of view of the laser scanner allows not only to detect the landmarks that lie ahead, but also behind the vehicle at every point in time. This is not the case for the pair of stereo cameras, that operate with a significantly lower field of view. Although the vertical field of view is significantly higher than with the laser scanner, this does not allow the identification of additional landmarks, given that the building facades are continuous and vertical until the rooftop, which cannot be detected with land-driven vehicles. The shortcoming caused by the stereo pair field of view can be tackled with the addition of further stereo pairs oriented in different directions, although increasing the overall cost of the multi-sensor system for the addition of sensor measurements that do not produce a significant increase in the performance of the adjustment (considering only its geometrical characteristics). Once the urban intersection is passed, showing an epoch-wise progressive decrease of sensor measurements intersecting with the planes that lie perpendicular to the direction of driving, the vehicles again enter an urban canyon situation till the end of the scenario. In this section, the solution goes back to the levels of accuracy and precision shown in the first segment of the scenario. Finally, it is worth mentioning that the GNSS + IMU solution remains steady for the rest of the trajectory, with lower overall accuracy and precision, provided that it remains unaffected by the environmental geometry.

Moreover, the environmental geometry is also the reason that prevents the evaluation of a sensor setup in which the GNSS measurements are omitted. In plane-based estimations, the urban canyon geometry is insufficient for the positioning in the AT (as shown in 6.2 results). Thus, the absence of GNSS leads to immediate divergence of the filter in AT direction, until the urban intersection geometry is reached. With this configuration, the errors exceed the two meter level already a few

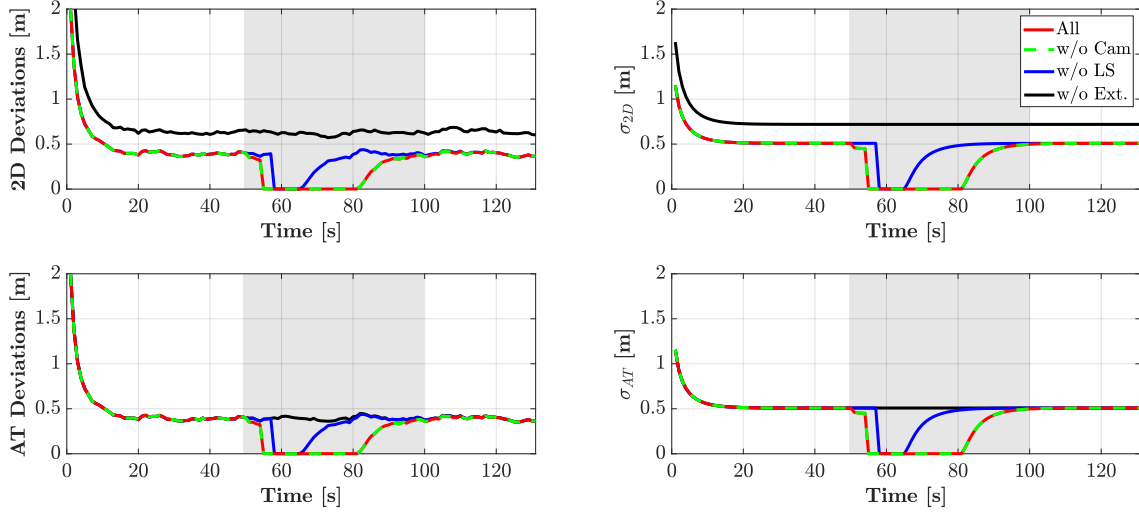


Figure 6.2: Varying sensor results of Vehicle-1. The results in the AT direction are expressed in absolute value to facilitate the readability of the illustration.

seconds after the start, thus compromising the visualization of the results obtained with a different sensor configuration.

In this simulation, the overoptimistic standard deviation selected for the attitude measurements leads to results at the level of 10^{-6} degree, aiming to neglect the influence of the vehicle dynamics on the simulated scenario. However, the importance of the IMU measurements is discussed in detail in the simulation carried out in the following Section 6.3.

Lastly, it is important to highlight the absence of qualitative information in the sensor measurement simulation, that affects crucially the evaluation of these results. Taking into account the previous description, one might think that if a laser scanner with this geometric characteristics (360° field of view and 16 lines of vertical aperture) is considered, the stereo cameras are not needed. However, the analysis does not consider the intrinsic qualitative information that is provided by the measurements such as RGB values that could help in feature recognition (laser scanners lack this information), multi-spectral information, etc. Therefore, this set of results may be interpreted only as an analysis by means of the sensor geometry, and only under the selected configuration. Simulations with a line scanner, monocular cameras, identifying landmarks represented as point features in the map or different filter designs would yield completely different results.

Sensor Quality

In the previous set of results, the filter sensitivity to different sensor combinations are evaluated. This serves not only to underline again the fact that the accuracy and precision of the system are dominated by the exteroceptive sensors in localization approaches (assuming the 3D city model to be known), but to validate the algorithm as well. In contrast to the sample run carried out in Section 5.2.2, the simplicity of this scenario enables the effortless recognition of the effects caused by the two prevailing environmental geometries, and the typical behavior of the EKF estimations (e.g.

Table 6.5: Overall Results of the MC simulation with varying sensor architectures. The overall RMSE and mean σ obtained from each of the four configurations introduced in Table 6.4, are displayed for the 2D, AT and XT position parameters in [cm].

		S-1	S-2	S-3	S-4
RMSE	2D	42.206	42.202	45.082	75.344
	AT	42.206	42.202	45.082	47.030
	XT	0.007	0.007	0.069	49.189
σ	2D	40.235	40.236	47.742	74.415
	AT	40.235	40.236	47.739	52.619
	XT	0.006	0.006	0.086	52.619

typical convergence time and stability in a rather steady estimation). However, although different sensor architectures are evaluated, the sensor measurement quality remains an open question.

In order to obtain answers, a specific MC simulation is designed using the same scenario as described in Section 6.2.1. Now, the focus is drawn to the assessment of the observation quality instead of the impact of the sensor itself. This is introduced in the adjustment by means of the standard deviation values used to model the measurement noise, which can be selected in accordance to the sensor specifications. It is worth remembering that the exteroceptive sensors show, besides inliers, outliers caused by reflections or occlusions. Using the actual model of the environment, the question of a specific outlier distribution is a troublesome task to accomplish. Consequently, both the outlier detection and the effects that undetected outliers have on the adjustment (internal and external reliability) are dismissed in this analysis, leaving the study of inliers generated by different sensors as the only feasible feature to be evaluated.

The MC-based experiment is implemented by defining a multi-variate domain, where each dimension is defined by the interval that contains feasible values, following an approach like the one described by BOFFI (2018), although with a higher dimensionality. First, this scenario contains the simulation of two trajectories, that describe the movement of two vehicles that navigate in opposite directions in an urban scenario describing a perfectly straight path at a constant velocity. Due to this situation, the necessity to include the IMU orientation, the GNSS velocity and the process noise parameters in the analysis is bypassed. Second, the influence of the V2V uncertainty is deeply analyzed in Chapter 7. As a result, the standard deviation of the inter-vehicle measurements and standard deviation of the IMU measurements are fixed in the experiment. Subsequently, the domain for the creation of the random MC samples is a three-dimensional parameter space, where the first dimension is defined by the laser scanner measurements standard deviation, the second is defined by the standard deviation of the stereo camera measurements and the third by the standard deviation of the GNSS measurements. The lower and upper bounds of the intervals are symbolically selected (not in accordance to any real sensor specifications) but in a pessimistic way so that it is guaranteed that all feasible values are contained in the parameter domain. With this in mind, the interval for the exteroceptive sensors consider observations with white noise in the interval $0.05\text{ m} \leq \sigma_{\text{LS}}, \sigma_{\text{CAM}} \leq 1.5\text{ m}$, and $0.4\text{ m} \leq \sigma_{\text{GNSS}} \leq 10\text{ m}$ (like e.g. RTK without ambiguities fixed). The error modeling under the lower bounds is considered to be overoptimistic

Table 6.6: Sensor measurement standard deviation and update rate: sensor quality assessment

<i>Sensor</i>	<i>Measurement</i>	σ	<i>Update Rate</i>
GNSS	$\mathbf{p}_{\text{GNSS}}^t$	$[0.4 - 10] \text{ [m]}$	1 Hz
	$\mathbf{v}_{\text{GNSS}}^t$	0.2 [m/s]	1 Hz
	V2V	2 [m]	1 Hz
IMU	$\phi \ \theta \ \psi$	0.0001 [rad]	1 Hz
Laser S.	r	$[0.05 - 1.5] \text{ [m]}$	1 Hz
Cameras	\mathbf{p}_{cam}	$[0.05 - 1.5] \text{ [m]}$	1 Hz

(adding to the fact that no outliers are generated), and over the upper bound the errors could be assumed to be outliers. The summary of the measurement noise configuration can be seen in Table 6.6.

As a last step of the simulation scenario definition, the filter is run 4000 times, each of them with a random combination of 3D values $s \in V^3$ (where $V^3 = \{[\sigma_{\text{LS}}], [\sigma_{\text{Cam}}], [\sigma_{\text{GNSS}}]\}$). In contrast with the previous experiment, the shared error magnitude from the random vector is fixed, so that the same magnitude is applied to each measurement identically in each run, so that the only variable parameter is s . Consequently, a set of general statistics (mean standard deviation and RMSE) is obtained from each run/score.

Figure 6.3 illustrates the distribution of the samples within the parameter space, achieved with **S-1** (cf. Table 6.4) sensor assembly. Then, each sample is color-coded by the selected score (XT RMSE for the left panel, and AT RMSE for the right panel). Here, the main difference between those two diagrams is the range between the lowest and highest score for each parameter. The previously identified higher impact of the **S-1** sensor combination in the XT with respect to the AT estimation is visible, showing all samples colored in dark-blue tones in the left panel (XT), in contrast to the multi-color solution obtained in the right panel (AT). The diagram that displays the results in the XT demonstrates also the high performance of the filter in terms of accuracy, regardless of the sensor noise used, showing a difference of 0.019 m between the sample that yielded the highest accuracy (RMSE = 0.008 m) and the sample that yielded the lowest (RMSE = 0.027 m). In the AT estimation, the outcome is slightly different. First, the sample that yields the most accurate overall result (0.189 m) is $s = \{0.409, 1.079, 0.220\}$, and it coincides with the sample that contains the closest GNSS measurement standard deviation to the lower bound of the dimension domain. Then, it is possible to see a progressive loss of accuracy of the system in the Z-direction of the graph, or what is the same, as the GNSS measurement standard deviation increases. This situation reveals that the AT estimation is dominated by the GNSS observations. This is expected since the results shown in Figure 6.2 reveal that the plane layout in urban canyons does not have any impact on the AT estimation. The geometrical characteristics of this environment are only sufficient for the complete 2D estimation in the central section, where the planes that lay perpendicular to the direction of driving (urban intersection) are detected. In addition, it is possible to see that the laser scanner and camera measurement standard deviations do not have a big impact on the state estimation. In this cases, the abundance of observations, together with the overoptimistic symmetry

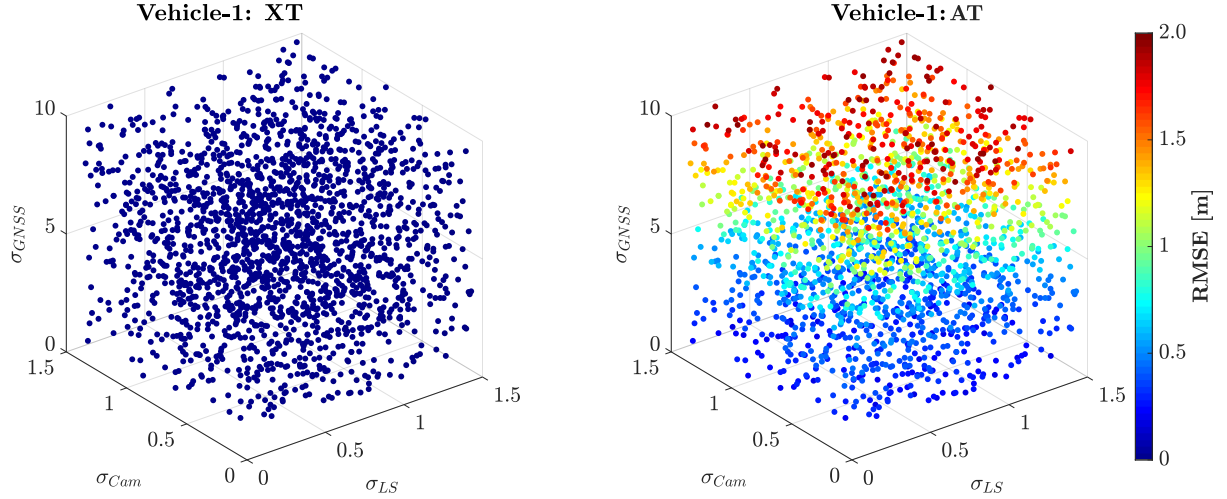


Figure 6.3: MC sample distribution in the parameter space for Vehicle-1 equipped with S-1 sensor combination (cf. Table 6.4). The samples are color coded by the RMSE obtained with the sample composed by the three parameter space directions for the XT (left panel) and AT (right panel). A different scale is used for the Z-direction for graph readability purposes.

of the environment mitigate the effects that the exteroceptive sensor measurement noise selected has on the estimation.

Visually, the previously identified tendency in the AT results seems evident in Figure 6.3. However, the visual interpretation of this graph depends on the illustration characteristics (e.g. perspective, color, size, etc.), and given the significant amount of information contained, the current display could be misleading. To avoid possible misinterpretations, the sensitivity is evaluated numerically.

If the 4000 three-dimensional samples are associated with their respective scores it is possible to analyze the possible correlations between the scores and the parameters. The correlation coefficients between two variables M and O with N scalar observations (with $N = 4000$ in our case) are computed with Eq. (6.2).

$$\rho(M, O) = \frac{1}{N-1} \sum_{i=1}^N \left(\frac{M_i - \mu_M}{\sigma_M} \right) \left(\frac{O_i - \mu_O}{\sigma_O} \right) \quad (6.2)$$

Therefore, the results for the four variables analyzed (σ_{LS} , σ_{Cam} , σ_{GNSS} and $RMSE_{AT}$) are shown in the following matrix:

$$\rho = \begin{bmatrix} 1.0000 & 0.0306 & -0.0265 & -0.0295 \\ 0.0306 & 1.0000 & -0.0134 & -0.0152 \\ -0.0265 & -0.0134 & 1.0000 & \mathbf{0.9771} \\ -0.0295 & -0.0152 & \mathbf{0.9771} & 1.0000 \end{bmatrix}. \quad (6.3)$$

Taking a look at the bold values displayed in Eq. (6.3), the high correlation between the third (σ_{GNSS}) and fourth ($RMSE$) dimensions of the defined domain (GNSS measurement standard deviation and sample RMSE) is exposed, indicating a strong sensitivity of the RMSE to small changes in the σ_{GNSS} . Then, the rather low values obtained for the cross-correlation of σ_{LS} and

σ_{Cam} reflect a low impact of those variables on the RMSE. Consequently, the large impact of the GNSS measurements in situations where the landmark layout is disadvantageous for the relative positioning is underlined. However, if clustering techniques (supervised or unsupervised) are to be applied in order to extend the analysis, a higher number of variables (like e.g. σ_{IMU} or σ_{V2V}) and a more complex scenario must be considered.

To conclude, it is possible to state that, in localization approaches and in favorable landmark layout situations, the simple addition of exteroceptive sensors is translated into a significant increase in the accuracy and precision of the adjustment. However, in disadvantageous landmark layout situations, the GNSS measurements take over as the most important observations in order to provide the system with the necessary accuracy to meet the navigation requirements.

6.3 Vehicle Dynamics Evaluation

It is well known that the estimation of the vehicle dynamics is a crucial task in multi-sensor fusion and intelligent traffic applications. SCHUBERT ET AL. (2008) survey numerous models with different degrees of complexity to investigate this topic. However, no matter the novelty of the motion model, it can never match the actual motion of the object flawlessly. Hence, it is necessary to evaluate how the inconsistencies created by imperfect motion models affect the state estimation, in order to identify suitable actions to guarantee the filter stability and accuracy. The EKF approach enables the compensation of the mentioned disruptions through the consideration of process noise in the prediction step. The designation of an adequate process noise model is a fundamental task in the estimation, provided that it does not only defines the amount of fluctuation allowed between the motion model selected and the actual movement of the vehicle, but also constraints the amount of variation that can be achieved in the correction step once the measurements are received. In other words, if no process noise is considered the predicted states are assumed to be perfect, and therefore, the state estimation is dominated by the prediction. On the contrary, a high process noise defines a vague prediction, transferring the burden of the estimation to the measurement update. For this reason, it is crucial to assess the Power Spectral Density (PSD) combinations that are suitable for the numerous ranges of maneuvers performed by the vehicles in urban scenarios.

The complexity of this task is constrained by the characteristics of the system at hand. In static and time-invariant estimations, the selection of adequate fixed processing parameters boosts the performance of the adjustment to the maximum (optimization), as the amount and distribution of the observational work remains stable throughout the complete trajectory. However, highly dynamic and time-variant systems (e.g. the scenario described in Section 5.2.2) require an epoch-wise evaluation since the distribution of observational work changes from epoch to epoch. Here, the selection of fixed values would not only produce a degraded solution in epochs where the process noise PSD combinations used are unsuitable for the measurement geometry or the vehicle maneuver, but also could lead to undesired biases caused by de-regularization of matrices (such as \mathbf{K}_k or \mathbf{P}_k^-) (ZHANG AND OLIVER, 2011).

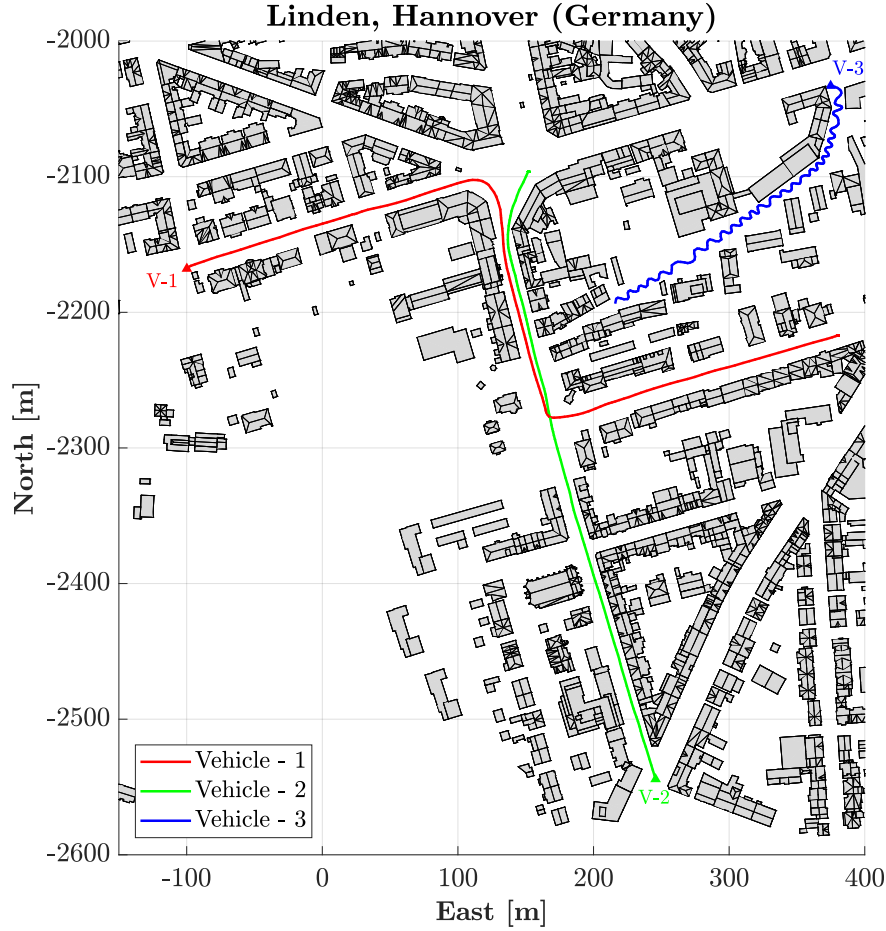


Figure 6.4: Scenario selected for the process noise to measurement noise optimization. The 3D City model is the selected model of the environment, focusing on an area of Linden neighborhood in Hannover (Germany).

In this section, MC-based approaches are presented, designed in order to find out suitable PSD combinations in dynamic time-variant and time-invariant systems. Also, the epochs with unstable estimations are pinpointed and associated with the vehicle scene, enabling in this way a diagnosis of the most vulnerable situations for inadequate process noise modeling.

6.3.1 Simulation Scenario and Setup

As in Section 5.2.2, the evaluation is built upon the simulation of an urban scenario where three vehicles navigate for approximately three minutes (cf. Figure 6.4). The selected model of the environment is the 3D city model with LoD-2, and the trajectories are generated from digitalized waypoints (see Section 5.1.1). Since the target is to evaluate the effect the process noise has on the estimation, each trajectory is generated with different degrees of turning maneuvers, and sequential accelerating and breaking maneuvers. It is possible to see in Figure 6.4 that the trajectory described by vehicle 1 contains two major turning maneuvers in different directions, describing an *s-shaped* trajectory. Vehicle 2, describes an almost straight trajectory, and vehicle 3 drives in south-west direction performing sequential turning maneuvers in a sinusoidal trajectory. If the

absolute amount of turning maneuvers is accumulated, vehicle 2 is the vehicle with the lowest value (1.35 rad), followed by vehicles 1 (5.09 rad) and 3 (57.28 rad). Simultaneously, vehicles 1 and 2 perform sequential breaking and accelerating maneuvers while turning, in order to achieve more realistic vehicle dynamics. Vehicle 3 remains at a fairly constant (low) velocity throughout the complete trajectory. In this scenario, the same sensors and their distribution in the vehicle frame (leverarm) as in Section 5.2.2 are considered.

This scenario is used in order to identify and evaluate an adequate process noise combination ($\mathbf{q}_{\text{vel}} - \mathbf{q}_{\text{att}}$) in Section 6.3.2, and also a suitable process noise to measurement noise relation ($\mathbf{q}_{\text{att}} - \boldsymbol{\sigma}_{\text{att}}$) in Section 6.3.3. Thus, the particular processing parameter configurations used for each purpose are described in each respective section.

6.3.2 Process Noise Assessment

In the experiment described in Section 5.2.1, the velocity and the attitude parameters are considered to be random walk variables, where the values of PSD that describe the magnitude of the process noise are fixed throughout the complete trajectory. In this example, different combinations were empirically tested, selecting for the evaluation the sample that yielded the most adequate results (cf. Table 5.4). However, it is obvious that this methodology is not entirely suitable to establish the optimum combination as the complete sampling of the domain has not been achieved. Additionally, the results from the sample experiment showed that the choice of a fixed PSD value for the process noise modeling is not suitable for dynamic environments, provided that the vehicles undergo a wide variety of maneuvers in a broad range of environmental situations.

In order to find an adequate process noise combination for the designed scenario, the MC methodology introduced in Section 4.4.2 is applied. This is because although a marginal idea about the behavior of the estimated parameters can be anticipated given the shape of the trajectories and the characteristics of the object dynamics, the dependencies between observations and the stochastic relationship between the parameters are too complex to define a suitable value for the complete range of maneuvers performed within a trajectory. However, it is possible to define the multi-variate domain (2D in this experiment) in which the optimum value is guaranteed to be contained, as in the methodology explained in section 6.2. Then, 4000 random samples are generated within the intervals described in Table 6.7 with a logarithmic distribution (cf. Figure 6.5). Afterward, the filter is run one single time with each sample (each time, the same seed for the random vector is used), obtaining the complete set of global statistics (e.g. RMSE or SD) and time series in each run.

To facilitate the analysis, the GNSS measurement noise model computed as a function of the DOP values is substituted by random white noise with the standard deviation displayed in Table 6.7. For the same reason, the filter is run as a localization approach (without uncertainty on the planes), and the strap-down navigation algorithm is neglected, using the roll, pitch and yaw/heading measurements in the update step, assuming that the results from the strap-down integration are obtained in advance. The update rate selected for these measurements is slightly higher (10 Hz)

Table 6.7: Sensor measurement standard deviation, random walk process noise spectral density and update rate: process noise assessment experiment.

<i>Sensor</i>	<i>Measurement</i>	σ	<i>Update Rate</i>
GNSS	$\mathbf{p}_{\text{GNSS}}^t$	2 [m]	1 Hz
	$\mathbf{v}_{\text{GNSS}}^t$	0.2 [m/s]	1 Hz
	V2V	2 [m]	1 Hz
IMU	$\phi \theta \psi$	2 [°]	10 Hz
Laser S.	r	0.1 [m]	1 Hz
Cameras	\mathbf{p}_{cam}	0.1 [m]	1 Hz
PSD	\mathbf{q}_{vel}	0 – 1.5 [m ² /s ³]	10 Hz
	\mathbf{q}_{att}	0 – 1 [rad ² /s]	10 Hz

Table 6.8: Initial covariance of the state parameters: process noise assessment experiment.

<i>Parameter</i>	\mathbf{P}_0
Position	2 [m ²]
Velocity	0.50 [m ² /s]
Attitude	0.3 [rad ²]

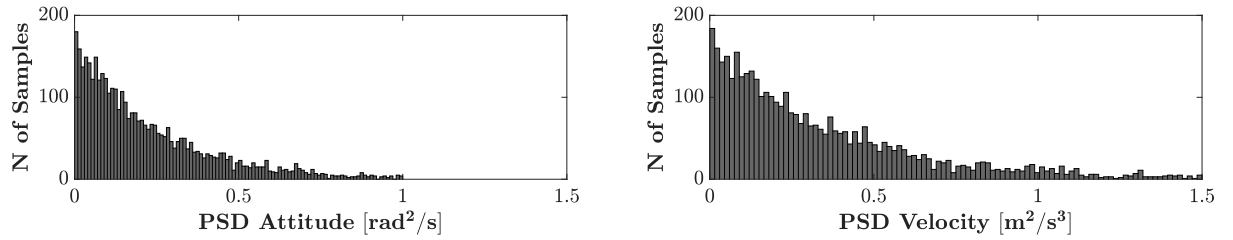


Figure 6.5: PSD attitude (left) and velocity (right) histogram samples.

than for the previous experiment (1 Hz). Otherwise, the disruption of the motion model during turning maneuvers (particularly in vehicle 3) introduce large errors that cannot be compensated; neither with the exteroceptive sensor measurements in the update step, nor with the process noise. Finally, the initial uncertainties of the state parameters are adapted to the new set of measurement noise standard deviation values (cf. Table 6.8).

Furthermore, the exteroceptive sensor measurements couple the position and attitude parameters in the update state. This, together with the fact that the position and velocity parameters are coupled within the prediction step, yields a scenario in which all parameters are coupled within the filter. For this reason, either the process noise considered for the velocity, or the process noise considered for the attitude, end up having an influence on all parameters. Should the exteroceptive sensor measurements not be considered, the dependencies and correlations between functional and stochastic variables change significantly. To evaluate these effects, the simulations are performed using two sensor combinations. One that combines simulated measurements from all available sensors (i.e. GNSS, IMU, laser scanner and stereo cameras), and another one in which the mea-

measurements from the exteroceptive sensors are neglected. With the latter configuration, the number of measurements considered in the update step is fixed throughout the whole estimation (the number of visible satellites is also not considered), so the system can be considered time-invariant (steady). One possible solution for these types of systems would be by computing the constant \mathbf{P}_∞ and \mathbf{K}_∞ with the well known DARE (SIMON, 2006). However, this methodology is ignored in these experiments since the solution is already suboptimal at the initial epochs of the estimation, while the filter did not converge yet. This approach would represent nonetheless a suitable option in estimations where the computational effort is still a primary consideration.

In Figure 6.6, the surfaces that result from applying a triangulation-based interpolation algorithm to the global 2D (top row) and heading (bottom row) RMSE results obtained for each randomly generated sample within the specified domain (cf. Table 6.7) are displayed for each vehicle. If the surfaces obtained with each vehicle are compared, the influence of the different vehicle dynamics is evident. First, the estimation of the 2D position and heading with vehicle 1 yields values of approx. 4cm and $6\cdot 7\cdot 10^{-4}\text{rad}$ (roughly 0.3°) with the vast majority of the samples revealing a rather low sensitivity of the RMSE with respect to the PSD combinations. Differently, the solutions obtained with vehicle 2 are slightly less accurate in the case of the 2D positioning estimation (approx. 8cm) excluding the region of the domain that contains the samples with low \mathbf{q}_{vel} . Hence, the motion model is not excessively disrupted in the prediction step. The overall loss in accuracy is originated due to the disadvantageous landmark layout, much more favorable in the region where vehicle 1 navigates than for vehicle 2 (with one long plane on the right side of the vehicle, see Figure 6.4). On the contrary, the mentioned landmark layout proves to be sufficient for the heading estimation, showing a marginal increase in accuracy with respect to vehicle 1. This outcome fits the expectations, as this trajectory is almost straight at an almost constant velocity. The suitability of the selected motion model is however an exception for this particular trajectory, and given the simplicity of the motion model used, inconsistencies are expected. Hence, adequate values must be selected in order to represent the discrepancies between the motion model and the real trajectory dynamics. One example is shown in the results from vehicle 3, which differ significantly from the ones obtained from the first two vehicles. Here, the larger position and heading RMSE results are shown in the region of the domain with lower \mathbf{q}_{att} . This is again a rather expected result, provided that the constant turn rate considered in the motion model is heavily violated during turning maneuvers, and therefore, larger \mathbf{q}_{vel} and \mathbf{q}_{att} must be considered to compensate these inconsistencies. The heading analysis provides a clear evidence to this allegation, in which the tones of the surface reveal effects that resemble overlapping rounded layers in the regions of the parameter space with low PSD values. This results in an area with dark-blue tones that contain the PSD combinations that maximize the overall accuracy of the heading estimation.

Although the mentioned overall results computed with fixed PSD combinations (throughout the complete trajectory) are sufficient for the identification of general patterns, the results from the sample experiment (see Section 5.2) showed this approach leads often to suboptimal epoch-wise estimations in dynamic environments. Therefore, the time series obtained from the MC simulation are displayed in Figures 6.7, 6.8 and 6.9 for vehicles 1, 2 and 3, respectively. On the one hand, the estimated 2D position and heading deviations relative to the reference trajectories are displayed in the first and third rows, separating the outcomes obtained with both sensor architectures (with

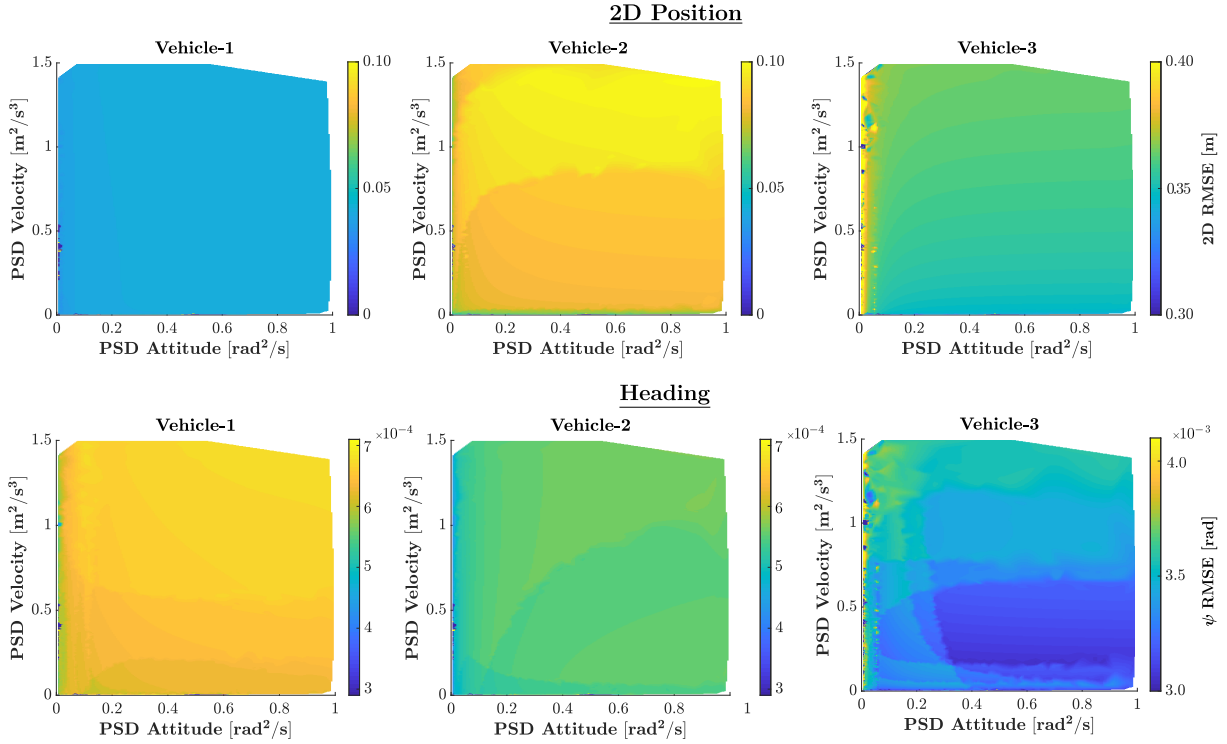


Figure 6.6: Surfaces obtained for the MC simulation for each vehicle. The scores (2D RMSE in the top row and RMSE heading in the bottom row) obtained with each of the randomly distributed samples within the specified domain in (cf. Table 6.7), are interpolated using a triangulation-based algorithm. Please note the different color-map interval for the third vehicle.

and without exteroceptive sensors) in the left and right columns. In these plots, three different sets of results are compared: (i) the epoch-wise mean of the 4000 runs (black line), (ii) the time series obtained using the fixed \mathbf{q}_{vel} and \mathbf{q}_{att} combination (Best Sample (BS)) that yields the best overall score (e.g. sample with the lower RMSE) (green line), and (iii) the result from computing the trajectory with the most adequate epoch-wise \mathbf{q}_{vel} and \mathbf{q}_{att} combination (red line). On the other hand, the epoch-wise PSD combinations used to obtain the most accurate 2D position and heading outcomes (red lines) are displayed in the graphs from the second and fourth rows, respectively. Here, it is crucial to clarify that the best epoch-wise combination is identified for the position and heading independently, so that it is possible to assess whether the combination is suitable for the estimation of both states (similar epoch-wise combinations) or only for one. Finally, in the last row, the absolute velocity and heading time series are displayed. In this way, it is not only possible to identify and quantify the accuracy loss due to inadequate PSD value selection, but also to relate the most vulnerable segments of the trajectories to particular maneuvers as well.

The results from vehicle 1 displayed in Figure 6.7 are fairly convenient to start the analysis, since they are derived from a straight trajectory at a constant velocity, clearly interrupted by two turning maneuvers, where the vehicle also performs the required sequential breaking and accelerating maneuvers to ensure safety. The first turning maneuver starts around 50s after the start (pink background). There, it can be seen from Figure 6.7c, that both the values required to minimize the deviations rise significantly, until the vehicle stops turning 65s after the start. This scene describes

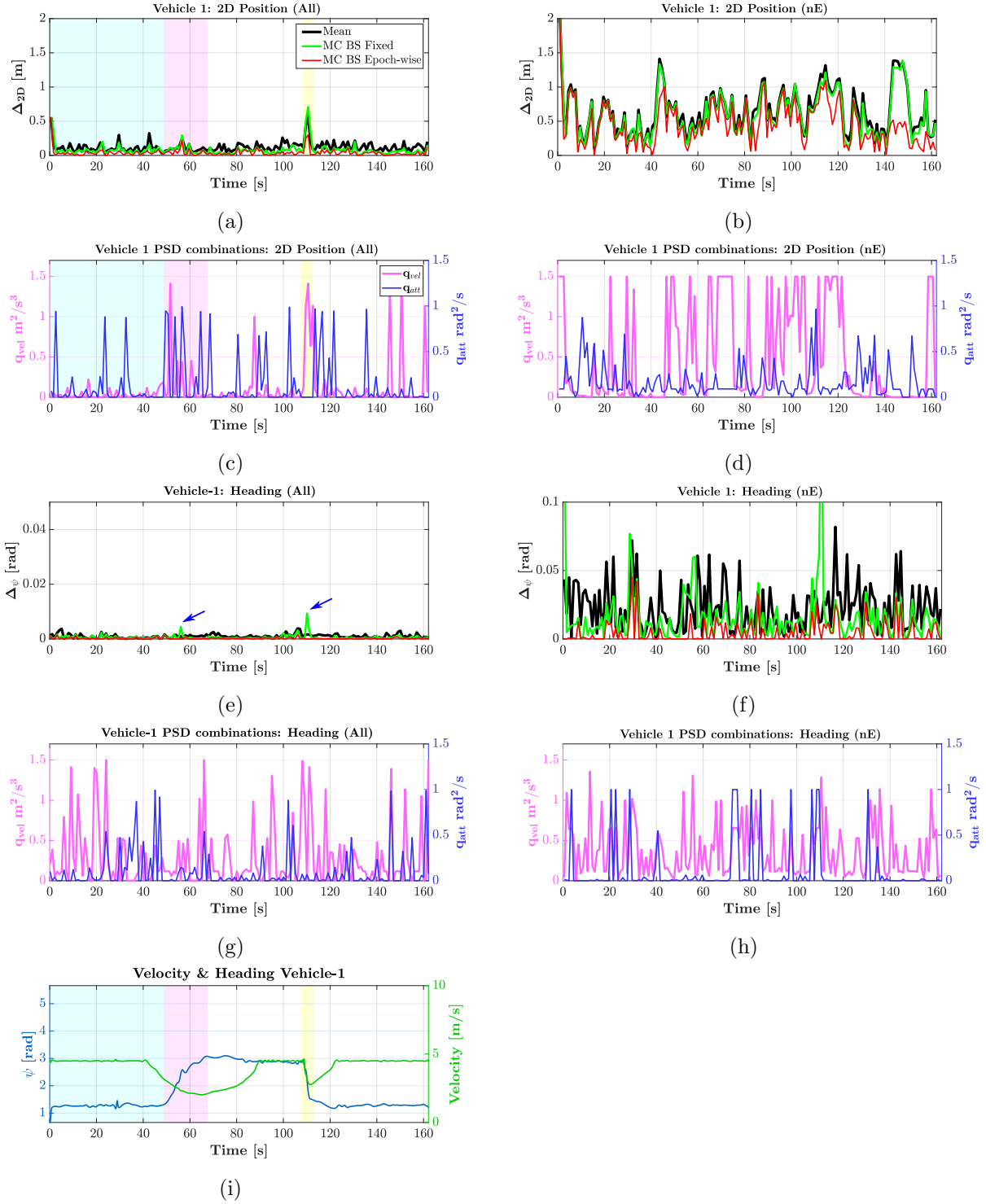


Figure 6.7: Vehicle 1 2D (first row) and heading (third row) deviations of the estimated trajectory relative to the reference solution using a sensor architecture with (left column) and without (right columns) exteroceptive sensor measurements. The most adequate epoch-wise PSD combinations obtained for the 2D and heading (independent) estimations are shown in the second and fourth rows, respectively. Finally, the absolute velocity and heading are displayed in the fifth row. Please note the different vertical scales used in Figures 6.7e and 6.7f.

perfectly the reason why the process noise is necessary. Until this maneuver, the vehicle navigates at a pretty straight trajectory at a constant velocity (cyan background). In these conditions, the

outcome from the prediction step using a decoupled linear constant velocity and constant turn rate motion model does would not differ much from the nominal trajectory in absence of additional sensor measurements. Hence, the rather low \mathbf{q}_{vel} values yielded by the MC simulation (Figure 6.7c, magenta line). However, in breaking/accelerating or turning maneuvers, the motion model is disrupted, and the inconsistencies between the actual motion of the object and the motion model need to be compensated with larger PSD. The second turning maneuver takes place approx. 110s after the start (yellow background). In contrast with the first turn, the vehicle starts breaking and turning at the same time, although leading to the same previously introduced outcome, with the \mathbf{q}_{vel} and \mathbf{q}_{att} rapidly rising in order to compensate the inconsistencies between the physical and motion of the object. Finally, it is also worth mentioning that the obtained \mathbf{q}_{att} values are moderately unstable compared with \mathbf{q}_{vel} . This happens due to the influence of the environmental geometry within the update step, which has an obvious influence on the state estimation, and also due to inconsistencies caused by trajectory mis-modeling (e.g. between 15-30 s).

The same interpretation can be drawn from the analysis of the heading. In this case, the time series reveal that the global minimum RMSE in Figure 6.6 is obtained by selecting a suitable PSD combination for the estimation during the straight sections of the trajectory. However, this combination leads to larger errors during turning maneuvers (blue arrows in Figure 6.7e), thus underlining again the inefficacy of fixed PSD values in dynamic time-variant systems. In these epochs, the selection of an adequate epoch-wise process noise mitigates errors in the heading larger than 0.01 rad (almost 0.6°).

Another interesting aspect from the impact of adequate PSD combinations can be seen in the 2D positioning results of vehicle 2. In this specific case, the fact that the vehicle describes a fairly straight trajectory at a constant velocity during almost the complete time, leads to the assumption that the motion model selected is quite suitable for the state prediction. Taking a look at Figure 6.8a, it is possible to see that adequate PSD combinations enable the mitigation of the errors caused by weak environmental geometries. One clear example is obtained in the region approximately between seconds 47 and 53 (gray background in Figures 6.8a and 6.8c). Here, the solution obtained from the prediction step is significantly more accurate and precise than the best solution that can be obtained given the observational work. Therefore, low PSD values can be used to bound the updated states by restricting the amount of correction allowed. When the consideration of low \mathbf{Qd}_k is coupled with a very precise prediction, the rather small \mathbf{P}_k^- leads to \mathbf{K}_k values really close to 0. As a result, the influence of the measurements is neglected, leaving the estimation completely dominated by the motion model. This situation is enhanced if no exteroceptive sensors are used (see Figures 6.8b and 6.8f) as the more precise measurements are neglected, and therefore the difference between the maximum precision that can be obtained from the set of measurements (laser scanner and stereo cameras) with respect to the prediction step is higher. In these cases, the accuracy improvements can reach the meter level in the 2D position, and 3° in the heading estimation, in some epochs (cf. Table 6.9).

The outcome from vehicle 3 serves to show the effects caused by the selection of an unsuitable motion model in EKF-based estimations. In an invariably turning trajectory, the constant turn rate model is continuously disrupted. Subsequently, the errors in the prediction step are transferred

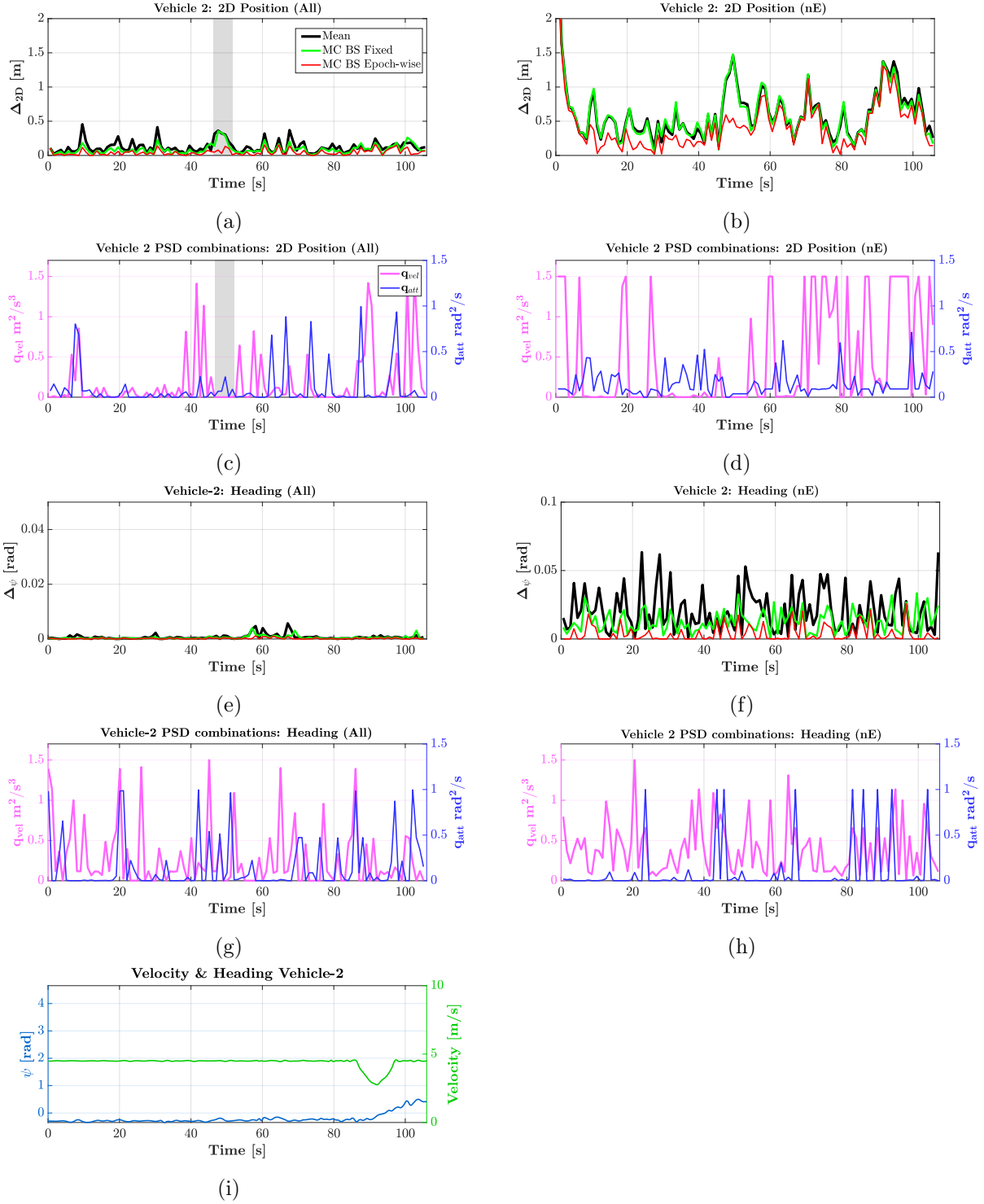


Figure 6.8: Vehicle 2 2D (first row) and heading (third row) deviations of the estimated trajectory relative to the reference solution using a sensor architecture with (left column) and without (right columns) exteroceptive sensor measurements. The most adequate epoch-wise PSD combinations obtained for the 2D and heading (independent) estimations are shown in the second and fourth rows, respectively. Finally, the absolute velocity and heading are displayed in the fifth row. Please note the different vertical scales used in Figures 6.8e and 6.8f.

to the update innovation, causing that neither the exteroceptive sensors nor the process noise can compensate such big errors in the 2D positioning. It is precisely in these dynamic trajectories,

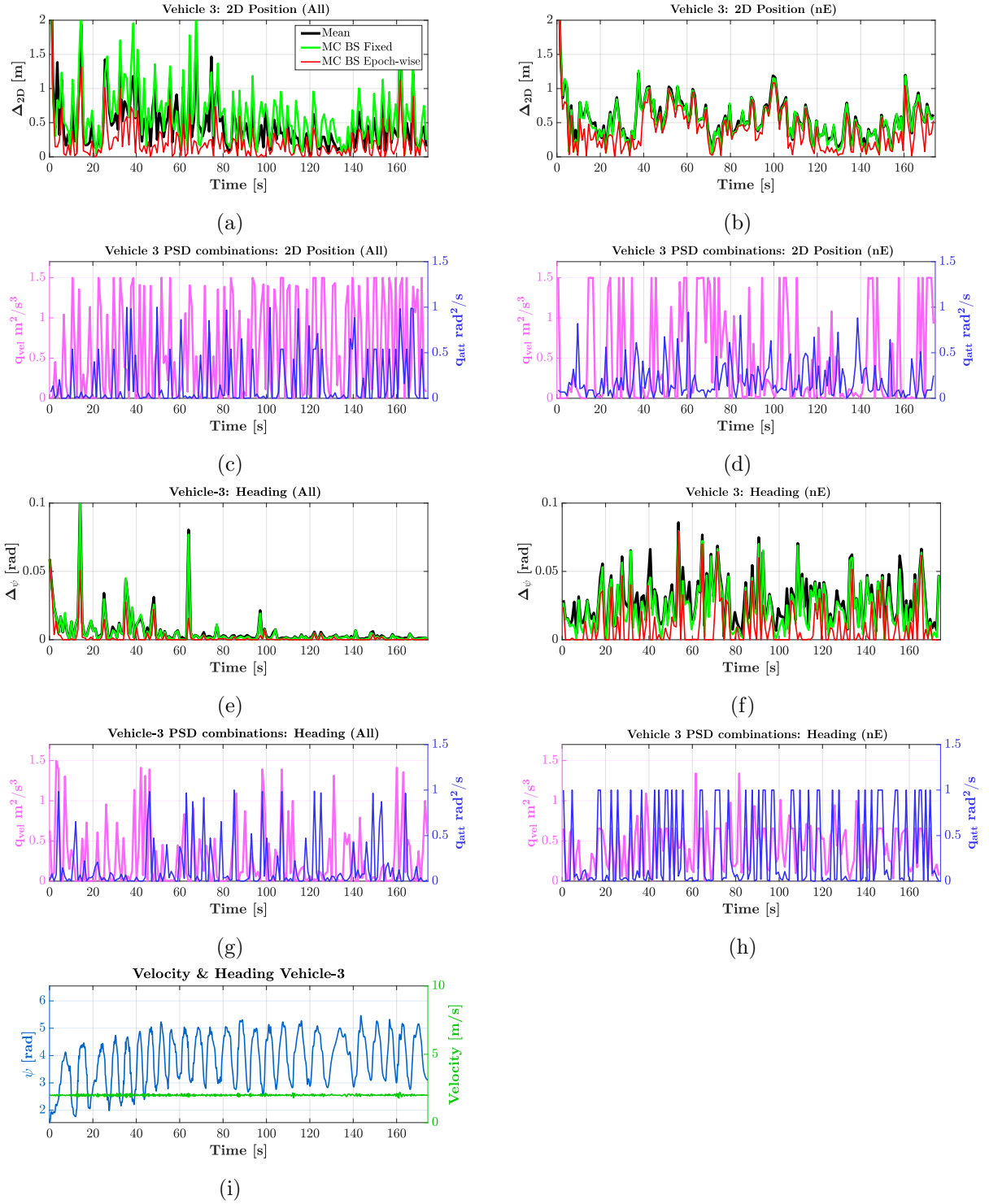


Figure 6.9: Vehicle 3 2D (first row) and heading (third row) deviations of the estimated trajectory relative to the reference solution using a sensor architecture with (left column) and without (right columns) exteroceptive sensor measurements. The most adequate epoch-wise PSD combinations obtained for the 2D and heading (independent) estimations are shown in the second and fourth rows, respectively. Finally, the absolute velocity and heading are displayed in the fifth row.

where highly precise IMU measurements play a decisive role within the estimation. The IMUs feed the system with high-rate measurements that describe the motion of the vehicle in real time. If

Table 6.9: Mean ($\bar{\mathbf{x}}$) and maximum (**Max**) differences between the optimum solution computed with the dynamic PSD combinations and the optimum solution computed with the fixed value (red and green solutions in Figures 6.7 - 6.9, respectively).

		2D [m]			Heading [$^{\circ}$]		
		Veh-1	Veh-2	Veh-3	Veh-1	Veh-2	Veh-3
All	$\bar{\mathbf{x}}$	0.041	0.046	0.397	0.023	0.017	0.212
	Max	0.411	0.300	1.982	0.533	0.218	3.518
nE	$\bar{\mathbf{x}}$	0.154	0.167	0.142	0.619	0.519	0.799
	Max	0.976	0.935	1.032	10.165	1.920	3.942

the well-known errors that affect these measurements are precisely estimated and compensated, the trajectory obtained could be used in the prediction step, mitigating most of the negative effects introduced within the scope of this analysis.

In summary, the highly varying epoch-wise combinations obtained from the MC simulations carried out in this section support the initial idea that one fixed PSD combination is not efficient in dynamic estimations. Also, given that the vehicle dynamics are not known in advance in real cases, the question of a certain PSD combination is very difficult to achieve. However, the results from the simulation reveal a significant improvement if epoch-wise $\mathbf{q}_{\text{vel}}\text{-}\mathbf{q}_{\text{att}}$ combinations are used (the red solutions are invariably better than the green ones, regardless of the sensor architecture or parameter of interest). In post-processing, these values can be estimated prior to the filter computation, ensuring the maximization of the filter performance. In online applications, the disruptions of the motion model could be mitigated by using high-end device able to feed the system with time-stable and highly-precise measurements like e.g. atom-interferometry sensors (TENNSTEDT AND SCHÖN, 2020). To support these statements, Table 6.9 displays the 2D and heading mean ($\bar{\mathbf{x}}$) and maximum (**Max**) differences between the solution computed with the most adequate epoch-wise combinations, relative to the solution obtained with the best fixed combination. These are also classified depending on the sensor architecture, with (**All**) and without exteroceptive sensors (**nE**). In this table, it is possible to see that for vehicles 1 and 2, the mean improvements with the epoch-wise combinations are at the centimeter level regarding the 2D position, and approx. $0.01\text{-}0.02^{\circ}$ for the heading. Nevertheless, the solution can show improvements at the decimeter level for the 2D positioning results, and more than 0.5° in the heading, hence underlining again the inefficiency of fixed combinations. Vehicle 3 shows significantly higher improvements, as the motion model selected proves to be unsuitable throughout the complete trajectory. Under these conditions, the selection of adequate epoch-wise PSD combinations entails improvements that in some epochs exceed the meter level and several degrees in the positioning and heading results, respectively.

If no exteroceptive sensors are considered (**nE** solutions in Table 6.9), the overall accuracy of the estimation decreases significantly, but the range of improvement with the epoch-wise best samples augments significantly. Here, it is interesting to see in vehicles that perform important turning maneuvers, are the most vulnerable to the inconsistencies generated by the utilization of a fixed PSD combination. In this context, the utilization of an adequate epoch-wise PSD combinations

Table 6.10: Sensor measurement standard deviation and update rate: process to measurement noise ratio.

<i>Sensor</i>	<i>Measurement</i>	σ	<i>Update Rate</i>
GNSS	$\mathbf{p}_{\text{GNSS}}^t$	2 [m]	1 Hz
	$\mathbf{v}_{\text{GNSS}}^t$	0.2 [m/s]	1 Hz
	V2V	2 [m]	1 Hz
IMU	$\phi \theta \psi$	0 – 30 [°]	10 Hz
Laser S.	r	0.1 [m]	1 Hz
Cameras	\mathbf{p}_{cam}	0.1 [m]	1 Hz
PSD	\mathbf{q}_{vel}	0.3 [m ² /s ³]	10 Hz
	\mathbf{q}_{att}	0 – 0.5 [rad ² /s]	10 Hz

translated into important improvements, exceeding 1 m and 10° in 2D position and heading (respectively) in some epochs.

Lastly, one might think that the large inconsistencies encountered in the filter could be expected in advance, as the highly non-linear and dynamic behavior of the vehicles is being described with a linear decoupled constant velocity constant turn rate motion model. However, a more suitable a-priori model (e.g. non linear constant turn rate and velocity (CTRV) or constant turn rate and acceleration (CTRA) (SCHUBERT ET AL., 2008)) might be able to reduce the magnitude of the inconsistencies, but in any case cannot completely compensate them, thus underlining the indisputable necessity to consider a suitable process noise model in the prediction step in order to ensure the filter accuracy and stability.

6.3.3 Process Noise to Measurement Noise Selection

It was found in the previous section that the process noise is a crucial point of the prediction step since it represents the inherent noise of the system model. If the process noise is small compared to the measurement noise, the error in the updated state is dominated by the motion model, and vice versa. With this in mind, it becomes clear that the results displayed in the previous section are only suitable for the fixed measurement noise configuration shown in Table 6.7. In addition, as introduced in Section 6.2.2, the standard deviation used to model the measurement noise is used to define the quality of the sensor used for the estimation. For example, a simulation scenario where very precise laser scanner ranging measurements are considered (low standard deviation) is interpreted as a scenario in which a high-end laser scanner is available. Hence, the measurement standard deviation should not be treated as an arbitrarily selected parameter. This situation differs from the one described in the previous analysis, with both targets of the optimization that can be epoch-wisely adjusted. Therefore, the question about impact of a selected PSD given a defined measurement noise configuration arises.

This evaluation is carried out by means of an MC simulation with the same characteristics as the one introduced in the previous section. Here, the scenario introduced in Section 6.3.1 is run 2000 times with the configuration shown in Table 6.10. In each run, a random combination of the

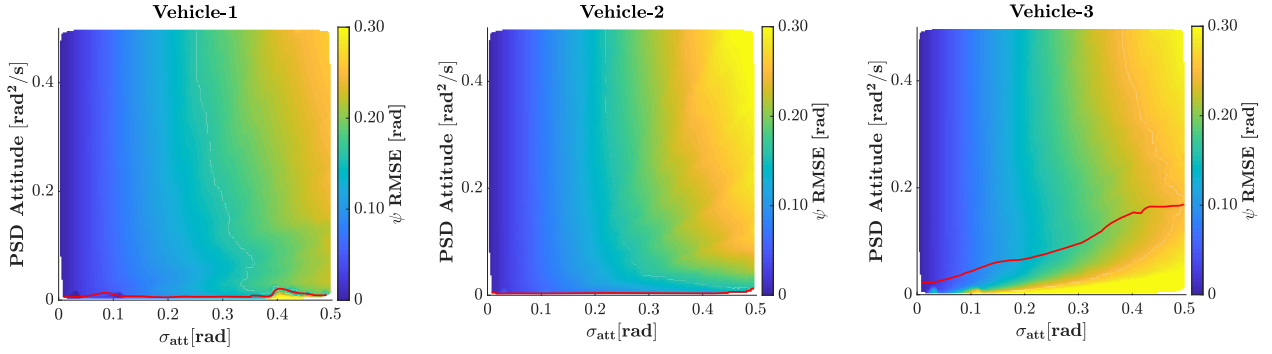


Figure 6.10: Surfaces obtained for the MC simulation for each vehicle. The scores (ψ RMSE in this simulation) obtained with each of the randomly distributed samples within the specified domain in (cf. Table 6.10), are interpolated using a triangulation-based algorithm (BOFFI, 2018).

attitude measurement noise and process noise PSD is selected, defining in this way a different two dimensional MC parameter domain from the one shown in Table 6.7. The decision to select only the attitude process noise and measurement noise is made, because in the absence of exteroceptive sensor measurements, the dependencies between those two variables are isolated, remaining unaffected by the rest of the sensor measurements and processing parameters.

The results obtained from the MC simulation are illustrated in Figure 6.10, and contains the surfaces obtained from interpolating the scores (heading RMSE) within the defined parameter space (feasible region) for each vehicle. As expected, the most accurate samples are the ones where low measurement noise is considered, regardless of the vehicle dynamics, showing the darkest blue tones at the left side of each graph. In these cases, the very low measurement noise causes the updated state to be always accurately corrected, mitigating the negative effects that might have been previously introduced by inconsistencies between the true and predicted states. Vehicle 2 represents a situation where the EKF prediction is suitable in a sense that the filter model matches the physical motion perfectly as the vehicle describes an almost straight trajectory. However, the presence of turning maneuvers within the trajectories described by vehicles 1 and 3 assess the fact that the implementation will always be disrupted at some point. The consideration of a model that assumes the process to be completely constant in time is a risky model since in the real world, inliers and/or biases alter this assumption (BROWN AND HWANG, 1997). This situation can also be identified in the set of results displayed in Figure 6.10, with the blue tones rapidly fading into green and yellow as a consequence of increases in the measurement noise. In order to lessen these effects and avoid potential divergences is to increase the process noise of the affected state. Again, the MC simulation results (particularly the ones obtained for vehicle 3) support this statement, with the grid cells that contain the samples with low PSD lead to less accurate overall results (yellow grid cells on the bottom right section of the graph) with the progressive increase of the measurement noise. As a result, provided that the measurement noise cannot be arbitrarily changed, the PSD that yields the most accurate results could be found by finding the column-wise minimums of σ_{att} , represented with a red line in Figure 6.10.

Given the complete outcome obtained from this and the previous experiments, the necessity to amplify the process noise in highly dynamic environment is demonstrated.

To conclude, the time series analysis is not shown in this experiment since the target of this experiment was to find the overall behavior shown by trajectories with different dynamics. However, the epoch-wise effects caused by inadequate PSD values can be analyzed in the results displayed in Section 6.3.1.

6.4 Summary and Conclusions

In this chapter, a methodology to identify the best sensor combinations - taking into account also sensor measurement quality - and the impact caused within the filter by inadequate process noise in dynamic time-variant and time-invariant estimations were assessed.

Firstly, in order to identify the most suitable sensor combinations, an MC-based simulation was designed where the results obtained with different sensor architectures were compared with the reference architecture (all available sensors are included). From this experiment, it is possible to learn that the utilization of exteroceptive sensors a field of view of 360° overshadow the impact from the other sensor measurements in localization approaches in situations with favorable landmark layout. The stereo cameras register information in a much smaller field of view than the considered laser scanner. For this reason, less landmarks are detected, and subsequently, the decrease in the filter performance becomes evident. In disadvantageous landmark geometries, the GNSS measurements become crucial in order to anchor the network to the global frame. Furthermore, the presence of an IMU able to feed the system with high-rate inertial measurements is crucial in order to mitigate the inconsistencies between the motion model selected in the prediction step and the actual motion model. In fact, this statement must be extended, since the presence of the IMU measurements are crucial in areas where the GNSS signal is degraded or unavailable in order to guarantee the location of the exteroceptive sensors (fundamental for the localization in the selected global frame).

As mentioned before, the study was focused on the geometric and intrinsic characteristics of each sensor measurement. However, additional characteristics of the sensors, that normally play a complementary role in multi-sensor systems (e.g. image RGB values, multi-spectral information, reflectivity, etc.) were ignored. As a result, additional considerations must be made prior to the design and implementation of real experiments built upon the findings described in this thesis.

Secondly, the effects caused in the filter by different \mathbf{q}_{att} and \mathbf{q}_{vel} combinations were evaluated. This is an essential factor to analyze in dynamic networks, given that the motion of the objects arises a number of additional challenges with respect to the classical geodetic network adjustment and optimization methodologies. In KF-based approaches, the object motion is introduced in the prediction step with non-linear continuous differential equations. Although sometimes these models can approximate the vehicle dynamics considerably well, they are far from being perfect. In order to mitigate the inconsistencies between the motion model and the physical motion, an adequate process noise model must be considered. From the results displayed in Section 6.3, using a linear decoupled constant velocity and constant turn rate motion model, it is possible to identify three different outcomes from the usage of adequate process noise combinations:

1. Large PSD values help to adjust the solution during turning and accelerating maneuvers.
2. Low PSD values restrict the amount of correction allowed during the update step, regardless of the observational work received.
3. The most adequate fixed PSD combination is the one that best fulfills the requirement set by the predominant maneuver.

Unfortunately, these three factors cannot be combined in the shape of one general outcome from the experiment, and each of the three conclusions represents an improvement in an specific situation. In addition, it is necessary to add that the most suitable combination for the 2D position estimation, does not necessarily have to be suitable for the heading estimation. Consequently, the identification of a process noise implementation suitable for the complete set of trajectories and vehicle maneuvers is complicated. Particularly in dynamic networks, also the challenges for the inter-vehicle relations must be added to the wide availability of sensors and their inner characteristics, and the range of different maneuvers that a vehicle undergoes in urban scenarios, as variables to take into account in the evaluation process. In addition, the update rate from the IMU measurements has also a large impact in the filter performance in terms of accuracy.

With all these factors in mind, different actions can be carried out in order to decrease the influence of inconsistencies generated by the motion of the objects. First, the motion model suitability depends on the maneuver performed by the vehicle. Therefore, a multi-model implementation that switches the model used in the prediction step could adapt the adjustment to the maneuver carried out by the vehicle at that instant. Here, the challenge would rely on the definition of the specifications that establish when the filter must automatically switch models, and which model is the target. Second, the utilization of a high-rate IMU operating within a robust estimator (efficient bias and mis-alignment corrections) could even substitute the motion model, feeding the updates with reliable and accurate information in (almost) real-time for the update. Lastly, the first action can be coupled with the adaptation of the process noise to the maneuver where the vehicle is involved. In fact, these three factors are complementary, and they can be coupled if necessary in order to maximize the performance of the adjustment.

7 Collaboration Versus Single Vehicle Estimation

The methodologies and the experiments carried out so far in this thesis are built upon the assumption that the vehicles navigate inter-connected by V2V measurements. In particular, the relative position between the vehicles is assumed to be obtained by the computation of GNSS baselines following the methodology described in section 3.1.2 (see Eq. (3.4)). However, the experiments described in chapters 5 and 6 focus primarily on the filter methodology evaluation and the selection of adequate processing parameters, ignoring the detailed evaluation of the benefits of collaborative navigation methodologies with respect to single vehicle approaches. In this chapter, the concept of the collaborative navigation is illustrated in Section 7.1. Then, the details of a suitable MC-based experiment for the analysis of collaborative navigation in terms of different navigation performance criteria are introduced in section 7.2, proceeding with the necessary evaluation of the results obtained in section 7.3. Finally, an overall discussion about the scenario strengths and limitations is given in section 7.4.

7.1 Collaborative Navigation: Concept

In order to properly evaluate the impact of collaborative scenarios with respect to single vehicle approaches, the scenario selected must enhance the influence of the V2V measurements (GNSS baselines) to facilitate the identification of singular events during the posterior analysis. This goal can be achieved in three different ways:

1. Considering vehicles with different sensor architectures (*favorable* \rightarrow *disadvantageous*).
2. Varying the precision of the V2V measurements.
3. Varying the number of vehicles involved in the collaboration scenario.

The first option would enable the evaluation of the mutual influence caused by the inter-connection of a fully equipped *aiding* vehicle (GNSS, IMU, laser scanner and stereo cameras) with an additional *aided* vehicle where only a GNSS receiver is mounted, that is the minimum architecture for collaborative positioning techniques with GNSS-based V2V measurements. Then, the overall amount of improvement would depend on the quality of the V2V measurements, and can be quantified by analyzing the response of the state estimation to varying their precision (second option). Finally, an increment of the number of vehicles involved in the collaborative scenario produces an obvious increase of the number of measurements, with its corresponding influence on the estimation.

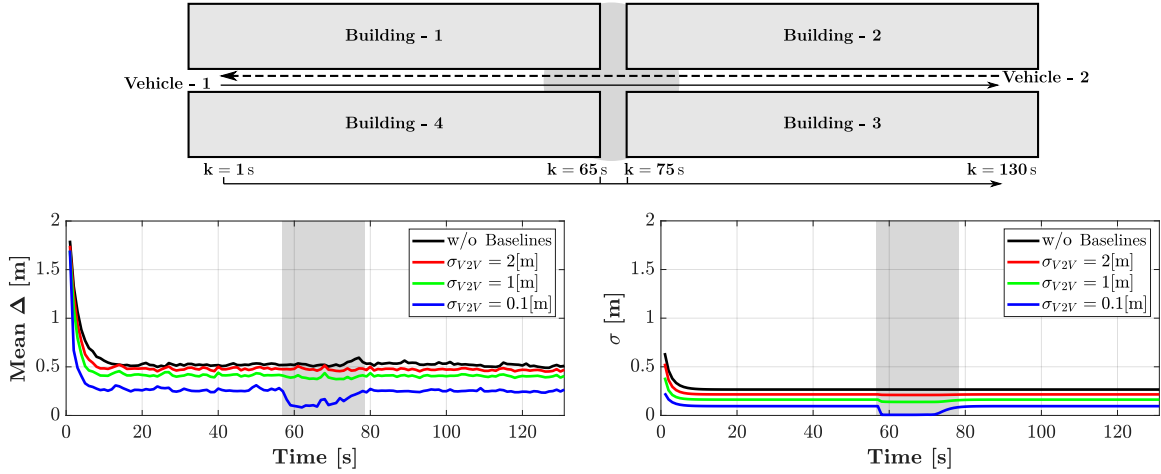


Figure 7.1: Proof of concept. Accuracy and standard deviation results for vehicle 2. The results obtained considering $\sigma_{GNSS} = \sigma_{V2V} = 2$ m (red line), $\sigma_{V2V} = 1$ m (green line) and $\sigma_{V2V} = 0.1$ m (blue line) are compared with the single vehicle approach results (black line). Top: scenario top view. The gray shadowed area matches the gray areas in the bottom left and right plots. Left: mean 2D position deviations over 500 runs. Right: 2D position standard deviation.

Although these three aspects must be evaluated together, the scenario described in Section 6.2 comes in handy for a first approximation to the concept, since the vehicles describe a perfectly straight trajectory at a constant velocity and the simplicity of the landmark layout assists the evaluation of the results. In this way, the outcome remains completely unaffected by changes in the vehicle dynamics, leaving the update step entirely dominated by the measurements. Given that the number of measurements is constant in the different runs, the effect of varying σ_{V2V} is isolated. To demonstrate this concept, a simple MC simulation (500 runs) is carried out considering that vehicle 1 is fully equipped with all available sensors, and vehicle 2 is only equipped with a GNSS receiver. In addition, the simulation is repeated using different σ_{V2V} .

In Figure 7.1, the results obtained for vehicle 2 are shown, divided in two graphs. The left graph contains the epoch-wise mean 2D position deviations of the estimated parameters relative to the true trajectory for the 500 runs. Also, the results obtained with the different σ_{V2V} are compared, displaying in red the solution with $\sigma_{GNSS} = \sigma_{V2V} = 2$ m, $\sigma_{V2V} = 1$ m in green and $\sigma_{V2V} = 0.1$ m in blue. The results obtained with the single vehicle approach (black) is used as a reference. The graph on the right illustrates the standard deviation results obtained with the same configurations previously introduced. In these graphs, the positive influence of the collaborative navigation approaches is evident. Even the results obtained with $\sigma_{GNSS} = \sigma_{V2V} = 2$ m are translated into a general - although marginal - increase in the accuracy and precision of the estimation, showing not even one epoch with the reversed behavior. Furthermore, should the V2V be sufficiently precise, the impact of the landmark geometry introduced in the system with the exteroceptive sensor measurements mounted in vehicle 1, can be identified in vehicle 2. In the single vehicle solution, the deviations of the estimated trajectory relative to the true trajectory remain stable after the typical convergence time of an EKF (16s after the start). However, the estimation with $\sigma_{V2V} = 0.1$ m shows, besides a general increase in accuracy (approx. 0.3 m) and precision (approx. 0.15 m), an additional event between seconds 57 and 78 (gray shadowed area). Here, vehicle 1 is able to detect

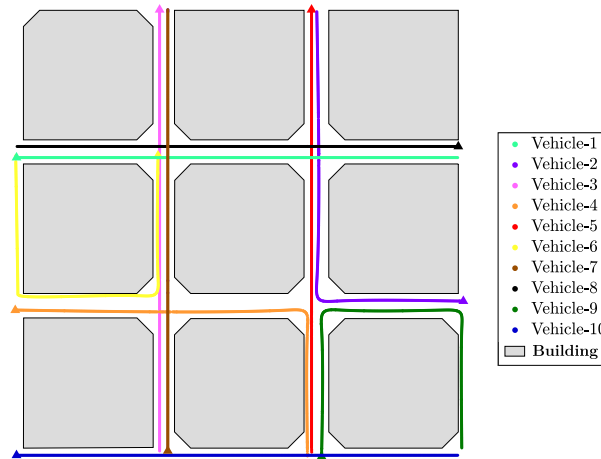


Figure 7.2: Representative visualization of the scenario used for the evaluation of collaborative navigation with respect to single vehicle approaches (proportions not kept).

the landmarks that lay perpendicular to the direction of driving, producing a sudden increase in accuracy in the AT direction, which is reflected in the results from vehicle 2 due to the very precise V2V measurements. Thus, highlighting the benefits of collaborative navigation.

However, the results obtained from this scenario are overoptimistic, as scenarios where vehicles navigate at a perfectly stable constant velocity and describing a perfectly straight trajectory are not achievable. Thus, taking into account the findings from section 6.3, the necessity to re-evaluate this set of results with a scenario where changes in the vehicle dynamics are introduced becomes clear. Lastly, the number of vehicles must be increased in order to analyze the response of the presented algorithm to the progressive addition of vehicles.

7.2 Experiment Scenario and Setup

In order to extend the initial results presented in the previous section, a particular scenario is designed (cf. Figure 7.2). First, the dynamics of ten different vehicles are generated from sets of digitized waypoints. Second, an elementary environment is generated, imitating the distribution of nine blocks of buildings. The goal of this scenario is to scale the previous situation and approximate it to a real case by considering different vehicle maneuvers, although still keeping an intermediate degree of simplicity on the model of the environment, so that the events related to the object of the study in this section are still evident in the outcome from the simulation. If too complex vehicle dynamics and environmental geometries are used, the natural impact of the collaborative navigation approach could be easily covered by other factors, and complicate the posterior analysis. The strategy followed with the sensor architecture of the vehicles is the same as the one introduced in section 7.1. Vehicle 1 is considered to be solely equipped with a GNSS receiver, that is able to retrieve the position and velocity of the object. The rest of the vehicles is assumed to be equipped with exteroceptive sensors - laser scanner with 360° of field of view and 16 lines of vertical aperture, and a pair of stereo cameras - that are able to capture the information from the environment and subsequently transfer their improved positioning information to vehicle 1 through

Table 7.1: Sensor measurement standard deviation and update rate: collaborative experiment

<i>Sensor</i>	<i>Measurement</i>	σ	<i>Update Rate</i>
GNSS	$\mathbf{p}_{\text{GNSS}}^t$	2 [m]	1 Hz
	$\mathbf{v}_{\text{GNSS}}^t$	0.2 [m/s]	1 Hz
	V2V	{0.1, 2} [m]	1 Hz
IMU	\mathbf{f}^b	0.002 [m/s ²]	100 Hz
	$\boldsymbol{\omega}_{\text{ib}}^b$	0.001 [rad/s]	100 Hz
Laser S.	r	0.1 [m]	1 Hz
Cameras	\mathbf{p}_{cam}	0.1 [m]	1 Hz
Env. Model	α	1 [°]	1 Hz
	Shift	0.1 [m]	1 Hz

Table 7.2: Random walk power spectral density: collaborative experiment.

<i>Parameter</i>	PSD
Velocity (\mathbf{q}_{vel})	0.03 [m ² /s ³]
Attitude (\mathbf{q}_{att})	0.01 [rad ² /s]

V2V measurements. The simulation setup, that contains the data rates, standard deviation values selected for the measurement noise, PSD values selected for the process noise, and the initial state parameter uncertainties are shown in Tables 7.1 to 7.3.

Table 7.3: Initial covariance of the state parameters: collaborative experiment.

<i>Parameter</i>	P₀
Position	2 [m ²]
Velocity	0.50 [m ² /s]
Attitude	0.1 [rad ²]

The benefits obtained with vehicle 1 from linking it to other vehicles with a more profitable sensor architecture are analyzed by comparing the results from two sets of MC simulations. First, the single-vehicle solution for vehicle 1 is computed to be used as reference by running the filter 100 times with the sensor setup described in Tables 7.1 to 7.3. Subsequently, these results are compared to the results obtained from linking vehicle 1 and vehicle 2. This operation is described four additional times, increasing the number of vehicles gradually two units per MC simulation. This leaves a total of six MC simulations where the filter is run 100 times, and the results enable the analysis of the tendency caused by the progressive addition of vehicles to the scenario. Second, this procedure is repeated two times, one with each of the two V2V measurements standard deviations introduced in Table 7.1 so that the impact of introducing V2V measurements of different quality on the state update is analyzed. In this way, the three requirements/conditions to enhance the impact of the V2V measurements relative to the other sensor measurements introduced in Section 7.1 are met.

7.3 Collaboration Results

In this section, the results obtained from the previously described MC simulations are evaluated in terms of the network robustness criteria introduced in Section 2.3.1. Nevertheless, the precision analysis is rather straightforward by comparing the results obtained by a gradual increment of vehicles. The standard deviation of the estimation depends on the number of measurements considered and their precision. In this experiment, the values of standard deviation selected for the measurement noise remain constant, and the number of measurements increases proportional to the number of vehicles used. As a result, the network precision increases always, proportional to the number of vehicles considered.

A detailed description of the results is presented in Sections 7.3.1 and 7.3.2, respectively.

7.3.1 Accuracy and Precision Analysis

Individual vehicle evaluation (local analysis)

The improvements of collaborative navigation with respect to the single vehicle approaches are first evaluated by analyzing the epoch-wise deviations relative to the nominal trajectory and quantified by means of the RMSE statistic. In Figure 7.3, the relative cumulative frequency of the 2D (first row) and 3D (second row) epoch-wise deviations of the updated states (100 MC runs) relative to the nominal values, are depicted for vehicle 1. Furthermore, the outcome is separated depending on the selected V2V measurement standard deviation σ_{V2V} ($\sigma_{V2V} = 0.1$ m in the left column and $\sigma_{V2V} = 2$ m to the right). The solution used as reference is the outcome from running the filter as a single vehicle (SV) approach (black line) with vehicle 1 (only one GNSS receiver). Then, the outcomes obtained from coupling it with a second vehicle (red line), three (orange), five (blue), seven (magenta), and nine (turquoise) additional vehicles are included.

In general, the results displayed in Figure 7.3 show that the tendency is to obtain more accurate results if the number of vehicles is increased, regardless of σ_{V2V} . However, the amount of improvement achievable is larger if the V2V measurements are highly precise (see also Table 7.4). Taking into account the graphs where the V2V and GNSS measurement standard deviations amount both to two meters ($\sigma_{GNSS} = \sigma_{V2V} = 2$ m), the single vehicle approach yields a percentage of around 60% of the results below the meter level. As the number of vehicles increases, this percentage rises, exceeding the 90%-mark in dynamic networks defined by at least six vehicles. Also, the highest influence of the update step with exteroceptive sensors on the XT direction has been shown in previous chapters of this thesis. This causes the improvements in the 2D directions to be slightly higher than in the 3D case. If the overall RMSE results listed in the last four rows of Table 7.4 are compared, the collaborative navigation improvements relative to the **SV** approach are always significant regardless of the number of vehicles. In particular, the outcomes obtained with ten vehicles (both 2D and 3D) entail an improvement greater than 50%.

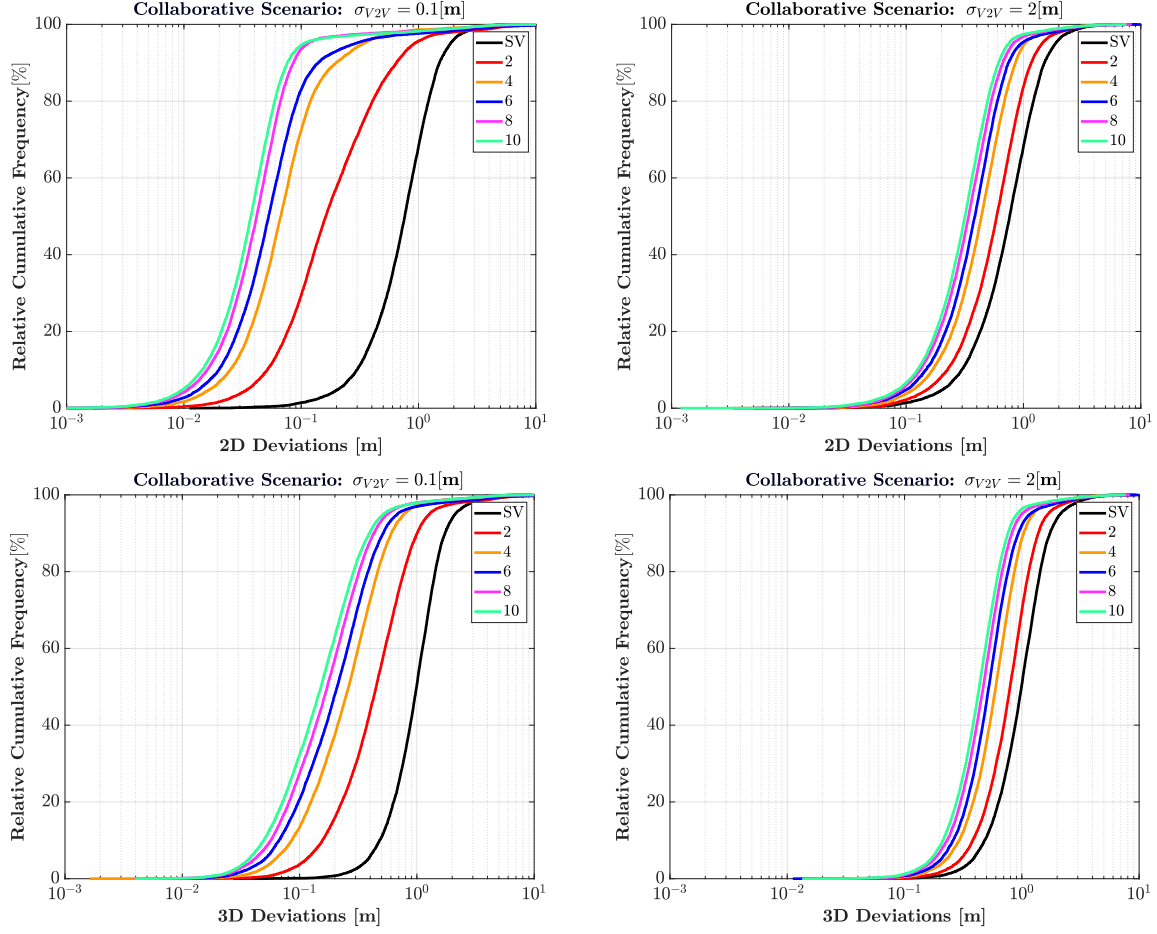


Figure 7.3: Relative cumulative frequency functions obtained from the collaborative MC simulations. Left: configuration with $\sigma_{V2V} = 0.1$ m. Right: Configuration with $\sigma_{V2V} = 2$ m.

Table 7.4: RMSE of the collaborative MC simulation from Vehicle 1 (aided vehicle). The 2D and 3D RMSE ([m]) obtained with different amount of vehicles considered in the navigation scenario are displayed for comparison. Also, the percentage of improvement obtained with each configuration relative to the single vehicle (SV) approach is shown.

		SV	2 Veh	4 Veh	6 Veh	8 Veh	10 Veh
$\sigma_{0.1\text{m}}$	RMSE 2D [m]	0.896	[0.298 - 0.364]	0.174	0.167	0.142	0.148
	%	0.00	[66.74 - 59.38]	80.61	81.38	84.17	83.52
	RMSE 3D [m]	1.063	[0.564 - 0.599]	0.387	0.328	0.287	0.270
	%	0.00	[46.94 - 43.64]	63.59	69.15	73.04	74.60
$\sigma_{2\text{m}}$	RMSE 2D [m]	0.896	[0.711 - 0.724]	0.555	0.493	0.445	0.415
	%	0.00	[20.65 - 19.19]	38.09	44.98	50.32	53.68
	RMSE 3D [m]	1.063	[0.880 - 0.889]	0.694	0.621	0.560	0.521
	%	0.00	[17.25 - 16.41]	34.69	41.59	47.34	51.00

The tendency described by the outcome obtained with $\sigma_{\text{GNSS}} = \sigma_{V2V} = 2$ m is enhanced if the precision of the V2V measurements is increased to 0.1 m. Figure 7.3 shows that more than 80% of the epoch-wise 2D deviations of the estimated solution relative to the true solution are at the

centimeter level. It is precisely in the 2D estimation, and with this specific configuration, where the largest improvements are obtained (cf. Table 7.4). Here, the modest consideration of one additional vehicle entails approximately 66–59% gain, already slightly superior to the improvements yielded by the ten vehicle solution with the previous configuration. The solution with two vehicles is displayed as an interval, that contains all possible outcomes obtained combining vehicle 1 with each of the other vehicles. Then, the accuracy increases with the progressive addition of vehicles, reaching a final overall RMSE of approx. 0.14 m, a gain of nearly 84 % with respect to the **SV** solution. Here, the addition of the last two vehicles leads to a marginal decrease in the overall RMSE (6 mm). However, Figure 7.3 displays a higher percentage of epoch-wise deviations below decimeter level in the ten-vehicle solution than in the eight-vehicle solution. Therefore, this minimal decrease comes as a result of a few epochs with a slightly less accurate solution, which leads to a lower overall RMSE. Moreover, given that the computation is carried out assuming that the map elements have an uncertainty of 0.1 m in the vertex, the room for further improvement with more than eight vehicles is minimum.

Until this point, the analysis has been focused on the assessment of the impact that a network of aiding vehicles produces in the aided vehicle. However, the effects that the networked estimation has on one of the aiding vehicles has not yet been discussed. For this reason, the overall RMSE results obtained from vehicle 2 are displayed in Table 7.5. On a first sight, it is possible to see that as in the case of the aided vehicle, the results obtained from the simultaneous estimation of state parameters of a group of vehicles lead also to a general improvement in terms of accuracy with respect to single-vehicle solutions (**SV**). Also, the strengths of CP are visible since the results improve with the progressive addition of vehicles to the navigation scenario, regardless of the V2V measurement quality considered. However, the quality of the V2V measurements determine the amount of improvement achieved with collaborative approaches, showing improvements over the 60% if $\sigma_{V2V} = 0.1$ m and lower ones (around 40%) if $\sigma_{V2V} = 2$ m. Finally, it is interesting to observe the similar results yielded by the eight- and ten-vehicle 2D RMSE solutions. This is a clear indication that the system reached the highest level of performance given the used configuration (note also the landmark uncertainty). This, added to the similar behavior of the aiding vehicle with the same configuration shows that, under the current configuration, solutions with more than eight vehicles only increase the complexity of the computation with no (or even negative) effects on the accuracy of the system. This event is not visible in the 3D results as the lack of influence of the exteroceptive sensors on the Up coordinate leaves much more room for improvement. Nevertheless, this situation is caused the geometrical characteristics of the 3D model of the environment, in which ground plane is unavailable.

Taking a look at the precision (standard deviation), the results obtained support the statement that the sequential addition of nodes and measurements to the system leads to an increase in the precision, regardless of the quality selected for the V2V measurements and of the number of vehicles involved in the navigation situation. As in the case of the accuracy, the improvement in the 2D precision is significant in both configurations, exceeding the 90% of improvement with respect to the single vehicle approach with highly precise V2V measurements, and 70% if $\sigma_{V2V} = 2$ m. Under this configuration, the improvements of the ten-vehicle solution with respect to the eight-vehicle solution are marginal (at the millimeter level), rising again the question of whether it is worth

Table 7.5: RMSE and mean standard deviation ($\hat{\sigma}$) of the collaborative MC simulation from Vehicle 2 (aiding vehicle). The 2D and 3D RMSE (m) obtained with different amount of vehicles considered in the navigation scenario are displayed for comparison. Also, the percentage of improvement obtained with each configuration relative to the single vehicle (**SV**) approach is shown.

		SV	2 Veh	4 Veh	6 Veh	8 Veh	10 Veh
$\sigma_{0.1\text{ m}}$	RMSE 2D [m]	0.444	0.342	0.184	0.153	0.139	0.139
	$\%_{\text{RMSE}}$	0.00	23.09	58.51	65.57	68.79	68.69
	$\hat{\sigma}_{2D}$ [m]	0.207	0.150	0.049	0.023	0.017	0.015
	$\%_{2D\text{ SD}}$	0.00	27.51	76.31	88.84	91.88	92.84
	RMSE 3D [m]	0.811	0.597	0.402	0.341	0.310	0.293
	$\%$	0.00	26.36	50.41	57.99	61.75	63.94
	$\hat{\sigma}_{3D}$ [m]	0.695	0.494	0.325	0.258	0.223	0.199
$\sigma_{2\text{ m}}$	$\%_{3D\text{ SD}}$	0.00	28.95	53.21	62.84	67.95	71.34
	RMSE 2D [m]	0.444	0.377	0.318	0.278	0.271	0.263
	$\%_{\text{RMSE}}$	0.00	15.12	28.43	37.37	39.08	40.76
	$\hat{\sigma}_{2D}$ [m]	0.207	0.186	0.154	0.136	0.125	0.116
	$\%_{2D\text{ SD}}$	0.00	28.64	56.46	66.48	71.34	74.37
	RMSE 3D [m]	0.811	0.679	0.560	0.487	0.464	0.441
	$\%_{\text{RMSE}}$	0.00	16.26	30.96	39.97	42.80	45.61
	$\hat{\sigma}_{3D}$ [m]	0.695	0.589	0.479	0.419	0.381	0.352
	$\%_{3D\text{ SD}}$	0.00	15.17	31.04	39.66	45.22	49.28

considering two additional vehicles (causing more expensive computations) obtaining such small improvements both in the accuracy and precision.

The availability of two sets of results obtained with different σ_{V2V} aid also the understanding on how the V2V measurements are treated within the C-EKF. If the precision of these measurements is higher relative to other sensor measurements the \mathbf{K}_k values applied to them are higher, and the solution converges over the theoretical minimum, defined by the number and standard deviation of the observations considered. On the contrary, if the V2V measurements are less precise relative to the rest of the observations considered, the \mathbf{K}_k assigned to those observations is rather low (in most cases close to 0). Therefore, these observations are ignored by the system and the solution converges over the single-vehicle solution. As a result, the solution of the C-EKF is bounded between the theoretical minimum and the single-vehicle solution in terms of accuracy.

Finally, the identification solutions in which no improvement is generated with the addition of vehicles in both aiding and aided vehicles (individually) reveals the necessity to evaluate the complete network in order to have a complete understanding of the C-EKF performance. This analysis is carried out in the following section *Overall network evaluation*.

Table 7.6: Overall network RMSE ([m]) and A-optimality (Z_A [m]) analysis with different amount of nodes (vehicles). The solutions obtained considering V2V measurements with two different precisions ($\sigma_{V2V} = 0.1$ m and $\sigma_{V2V} = 2$ m) are contrasted.

		2 Veh	4 Veh	6 Veh	8 Veh	10 Veh
$\sigma_{0.1m}$	RMSE 2D Col. [m]	0.356	0.161	0.140	0.116	0.117
	RMSE 2D SV. [m]	0.732	0.570	0.511	0.476	0.459
	$Z_{A,2D}$ Col. [m²]	13.264	4.288	1.048	0.555	0.526
	$Z_{A,2D}$ SV. [m²]	105.748	130.063	157.663	184.818	216.006
	RMSE 3D Col. [m]	0.582	0.374	0.316	0.281	0.261
	RMSE 3D SV. [m]	0.847	0.726	0.701	0.680	0.675
	$Z_{A,3D}$ Col. [m²]	18.272	4.623	1.275	0.778	0.763
	$Z_{A,3D}$ SV. [m²]	157.003	190.140	223.773	264.807	318.505
σ_{2m}	RMSE 2D Col. [m]	0.587	0.373	0.309	0.273	0.246
	RMSE 2D SV. [m]	0.732	0.570	0.511	0.476	0.459
	$Z_{A,2D}$ Col. [m²]	62.297	50.870	48.943	49.358	51.372
	$Z_{A,2D}$ SV. [m²]	105.748	130.063	157.663	184.818	216.006
	RMSE 3D Col. [m]	0.775	0.569	0.495	0.452	0.418
	RMSE 3D SV. [m]	0.847	0.726	0.701	0.680	0.675
	$Z_{A,3D}$ Col. [m²]	78.223	57.827	50.192	45.171	41.929
	$Z_{A,3D}$ SV. [m²]	157.003	190.140	223.773	264.807	318.505

Overall network evaluation (global analysis)

In a next step, the network results are evaluated as a whole, in order to identify the configurations that lead to an overall better performance of the network-based estimation with respect to the **SV** approaches and validate the outcome from the local analysis. In order to do that, the RMSE of the complete network is computed with (**Col.**) and without (**SV**) V2V measurements, along with the A-optimality ($Z_{A,2D}$, Eq. (2.33)) scores used to measure the overall network precision.

This outcome is displayed in Table 7.6, both for the configuration with $\sigma_{V2V} = 0.1$ m and $\sigma_{V2V} = 2$ m. In this table, the results show that also taking into account the overall RMSE and Z_A (A-optimality) of the network, CP approaches lead to an increase in the performance with respect to single-vehicle approaches and there is a clearly positive tendency to the progressive addition of vehicles, both in terms of accuracy and precision. Again, the overall 2D RMSE of the network achieves approximately decimeter level in networks with at least than four vehicles, considering highly precise V2V measurements. With less supportive V2V measurements, the overall accuracy of the network decreases to a few decimeters, although in any case exceeding the RMSE values obtained with single-vehicle approaches. With $\sigma_{V2V} = 0.1$ m, the ten-vehicle solution obtained is again showing a marginal decrease in the accuracy with respect to the eight-vehicle solution, revealing again the fact that the networked estimation reaches the theoretical maximum achievable performance already with eight vehicles. This event arises also the question an optimal topological relation between the dynamic nodes of the network. With a different inter-vehicle connection

distribution (different than *each node to all*), the ten-vehicle solution might achieve a higher accuracy and reliability (a higher redundancy is achieved in general) than the eight-vehicle solution, without giving up a significant amount of computational efficiency. The dynamic network topology effects, as well as the assessment of the dynamic network reliability will be relevant paths in future investigations.

Taking into account the precision of the network measured by the A-optimality coefficient (\mathbf{Z}_A), the same overall behavior is visible as in the case of the accuracy. In this experiment, the precision obtained with the networked-based estimation improves thoroughly with respect to single-vehicle approaches, an amount proportional to the number of dynamic nodes and the quality of the inter-nodal measurements.

7.3.2 Integrity Analysis

In Figure 7.4, the Stanford diagrams that depict the integrity information by relating the PE with the PL and the AL are shown. Given that the results from Section 7.3.1 showed that the most accurate results are yielded by the ten vehicles collaborative navigation scenario, the integrity analysis is carried out by contrasting the ten-vehicle dynamic network results with both configurations, $\sigma_{V2V} = 2$ m (second row), and $\sigma_{V2V} = 0.1$ m (third row), with the single vehicle approach as reference. Subsequently, the PE, PL and AL are computed in the XT and AT direction, following the approach from REID ET AL. (2019) introduced in Section 2.3.1. Lastly, in order to facilitate the visualization, the AL and PL are computed assuming a vehicle with a width $w_v = 2.5$ m and length $l_v = 5.5$ m that navigates in a bounding box of $w_r = 6$ m and $l_r = 9$ m (yielding $AL = 1.75$ m).

By comparing the graphs from each column, the benefits of collaborative navigation are evident. First, the analysis of the graphs from top to bottom reveal a higher concentration of epoch-wise solutions in the regions with low PE. In the single-vehicle approach, the dominance of the GNSS measurements is noticeable since the grid illustrates a Gaussian-like distribution of the PE-PL along the dashed line that bisects the nominal operations from the misleading operations. As in the integrity study carried out in Section 5.2.2, the filter stability in terms of integrity is higher in the XT direction rather than in the AT (even in the single-vehicle approach), showing regularly solutions where the PE to PL ratio is higher. This is illustrated in Figure 7.4, with the solution clusters disseminated slightly to the left, and it means that the margin between the nominal and misleading operations is higher.

Moreover, although the ten-vehicle solution with $\sigma_{V2V} = 0.1$ m shows reasonably lower PE and PL than the other two configurations included in Figure 7.4, the outcome reveals epoch-wise solutions far from the cluster that contains the higher percentage of results. This happens due to the inclusion of the epoch-wise estimations at the starting instants of the trajectory when the filter has not yet converged resulting in uncertain estimations contained in the range defined by the initial standard deviation for each state parameter (see Table 7.1). However, since these epochs entail less than 1% of the total amount (12000 epochs), they do not encompass an obstacle in the interpretation of the graphs, and hence they are not neglected. Lastly, an even lower percentage of these weak

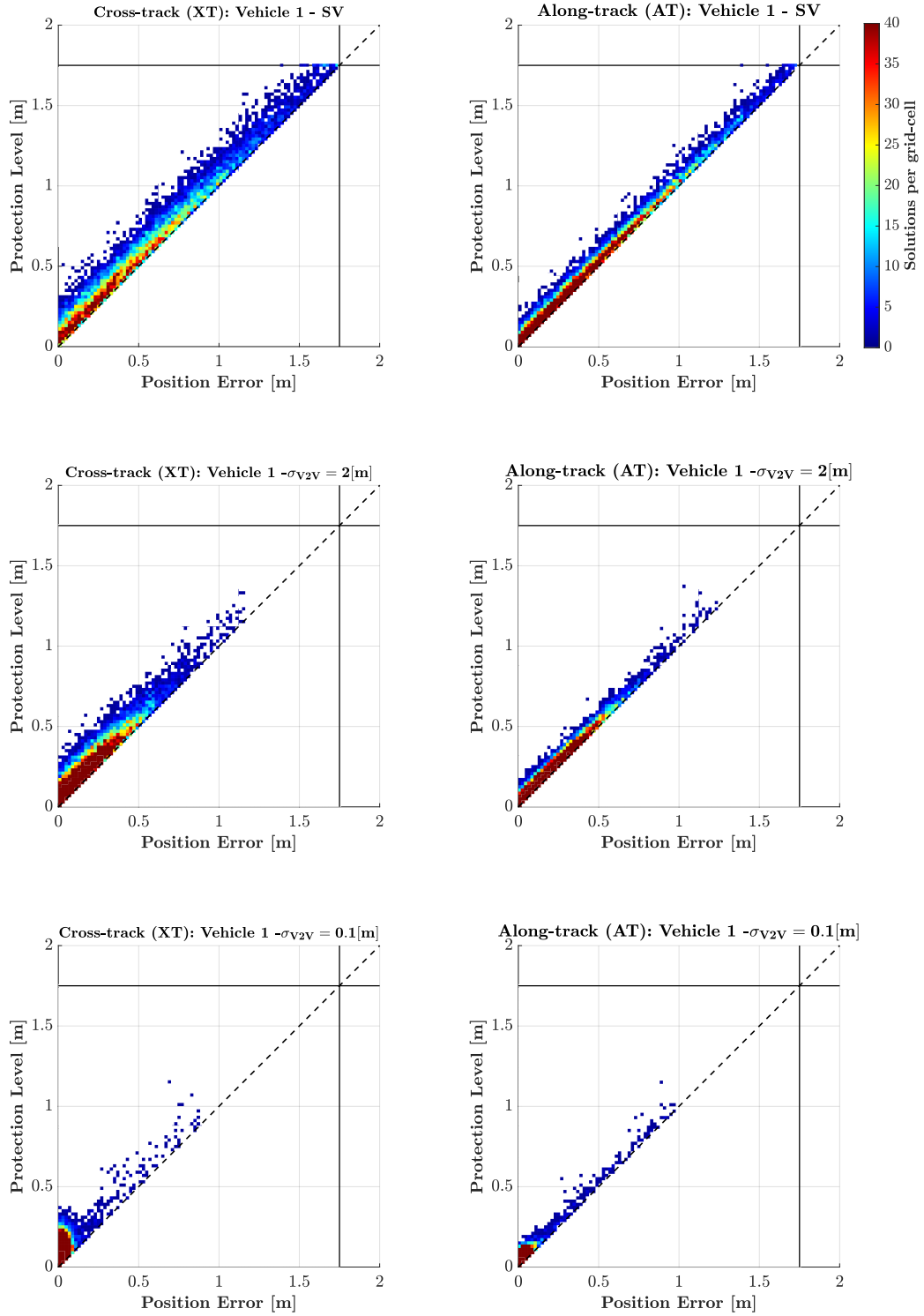


Figure 7.4: Integrity plots (Stanford Diagrams) from the collaborative navigation simulation. In the first row, the graphs for the XT (left panel) and AT (right panel) updated states obtained from the single vehicle (SV) approach are shown. The second and third rows display the integrity results obtained from both 10 vehicles MC simulations, the configuration $\sigma_{\text{GNSS}} = \sigma_{\text{V2V}} = 2\text{ m}$ in the second row and $\sigma_{\text{V2V}} = 0.1\text{ m}$ in the third.

solutions emanate from the inconsistencies between the motion model and actual motion of the vehicles introduced in Chapter 6.

Finally, the integrity requirements for autonomous vehicle localization are established by the governmental organizations, so they can differ largely depending on the requirements of each country. In this direction, REID ET AL. (2019) contains the methodologies to AL and PL depending on the mean road width (type of road), minimum road curvature, and vehicle types in the United States. The given values are considerably smaller than the ones used to display the results in Figure 7.4, with values for local roads in the range of the 0.3–0.5 m (considering an integrity risk of 10^{-8}), both in the XT and AT directions. It is clear from the single-vehicle MC simulation results that most of the solutions are contained in the integrity region that exceeds these AL requirements, demonstrating that a vehicle equipped with a single GNSS receiver under challenging GNSS reception situations is not enough to guarantee the integrity of the system. Nevertheless, the collaborative approaches improve this results, yielding a 95% quantile of the PE below 0.55 m considering $\sigma_{V2V} = 2$ m, and below 0.08 m considering $\sigma_{V2V} = 0.1$ m. Finally, it is worth mentioning that these quantitative values are computed with the configurations shown in Tables 7.1 to 7.3, and they change drastically if a different measurement noise distribution is selected. This together with the fact that most of the weaker solutions are caused by suboptimal estimations leads to the necessity to emphasize that the quantitative results are only computed in order to support the analysis of the impact that the progressive addition of vehicles has on the complete estimation in terms of integrity.

7.4 Summary and Discussion

In this chapter, the advantages of using collaborative methodologies with respect to single-vehicle approaches were presented and assessed with different sets of numerical results. First, an elementary scenario was used in order to demonstrate the PoC, showing that the addition of vehicles to the navigation scenario, inter connected by V2V measurements, result in an increase of accuracy and precision of the estimated parameters. Then, the tendencies identified in the overoptimistic elementary scenario are supported with the evaluation of an MC simulation built upon a more complex scenario, where up to ten vehicles were considered. The profits in the accuracy and precision obtained from the collaborative approach with respect to the single-vehicle approach are significant for all sensor configurations used, regardless of the number of vehicles participating in the navigation scenario and the quality of the V2V measurements. Besides, the performance of the collaborative approach was evaluated in terms of accuracy by computing the overall RMSE of the network, and in terms of precision by examining the network suitability in terms of the A-optimality. This process is repeated by progressively increasing the size of the network, so that the benefits of the collaborative navigation methodologies can also be related to the number of vehicles included in the navigation scenario. This set of results demonstrates the expected outcome in networked-based estimations, showing a general increase in accuracy and precision of the estimation with the progressive addition of vehicles.

In the proposed centralized methodology, the solutions with a high number of vehicles (e.g. ten-vehicle solution) reveal a convergence to a maximum level of accuracy, which is defined by the number of observations considered in the scenario and their precision. Considering the high relevance of the matter, the assessment of the optimum number of dynamic nodes given a certain V2V measurement configuration and the effects of the dynamic network geometry/topology on the estimation remain as open questions for future investigations.

Furthermore, one of the most discussed issues in collaborative scenarios is the time synchronization problem. In the case at hand, the V2V measurements are realized by means of GNSS baselines, which refer to the same time reference so that they can be assumed to be perfectly synchronized. However, in real scenarios this does not happen. On the one hand, the time stability of the receiver clocks contains drifts and random walk errors. These sources of error are crucial to guarantee the robustness of the solution of each individual, since clock errors at the ns level for the GNSS solution are translated into positioning errors at the meter level. On the other hand, the centralized algorithm is assumed to receive the data collected by each individual vehicle in real time. This is also never the case in real scenarios, where the time delay between the data signal emission and reception is directly proportional to the distance to the physical realization of the communication used for the wireless. As a result, the proposed algorithm is only applicable in post-processing. Should the algorithm be adapted for real-time collaborative scenarios, the above-mentioned effects must be deeply studied, so the deterioration of the adjustment is minimized.

In spite of these limitations, the tendencies identified during the evaluation of the collaborative navigation are unequivocal, and the increase shown by the collaborative approach relative to single-vehicle filtering in terms of accuracy, precision and integrity is evident.

8 Conclusions

8.1 Summary

The developments in autonomous navigation and intelligent vehicles require the improvement of algorithms that support the coordination and communication between vehicles. In this framework, the concept of Collaborative Positioning (CP) has been developed as a methodology that enhances the performance of the navigation solution and anticipates events that could optimize the traffic flow and reduce the possibility of accidents. In this thesis, the concept of CP was explored in order to extend the knowledge of dynamic networks, which subsequently aids in the designing phase and assists with the decision about how the network nodes should behave or which instruments must be selected to fulfill a desired target. In addition, the impact of CP in terms of the navigation performance criteria is contrasted with the correspondent single-vehicle approaches.

The evaluation of dynamic networks requires the execution of numerous experiments, which entail the continuous variation of sensor architectures, observational work, number of multi-sensor systems considered, environmental conditions and vehicle dynamics, so that the specific impact of each of these factors in the collaborative scenarios is evaluated. It seems indisputable that the realization of these experiments encompasses an extensive number of resources, and that they can be potentially hazardous for the participants in certain scenarios. As a result, a simulation framework was designed and implemented, which is capable of cost-effectively and safely reproduce collaborative scenarios. The desired scenario for the analysis was achieved by performing four steps: trajectory generation, model of the environment (in 2D or 3D) selection, measurement generation (with the proprio- and exteroceptive sensors available at the i.c.sens project) and estimation with a sensor measurement fusion algorithm. In order to materialize the dynamic network, the V2V links are achieved by computing the GNSS baselines between pairs of vehicles.

In the last step, a specific sensor measurement algorithm was designed which is suitable to simultaneously estimate the state parameters of a group of vehicles. For this purpose, a centralized plane-based Collaborative-Extended Kalman Filter (C-EKF) was selected. The KF-based implementation proves to be adequate for dynamic networks, since it enables the representation of the individual motion of the nodes with continuous-time differential equations, illustrating the network with the discrete-time measurements in the update step. Also, the centralized strategy allows to assess not only the consistency of the data, but also the analysis and evaluation of the dynamic network as a whole, which is the primary target of the thesis. Lastly, the filter considers only planar surfaces identified with the exteroceptive sensors as landmarks for relative positioning of the vehicles with respect to the elements of the environment, given that the 3D city model with

LoD-2 is built up with planar elements. For this reason, this is the only environmental model used for the experiments in the scope of this thesis.

The described simulation framework is used in order to answer the research questions formulated in the introduction of this thesis. Primarily, the filter performance is tested within a complex and realistic scenario by executing the filter with three different approaches that depend on the degree of prior-knowledge assigned to the map elements: (1) localization (without landmark uncertainty), (2) localization with landmark uncertainty, or (3) SLAM. Although the localization approach is the one that yields the most accurate solutions in the simulations, its usage might encompass inconsistencies when relative positioning measurements are fused with absolute measurements in real scenarios. In general, the elements of the map are associated to the accuracy and precision of the technique used to determine its geo location within a certain geodetic reference frame or projection. If imprecise geo-located elements of the environment are introduced in the system as perfectly geo-located elements, the position of the vehicle is biased according to the errors in the location of the detected landmarks, given the much higher proportion and precision of the exteroceptive sensor measurements with respect to the absolute positioning measurements. For this reason, the consideration of the landmark uncertainty for the estimation leads to more accurate results in areas where the geo-location of the environmental elements was not precisely determined. In any case, the mere availability of a model of the environment enables the possibility to solve the computational problem as a localization approach, which yields normally results at the centimeter and decimeter level in the Cross-Track (XT) and Along-Track (AT) directions, respectively. The absence of a map forces the vehicles to reconstruct the scene while simultaneously localizing themselves (SLAM). The unknown geo-location of the environmental elements leads to a general decrease in the overall accuracy and precision of the system, as the estimation loses the fundamental piece of information to anchor the network to a known reference frame. In these estimations, the referencing task relies mainly on the proprioceptive sensors, and more specifically on the GNSS measurements. Furthermore, in absence of GNSS the uncertainty on the initial pose of the vehicle is transferred to the complete map and can only be corrected if absolute measurements are received. Consequently, the influence of the exteroceptive sensor measurements in the estimation stays constrained to the prior availability of a map and to the geo-referencing capabilities of the proprioceptive sensors.

Although the experiment carried out in order to evaluate the simulation and filter specifics already reveal some of the characteristic effects that emanate within dynamic estimations, specific MC-based experiments are designed in order to individually analyze each aspect of the estimation. First, in the transition from the traditional geodetic network optimization methodologies to dynamic network analysis, the biggest challenges arise from the motion of the network nodes. In geodetic networks, the fact that the nodes are stable in time lead to a rather static scene, with no significant changes in the characteristics of the environment and the observational work. As a result, it is possible to compute sets of processing parameters that maximize an objective function used to describe the quality of the network. However, in dynamic networks, the nodes are changing their positions with respect to time, leading not only to high variations in the geometric characteristics of the environment, but also to additional challenges that arise from the vehicle motion itself. As a result, different experiments were carried out in order to evaluate the impact that different network

geometries (different sensor architectures and sensor qualities) and vehicle dynamics have in the estimation.

Firstly, the impact that each sensor has on accuracy and precision of the estimation was evaluated by computing the results obtained with different sensor architectures in a localization approach. The major outcome from this experiment is that in regions with favorable landmark layout (e.g. urban intersection with central symmetry plane layout), the estimation is utterly dominated by the laser scanner and stereo cameras measurements. This happens due to the much higher redundancy and precision of each of the measurements, yielding theoretical values at the millimeter level. Also, since only the geometrical characteristics of the exteroceptive measurements are considered, the stereo cameras seem to be overshadowed by the laser scanner. In our case, the laser scanner is assumed to perform with a field of view of 360° that leads to the possibility to reconstruct not only the elements that lay ahead of the vehicle, but also behind, leading to a general increase in the filter performance. On the contrary, if the landmark layout detected by the exteroceptive sensors is disadvantageous (e.g. urban canyon with almost symmetric parallel planes), the overall accuracy and precision of the solution is constrained by the quality of the GNSS measurements. This, together with the passive character of the exteroceptive sensor measurements (relative positioning), underlines the necessity to include GNSS receivers in the sensor architecture in order to achieve a high performance navigation solution.

Secondly, the motion of the vehicles that form the dynamic network is another crucial factor within the estimation. The prediction step of the C-EKF contains a motion model that anticipates the actions of the vehicles. In dynamic estimations the vast diversity of vehicle maneuvers performed in urban areas causes the motion model to be disrupted at some point, regardless of the model selected. In KF-based approaches, the inconsistencies between the motion model and the actual motion of the object are considered by the process noise, and it must be introduced an amount proportional to the degree of sequential maneuvers performed by the vehicle. In addition, the inefficacy of fixed PSD values in dynamic estimations was demonstrated and the amount of improvement that can be obtained with the most adequate epoch-wise estimations was assessed. Here, the differences between fixed and epoch-wise PSD combinations can exceed the meter level in the 2D position estimations and ten degrees in the heading at some points in time. However, it is difficult to give an answer to the question of an adequate process noise model, that is suitable for the complete set of maneuvers to be performed and for the estimation of the complete set of state parameters. This problem reveals the reason why IMU measurements are normally included in the sensor architecture (besides supporting the geo-location task in GNSS challenging areas). A high-rate ($> 100\text{ Hz}$) device can feed the system with inertial measurements that describe the actual motion of the vehicle in real-time, and consequently reduce the importance of the process noise model in the estimation.

Finally, the benefits of collaborative navigation with respect to single-vehicle approaches are demonstrated. The results show significant improvements of using collaboration in an amount proportional to the quality of the V2V measurements and the number of vehicles (dynamic nodes). The 2D estimations with at least six vehicles interconnected by high quality V2V measurements exceed the 80% of improvement in the accuracy (approx. 0.70 m) of the aided vehicle and 60%

(approx. 0.3 m) in aiding vehicles, with respect to single vehicle approaches with the used configuration. This tendency is also observed in the global analysis (overall network), in which the six-vehicle solution already exceeds the 70% improvement in 2D, if high quality V2V measurements are available. In any case, the results generally reveal that the accuracy and precision of the 2D and 3D positioning estimations increase with the progressive addition of vehicles, although showing marginal disadvantages are observed in the ten-vehicle solution. Thus, the benefits of collaborative navigation are underlined.

To conclude, both the simulation framework and filter methodology designed prove to be very capable in order to create scenarios that aid in the understanding of the dynamic networks and collaborative navigation methodologies. The simulations highlight the individual role played by every sensor within the estimation. Here, we could learn that to maximize the filter performance in terms of accuracy, precision and integrity, the minimum-cost sensor architecture to be considered contains a 3D laser scanner with 360° field of view, a GNSS receiver and a high-rate IMU. The addition of stereo-camera observations as purely geometrical measurements to the mentioned architecture does not lead to substantial improvements. The benefits of the inclusion of stereo cameras are derived from the powerful capabilities in landmark identification and reconstruction tasks, essential in multi-sensor fusion methodologies. However, for a complete reconstruction of the scene, several cameras should be oriented in different directions, slightly rising the cost of the sensor architecture. Furthermore, the selection of an adequate process noise model is fundamental to maximize the performance of the filter. Finally, the collaborative techniques outperform the available single-vehicle approaches significantly in terms of accuracy, precision and integrity, proving to be fairly powerful to achieve safe and robust navigation solutions in autonomous navigation.

8.2 Outlook

The methodologies described in this thesis reveal the versatility of the developed simulation framework in order to obtain answers that can aid the design process of collaborative experiments. However, the simulation framework is constrained to the needs defined within the scope of this thesis, regarding topics such as sensor measurement generated, sensor measurement fusion algorithm or types of vehicles considered. In the future, this work can be extended, with the addition of sensor measurements (e.g. odometer) and noise models in accordance with real sensor specifications, different motion models (adequate also for UAVs), more realistic models of the environment or the possibility to perform the estimation with different methodologies (e.g. particle filter and maximum likelihood approaches). Hence, the strengths and weaknesses of each estimator in collaborative estimations can be assessed. Also, the utilization of a more realistic model of the environment, where the elements of the urban furniture (e.g. trees, walkways etc.) enable a more detailed evaluation of the signal reception. If the satellite visibility is accurately assessed, it would be possible to introduce GNSS pseudorange measurements in a *deeply-coupled* filter implementation, and perform a much more detailed assessment of the benefits of collaborative navigation techniques with respect to single-vehicle approaches.

Furthermore, the impact that each observation has on the estimation is determined numerically. In this experiment, the scenario characteristics constrained the analysis to a three-dimensional parameter space. However, the number of variables (dimensions) considered can be easily expanded given the larger availability of processing parameters. Therefore, the complete set of processing parameters can be used in future investigations in order to define a multi-dimensional domain that contains the feasible values for each parameter. With the expansion of the dimensionality the complexity of the analysis grows significantly, and the tendencies expected within such a complex parameter domain cannot be foreseen. In this matter, machine learning methodologies can be used in order to train the function (the used estimator) with a large number of samples (processing parameter combinations), and obtain as a result an overall idea about the dependencies between processing parameters. Finally, cluster techniques can be used in order to identify patterns within the samples that fulfill the desired target.

Lastly, the dynamic network defined within the scope of this thesis always considers the vehicles as dynamic nodes. Thus, future work could go one step further in by considering the position of each individual sensor as a network node. This would enable the independent evaluation of each sub-network defined by the sensor architecture, which once coupled with realistic vehicle models, allow the determination of the optimum position and orientation of the sensors within the vehicle frame. The outcome would comprise a fundamental piece of information in order to maximize the performance of the multi-sensor system.

Bibliography

- 5GAA, 2016. The case for cellular V2X for safety and cooperative driving. 5G Automotive Association.
- Achtelik, M., Weiss, S., Chli, M., Dellaert, F. and Siegwart, R., 2011. Collaborative Stereo. *in Proceedings of the IEEE/RSJ International Conference on Intelligent Robots and Systems (IROS)* pp. 2242–2248.
- Alam, N., Balaei, A. and Dempster, A., 2011. A DSRC Doppler-Based Cooperative Positioning Enhancement for Vehicular Networks With GPS Availability. *IEEE Transactions on Vehicular Technology* 60(9), pp. 4462–4469.
- Ansari, K., Wang, C., Wang, L. and Feng, Y., 2013. Vehicle-to-Vehicle Real-Time Relative Positioning Using 5.9 GHz DSRC Media. *IEEE 78th Vehicular Technology Conference (VTC Fall)* PP(99), pp. 1–13.
- ArcMap, 2010. ESRI 2011. ArcGIS Desktop: Release 10. Redlands, CA: Environmental Systems Research Institute. <https://desktop.arcgis.com/en/>.
- Avanzini, G., Busato, A. and de Matteis, G., 2001. Trajectory Generation and Tracking for Ship Deck Landing of a VTOL Vehicle. *AIAA Atmospheric Flight Mechanics Conference and Exhibit, Montreal, Canada* pp. 1–10.
- Baarda, W., 1968. *A testing procedure for use in geodetic networks*. Publications on Geodesy: New Series, 2(5), Netherlands Geodetic Commission, Delft.
- Bagheri, M., Siekkinen, M. and Nurminen, J., 2014. Cellular-based Vehicle to Pedestrian (V2P) Adaptive Communication for Collision Avoidance. *2014 International Conference on Connected Vehicles and Expo (ICCVE)* pp. 450–456.
- BeiDOU, 2012. BeiDou Navigation Satellite System - Signal In Space - Interface Control Document - Open Service Signal B1I. <http://www.beidou.gov.cn/xt/gfxz/201805/P020180507527106075323.pdf>.
- Berefelt, F., Boberg, B., Nygård, J. and Strömbäck, P., 2004. Collaborative GPS/INS Navigation in Urban Environment. *ION NTM* pp. 1114–1125.
- Bétaille, D., Peyret, F., Ortiz, M., Miquel, S. and Fontenay, L., 2013. A New Modeling Based on Urban Trenches to Improve GNSS Positioning Quality of Service in Cities. *IEEE Intelligent Transportation Systems Magazine* pp. 59–70.
- Bill, R., 1985. Kriteriummatrizen ebener geodätischer Netze. PhD thesis, DGK Reihe A 102, Deutsche Geodätische Kommission, München.
- Boffi, G., 2018. Uncertainty Prediction and Accuracy Assessment for Highly Accurate GNSS-Based Trajectory and Velocity Determination. PhD thesis, Institute of Geodesy and Photogrammetry, ETH Zurich.
- Borre, K., Akos, D., Bertelsen, N., Rinder, P. and Jensen, S., 2007. *A Software-Defined GPS and Galileo Receiver. A Single Frequency Approach*. Birkhäuser Boston Basel Berlin.

- Brenner, C., 2016. Scalable estimation of precision maps in a MapReduce framework. In: *24th ACM SIGSPATIAL International Conference on Advances in Geographic Information Systems*, pp. 1–10.
- Brown, R. and Hwang, P. Y. C., 1997. *Introduction to Random Signals and Applied Kalman Filtering: with MATLAB exercises*. John Wiley and Sons, Inc.
- Bryson, M. and Sukkarieh, S., 2009. Architectures for Cooperative Airborne Simultaneous Localisation and Mapping. *Journal of Intelligent and Robotic Systems* 55, pp. 267–297.
- Choe, Y., Song, J. and Park, C., 2018. Cluster Sampling Kalman Filter for Urban Canyon Navigation. *31st International Technical Meeting of the Satellite Division of the Institute of Navigation (ION GNSS+ 2018)*, Miami, Florida pp. 244–252.
- Coenen, M. and Rottensteiner, F., 2019. Precise Vehicle Reconstruction for Autonomous Driving Applications. *ISPRS Annals of the Photogrammetry, Remote Sensing and Spatial Information Sciences* IV(2/W5), pp. 21–28.
- Colomina, I. and Blázquez, 2004. A Unified Approach to Static and Dynamic Modelling in Photogrammetry and Remote Sensing. *ISPRS - The International Archives of the Photogrammetry Remote Sensing and Spatial Information Sciences* 35, pp. 178–183.
- Cucci, D. and Skaloud, J., 2019. On Raw Inertial Measurements in Dynamic Networks. *ISPRS Annals of the Photogrammetry, Remote Sensing and Spatial Information Sciences* IV-2/W5, pp. 549–557.
- Cunningham, A., Indelman, V. and Dellaert, F., 2013. DDF-SAM 2.0: Consistent Distributed Smoothing and Mapping. *IEEE International Conference on Robotics and Automation, Karlsruhe, Germany* pp. 5520–5527.
- Dang, T., Hoffmann, C. and Stiller, C., 2009. Continuous Stereo Self-Calibration by Camera Parameter Tracking. *IEEE Transactions on Image Processing* 18(7), pp. 1536 – 1550.
- de Ponte-Müller, F., 2017a. Cooperative Relative Positioning for Vehicular Environments. PhD thesis, Universität Passau.
- de Ponte-Müller, F., 2017b. Survey on Ranging Sensors and Cooperative Techniques for Relative Positioning of Vehicles. *Sensors* 17(2), pp. 1–27.
- de Ponte-Müller, F., Diaz, E. M., Kloiber, B. and Strang, T., 2014. Bayesian Cooperative Relative Vehicle Positioning using Pseudorange Differences. In *2014 IEEE/ION Position, Location and Navigation Symposium - PLANS 2014* pp. 434–444.
- de Ponte-Müller, F., Munoz-Diaz, E. and Rashdan, I., 2016. Cooperative Positioning and Radar Sensor Fusion for Relative Localization of Vehicles. *2016 IEEE Intelligent Vehicles Symposium Gothenburg, Sweden* IV, pp. 1060–1065.
- Dong, J., Nelson, E., Indelman, V., Michael, N. and Dellaert, F., 2015. Distributed Real-time Cooperative Localization and Mapping using an Uncertainty-Aware Expectation Maximization Approach. *IEEE International Conference on Robotics and Automation (ICRA)*, Seattle, Washington pp. 5807–5814.
- Duda, H., Gerlach, T., Advani, S. and Potter, M., 2013. Design of the DLR AVES Research Flight Simulator. *AIAA Modeling and Simulation Technologies (MST) Conference, Boston, MA* pp. 1–14.
- Farrell, J. A., 2006. *Aided Navigation Systems: GPS and High Rate Sensors*. New York, NY, McGraw-Hill.

- Fayad, F. and Cherfaoui, V., 2007. Tracking objects using a laser scanner in driving situation based on modeling target shape. *Proceedings of the 2007 IEEE Intelligent Vehicles Symposium* pp. 44–49.
- Förstner, W. and Wrobel, B., 2016. *Photogrammetric Computer Vision. Statistics, Geometry, Orientation and Reconstruction*. Springer International Publishing Switzerland.
- Gade, K., 2005. NavLav, a Generic Simulation and Post-processing Tool for Navigation. *Modeling, Identification and Control* 26(3), pp. 135–150.
- Gamdhi, T. and Trivedi, M., 2007. Pedestrian Protection Systems: Issues, Survey, and Challenges. *IEEE Transactions On intelligent Transportation Systems* 8(3), pp. 413–430.
- Garcia-Fernandez, N. and Schön, S., 2017. Development of a Simulation Tool for Collaborative Navigation Systems. *14th Workshop on Positioning, Navigation and Communication (WPNC)* pp. 1–6.
- Geiger, A., Ziegler, J. and Stiller, C., 2011. StereoScan: Dense 3D reconstruction in real-time. *Intelligent Vehicle, IEEE Symposium IV*, pp. 963–968.
- Gentle, J. E., 2003. *Random Number Generation and Monte Carlo Methods*. Springer-Verlag New York.
- Giroux, R., Landry, R. J., Leach, B. and Gourdeau, R., 2003. Validation and Performance Evaluation of a Simulink Inertial Navigation System Simulator. *Canadian Aeronautics and Space Journal* 49(4), pp. 149–161.
- GLONASS, 2016. Global navigation Satellite System GLONASS - Interface Control Document. <http://russianspacesystems.ru/wp-content/uploads/2016/08/ICD-GLONASS-CDMA-General.-Edition-1.0-2016.pdf>.
- Görcke, L., Holzapfel, F. and Dambeck, J., 2013. Aerodynamic Flight Simulation in Inertial Quality. *Proceedings of the 2013 International Technical Meeting of The Institute of Navigation* pp. 415–425.
- GPS-Standard, 2008. Global Positioning System Standard. Positioning Service Performance Standard. <https://www.gps.gov/technical/ps/>.
- Grafarend, E. W., 1974. Optimization of Geodetic Networks. *Bolletino di Geodesia a Science Affini* 33(4), pp. 351–406.
- Grafarend, E. W. and Sansò, F., 1985. *Optimization and Design of Geodetic Networks*. Springer-Verlag Berlin Heidelberg New York Tokyo.
- Groves, P. D., 2013. *Principles of GNSS, Inertial, and Multisensor Integrated Navigation Systems*. 2 edn, GNSS Technology and Applications Series. Artech House: Boston, MA, USA.
- Guo, C. X., Kourosh, S., DuToint, R., Georgiou, G., Li, R., O’Leary, J., Nerurkar, E., Hesch, J. and Roumeliotis, S., 2018. Resource-Aware Large-Scale Cooperative Three-Dimensional Mapping Using Multiple Mobile Devices. *IEEE Transactions on Robotics* 34(5), pp. 1349–1369.
- Hajieghrary, H., Kularatne, D. and Hsieh, M., 2018. Differential Geometric Approach to Trajectory Planning: Cooperative Transport by a Team of Autonomous Marine Vehicles. *2018 Annual American Control Conference (ACC)* pp. 858–863.
- Harding, J., Powell, G., Yoon, R., Fikentscher, J., Doyle, C., Sade, D., Lukuc, M., Simons, J. and Wang, J., 2014. Vehicle-to-Vehicle communications: Readiness of V2V technology for application. (*Report No. DOT HS 812 014*). Washington, DC: National Highway Traffic Safety Administration.

- Hartenstein, H. and Laberteaux, K., 2010. *VANET Vehicular Applications and Inter-Networking Technologies*. John Wiley & Sons. Berlin, Germany.
- Heng, L. and Gao, G., 2017. Accuracy or Range-Based Cooperative Positioning: A Lower Bound Analysis. *IEEE Transactions on Aerospace and Electronic Systems* 53(5), pp. 2304–2316.
- Hewitson, S. and Wang, J., 2006. GNSS receiver autonomous integrity monitoring (RAIM) performance analysis. *GPS Solutions* 10(3), pp. 155–170.
- Hofmann-Wellenhof, B., 2008. *GNSS Global Navigation Satellite Systems. GPS, GLONASS, Galileo & more*. Springer Wien New York.
- Howard, A., Matarić, M. and Sukhatme, S., 2002. Localization for Mobile Robot Teams Using Maximum Likelihood Estimation. in *Proceedings of the 2002 IEEE/RSJ Intl. Conference on Intelligent Robots and Systems EPFL, Lausanne, Switzerland* pp. 434–439.
- Hsu, L., Gu, Y., Huang, Y. and Kamijo, S., 2016. Urban Pedestrian Navigation Using Smartphone-Based Dead Reckoning and 3-D Map-Aided GNSS. *IEEE Sensors Journal* 16(5), pp. 1281 – 1293.
- ICAO, 2006. *Convention on International Civil Aviation. Annex 10: Aeronautical Telecommunications. Volume I: Radio Navigation Aids. 6th Edition*. URL: https://www.icao.int/Meetings/anconf12/Document%20Archive/AN10_V2_cons%5B1%5D.pdf (visited in 2020).
- Indelman, V., Williams, S., Kaess, M. and Dellaert, F., 2013. Information fusion in navigation systems via factor graph based incremental smoothing. *Robotics and Autonomous Systems* 61, pp. 721–738.
- Intelligent Transport Systems (ITS)., 2009. European profile standard for the physical and medium access control layer of Intelligent Transport Systems operating in the 5 GHz frequency band. https://www.etsi.org/deliver/etsi_es/202600_202699/202663/01.01.00_50/es_202663v010100m.pdf (visited in 2020).
- Jäger, R., 1988. Analyse und Optimierung geodätischer Netze nach spektralen Kriterien und mechanische Analogien. PhD thesis, DGK Reihe C 342, Deutsche Geodätische Kommission, München.
- Jekeli, C., 2000. *Inertial Navigation Systems with Geodetic Applications*. Walter de Gruyter, New York, NY., USA.
- Jwo, D.-J., Shih, J.-H., Hsu, C.-S. and Yu, K.-L., 2014. Development of a Strapdown Inertial Navigation System Simulation Platform. *Journal of Marine Science and Technology* 22, pp. 381–391.
- Kalman, R. E., 1960. A New Approach to Linear Filtering and Prediction Problems. *Journal of Basic Engineering* 82(1), pp. 35–45.
- Karrer, M., Schmuck, P. and Chli, M., 2018. CVI-SLAM-Collaborative visual-inertial SLAM. *IEEE Robotics and Automation Letters* 3(4), pp. 2762–2769.
- Kealy, A., Retscher, G., Toth, C., Hasnur-Rabiain, A., Gikas, V., Grejner-Brzezinska, D., Danezis, C. and Moore, T., 2015. Collaborative Navigation as a Solution for PNT Applications in GNSS Challenged Environments - Report on Field Trials of a Joint FIG / IAG Working Group. *Journal of Applied Geodesy* 9, pp. 244–263.
- Koch, K., 1985. First Order Design: Optimization of the Configuration of a Network by Introducing Small Position Changes. In: *Optimization and Design of Geodetic Networks*, Springer Verlag Berlin Heidelberg New York Tokyo, pp. 56–73.

- Koch, K., 1988. *Parameter estimation and hypothesis testing in linear models*. Springer-Verlag Berlin.
- Koch, P., May, S., Schmidpeter, M., Kühn, M., Pfitzner, C., Merkl, C., Koch, R., Fees, M., Martin, J., Ammon, D. and Nüchter, A., 2016. Multi-Robot Localization and Mapping Based on Signed Distance Functions. *Journal of Intelligent and Robotic Systems* 83(3-4), pp. 409–428.
- Kokuti, A., Hussein, A., Marin-Plaza, P., de-la Escalera, A. and Garcia, F., 2017. V2X Communications Architecture for Off-Road Autonomous Vehicles. *2017 IEEE International Conference on Vehicular Electronics and Safety (ICVES)* pp. 69–74.
- Koppanyi, Z., Toth, C. K. and Grejner-Brzezinska, D., 2018. Scalable Ad-hoc UWB Network Adjustment. In: *ION PLANS*, pp. 1502–1508.
- Kraftfahrt-Bundesamt, 2018. Verkehr in Kilometern – länderfahrleistung. https://www.kba.de/DE/Statistik/Kraftverkehr/VerkehrKilometer/pseudo_verkehr_in_kilometern_node.html.
- Kuang, S.-L., 1991. Optimization and Design of Deformation Monitoring Schemes. PhD thesis, Department of Geodesy and Geomatics Engineering, University of New Brunswick.
- Kuang, S.-L., 1996. *Geodetic Network Analysis and Optimal Design*. Ann Arbor Press in Chelsea, Mich.
- Laneurit, J. and Blanc, 2003. Multisensorial data fusion for global vehicle and obstacles absolute positioning. in *Proceedings of the IEEE Intelligent Vehicles Symposium IV*, pp. 138–143.
- Le Marchand, O., Bonnifait, P. Ibañez-Guzmán, J., Betaille, D. and Peyret, F., 2009. Characterization of GPS multipath for passenger vehicles across urban environments. *ATTI dell’Istituto Italiano di Navigazione* pp. 77–88.
- Lee, Y., Suh, Y. and Shibasaki, R., 2008. A simulation system for GNSS multipath mitigation using spatial statistical methods. *Computers and Geosciences* 34, pp. 1597–1609.
- Li, J., Bisheng, Y., Chen, C., Huang, R., Dong, Z. and Xiao, W., 2018. Automatic registration of panoramic image sequence and mobile laser scanning data using semantic features. *ISPRS Journal of Photogrammetry and Remote Sensing* 136, pp. 41–57.
- Lindner, P. and Wanielik, G., 2009. 3D LIDAR Processing for Vehicle Safety and Environment Recognition. *IEEE Workshop on Computational Intelligence in Vehicles and Vehicular Systems* pp. 66–71.
- Martinelli, A., Pont, F. and Siegwart, R., 2005. Multi-Robot Localization Using Relative Observations. in *Proceedings of the 2005 IEEE International Conference on Robotics and Automation* pp. 2797–2802.
- Matlab, 2019. MATLAB and Statistics Toolbox Release 2019a, The MathWorks, Inc., Natick, Massachusetts, United States. <https://de.mathworks.com/products/matlab.html>.
- Minetto, A., Nardin, A. and Dovis, F., 2019. GNSS-only Collaborative Positioning Among Connected Vehicles. in *Proceedings of the 1st ACM MobiHoc Workshop on Technologies, Models, and Protocols for Cooperative Connected Cars* pp. 37–42.
- Misra, P. and Enge, P., 2006. *Global Positioning System: Signals, Measurements, and Performance*. Ganga-Jamuna Press, Lincoln MA, 2nd Edition.
- Morrison, J., Galvez-Lopez, D. and Sibley, G., 2016. MOARSLAM: Multiple operator augmented RSLAM. In: *Distributed Autonomous Robotic Systems*, Springer Verlag Japan, pp. 119–132.
- Mourikis, A. and Roumeliotis, S., 2006. Predicting the Performance of Cooperative Simultaneous Localization and Mapping (C-SLAM). *The International Journal of Robotics Research* 25(12), pp. 1273–1286.

- Murray, R., 2007. Recent Research in Cooperative Control of Multivehicle Systems. *Journal of Dynamic Systems, Measurements, and Control* 129(5), pp. 571–583.
- Navipedia, 2014. The Stanford ESA Integrity Diagram: Focusing on SBAS Integrity. [Online]. Available: http://www.navipedia.net/index.php?title=The_Stanford_%E2%80%93_ESA_Integrity_Diagram:_Focusing_on_SBAS_Integrity&oldid=13148.
- Nguyen, U., Rottensteiner, F. and Heipke, C., 2019. Confidence-Aware Pedestrian Tracking Using a Stereo Camera. *ISPRS Annals of the Photogrammetry, Remote Sensing and Spatial Information Sciences* pp. 53–60.
- Noureldin, A., Karamat, T. and Georgy, J., 2013. *Fundamentals of Inertial Navigation, Satellite-based Positioning and their Integration*. Springer-Verlag Berlin Heidelberg.
- Nurmi, J., Lohan, E. and Hurskainen, H., 2015. *GALILEO Positioning Technology*. Springer Netherlands.
- Oleynikova, H., Burri, M., Lynen, S. and Siegwart, R., 2015. Real-Time Visual-Inertial Localization for Aerial and Ground Robots. *IEEE/RSJ International Conference on Intelligent Robots and Systems (IROS)* pp. 3079–3085.
- OpenStreetMap Contributors, 2017. <https://www.openstreetmap.org>.
- Papdimitratos, P., de La Fortelle, A., Evenssen, K., Brignolo, R. and Conseza, S., 2009. Vehicular communication systems: Enabling technologies, applications, and future outlook on intelligent transportation. *IEEE Communications Magazine* 11(47), pp. 84–95.
- Parés, M., Navarro, J. and Colomina, I., 2015. On the generation of realistic simulated inertial measurements. *Inertial Sensors and Systems Karlsruhe, Germany* pp. 1–15.
- Park, C. and Teunissen, P., 2003. A New Carrier Phase Ambiguity Estimation for GNSS Attitude Determination Systems. *Proceedings of international GPS/GNSS symposium, Tokyo* pp. 283–290.
- Parker, R. and Valaee, S., 2007. Cooperative Vehicle Position Estimation. *IEEE International Conference on Communications* pp. 5837–5842.
- Petersen, A. and Koch, R., 2010. Statistical Analysis of Kalman Filters by Conversion to Gauß-Helmert-Models with Applications to Process Noise Estimation. *Pattern Recognition (ICPR), 2010 20th International Conference* pp. 2386–2389.
- Petovello, M. G., 2003. Real-Time Integration of a Tactical-Grade IMU and GPS for High-Accuracy Positioning and Navigation. PhD thesis, University of Calgary.
- Petovello, M., O’Keefe, K., Chan, B., Spiller, S., Pedrosa, C., Xie, P. and Basnayake, C., 2012. Demonstration of Inter-Vehicle UWB Ranging to Augment DGPS for Improved Relative Positioning. *Journal of Global Positioning Systems* 11(1), pp. 11–21.
- Piasco, N., Marzat, J. and Sanfourche, M., 2016. Collaborative localization and formation flying using distributed stereo-vision. *IEEE International Conference on Robotics and Automation (ICRA)* pp. 1202–1207.
- QGIS, 2019. QGIS Geographic Information System. <https://www.qgis.org/en/site/>.
- Åkesson, B., Jørgensen, J., Poulsen, N. and Jørgensen, S., 2007. A Tool for Kalman Filter Tuning. *17th European Symposium on Computer Aided Process Engineering - ESCAPE17* 24, pp. 859–864.

- Reid, T., Houts, S., Cammarata, R., Mills, G., Agarwal, S., Vora, A. and Pandey, G., 2019. Localization Requirements for Autonomous Vehicles. *Proceedings of the WCX SAE World Congress Experience 2019, Detroit, MI, USA, 9-11 April* pp. 1–16.
- Riazuelo, L., Civera, J. and Montiel, J., 2014. C2TAM: A Cloud framework for cooperative tracking and mapping. *Robotics and Autonomous Systems* 62(4), pp. 401–413.
- Roth, J., Schaich, T. and Trommer, G., 2012. Cooperative GNSS-Based Method for Vehicle Positioning. *Gyroscopy and Navigation* 3(4), pp. 245–254.
- Schaffrin, B., 1985. Aspects of Network Design. In: Grafarend E.W. and Sansò, F. (ed.), *Optimization and Design of Geodetic Networks*, Springer-Verlag Berlin Heidelberg New York Tokyo, pp. 548–597.
- Schlingelhof, M., Bétaille, D., Bonnifait, P. and Demaseure, K., 2008. Advanced positioning technologies for co-operative systems. *IET Intelligent Transport Systems* 2(2), pp. 81–91.
- Schmitt, G., 1982. Optmimization of Geodetic Networks. *Reviews of Geophysics and Space Physics* 20(4), pp. 877–884.
- Schmitt, G., 1985a. Review of Network Designs: Criteria, Risk Functions, Design Ordering. In: *Optimization and Design of Geodetic Networks*, Springer-Verlag Berlin Heidelberg New York Tokyo.
- Schmitt, G., 1985b. Second Order Design. In: *Optimization and Design of Geodetic Networks*, Springer Verlag Berlin Heidelberg New York Tokyo.
- Schmitt, G., 1985c. Third Order Design. In: *Optimization and Design of Geodetic Networks*, Springer Verlag Berlin Heidelberg New York Tokyo.
- Schmuck, P. and Chli, M., 2018. CCM-SLAM: Robust and efficient centralized collaborative monocular simultaneous localization and mapping for robotic teams. *Journal of Field Robotics* 36(10), pp. 763–781.
- Schön, S., 2003. Analyse und Optimierung Geodätischer Messanordnungen unter besonderer Berücksichtigung des Intervallansatzes. PhD thesis, DGK Reihe C 342, Deutsche Geodätische Kommission, München.
- Schön, S., Brenner, C., Alkhatib, H., Coenen, M., Dbouk, H., Garcia-Fernandez, N., Fischer, C., Heipke, C., Lohmann, K., Neumann, I., Nguyen, U., Paffenholz, J.-A., Peters, T., Rottensteiner, F., Schachtschneider, J., Sester, M., Sun, L., Vogel, S., Voges, R. and Wagner, B., 2018. Integrity and collaboration in dynamic sensor networks. *Sensors* 18(7), pp. 1–21.
- Schubert, R., Richter, E. and Wanielik, G., 2008. Comparison and Evaluation of Advanced Motion Models for Vehicle Tracking. *11th International Conference on Information Fusion* pp. 1–6.
- Simon, D., 2006. *Optimal State Estimation*. John Wiley and Sons, Inc. Hoboken, New Jersey.
- Solà, J., Monin, A., Devi, M. and Vidal-Calleja, T., 2008. Fusing Monocular Information in Multicamera SLAM. *IEEE Transactions on Robotics* 24(5), pp. 958–968.
- Soloviev, A., 2008. Tight Coupling of GPS, Laser Scanner, and Inertial Measurements for Navigation in Urban Environments . In *IEEE/ION Position, Location and Navigation Symposium (PLANS)* pp. 511–525.
- Sørensen, J. and Madsen, H., 2004. Efficient Kalman filter techniques for the assimilation of tide gauge data in three-dimensional modeling of the North Sea and Baltic Sea system. *Journal of Geophysical Research* 109, pp. 1–14.

- Spangenberg, R., Goehring, D. and Rojas, R., 2016. Pole-based Localization for Autonomous Vehicles in Urban Scenarios. *IEEE/RSJ International Conference on Intelligent Robots and Systems (IROS)* pp. 2161–2166.
- Strandjord, K. and Axelrad, P., 2018. Framework and Techniques for Cooperative Group Situational Awareness in Urban Environments. *31st International Technical Meeting of the Satellite Division of the Institute of Navigation (ION GNSS+ 2018), Miami, Florida* pp. 253–270.
- Tahir, M., Afzal, S., Chughtail, M. and Ali, K., 2019. On the Accuracy of Inter-Vehicular Range Measurements Using GNSS Observables in a Cooperative Framework. *IEEE Transactions on Intelligent Transportation Systems* 20(2), pp. 682–691.
- Teng, Y. and Wang, J., 2017. New Characteristics of Geometric Dilution of Precision (GDOP) for Multi-GNSS Constellations. *The Journal of Navigation* 67, pp. 1018–1028.
- Tennstedt, B. and Schön, S., 2020. Dedicated Calculation Strategy for Atom Interferometry Sensors in Inertial Navigation. *2020 IEEE/ION Position, Location and Navigation Symposium (PLANS)*.
- Teunissen, P. J. G., 1985. Zero Order Design: Generalized Inverses, Adjustment, the Datum Problem and S-Transformations. In: *Optimization and Design of Geodetic Networks*, Springer Verlag Berlin Heidelberg New York Tokyo.
- Teunissen, P. J. G. and Khodabandeh, A., 2014. Review and principles of PPP-RTK methods. *Journal of Geodesy* 89(3), pp. 217–240.
- Thrun, S., 2001. A Probabilistic On-Line Mapping Algorithm for Teams of Mobile Robots. *The International Journal of Robotics Research* 20(5), pp. 335–363.
- Thrun, S., Burgard, W. and Fox, D., 2000. A Real-Time Algorithm for Mobile Robot Mapping with Applications to Multi-Robot and 3D Mapping. *IEEE International Conference on Robotics and Automation* 1, pp. 321–328.
- Thrun, S., Burgard, W. and Fox, D., 2006. *Probabilistic Robotics*. MIT Press.
- Tideman, M. and van Noort, M., 2013. A Simulation Tool Suite for Developing Connected Vehicle Systems. *IEEE Intelligent Vehicles Symposium IV*, pp. 713–718.
- Toledo-Moreo, R., Bétaille, D., Peyret, F. and Laneurit, J., 2009. Fusing GNSS, Dead-Reckoning, and Enhanced Maps for Road Vehicle Lane-Level Navigation. *IEEE Journal of Selected Topics in Signal Processing* 3(5), pp. 798–809.
- Tossaint, M., Samson, J., Toran, F., Ventura-Traveset, J., Sanz, J., Hernandez-Pajares, M. and Juan, J., 2006. The Stanford – ESA Integrity Diagram: Focusing on SBAS Integrity. *Proceedings of the 19th International Technical Meeting of the Satellite Division of The Institute of Navigation (ION GNSS 2006)* pp. 894–905.
- Vidal-Calleja, T., Berger, C., Solà, J. and Lacroix, S., 2011. Large scale multiple robot visual mapping with heterogeneous landmarks in semi-structured terrain. *Robotics and Autonomous Systems* 59, pp. 654–674.
- Vosselman, G. and Maas, H. G., 2010. *Airborne and terrestrial laser scanning*. Dunbeath Caithness: Whittles Publishing.
- Wallentowitz, H. and Reif, K., 2010. *Handbuch Kraftfahrzeugelektronik. Grundlagen, Komponenten, Systeme, Anwendungen*. ATZ/MTZ-Fachbuch, Vieweg+Teubner Verlag.

- Wang, J., Gao, Y., Li, Z., Meng, X. and Hancock, C., 2016. A Tightly-Coupled GPS/INS/UWB Cooperative Positioning Sensors System Supported by V2I Communication. *Sensors* 16(7), pp. 1–16.
- Wieser, A., 2007. GPS based velocity estimation and its application to an odometer. Habilitation, Shaker-Verlag, Aachen.
- Win, M., Shen, Y. and Dai, W., 2018. A Theoretical Foundation of Network Localization and Navigation. *Proceedings of the IEEE* 106(7), pp. 1136–1165.
- Wymeersch, H., Lien, J. and Win, M., 2009. Cooperative Localization in Wireless Networks. *Proceedings of the IEEE* 97(2), pp. 427–450.
- Xu, G., 2007. *GPS. Theory, Algorithms and Applications*. Springer Verlag Berlin Heidelberg.
- Zhang, G., Wen, W. and Hsu, L.-T., 2018. Collaborative GNSS Positioning with the Aids of 3D City Models. *31st International Technical Meeting of the Satellite Division of the Institute of Navigation (ION GNSS+ 2018)*, Miami, Florida pp. 143–149.
- Zhang, Y. and Oliver, D., 2011. Evaluation and error analysis: Kalman gain regularization versus covariance regularization. *Computational Geosciences* 15(3), pp. 489–508.
- Zhou, X. and Roumeliotis, S., 2006. Multi-robot SLAM with Unknown Initial Correspondence: The Robot Rendezvous Case. *2006 IEEE/RSJ International Conference on Intelligent Robots and Systems* pp. 1785–1792.
- Zhu, C., Steinmetz, C., Belabbas, B. and Meurer, M., 2019. Feature Error Model for Integrity of Pattern-based Visual Positioning. *Proceedings of the 32nd International Technical Meeting of the Satellite Division of The Institute of Navigation (ION GNSS+ 2019)* pp. 2254–2268.
- Zou, D. and Tan, P., 2013. CoSLAM: Collaborative Visual SLAM in Dynamic Environments. *IEEE Transactions on Pattern Analysis and Machine Intelligence* 35(2), pp. 354–366.

Acknowledgements

This thesis was developed during my employment at the Institut für Erdmessung (IfE) at the Leibniz Universität Hannover, and it was supported by the German Research Foundation (DFG) as a part of the Research Training Group (RTG) i.c.sens [GRK2159].

First of all, I would like to thank my supervisor Prof. Dr.-Ing. Steffen Schön for his excellent guidance through each stage of the process. He was always an essential source of knowledge and motivation that triggered my curiosity, and encouraged the developments carried out within the scope of this thesis. Furthermore, I would also like to thank my two co-reviewers, Prof. Dr. Andreas Wieser and Prof. Dr.-Ing.habil. Christian Heipke for taking the time to review the work and provide constructive criticism.

I am also grateful to apl. Prof. Dr.-Ing. Claus Brenner and Dr.-Ing. Hamza Alkhatib for taking the time from their busy schedules to meet and provide me with really valuable advice that surely has had an impact on the quality of the results.

I am extremely grateful to my colleagues as well for their continuous willingness to exchange ideas, being always able to have scientific discussions while having fun in the process. Here, a special mention is due to Max Coenen, Max Mehlretter, Raphael Voges and Thomas Krawinkel for constantly supporting me and providing me with fundamental feedback during the writing stages of the dissertation.

Gustaríame tamén agradecer á miña familia todo o apoio que recibín dende que comecei os estudos. Tanto ós meus pais como o meu irmán, porque nunca faltou na casa o exemplo de que as cousas só se conseguen con traballo duro e de que os riscos sempre pagan a pena. Moitísimas gracias por confiar sempre en min.

Gardo o último lugar para o agradecemento máis especial á miña muller, Lorena, pola súa paciencia, empatía e ánimo incondicionais. A miña persoa favorita. Gracias por todo.

Nicolas Garcia-Fernandez

March 2020

Curriculum Vitae

Personal Information

Name	Nicolas Garcia-Fernandez
Date of birth	12.06.1988 in Betanzos, Spain

Work Experience

since Dec. 2016	Leibniz University Hannover (Germany) Institute für Erdmessung <i>Research Assistant</i>
2012-2014	Toponort S.A. <i>Survey Engineer</i>

Education

2012 - 2016	Hochschule Karlsruhe (Germany) Geomatics <i>Master of Science</i>
2013 - 2014	Universidade de Santiago de Compostela (Spain) Course Geomatics and Geodesy <i>Bachelor of Science</i>
2008 - 2011	Universidade de Santiago de Compostela (Spain) Course Survey Engineering <i>Bachelor of Science</i>
2000 - 2006	High School <i>A-levels</i>